Time-Domain TeraHertz Spectroscopy and Observational Probes of Prebiotic Interstellar Gas and Ice Chemistry

Thesis by

Brett Andrew McGuire

In Partial Fulfillment of the Requirements

for the Degree of

Doctor of Philosophy

California Institute of Technology

Pasadena, California

2015

(Defended May 21, 2014)

For Mom & Dad

Acknowledgements

If my time thus far in science has taught me one thing, it is that progress does not occur in isolation. There are numerous names that should share the author list on this thesis with my own. I can only hope to include them all here, and suffer the inevitable cringe after printing when I realize the list will never be complete.

First and foremost I must acknowledge the guidance, support, and encouragement of my parents, Mark and Mary, not only for their love and kindness through the years, which have been endless, but for hooking me on science from the very beginning. Some of my earliest memories are of my mother hosting an after-school science class at our house. We put Ziploc bags over the leaves of trees and watched the condensation grow within as the plants processed water and light. When my father was stuck with me because school was out, but college was still running, he would sit me down at a table during his lectures and give me indicator solutions to play with – my very first exposure to the world of chemistry (and spectroscopy!). I'm also blessed, and occasionally cursed, with having Lindsay not only as a great sister, but as the only world record-setting powerlifter in the family (that's in print now, Linz, in a library!).

My journey into astrochemistry is solely due to the influence of one man, Professor Ben McCall, who captured my imagination one rainy evening the fall of my sophomore year when I learned all about the wacky, crazy chemistry going on in space. Ben took a wildly inexperienced undergrad and entrusted me with my own project immediately, giving me a sense of being able to operate independently that I'd never really had previously. Over the years he has continued to be a constant and invaluable source of wisdom and counsel. I'm also grateful to the entire McCall research group (more than 20 people during my time there!) for being a second family away from my home.

Three individuals bear special recognition for their advice and assistance, both in science and in life: Colonel Brian Tom, Kyle Crabtree, and Nick Indriolo.

While Ben started me on my path in this field, it was my Master's advisor, Professor Susanna Widicus Weaver, who taught me how to be a graduate student, and first introduced me to the world of observational astronomy. Susanna also invested a great deal of time, effort, and resources in getting me out of the lab and into both the field, training me to operate a radio telescope hands-on, and in the community. My professional network expanded exponentially during my time in her group, and it has lead to many great collaborations since. Once again, my labmates were a second family to me, and made my experience there a memorable one – thanks Jay, Mary, Jake, and Brian! I also made some life-long friends during my time at Emory who were instrumental in helping to maintain my sanity – Jen, David, Lisa, Caitlin, and Mike, especially!

Since moving to Caltech, I've had the fortune to make more friends in one space than I think I've had my entire life, who have made the stresses of grad school far more manageable, and though I can't list them all here, I'd like to acknowledge those that have had the largest impact on my time here – Mike, Julian, Marti, Lauren, Beau, Tania, Greg, Matt, and Christine. My labmates – Dan, Ian, Nate, Jacob, Matt, Xander, Masha, Coco, Alex, and Dana have been fantastic to work with and great friends. Particular shout-outs go to Sergio Ioppolo and Marco Allodi. Thanks to Sergio for bringing his years of experience in laboratory spectroscopy to the table, and for being patient and willing to share that expertise with me. Thanks to Marco, not only I can operate a high-powered laser system without destroying it or burning the building to the ground, but my English grammar has greatly improved, and I've learned how to play the Frequent Flier programs like an expert. And finally, my greatest of thanks go to Brandon Carroll, who has stuck with me since my grad school adventure started more than 5 years ago in Atlanta, and has been an invaluable friend, research partner, and source of strength through the years.

My thesis is divided into to parts: observational astronomy and laboratory astrophysics. I am forever indebted to Dr. Anthony Remijan for going out on a limb and trusting me with my first fully-astronomy-based publication and for sticking with me since. Tony is a never-ending source of

fantastic ideas, a wealth of astronomical knowledge, and a no-nonsense problem solver who always has my back. Through Tony, I have made numerous forays into the world of radio astronomy and made connections and collaborations that have advanced my career in this field further than I could have imagined. I'm lucky enough to continue with Tony as my postdoctoral advisor and look forward to many great years to come.

And finally, I'm inexpressively thankful to Professor Geoff Blake. Geoff welcomed me into his group at a time when even I was unsure whether I would ultimately succeed in this effort. I couldn't ask for a better mentor as I chase a career in both laboratory chemistry and observational astronomy than one of the pioneers of the practice himself. He has provided me not only the freedom to explore the questions that I find interesting, but has lent his vast knowledge and experience, encouragement, and resources to those explorations. As I pursue my own career in academia, I can only hope to emulate him by providing my own future students the same incredible experience, and to inspire in them the same curiosity and love for research that he has in me.

Abstract

Understanding the origin of life on Earth has long fascinated the minds of the global community, and has been a driving factor in interdisciplinary research for centuries. Beyond the pioneering work of Darwin, perhaps the most widely known study in the last century is that of Miller & Urey, who examined the possibility of the formation of prebiotic chemical precursors on the primordial Earth [1]. More recent studies have shown that amino acids, the chemical building blocks of the biopolymers that comprise life as we know it on Earth, are present in meteoritic samples, and that the molecules extracted from the meteorites display isotopic signatures indicative of an extraterrestrial origin [2]. The most recent major discovery in this area has been the detection of glycine (NH_2CH_2COOH), the simplest amino acid, in pristine cometary samples returned by the NASA STARDUST mission [3]. Indeed, the open questions left by these discoveries, both in the public and scientific communities, hold such fascination that NASA has designated the understanding of our "Cosmic Origins" as a key mission priority.

Despite these exciting discoveries, our understanding of the chemical and physical pathways to the formation of prebiotic molecules is woefully incomplete. This is largely because we do not yet fully understand how the interplay between grain-surface and sub-surface ice reactions and the gas-phase affects astrophysical chemical evolution, and our knowledge of chemical inventories in these regions is incomplete. The research presented here aims to directly address both these issues, so that future work to understand the formation of prebiotic molecules has a solid foundation from which to work.

From an observational standpoint, a dedicated campaign to identify hydroxylamine (NH_2OH), potentially a direct precursor to glycine, in the gas-phase was undertaken. No trace of NH_2OH was

found. These observations motivated a refinement of the chemical models of glycine formation, and have largely ruled out a gas-phase route to the synthesis of the simplest amino acid in the ISM. A molecular mystery in the case of the carrier of a series of transitions was resolved using observational data toward a large number of sources, confirming the identity of this important carbon-chemistry intermediate B11244 as l-C_3H^+ and identifying it in at least two new environments. Finally, the doubly-nitrogenated molecule carbodiimide HNCNH was identified in the ISM for the first time through maser emission features in the centimeter-wavelength regime.

In the laboratory, a TeraHertz Time-Domain Spectrometer was constructed to obtain the experimental spectra necessary to search for solid-phase species in the ISM in the THz region of the spectrum. These investigations have shown a striking dependence on large-scale, long-range (i.e. lattice) structure of the ices on the spectra they present in the THz. A database of molecular spectra has been started, and both the simplest and most abundant ice species, which have already been identified, as well as a number of more complex species, have been studied. The exquisite sensitivity of the THz spectra to both the structure and thermal history of these ices may lead to better probes of complex chemical and dynamical evolution in interstellar environments.

Contents

List of Figures

List of Tables

Part I

Introduction

NASA missions have found some of the most chemically-diverse organic materials ever detected in astronomical environments, yet there is no agreed-upon chemical pathway as to their formation. We know from meteorites and, more recently, cometary samples returned by the STARDUST mission that amino acids, the building blocks of life as we understand it, are present in extraterrestrial sources [3]. In the last decade, complex gas-grain chemical models have become widely-used tools in the attempt to understand the chemical pathways that can result in the species observed and their abundances in interstellar environments. A key goal of these models is to predict the most likely chemical pathways for the formation of life-essential molecules, such as amino acids. Once found, observational studies can then be conducted in an attempt to discover the precursor molecules involved in the reactions predicted by the model. While such methods can be valuable, they suffer from a lack of both laboratory and observational data with which to constrain them. Thus, observational follow-ups to these studies are vital.

My work, both in laboratory astrophysics and observational astronomy, aims to address both of these issues and advance the quest towards the definitive detection and characterization of life-essential molecules such as glycine in the interstellar medium (ISM). The quest to understand the chemical evolutionary history of life-essential polymers such as proteins, sugars, and amino acids, has been a driving force in molecular astrochemistry for several decades. The discovery of these biopolymer building blocks in meteorites and cometary samples represents a significant clue to the mechanisms that could eventually lead to the delivery of biotic and prebiotic molecules to planetesimals, the rocky precursors to planets, but it does not provide a definitive answer to one of the biggest remaining open questions: *Where and when do the majority of these species form?* Do they form in the gas phase before incorporation into comets or directly into planetesimals? Do they form in the icy mantles of dust grains or comets themselves before delivery? Or, are they largely formed from precursor molecules after or upon impact with planetesimals? My work has focused on approaching these questions through a combined effort of observational astronomy and laboratory astrophysics.

To truly begin to understand the complexities of the chemical processes that give rise to species such as glycine, a thorough understanding of the chemical inventories, and the physical conditions in which they exist, is essential. Such an understanding requires that observational work encompass the full range of states in which these species can be formed - from cm- and mm-wave observations of gas-phase species, to observations of condensed-phase species in the near- to far-infrared. In turn, the scope and direction of laboratory work is necessarily informed and shaped by these observations.

The observational work presented in Part II is aimed at understanding the breadth of molecular complexity present in the ISM, and how that complexity is affected by, and can be used to understand, both the physical environments in which molecules are present and the evolution of those environments. This work relies heavily on complementary laboratory data. While gas-phase species, such as those discussed in Part II, are relatively well-studied in the laboratory, the body of work relating to solid-phase species of astrophysical-interest lacks a corresponding depth. The work presented in Part III aims to address this issue through the construction of a spectrometer and collection of spectra of astrophysically-relevant species in the largely unexplored TeraHertz (THz) region of the spectrum. This historically opaque frequency regime has recently become illuminated through the commissioning of a number of astronomical observatories that operate in this range.

Part II

Observational Astronomy

Chapter 1

Hydroxylamine (NH_2OH)

The bulk of this chapter is reproduced from "A search for hydroxylamine (NH_2OH) toward select astronomical sources," by R.L. Pulliam, B.A. McGuire, and A.J. Remijan, Astrophysical Journal, 751, 1 (2012) [4].

1.1 A Brief History of Hydroxylamine

Hydroxylamine (NH_2OH) has been suggested as a possible reactant precursor in the formation of interstellar amino acids [5; 6] through the reaction of the neutral, ionized, or protonated species with with acetic or propanoic acid. In 2008, a state-of-the-art gas-grain model of complex chemistry in star-forming regions predicted an NH_2OH column density as high as 10^{16} cm^{-2} toward typical hot core sources [7]; easily within the detectable limits of modern radio telescopes. Motivated by this surprisingly large predicted abundance, we searched for NH_2OH using the NRAO 12 m Telescope on Kitt Peak towards IRC+10216, Orion KL, Orion S, Sgr B2(N), Sgr B2(OH), W3IRS5, and W51M. We found no evidence for NH_2OH in any of the sources, and in fact derived upper limits as six orders of magnitude lower than predicted by models [4]. The details of this work are described in the remaining sections of this chapter.

Concurrently, laboratory investigations were undertaken by a laboratory astrophysics group in Leiden to elucidate the mechanisms of NH_2OH formation on grain surfaces [8]. In our work, we assert that there is no reason to assume that hydrogenation of NO proceeds to NH_2OH via the same pathways as CO hydrogenation proceeds to CH_3OH, as assumed by [7]. This was confirmed by [8],

when it was determined that unlike CO hydrogenation, in which several steps possess a non-trivial barrier to reaction, NO hydrogen proceeds with no reaction barriers. Using their experimentally-determined reaction pathways and a model for dark cloud chemistry, they predict peak gas-phase NH_2OH abundances that are well aligned with the upper limits in our observations. Not long after, the original model of [7] was refined, taking the laboratory work of [8] and others other into account, and the new model also predicts peak abundances in line with our observed upper limits [9].

Our recent efforts to detect this model have focused on the shocked outflow region L1157-B1. This region is known to be rich in complex organic molecules despite relatively cool temperatures, indicating that molecules are formed in the solid phase before being non-thermally desorbed into the gas phase. We think such regions are ideal candidates for locating NH_2OH in sufficiently high abundance, as these shock processes may liberate additional NH_2OH into the gas phase beyond that which would be present under thermal equilibrium between the grain surface and the surrounding gas.

1.2 Introduction

The presence of amino acids in the gas-phase toward astronomical environments would have a profound impact on the effort to understand the origin of complex molecular material in space. The recent discovery of the simplest amino acid glycine (NH_2CH_2COOH) in cometary samples collected by the Stardust mission has provided new clues towards our understanding of the delivery of prebiotic material to planetesimals [3], yet not to their initial formation. That is, are complex prebiotic molecules, such as glycine, formed via reactions of smaller precursors *after* their incorporation into cometary bodies, or do these complex molecules form first in the gas phase before accretion? The search for interstellar, gas-phase glycine has therefore attracted much attention, but has yet to be unambiguously confirmed in space [10; 11]. Recently, laboratory experiments have shown that ionized NH_2OH, reacting in the gas phase with acetic acid (CH_3COOH) and propanoic acid (CH_3CH_2COOH), can lead to the formation of glycine and the amino acids α- and β-alanine ($CH_3CH(NH_2)COOH$) [5; 6]. As acetic acid has already been observed in various environments ([12]

and references therein), the detection of NH_2OH would be of much interest to the astrochemistry community, helping to answer the question of how these large complex molecules form in astronomical environments.

There are few laboratory studies of NH_2OH formation. Nishi et al. (1984) [13] proposed a route for synthesis of NH_2OH involving ice mixtures of water and ammonia where a radical recombination reaction (Equation 1.1) on the surface of the ice under irradiated conditions produces NH_2OH.

$$NH_2 + H + H_2O \rightarrow NH_2OH + H_2 \tag{1.1}$$

Additionally, Zheng & Keiser (2010) [14] have recently produced NH_2OH through electron irradiation of water-ammonia ices. They propose that NH_2OH results from the radical recombination of NH_2 and OH inside the ices. The results of both of these studies suggest that radical reactions within ice mantles on grain surfaces may be responsible for NH_2OH production.

In fact, two recent gas-grain chemical models employ such reactions of radicals in their simulations. Charnley et al. (2001) [15] assumed that nitrogen atoms will first react with OH in the gas-phase to produce large amounts of NO (Equation 1.2). A fraction of NO ($\sim$10%) is then accreted onto dust grains, where it can then be converted to form species such as HNO and NH_2OH through H addition reactions. This formation pathway is contingent upon the depletion of NO onto dust grains in significant quantities in astronomical environments, though solid evidence for NO on grain surfaces is limited. Observational evidence for the presence of NO on grain mantles was first reported in the infrared by Allamandola & Norman (1978) [16] via the fundamental rovibrational band at 5.3 μm. More recently, Akyilmaz et al. (2007) [17] have shown that gas-phase NO is depleted towards the peak of dust emission in two sources, suggesting that NO has accreted onto the grains in these regions.

$$N + OH \rightarrow NO + H \tag{1.2}$$

A more recent model by Garrod et al. (2008) [7] employs a more expansive network of radical-radical reactions within the ice-mantle, incorporating large radicals formed from photolysis of the

ice constituents already known to be present. These radical "fragments" then react to build up more complex species as they become mobile on the grain surface through a gradual warm-up process before being liberated into the gas phase. Formation of NH_2OH is predicted to start from the radical-radical reaction of NH+OH addition on grain surfaces, followed by hydrogenation or directly by the reaction of OH+NH_2. The model predicts an NH_2OH column density as high as 10^{16} cm^{-2}; easily within the detectable limits of modern radio telescopes.

Given the potential importance of NH_2OH to prebiotic chemistry and the high predicted abundances, we conducted a search for NH_2OH towards seven sources: IRC+10216, Orion KL, Orion S, Sgr B2(N), Sgr B2(OH), W3IRS5, and W51M in the frequency range of 130-170 GHz. While these sources are known to contain copious amounts of complex molecular material, no definitive evidence was found for NH_2OH toward any of these sources. Upper limits to the beam averaged column density of NH_2OH were calculated based on the 1σ rms noise limit of the observed spectra, and we discuss possible explanations for the lower than expected abundances.

1.3 Observations

A 2 mm spectral line survey of IRC+10216, Orion KL, Orion S, Sgr B2(N), Sgr B2(OH), W3IRS5, and W51M (hereafter, the Turner 2mm Survey) was conducted using the NRAO[1] 12 m telescope on Kitt Peak by B. E. Turner between 1993 and 1995[2]. Table 1.1 lists the observing parameters for each source in the survey. The frequency range covered by this survey was between 130-170 GHz, and the half-power beam width (HPBW) varied from $38'' - 46''$ across the band. The observations were taken using a dual channel, SIS junction single side band receiver with typical receiver noise ranging from 75 - 100 K. The backend consisted of a 768 channel, 600 MHz bandwidth hybrid spectrometer with spectral resolution of 0.781 MHz per channel, or $\sim$1.3 km s^{-1} at 150 GHz. The intensity scale at the NRAO 12m is given as T_R^* and corrects for forward spillover loss. The radiation temperature

[1]The National Radio Astronomy Observatory (NRAO) is a facility of the National Science Foundation, operated under cooperative agreement by Associated Universities, Inc.

[2]The survey data are available online (http://www.cv.nrao.edu/Turner2mmLineSurvey) with the Spectral Line Search Engine (SLiSE) developed by A. J. Remijan and M. J. Remijan. Further details of the Turner 2mm survey including the motivation for a complete survey of these sources are described in Remijan et al. 2008, arXiv:0802.2273v1 [astro-ph]

Table 1.1: Observed sources and coordinates (J2000), spectral line widths, and v_{LSR} for each source.

Source	RA	Dec	ΔV (km s^{-1})	v_{LSR} (km s^{-1})
Orion KL	05 35 14.5	-05 22 32.6	4.5	$+9^a$
Orion S	05 35 16.5	-05 19 26.7	4.5	$+7^b$
IRC+10216	09 47 57.3	+13 16 43.0	9.0	-26^c
Sgr B2(OH)	17 47 20.8	-28 23 32.2	9.0	$+60^d$
Sgr B2(N)	17 44 11.0	-28 22 17.3	9.0	$+62^e$
W51M	19 16 43.8	+14 30 07.5	9.0	$+57^f$
W3IRS5	02 27 04.1	+61 52 21.4	9.0	-39^g

References. – a) [21] b) [22] c) [23] d) [24] e) [25] f) [26] g) [27]

is defined in Equation 1.3, where ζ_c is the beam efficiency. These data were mined for the all of the available 2 mm lines of NH_2OH listed in Table 1.2.

$$T_R = T_R^*/\zeta_c \tag{1.3}$$

In total, 54 transitions of NH_2OH are reported between 130 and 170 GHz from the published literature [18; 19; 20]. Of these 54 transitions, 14 were selected, five *a*-type transitions and nine *c*-type transitions, for this search because these 14 transitions had the largest line strength and lowest upper-state energy level. Table 1.2 is a summary of each transition targeted in this search. Other relevant spectroscopic parameters such as the NH_2OH dipole moments, partition function and rotational constants are listed in the Notes of Table 1.2.

1.4 Data Analysis and Results

Figures 1.1-1.3 show the observed spectra (black trace) for each source in the frequency range of the NH_2OH target transitions. Shown in red is a simulated spectrum of the expected transition line strengths from NH_2OH using the total column density predicted for Sgr B2(N) from the Garrod et al. (2008) [7] model and source-appropriate rotational temperatures and linewidths (Equation 1.4). While the total column density of NH_2OH in sources other than Sgr B2(N) can be expected to vary based on chemical composition and physical environment, the simulations serve to show in

Table 1.2: Observed transitions of NH_2OH, beam size, and parameters used to simulate the spectra and calculate NH_2OH beam averaged column densities (see Equation 1.4).

Rest Frequency (MHz)	Transition $J_u(K_aK_c) - J_l(K_aK_c)$	θ_b ($''$)	E_u (cm^{-1})	Type	$Log_{10}(A_{ij})$ (s^{-1})	g_{J_u}
151020.70	3(1,3)-2(1,2)	41.52	10.57	a	-5.27587	7
151101.99	3(2,2)-2(2,1)	41.50	27.16	a	-5.47928	7
151102.32	3(2,1)-2(2,0)	41.50	27.16	a	-5.47928	7
151117.67	3(0,3)-2(0,2)	41.49	5.04	a	-5.22390	7
151207.01	3(1,2)-2(1,1)	41.47	10.57	a	-5.27422	7
164340.78	9(1,9)-9(0,9)	38.15	75.59	c	-7.02982	19
164627.49	8(1,8)-8(0,8)	38.09	60.48	c	-7.02783	17
164883.24	7(1,7)-7(0,7)	38.03	47.04	c	-7.02617	15
165107.71	6(1,6)-6(0,6)	37.98	35.28	c	-7.02472	13
165300.63	5(1,5)-5(0,5)	37.93	25.2	c	-7.02335	11
165461.76	4(1,4)-4(0,4)	37.89	16.8	c	-7.02237	9
165590.89	3(1,3)-3(0,3)	37.87	10.08	c	-7.02148	7
165687.89	2(1,2)-2(0,2)	37.84	5.04	c	-7.02079	5
165752.62	1(1,1)-1(0,1)	37.83	1.68	c	-7.02037	3

a) Molecular data were obtained from the Cologne Database for Molecular Spectroscopy [18] available at www.splatalogue.net [28]. The uncertainties of the transition frequencies are 50 kHz [19].
b) Degeneracies calculated as: $g_{J_u} = 2J + 1$, $g_{K_u=0} = 1$, $g_{K_u\neq 0} = 2$
c) Rotational constants from the CDMS Database:
A = 190976.2 MHz, B = 25218.73 MHz, C = 25156.66 MHz
d) NH_2OH dipole moments in Debye [18]: μ_A=0.589; μ_C=0.060
e) The functional form of the rotational partition function was determined from Equation 3.69 of [29] - $Q_{rot}=0.5T_{rot}^{1.5}$, and confirmed by a fit to the partition function data given in [18].

a qualitative sense that the searched-for transitions of NH_2OH are not present toward these sources beyond the 1σ RMS noise limit, and certainly not present in the abundances predicted by the model. In several sources, emission features are present at a number of the appropriate center frequencies for NH_2OH. Yet, the strongest transitions of NH_2OH in this band are the $J = 3$-2 manifold near 151 GHz, and in no source are all of the expected transitions observed. This indicates that the observed emission features are coincidental overlap with other molecular transitions, and that NH_2OH is not observed in these sources.

The column density of an observed species can be calculated using Equation 1.4, following the convention of [30] (c.f. [31]).

$$N_T = \frac{3k}{8\pi^3} \times \frac{Q_r e^{E_u/T_{ex}}}{\nu S\mu^2} \times \frac{\sqrt{\pi}}{2ln2} \times \frac{\Delta T_A^* \Delta V/\eta_b}{1 - \frac{(e^{h\nu/kT_{ex}}-1)}{(e^{h\nu/kT_{bg}}-1)}} \text{ cm}^{-2} \tag{1.4}$$

Here, N_T is the total column density, Q_r is the rotational partition function, E_u is the upper state energy, T_{ex} is the excitation temperature, ν is the frequency of the transition, $S\mu^2$ is the transition strength, ΔT_A^* is the peak line intensity, ΔV is the line width, η_b is the beam efficiency at frequency ν, and T_{bg} is the background temperature. The source of the observed emission is assumed to completely fill the beam.

Using Equation 1.4, upper limits to the beam averaged column density based on the 1σ RMS noise limit were calculated, and are reported in Table 1.3. An approximate rotational temperature appropriate for each source was used based on data available in the references shown in Table 1.3. For the purposes of this work, CH_3OH was used as a primary source of temperature information when available. CH_3OH was chosen due to it structural similarities with NH_2OH and its presence in the majority of these sources, allowing for greater consistency than would be possible using other molecules, such as amines. Further, the wealth of observational data on CH_3OH makes temperatures derived from its observations more accurate. In any case, the upper limits presented here are fairly insensitive to the relatively minor range of rotational temperatures observed in these sources. Fractional abundances with respect to molecular hydrogen were calculated for each source based on these upper limits. In the case of Sgr B2(N), the Garrod et al. (2008) [7] model predicts

Table 1.3: 1σ RMS level of T_R^*, upper limits on column density of NH_2OH, H_2 column density, relative abundance of NH_2OH, and assumed value of T_{rot}.

Source	T_R^* (mK)	N_{NH_2OH} (cm^{-2})	N_{H_2} (cm^{-2})	N_{NH_2OH}/N_{H_2}	T_{rot} (K)
Orion KL[a]	6.4	$<2 \times 10^{13}$	7.0×10^{23}	$<3 \times 10^{-11}$	120
Orion S[b]	4.0	$<9 \times 10^{12}$	1.0×10^{23}	$<9 \times 10^{-11}$	80
IRC+10216[c]	5.1	$<8 \times 10^{13}$	3.0×10^{22}	$<3 \times 10^{-9}$	200
Sgr B2(OH)[d]	7.0	$<3 \times 10^{13}$	1.0×10^{24}	$<3 \times 10^{-11}$	70
Sgr B2(N)[e]	6.6	$<2 \times 10^{13}$	3.0×10^{24}	$<8 \times 10^{-12}$	70
W51M[f]	7.7	$<4 \times 10^{13}$	1.0×10^{24}	$<4 \times 10^{-11}$	100
W3IRS5[g]	4.3	$<2 \times 10^{13}$	5.0×10^{23}	$<3 \times 10^{-11}$	70

a) T_{rot} from [21]; N_{H_2} from [32] and Refs. therein.
b) T_{rot} from [22]; N_{H_2} from [32] and Refs. therein.
c) T_{rot} from [33]; N_{H_2} from [34]
d) T_{rot} from [24]; N_{H_2} from [32] and Refs. therein.
e) T_{rot} and N_{H_2} from [25]
f) T_{rot} from [26]; N_{H_2} from [32] and Refs. therein.
g) T_{rot} and N_{H_2} from [27]

a relative abundance for NH_2OH of 3.5×10^{-7} - 4.2×10^{-6}, which is up to six orders of magnitude higher than the observed upper limits.

1.5 Discussion

In this paper, we reported on the negative detection of hydroxylamine (NH_2OH) towards several astronomical sources. Upper limits to the beam averaged column density have also been determined for each source based on the 1σ RMS noise level in each spectra. Recent chemical models introduced a new gas-grain chemical network utilizing radical-radical reactions as formation mechanisms [7]. The model reproduces the beam averaged column densities of species such as methanol (CH_3OH), acetaldehyde (CH_3CHO), and even glycolaldehyde ($CH_2(OH)CHO$) with excellent agreement with current observed abundances toward the Sgr B2(N) star-forming region [7]. However, for NH_2OH, the predicted abundances are 3.5×10^{-7} - 4.2×10^{-6}, nearly six orders of magnitude higher than the observed upper limits reported in this study. The following sections discuss possible explanations for this surprising difference, focusing on possible formation and destruction mechanisms.

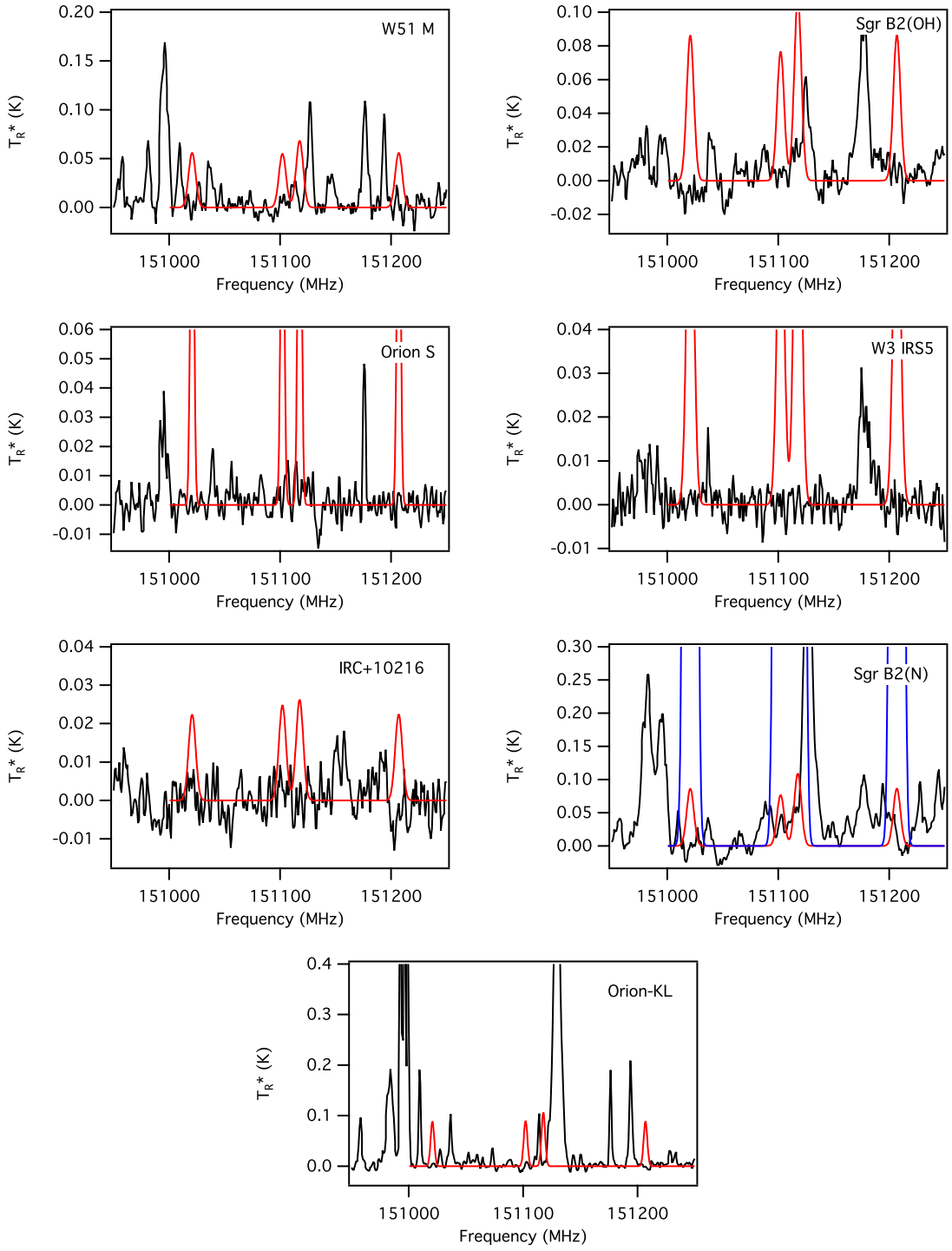

Figure 1.1: Observed *a*-type transitions of NH_2OH are simulated in red over the observed spectrum in black. Simulated spectra are shown divided by a factor of 100. An unscaled simulation is shown in blue for Sgr B2(N), for illustrative purposes.

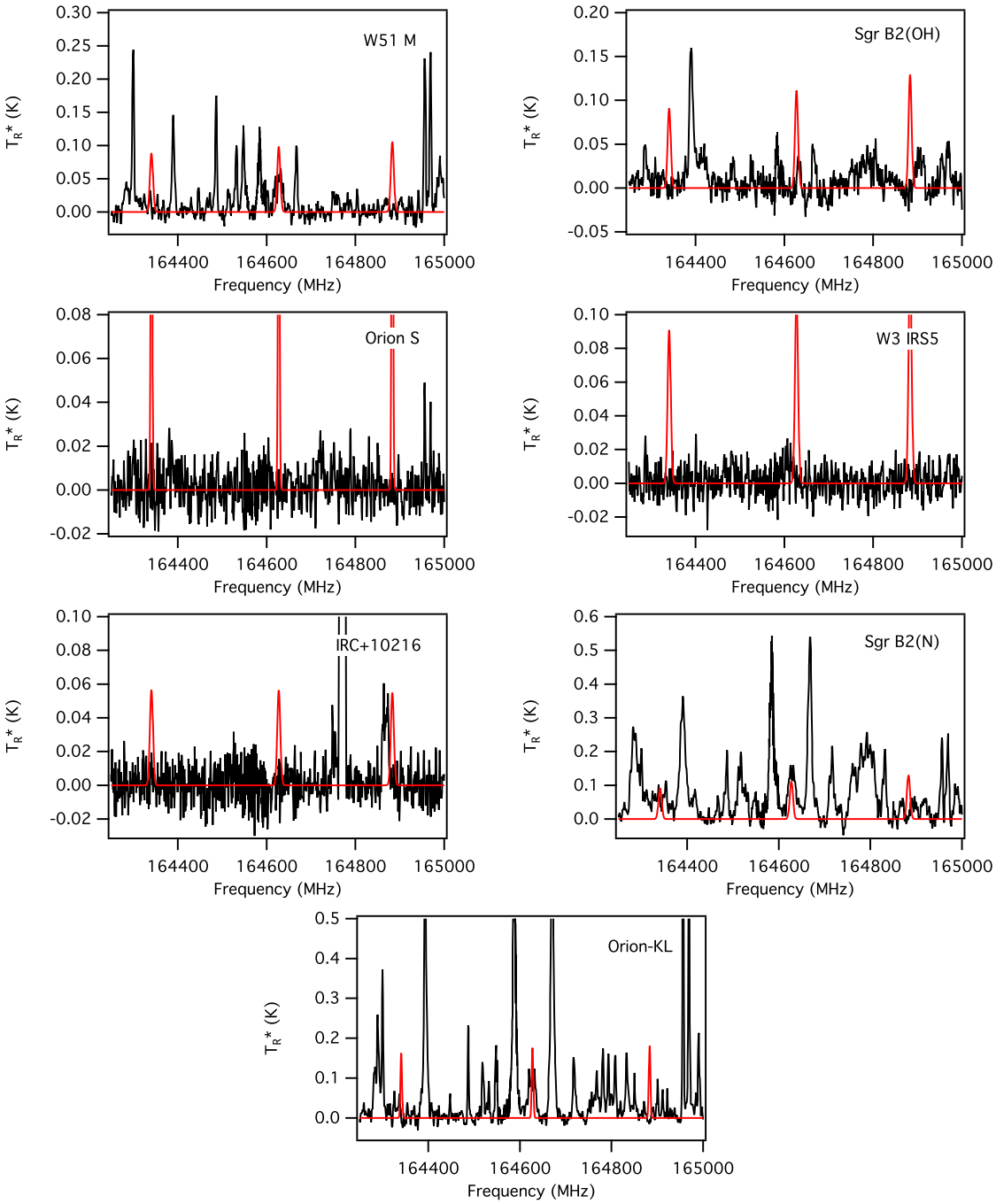

Figure 1.2: Observed *c*-type transitions of NH_2OH are simulated in red over the observed spectrum in black. No scaling factor has been applied to the simulated spectra.

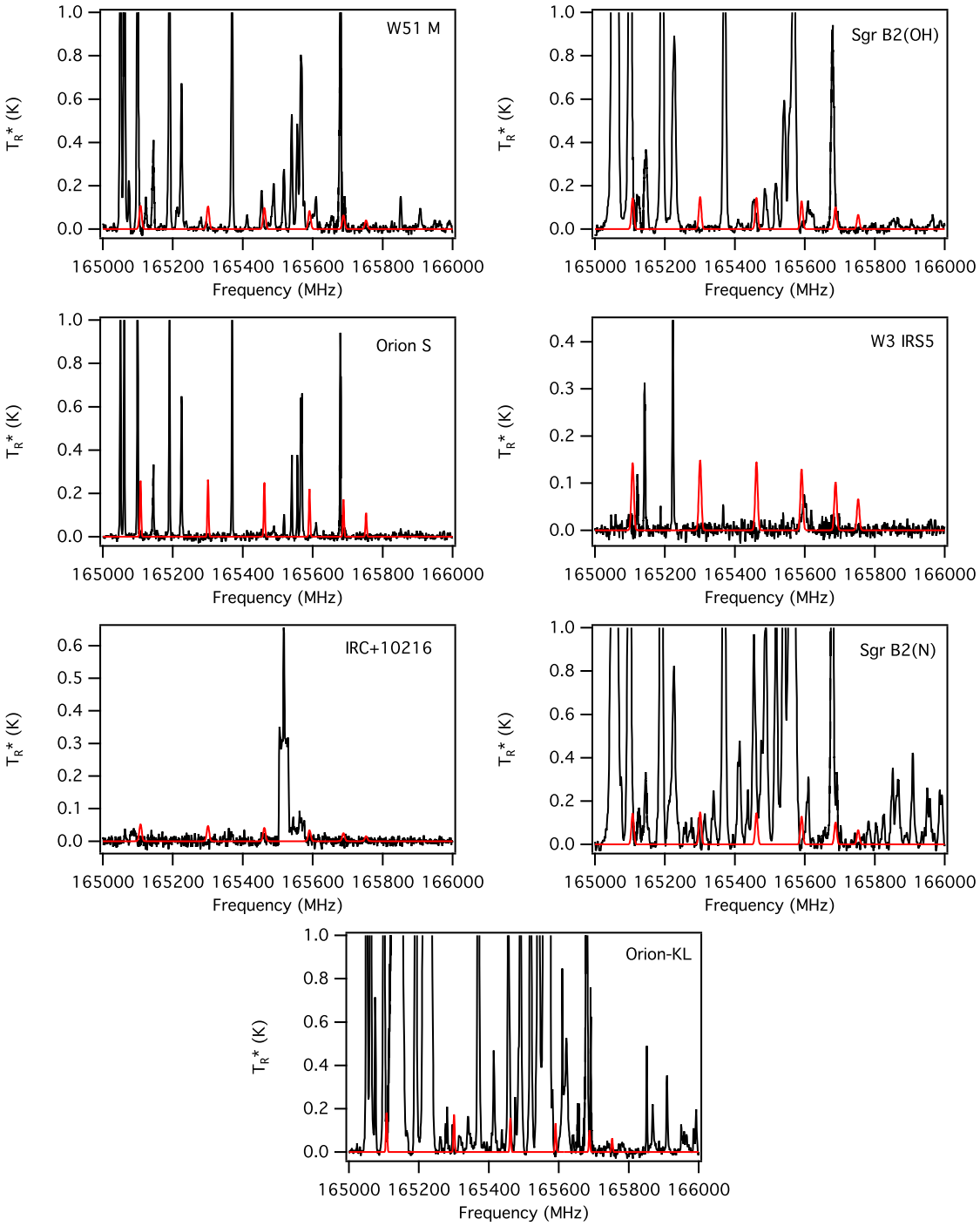

Figure 1.3: Observed *c*-type transitions of NH_2OH are simulated in red over the observed spectrum in black. No scaling factor has been applied to the simulated spectra.

1.5.1 Formation Mechanisms

The formation of NH_2OH within ice grains was first proposed by Nishi et al. (1984) [13] as shown in Equation 1.1. Previous experimental attempts to produce NH_2OH within the gas phase through the reaction of HNO^+ with H_2 have failed [5; 35]. The Garrod et al. (2008) [7] grain chemistry model assumes two formation mechanisms for NH_2OH, both of which assume radical-radical reactions within the grain mantle. In early times, NH_2OH is formed through the barrierless (see Figure 1 of [7]) reactions of the hydroxyl radical (-OH) with NH followed by hydrogenation (Equations 1.5 and 1.6) similar to the well-studied hydrogenation reactions of CO forming CH_3OH [36].

$$NH + OH \rightarrow HNOH \tag{1.5}$$

$$HNOH + H \rightarrow NH_2OH \tag{1.6}$$

However, there is no current theoretical or experimental work to suggest this hydrogenation reaction proceeds in a manner similar to CO as the model assumes. In fact, given the different states of these molecules, CO having a $^1\Sigma^+$ electronic configuration while NO is a $^2\Pi$, it is likely that the hydrogenation of NO will proceed quite differently from that of CO. This difference could account for the higher abundances predicted by the Garrod et al. (2008) [7] model at lower temperatures.

As warming takes place and the hydroxyl radical becomes more mobile on the surface of the grain, the model predicts the barrierless reaction with NH_2 to become dominant (Equation 1.7).

$$NH_2 + OH \rightarrow NH_2OH \tag{1.7}$$

However, experimental studies have shown that in an isolated argon matrix, NH_2 quickly combines with a free hydrogen radical to form NH_3 when a temperature of 20 K is reached [37]. The question then becomes whether NH_2 and OH have a higher probability to react to form NH_2OH in interstellar ices before they recombine with free hydrogen to form NH_3 and H_2O, respectively.

Interstellar ices are considerably more complex than the isolated matrices used in the Schnepp & Dressler (1960) laboratory study [37], as are the ices considered in the Garrod et al. (2008) [7]

model, which contain a number of other simple species (e.g. CH_4, CH_3OH, NH_3, CO, CO_2, HCOOH, H_2O). As such, NH_2 and OH are not the only species present to react with free hydrogen, which may instead react with itself (to form H_2) or with other smaller species. An examination of the rates of reaction of free hydrogen with these species might therefore be in order to help determine whether NH_2 and OH would be available in sufficient quantities to form a detectable abundance of NH_2OH in the ISM.

There is experimental evidence to support the radical-radical formation of NH_2OH from NH_2 and OH precursors in electron-irradiated ammonia-water ice samples [14]. Upon irradiation, an NH_3 species is found to undergo unimolecular decomposition to form the NH_2 radical and a free hydrogen atom (Equation 1.8).

$$NH_3 \rightarrow NH_2 + H \tag{1.8}$$

Water decomposes in a similar fashion, forming OH and H. After irradiation, a new absorption peak at $\sim$1500 cm^{-1} was observed and attributed to NH_2 formation. As the ice samples were warmed, the species released in the gas phase were monitored by IR and mass spectroscopy. The presence of NH_2OH was first noted in the IR measurements as the sample reached 174 K. As the temperature continued to rise, the abundance of NH_2OH decreased until non-detection at 200 K. NH_2OH was also observed in the mass spectroscopy measurements from 160 - 180 K. It is important to note that NH_2OH is observed at temperatures above which most, if not all, of the water and ammonia have sublimed.[3]

While this study does support the formation of NH_2OH through radical-radical recombination within interstellar ices, it also provides potential evidence as to why NH_2OH is not currently observed in the ISM. Is there a possible temperature problem? The Garrod et al. (2008) [7] model predicts the high abundance of NH_2OH with a temperature on the order of $\sim$130 K. According to the experimental data, NH_2OH was not observed in the gas phase until temperatures exceeded 160 K. Unfortunately, strong water absorption bands obscure NH_2OH absorption features, making

[3]Since the publication of this work, the desorption temperature in the ISM has been revised to a lower value of $\sim$120 K (S. Ioppolo, Private Communication [2013]).

its detection using infrared observations towards hot core regions impossible. However, using the temperature determined from the laboratory experiments as a basis for subsequent observations, for regions where the temperature exceeds 160 K, detection in the gas phase should be possible using millimeter wave observations. It is possible that the NH_2OH emission is confined to very compact ($<5''$) hot core regions such as the SgrB2(N-LMH) [38], and that the single dish observations from this survey are too beam-diluted to detect the emission from this compact region. As such, higher spatial resolution interferometric observations are needed to more thoroughly couple to the higher temperature regions in order to detect this species.

Alternatively, observations could be conducted towards molecular sources in shocked regions such as the bipolar outflow L1157(B) or the Galactic Center. In these types of sources, molecules that are formed on grain surfaces but that are not liberated into the gas phase by thermal desorption due to low temperatures are instead ejected into the gas phase by shocks [39]. Detection of NH_2OH in these sources would provide valuable insight into the mechanisms behind its formation pathways and eventual release into the gas phase.

1.5.2 Protonated Hydroxylamine

Next, we examine possible pathways for the destruction of NH_2OH once it enters the gas phase. It is well-known that ion-molecule reactions are important in gas-phase interstellar chemistry, and that protonated species play an important role in reaction mechanisms. NH_2OH, having a high proton affinity ($\sim$193.5 kcal mol^{-1}), is particularly susceptible to protonation from other species such as H_3^+, HCO^+, CH_5^+, H_3O^+ ([5] and references therein). The energies of protonation of NH_2OH by H^+ and the possibility of proton transfer by H_3^+ have been predicted by theory [40; 41; 42]. As a result of protonation, two stable species were reported: NH_3OH^+ and $NH_2OH_2^+$, with NH_3OH^+ found to be more stable by $\sim$100 kJ mol^{-1}.

The reaction of NH_2OH with either H^+ or protonated methanol ($CH_3OH_2^+$) was predicted to be very exothermic, and it was proposed that the excess energy would either dissociate the species or could lead to the rearrangement of the species to the higher energy $NH_2OH_2^+$. This could result in

an enhanced abundance of $NH_2OH_2^+$ in the ISM. Once in the gas phase, recent theoretical work has shown that the reaction of ionized and protonated NH_2OH with H_2, its most likely collision partner, is highly unfavorable [43]. These species, therefore, are likely to remain as reaction partners for further chemistry.

Given these considerations, even if NH_2OH is produced on ice grains through radical-radical reactions, upon its release into the gas phase, NH_2OH may quickly undergo protonation. This would result in very low observed abundances of NH_2OH in the ISM. Once protonated, the reaction with H_2, by far the most likely collision partner, is highly unfavorable, and the lifetimes of these species should therefore be greatly enhanced. A search, therefore, for $NH_2OH_2^+$ and NH_3OH^+ within these star forming regions might therefore be prudent, although dissociative recombination reactions could result in lowered abundances of these species. This would first require the acquisition of the rotational spectra of these species in the laboratory to enable astronomical searches.

NH_3OH^+ is also fundamentally interesting as a prebiotic molecule, having been shown to be a precursor to amino acid formation [6]. As shown in Equations 1.9-1.11, protonated hydroxylamine can react with CH_3COOH (Equation 1.9) and CH_3CH_2COOH (Equations 1.10 and 1.11) to produce protonated glycine and protonated β- and α-alanine, respectively. Since CH_3COOH is a well-established interstellar molecule [44], the detection of NH_3OH^+ in the ISM would greatly enhance our understanding of the possible formation route to glycine and possibly other simple amino acids in interstellar environments.

$$NH_3OH^+ + CH_3COOH \rightarrow NH_3CH_2COOH^+ + H_2O \tag{1.9}$$

$$NH_3OH^+ + CH_3CH_2COOH \rightarrow NH_3CH_2CH_2COOH^+ + H_2O \tag{1.10}$$

$$NH_3OH^+ + CH_3CH_2COOH \rightarrow CH_3CH(NH_3)COOH^+ + H_2O \tag{1.11}$$

1.6 Conclusions

We report the non-detection of NH_2OH towards seven sources. Calculated upper limits for the abundance of this molecule are as much as six orders of magnitude lower than those predicted

for the species by recent models. Several factors could account for this discrepancy, including the rapid removal of precursor molecules from ice mantles through reaction with free hydrogen or the rapid protonation (and subsequent dissociative recombination) of NH_2OH by H^+, H_3^+, CH_5^+, and other efficient protonation mechanisms. The single dish observations presented here are likely highly beam-diluted. Higher-resolution interferometric observations could provide the sensitivity required for detection, and therefore allow better refinement of models that currently predict the presence of NH_2OH in high abundance.

Chapter 2

Propynylidynium (l-C_3H^+)

Significant portions of this chapter have been reproduced from "A search for l-C_3H^+ and l-C_3H^- in Sgr B2(N), Sgr B2(OH), and the dark cloud TMC-1" by B.A. McGuire et al., Astrophysical Journal, 774, 56 (2013) [45], *"An observational investigation of the identity of B11244 (l-C_3H^+ /C_3H^- ?)" by B.A. McGuire et al., Astrophysical Journal, 783, 36 (2014)* [46], and *"A CSO Search for l-C_3H^+ : detection in the Orion Bar PDR" by B.A. McGuire et al., Monthly Notices of the Royal Astronomical Society, 442, 2901 (2014) [47].*

2.1 A Brief History of l-C_3H^+

The identification and characterization of molecular species in the interstellar medium (ISM) has traditionally followed a linear progression. Species of interest, perhaps highlighted by chemical models, are obtained or produced in the laboratory, and their characteristic spectra (rotational, vibrational, etc.) are measured. These spectra are fit to constants unique to each species that can then be used, with knowledge of the Hamiltonian, to reproduce the spectra and predict the appearance of additional features under interstellar conditions. Observations of either the measured lab features or calculated transitions in the ISM can then be used to unambiguously identify and characterize new molecules in astronomical environments.

In 2012, Pety et al. reported the detection of a series of eight transitions arising from an unidentified molecular carrier in an Institut de Radioastronomie Millimtrique (IRAM) 30 m telescope spectral line survey of the Horsehead Photodissociation Region (PDR) [48]. The pattern present in the transitions indicated a closed-shell linear molecule in its electronic ground state. Based on this assumption, Pety et al. (2012) fit the transitions using a standard linear-rotor Hamiltonian and derived the rotational constants shown in Table 2.1. Although no laboratory work was found in the

Table 2.1: Results of the spectroscopic fit of [48] to the eight unidentified transitions.

Parameter	Value	Unit
B	11244.9512(0015)	MHz
D	7.766(040)	kHz
H	0.56(0.19)	Hz

Note – Uncertainties given in parentheses in units of the last significant digit.

literature for a linear molecule with such a constant, theoretical studies indicated the l-C_3H^+ cation to be an excellent match [49].

Pety et al. (2012) [48] further bolster their assignment by examining the chemistry of l-C_3H^+ in the Horsehead PDR using the Muedon PDR code for gas-grain chemistry with the Ohio State University gas-phase chemical network [50; 51]. They find that the dominant formation pathway is through Reaction 2.1 of C_2H_2 with C^+, while destruction occurs rapidly via Reactions 2.2 & 2.3 with H_2.

$$C_2H_2 \xrightarrow{C^+} C_3H^+ + H \tag{2.1}$$

$$C_3H^+ \xrightarrow{H_2} C_3H_2^+ \xrightarrow{e^-} C_3H + H \tag{2.2}$$

$$C_3H^+ \xrightarrow{H_2} C_3H_3^+ \xrightarrow{e^-} C_3H_2 + H \tag{2.3}$$

Indeed, these reactions are thought to be the most important gas-phase channels to form other small hydrocarbons, like C_3H and C_3H_2, which are widely observed in different environments [52; 53]. However, the observed abundances of C_3H and C_3H_2 in PDRs are much higher than what pure gas-phase models predict. One possible explanation is that polycyclic aromatic hydrocarbons (PAHs) are fragmented into these small hydrocarbons in PDRs due to the strong UV fields (see, e.g., [54; 55; 56]). Observations of l-C_3H^+ would thus brings further constraints to the formation pathways of the small hydrocarbons in these environments, perhaps providing an alternative explanation for their over-abundance.

Shortly after the initial detection by Pety et al. (2012) [48], Huang and co-workers challenged the assignment of the carrier to l-C_3H^+ based on new, high-level theoretical calculations [57]. They found that while their calculations for l-C_3H^+ agree (within typical accuracies) with the fitted value of B from [48], their D constant differed by more than 40%, while their calculated value for H differed by three orders of magnitude. These differences fall well outside the predicted accuracy of the calculations, and form the basis for their dispute of the assignment to l-C_3H^+ .

Around the same time, we began to approach the topic from an observational and chemistry-based perspective. Due to the ambiguity in the identity, we adopted the convention of referring to the carrier as B11244. Our first goal was to test the predictive power of the spectroscopic fit to the observations in the Horsehead PDR. If the fit was indeed valid, then the two lowest-lying rotational transitions, the $J = 1 - 0$ and $J = 2 - 1$ lines at 22.5 and 45.0 GHz, respectively, fell within the range of our existing observations of Sgr B2(N), Sgr B2(OH), and the dark cloud TMC-1. We found a detection of both transitions of B11244 in Sgr B2(N), and tenuous evidence for its presence in Sgr B2(OH). The results of this investigation are detailed in §2.2 and in [45].

Shortly thereafter, Fortenberry and co-workers proposed the anion C_3H^- as a more likely candidate for the carrier, based on similarly high-level quartic force field calculations [58]. The theoretical predictions show that the observed transitions from [48] could be well-fit to the $K_a = 0$ transitions of the quasi-linear C_3H^- . Further, the calculated value for D for C_3H^- was three times closer to the experimentally-fit value in the Horeshead PDR than that calculated for l-C_3H^+ .

Fortenberry et al. (2013) assert that C_3H^- is a likely interstellar molecule based on favorable formation chemistry. The most likely path to the formation of C_3H^- proceeds through radiative association (see Reaction 2.4).

$$C_3H + e^- \rightarrow [C_3H^-]^* \rightarrow C_3H^- + h\nu \tag{2.4}$$

Here, an electron capture by C_3H promotes the complex into an electronically-excited state that then radiatively decays to the ground electronic state, emitting a photon. These processes work efficiently only if the electronically-excited state lives longer than the timescale for photon emission – i.e., the electronically excited state must be bound. For most interstellar anions formed through this pathway (see, e.g. C_4H^-, C_6H^-, C_8H^- [59]), the only such state available is a dipole-bound excited state. While C_3H^- does possess a dipole-bound excited state, it also has a relatively low-lying valence-bound excited state [58]. Thus, Fortenberry et al. (2013) [58] argue that the formation pathways for C_3H^- heavily favor its existence in relatively high abundance.

Motivated by this work, we re-examined our observations of Sgr B2(N) and TMC-1, as well as the Horsehead PDR survey from J. Pety and the Barry E. Turner legacy survey of IRC+10216 in the context of discussing: "What if B11244 is actually C_3H^- ?" We found no evidence for B11244 in IRC+10216, and no evidence in any source of the $K_a = 1$ transitions that should be present, at detectable intensity, if B11244 were C_3H^- , due to the quasi-linear nature of the molecule. Based on these findings, and a detailed analysis of the physical and chemical conditions under which B11244

is to be and to not be present, we found no evidence to support the assignment of B11244 to C_3H^-. The results of this investigation are detailed in §2.3 and in [46].

In early 2014, Brünken and co-workers [60] measured several transitions of l-C_3H^+ in the laboratory using mass-selective action spectroscopy, and confirmed the assignment of B11244 to l-C_3H^+ . This was followed shortly thereafter by theoretical calculations accounting for the vibrational coupling contributions of a shallow CCC bending potential, with the results further supporting the attribution to l-C_3H^+ [61].

Finally, while the question of identity has now been resolved, questions remain surrounding the formation conditions and chemical implications of l-C_3H^+ . Because l-C_3H^+ has been definitively detected in only two environments – the Horsehead PDR and Sgr B2(N) – efforts to explore these questions are hampered by a lack of information. In an attempt to address this deficiency, we conducted a wide search of PDRs and complex molecular sources in search of l-C_3H^+ . In §2.4 and in [47], we present the results of a brief, targeted campaign of 14 astronomical sources with the Caltech Submillimeter Observatory (CSO) covering the $J = 10 - 9$ and $J = 12 - 11$ transitions of l-C_3H^+ . We also examine the $J = 10 - 9$ transition in broadband unbiased line surveys of a further 25 sources.

2.2 A Search for l-C_3H^+ and l-C_3H in Sgr B2(N), Sgr B2(OH), and the Dark Cloud TMC-1

The identification by Pety et al. (2012) [48] of l-C_3H^+ is significant – the number of molecular species detected in the ISM via rotational transitions without the *a priori* knowledge of laboratory spectra or constants is quite small. Notable among these is the detection of the HCO^+ ion, popularly attributed to unidentified features in observations by Buhl and Snyder in 1970 [62] dubbed "xogen," but not definitively detected until laboratory measurements were available nearly six years later [63] following the suggested theoretical assignment of Klemperer (1970) [64]. The N_2H^+ ion was detected in 1975 [65; 66] following observation in 1974 [67], which was confirmed by laboratory studies in 1976 [68]. Shortly thereafter, Guélin, Green, & Thaddeus identified the C_3N [69] and C_4H [70] radicals based on their observations, which were confirmed by theoretical studies [71] and laboratory measurements several years later [72]. More recently, strong evidence for the detection of the C_5N^- anion has been found towards IRC+10216 in work by Cernicharo et al. (2008) [73], supported by the *ab initio* calculations of Botschwina et al. (2008) [74].

In light of the work by Huang et al. (2013) [57], we examined observational data toward three sources beyond the Horsehead PDR – Sgr B2(N), Sgr B2(OH), and TMC-1 – in an attempt to confirm the robustness of the spectroscopic fit determined in [48], and to provide context for the debate. The results of those observations are presented here.

2.2.1 Observations

The cm-wave data presented here towards Sgr B2(N) were taken as part of the **PR**ebiotic **I**nterstellar **MO**lecular **S**urvey (PRIMOS) project using the National Radio Astronomy Observatory's (NRAO) 100-m Robert C. Byrd Green Bank Telescope. The PRIMOS key project began in January of 2008, and observations continue to expand its frequency coverage. This project provides high-resolution, high-sensitivity spectra of the Sgr B2(N-LMH) complex centered at (J2000) $\alpha = 17^h47^m19^s.8$, δ = -28°22′17″ with nearly continuous frequency coverage from 1 - 50 GHz. The 2 mm observations (hereafter the Turner Survey) were conduced by Barry E. Turner using the NRAO 12-m Telescope on Kitt Peak between 1993 – 1995 towards a number of sources, including Sgr B2(N) and the associated

Sgr B2(OH). A complete description of the PRIMOS observations is given in [75].[1] Details of the Turner Survey can be found in [4] or in [76].[2]

2.2.1.1 Sgr B2(N)

The observed $J = 1 - 0$ and $J = 2 - 1$ transitions of l-C_3H^+ towards Sgr B2(N) are shown in Figure 2.1, with each spectral region shifted to the rest frequency as predicted by [48], and assuming a V_{LSR} = +64 km s^{-1}. There are clear absorption signals for both transitions at the +64 km s^{-1} component. A less intense, but visible, absorption feature is observed in the +82 km s^{-1} component for the $J = 1-0$ line. This is consistent with previous observations of molecular signals in this source (e.g. HNCNH, [77]), where much weaker signals are observed in the +82 km s^{-1} component. At higher frequencies from the Turner Survey, weak emission is seen at the frequencies of the $J = 6 - 5$ and $J = 7 - 6$ transitions. The observed intensities of these features are consistent with the column densities and temperatures derived in §2.2.2, and provide a constraint on the continuum temperature at these frequencies. The observed intensities and linewidths are given in Table 2.2.

To further confirm the detection, we have performed an analysis of the probability of coincidental overlap of the $J = 1 - 0$ and $J = 2 - 1$ transitions following the convention of [75]. Using the parameters from [75] for the line density of absorption features and weak absorption features, and assuming a conservative FWHM of 25 km s^{-1}, we find the probability of a single coincidental overlap to be ∼0.05. For two coincidental transitions, this probability falls to ∼0.003.

For comparison, we have also searched for the $J = 3/2-1/2$ rotational branch of the neutral l-C_3H molecule occurring around 32.6 GHz. The PRIMOS spectra are shown in Figure 2.3. Absorption is clearly observed in all lines at +64 km s^{-1}, while weaker absorption is seen in the +82 km s^{-1} component. The weaker absorption in the +82 km s^{-1} component compared to the +64 km s^{-1} is consistent with observations of the l-C_3H^+ species. The observed intensities and linewidths are given in Table 2.3.

2.2.1.2 Sgr B2(OH)

Our coverage of Sgr B2(OH) includes only the $J = 6 - 5$ and $J = 7 - 6$ transitions of l-C_3H^+ . In the Sgr B2(OH) complex, these signals are much clearer in the +64 km s^{-1} component than in Sgr B2(N), but no signal is seen in the +82 km s^{-1} component (see Figure 2.2). The lines are observed

[1] Specifics on the observing strategy, including the overall frequency coverage and other details for PRIMOS, are available at http://www.cv.nrao.edu/∼aremijan/PRIMOS/.

[2] Access to the entire PRIMOS dataset and complete Turner Survey are available at http://www.cv.nrao.edu/∼aremijan/SLiSE.

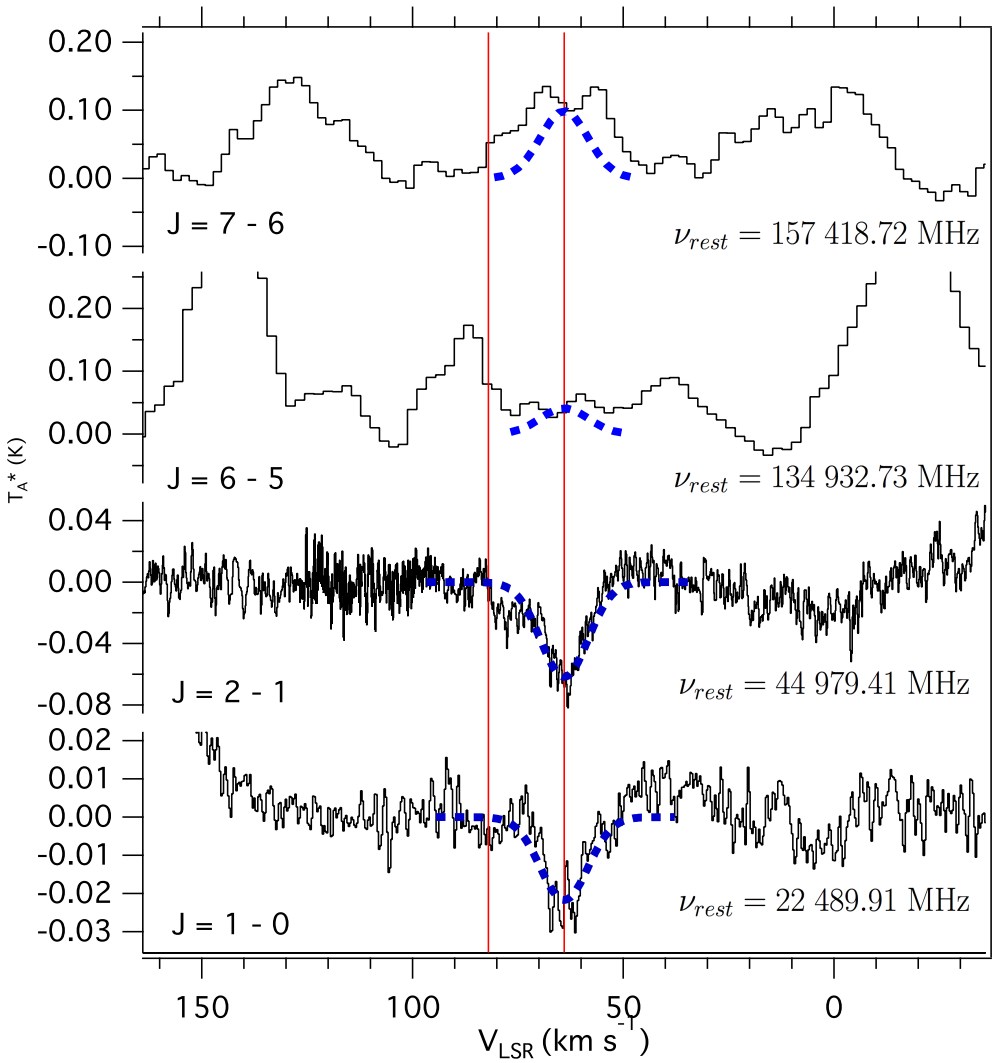

Figure 2.1: Observed transitions of l-C_3H^+ towards Sgr B2(N). Plots are on a common velocity scale, with rest frequencies assuming a V_{LSR} = +64 km s^{-1} and line centers taken as those fitted by [48]. Blue and red lines indicate the +64 and +82 km s^{-1} common velocity components in observations of Sgr B2, respectively. Predictions of line profiles and intensities in the Sgr B2(N) observations based on the best fit temperature and column density determined from the $J = 1 - 0$ and $J = 2 - 1$ transitions are shown as a dashed profile in blue.

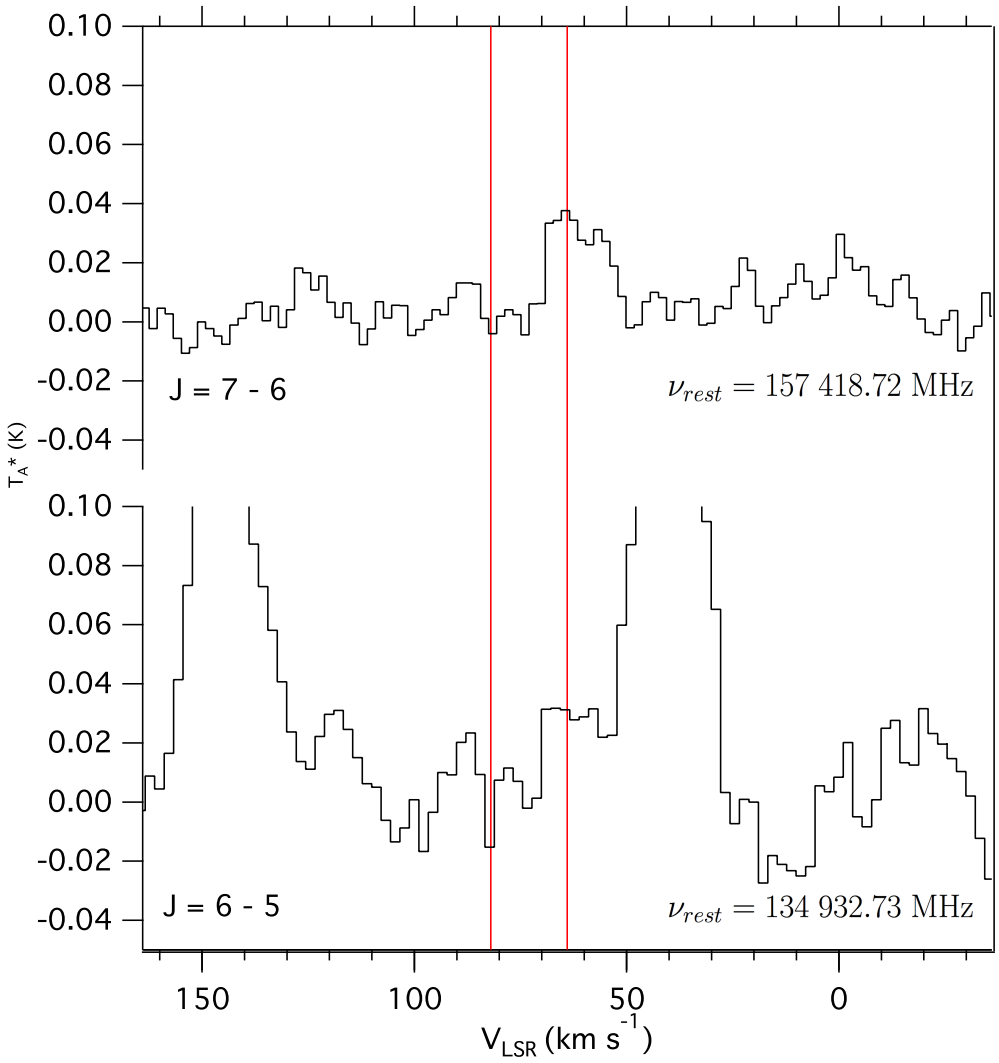

Figure 2.2: Observed transitions of l-C_3H^+ towards Sgr B2(OH). Plots are on a common velocity scale, with rest frequencies assuming a V_{LSR} = +64 km s^{-1} and line centers taken as those fitted by [48]. Blue and red lines indicate the +64 and +82 km s^{-1} common velocity components in observations of Sgr B2, respectively.

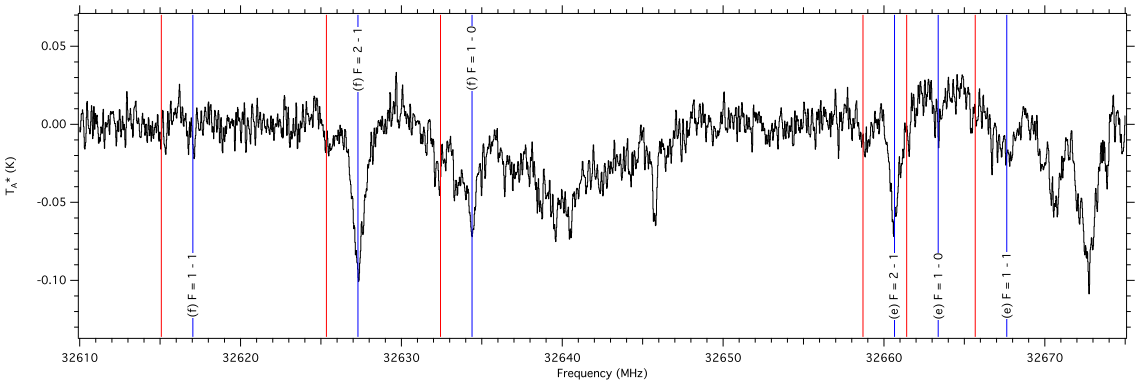

Figure 2.3: The $J = 3/2 - 1/2$, $\Omega = 1/2$ transitions of l-C_3H toward Sgr B2(N) from PRIMOS. Rest frequency is adjusted for a $V_{LSR} = +64$ km s^{-1}. Blue and red lines indicate the +64 and +82 km s^{-1} common velocity components in observations of Sgr B2, respectively.

in emission, and are likely blended with neighboring transitions. No signal from neutral l-C_3H is observed in the available data toward Sgr B2(OH).

2.2.1.3 TMC-1

Kaifu et al. (2004) [78] observed the $J = 3/2 - 1/2$ hyperfine transitions of l-C_3H in their survey of TMC-1, building on a previous detection of the molecule in this source and in IRC+10216 [79]. In their survey, Kaifu et al. observed two additional transitions of l-C_3H, the two weakest $F = 1 - 1$ hyperfine lines, and used these measurements to further refine the constants originally derived by [79], and in the laboratory by [80]. The detected transitions are shown in Figures 2.4 and 2.5, and the parameters reported by [78] are given in Table 2.3. Details of the observations are given in [78].

No evidence for the $J = 1 - 0$ transition of l-C_3H^+ in emission or absorption is present in the TMC-1 data. Very weak absorption is seen at the frequency of the $J = 2 - 1$ transition, as shown in Figure 2.6. While tantalizing, it is certainly not definitive evidence of the presence of l-C_3H^+ .

2.2.2 Results

Column densities and temperatures were determined using Equation 1.4, and the results are presented in the following sections.

2.2.2.1 Sgr B2(N)

Using Equation 1.4, a best fit value of $T_{ex} \simeq 10$ K is found for the transitions observed towards Sgr B2(N), giving a total column density of l-C_3H^+ of $\sim 10^{13}$ cm^{-2}. Linewidths of 13.4 and 14.7 km^{-1}

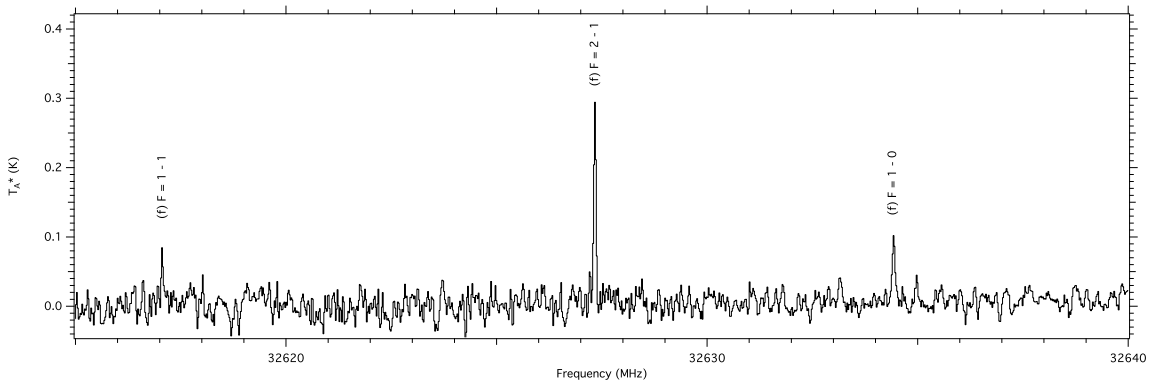

Figure 2.4: The $J = 3/2 - 1/2$, f-parity transitions of l-C_3H toward TMC-1 from [78]. Rest frequency is adjusted for a $V_{LSR} = +5.85$ km s^{-1}

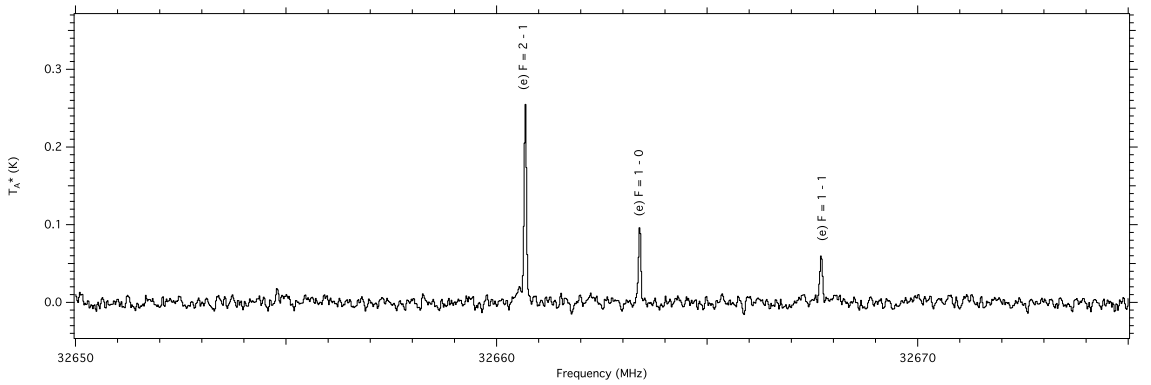

Figure 2.5: The $J = 3/2 - 1/2$, e-parity transitions of l-C_3H toward TMC-1 from [78]. Rest frequency is adjusted for a $V_{LSR} = +5.85$ km s^{-1}

Table 2.2: Transitions of l-C_3H^+ observed toward Sgr B2(N), Sgr B2(OH), and TMC-1.

				Sgr B2(N)				Sgr B2(OH)		TMC-1	
				+64 km s^{-1}		+82 km s^{-1}					
	Frequency	E_u		T_A^*	ΔV	T_A^*	ΔV	T_A^*	ΔV	T_A^*	ΔV
Transition	MHz	K	$S_{ij}\mu^2$	mK	km s^{-1}	mK	km s^{-1}	mK	km s^{-1}	mK	km s^{-1}
J 1 $\rightarrow$ 0	22 48106	1.079	8.999	-27(1)[c]	13.4(1)[c]	$\geq$ -7	...	...	...	$\geq$ -17	...
J 2 $\rightarrow$ 1	44 979.54	3.238	18.001	-70(2)[c]	14.7(7)[c]	$\geq$ -9	...	...	...	-46(18)[c]	3(1)[c]
J 6 $\rightarrow$ 5	134 932.73	22.665	53.998	$\leq$52	...	$\leq$ 71	...	28[b]	9[a]	...	...
J 7 $\rightarrow$ 6	157 418.72	30.220	63.002	99[b]	...	$\leq$ 34	...	34[b]	9[a]	...	...

a) Velocity width taken from [4]
b) Blended
c) Results of Gaussian fits to the observations, with 1σ uncertainties given in units of the last significant figure.

Table 2.3: Transitions of l-C_3H observed toward Sgr B2(N) and TMC-1.

						Sgr B2(N)				TMC-1[a]	
						+64 km s^{-1}		+82 km s^{-1}			
Transition			Frequency[a]	E_u		T_A^*	ΔV	T_A^*	ΔV	T_A^*	ΔV
$J' - J''$	Parity	$F' - F''$	MHz	K	$S_{ij}\mu^2$	mK	km s^{-1}	mK	km s^{-1}	mK	km s^{-1}
$3/2 - 1/2$	f	$1 - 1$	32 617.016	1.56622	4.189	-22[c]	...[c]	$\geq$ -7	...	78	0.39
		$2 - 1$	32 627.297	1.56672	20.932	-88(1)	11.5(2)	-19	...	287	0.47
		$1 - 0$	32 634.389	1.56619	8.370	-59(2)	14.6(7)	-42	...	96	0.75
	e	$2 - 1$	32 660.645	1.56990	20.932	-60(2)	9.0(3)	-15	...	251	0.47
		$1 - 0$	32 663.361	1.57032	8.372	-9[b], c	...[c]	$\geq$ -7	...	99	0.43
		$1 - 1$	32 667.668	1.57024	4.184	-22[c]	...[c]	$\geq$ -7	...	61	0.48

Note – Except where noted, values of T_A^* and ΔV for the Sgr B2(N) +64 km s^{-1} data were obtained by Gaussian fits with 1σ uncertainties given in units of the last significant digit. In the case of Sgr B2(OH), no fits were performed, and T_A^* is listed either as peak intensity or as an RMS noise level.

a) Values from [78]

b) Affected by local, non-zero baseline

c) Unable to fit a Gaussian – T_A^* taken as peak intensity, no linedwidth determined.

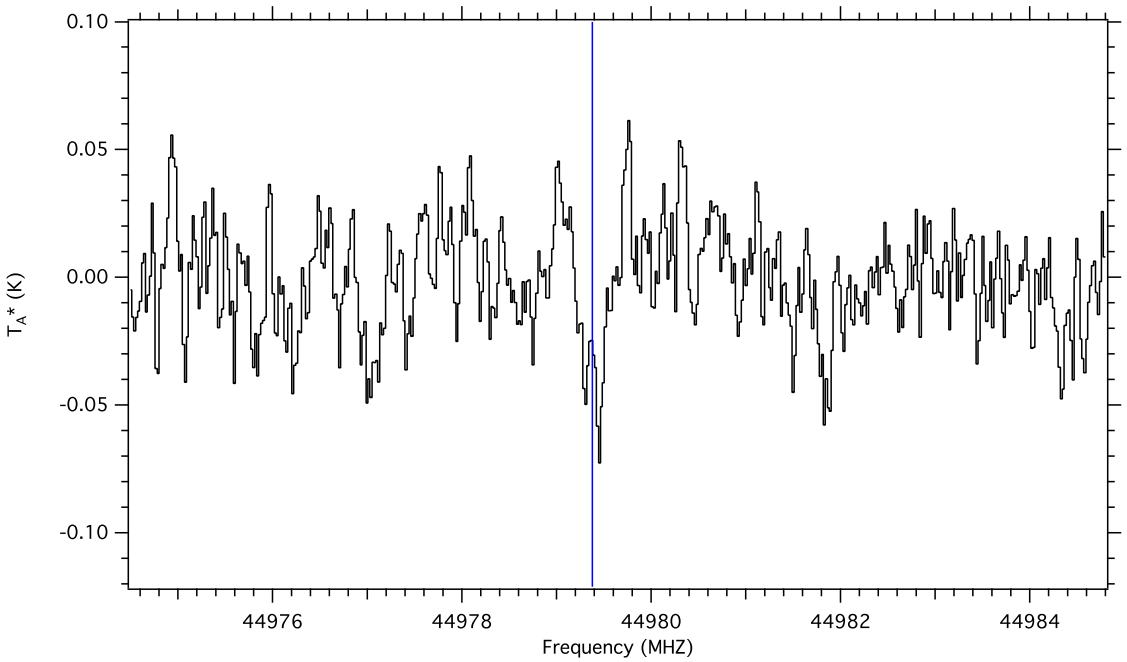

Figure 2.6: The $J = 2 - 1$ transition of l-C_3H^+ toward TMC-1 from the [78] data. Rest frequency is adjusted for a $V_{LSR} = +5.85$ km s^{-1}, and indicated by a blue line.

were assumed based on Gaussian fits to the absorption profiles, and a dipole moment of $\mu = 3$ Debye was used following [48]. Predicted line profiles for the these transitions are shown as dashed blue lines in Figure 2.1 using the derived values for T_{ex} and column density. The observations of l-C_3H^+ absorption in Sgr B2(N) indicate that the signal likely arises from cold, diffuse gas surrounding the hot, dense core, rather than from the hot core itself, consistent with observations of other cold, extended species in this source (see e.g. [75; 30]). The derived abundance is similar to those derived in previous observations of small organic molecules toward this source [25].

For comparison, we calculated an approximate column density of neutral l-C_3H using the transitions shown in Figure 2.3 from PRIMOS and Equation 1.4. Although six transitions of neutral l-C_3H are observed, all are hyperfine components of the single $J = 3/2 - 1/2$ manifold. As a result, two parameter (T_{ex} and N_T) fits are not well-constrained. We have therefore proceeded on the assumption that, as they are both observed in absorption and are likely co-spatial, neutral l-C_3H and l-C_3H^+ will be similar in excitation temperature. We find a value of $T_{ex} \simeq 8.7$ K with a column density of $\sim 10^{14}$ cm^{-2} provides a good approximation. This results in a ratio of neutral:l-C_3H^+ in Sgr B2(N) of $\sim$6:1, consistent with the ratio Pety et al. (2012) [48] derived of $\sim$4:1 in the Horsehead PDR. High-resolution maps of both neutral l-C_3H and l-C_3H^+ would greatly aid in determining the validity of these assumptions.

The observed behavior of l-C_3H^+ in moving from absorption to emission with increasing frequency is not unique to this molecule in Sgr B2(N). For example, CH_2OHCHO [30], CNCHO [81], CH_3CHO [82], and especially HCCCHO (R. Loomis, private communication), among others (including CH_3OH and H_2CO), display similar behavior. This is largely a function of decreasing continuum temperature with frequency. In fact, the $J = 6 - 5$ and $J = 7 - 6$ transitions provide a constraint on the background continuum temperatures above the CMB of ∼1 K at 135 GHz, and ∼0.5 K at 157 GHz.

2.2.2.2 Sgr B2(OH)

In Sgr B2(OH), only two lines fall within the frequency of the Turner Survey observations, the lower of which (at 135 GHz) is clearly blended (see Figure 2.2). As such, here we calculate only an upper limit to l-C_3H^+ column density on the assumption that all of the emission at the peak of each signal arises from l-C_3H^+ . A line width of 9 km s^{-1} was assumed based on the analysis of nearby spectral regions from the same dataset by [4]. Based on these values, a best fit T_{ex} of ∼79 K gives an upper limit on the column density of $\leq 1.5 \times 10^{13}$ cm^{-2}.

2.2.2.3 TMC-1

The lack of any definitive signal from l-C_3H^+ towards TMC-1 precludes any quantitative determination of a column density. However, assuming the weak absorption signal at 44.9 GHz does arise from $J = 2 - 1$ of l-C_3H^+ , a zeroth-order approximation of the column density can be obtained using Equation 1.4 and an estimated temperature of ∼9 K [83]. Such an analysis results in an estimated upper limit to the column density of $\sim 6 \times 10^{11}$ cm^{-2}.

For comparison, the column density of neutral l-C_3H, assuming the same temperature of ∼9 K, is $\sim 9 \times 10^{12}$ cm^{-2} in this source. This results in a ratio of 15:1, two and a half times that in Sgr B2(N), and almost four times that in the Horsehead PDR. Given the large uncertainties involved, however, these numbers are not inconsistent.

2.2.3 Spectral Fitting

The spectroscopic parameters and line list for l-C_3H^+ as listed in the CDMS catalog is accessible in full via www.splatalogue.net. Huang et al. (2013) [57] question the assignment of the observed transitions to l-C_3H^+ based on large discrepancies between observed and calculated values for the D and H distortion constants. The predictions of [48] were robust enough to predict the $J = 1 - 0$

and $J = 2 - 1$ transitions presented in §2.2.1.1. However, in an effort to confirm their values for the D and H constants, we have refit the molecular signals using the frequencies for the $J = 1 - 0$ and $J = 2 - 1$ transitions determined from our observations.

The observed transitions of l-C_3H^+ were fit using the CALPGM [84] program suite, using a standard linear rotor Hamiltonian giving energies as shown in Equation 2.5.

$$E(J) = BJ(J+1) - D(J(J+1))^2 + H(J(J+1))^3 + L(J(J+1))^4 + M(J(J+1))^5 + (...) \quad (2.5)$$

CALPGM is designed to fit spectroscopic constants of a model Hamiltonian to a set of observed transitions using an iterative least-squares fitting algorithm. Following Pety et al. (2012) [48], we include first (D) and second (H) order centrifugal distortion constants in the Hamiltonian, producing a fit to the unshifted transitions with an RMS observed minus calculated value of 0.0862 MHz, below the average observational uncertainty of 0.1015 MHz. Addition of higher order terms L and M in equation 2.5 is found to improve the RMS of the fit by ∼10 kHz for each additional term, and give a RMS change in the predicted frequencies of ∼90 kHz and 80 kHz for L and M respectively. These corrections are below the experimental uncertainty, and therefore of questionable physical significance; thus, only the first and second order corrections are included in the final fits. As a final step, the 1σ uncertainty of all fit parameters was computed using the PIFORM program.[3]

The spectral resolution of the PRIMOS observations is significantly higher than those from [48]; ∼21 kHz versus 49 and 195 kHz. However, the linewidths of the observed transitions in Sgr B2(N) used in the fit are broad compared to those observed by Pety et al. (2012) [48] in the Horsehead PDR (13.3 & 14.7 km s^{-1} versus ∼1 km s^{-1}), thus introducing additional uncertainty in the measurement of the line centers. Further, as discussed by Pety et al. (2012) [48], the absolute accuracy of the spectroscopic constants is determined by the accuracy to which the V_{LSR} velocity of l-C_3H^+ emission is known. The use of two independent observational datasets towards two separate sources compounds this issue.

While we cannot mitigate the uncertainty due to the broad lineshapes, we have attempted to minimize the effects of uncertainty in V_{LSR}. To account for this, a minimization of the fit RMS was performed by varying the V_{LSR} offsets for the PRIMOS dataset and the IRAM dataset independently over a range of -3 km s^{-1} to +3 km s^{-1}. The results of this analysis indicate that convergence is quickly reached with minimal variation in either dataset. Based on their observations of similar molecules, Pety et al. (2012) [48] determined an uncertainty level of ±0.2 km s^{-1} for the IRAM

[3] Z. Kisiel, PIFORM available at http://www.ifpan.edu.pl/∼kisiel/asym/asym.htm#piform

Table 2.4: Best-fit spectroscopic constants obtained by shifting V_{LSR} for the PRIMOS and IRAM datasets.

ΔV_{LSR} (km s^{-1}) IRAM -0.2, PRIMOS 0.4			ΔV_{LSR} (km s^{-1}) IRAM 0.2, PRIMOS 0.8		
B	11244.9421(41)	MHz	B	11244.9571(41)	MHz
D	7.745(80)	kHz	D	7.745(80)	kHz
H	0.49(37)	Hz	H	0.49(37)	Hz
Fit RMS	31.9	kHz	Fit RMS	31.9	kHz

Note – 1σ uncertainties on spectroscopic constants (type A, k = 1 [85]) are given in parentheses in units of the last significant digit.

dataset. Under these constraints, a minimum RMS is achieved with offsets to the PRIMOS dataset of 0.4 - 0.8 km s^{-1} – equivalent to approximately twice the resolution of the observations at 22 GHz. For comparison, a PRIMOS offset of 0.0 km s^{-1} requires an IRAM offset of -0.6 km s^{-1} for minimization.

The best fit rotational constants found at the outer limits of the best fit region (assuming $\pm$0.2 km s^{-1} offsets to the IRAM data) are shown in Table 2.4. The absolute variance in the B rotational constant at the outer limits of the IRAM offsets is found to be 15 kHz, much less than the resolution of the observations. The implications of these results are discussed in the following section.

2.2.4 Discussion

At first glance, the presence of l-C_3H^+ would be remarkable, as the species is known to react readily (and destructively) with H_2 [86]. The arguments for the assignment of these features to l-C_3H^+ in [48], however, appear robust. l-C_3H^+ is thought to be a key intermediate in the production of small hydrocarbon molecules, including l-C_3H. Indeed, the detected abundance of l-C_3H^+ in the Horsehead PDR is remarkably consistent with chemical models of the region performed by Pety et al. (2012) [48]. Additionally, as discussed in [48], the reaction rate of the destructive reaction of l-C_3H^+ with H_2 is strongly dependent on the gas temperature, with very low temperatures ($T < 20$ K), and especially warmer temperatures ($T > 50$ K), decreasing the reaction rate coefficients [87]. Therefore, perhaps it is not surprising to have found cold l-C_3H^+ ($T < 11$ K) in Sgr B2(N) and possibly TMC-1, but warm ($T \sim$80 K) l-C_3H^+ in Sgr B2(OH).

Due to the challenges discussed in §2.2.3, the constants we determine from our spectroscopic fit have greater uncertainties than those determined in [48]. These may, in fact, be more of a faithful reflection of the true uncertainties than those presented in [48], as our fit takes into account the inherent uncertainties in V_{LSR}. Nevertheless, our analysis agrees quite well with that in [48]; we

find that the values for D and H do not vary from theirs within the stated uncertainties. Thus, we conclude that the fit presented in [48] is a faithful representation of the detected molecular signatures, and is consistent with a closed-shell, linear molecule. Further, the abundances and physical conditions are consistent with the current understanding of l-C_3H^+ and l-C_3H chemistry.

Resolving the discrepancies presented in [57] through astronomical observations will certainly require further, higher-frequency observations of the molecule. As the effects of the D and H constants become exponentially more pronounced with higher J-levels, each additional line measured beyond those found by Pety et al. (2012) will serve to lock these values into place. Indeed, by 315 GHz, the difference in the predicted line frequencies using the D and H constants of [48] and [57] differ by more than 9 km s^{-1}. Thus, observation of these lines in Sgr B2(OH), where the warmer conditions favor lines in this frequency range, could help to resolve this issue despite the broad linewidths observed there.

There is, however, no substitute for laboratory data, and although further astronomical observations could certainly help to resolve the question, they cannot approach the level of confidence found in experiments in a laboratory setting. Thus, laboratory measurements using absolute frequency standards and controlled production conditions are warranted to expand the spectroscopic study of l-C_3H^+ . The laboratory observation of small hydrocarbon and hydrocarbon chain neutrals, cations, and anions is a well-established, if non-trivial process (see e.g. [88; 89]).

2.2.5 Conclusions

Here, we have presented observations of the $J = 1 - 0$ and $J = 2 - 1$ transitions of the l-C_3H^+ molecule in Sgr B2(N), and observations of the $J = 6 - 5$ and $J = 7 - 6$ transitions in Sgr B2(N) and Sgr B2(OH) using the publicly-available PRIMOS data and the Barry E. Turner Legacy Survey. Neutral l-C_3H has been detected in Sgr B2(N) in a ratio consistent with that found in the Horsehead PDR. Observations of TMC-1 reveal strong l-C_3H signals and a tentative detection of a weak l-C_3H^+ transition. A spectroscopic fit of the molecule, including the newly-observed $J = 1 - 0$ and $J = 2 - 1$ transitions, agrees with that of [48], but does not resolve the discrepancy with the calculated constants of [57]. Follow-up observational and laboratory studies are warranted to definitively identify the molecule.

2.3 An Observational Investigation of the Identity of B11244 (l-C_3H^+ /C_3H^-)

In this section, we re-examine the observations of Pety et al. (2012) [48] toward the Horsehead PDR, as well as PRebiotic Interstellar MOlecular Survey (PRIMOS) observations of Sgr B2(N), the Kaifu et al. (2004) [78] survey of TMC-1, and the Barry E. Turner legacy survey of IRC+10216 in the context of discussing: "What if B11244 is actually C_3H^- ?" Due to the uncertainty in the assignment, here we adopt the convention of referring to the carrier as B11244. In §2.3.1, we discuss the spectroscopy of C_3H^- using the properties derived by Fortenberry et al. (2013) [58], and present simulated spectra. In §2.3.2, we briefly outline the observations used, and in §2.3.3 discuss the analysis of these observations. Finally, in §2.3.4, we present the results of our findings, and discuss them in the context of determining the identity of B11244.

2.3.1 Spectroscopic Analysis

Table 2.6 provides the rotational constants and dipole moments used in this work to describe B11244, assuming it is l-C_3H^+ or C_3H^- . The spectroscopic constants and fit for l-C_3H^+ are provided in [48], and their predictive power confirmed in [45]. Fortenberry et al. (2013) [58] provide a high-accuracy equilibrium structure for C_3H^- , rotational constants, and dipole moments. These moments are not in the principal axis (PA) system, but can readily be converted to the PA system with a simple coordinate rotation resulting in $\mu_x \rightarrow \mu_a = 1.63$ Debye and $\mu_y \rightarrow \mu_b = 1.41$ Debye. Indeed, the magnitude of this rotation is small, such that the value of these dipole moments remains essentially unchanged. Were the observed transitions in [48] and [45] due to C_3H^- , they would be a-type, $K_a = 0$ transitions, and thus $(B + C)$ and D_J could be well-determined from these lines. To obtain these constants, the observed transitions were fit using the CALPGM suite of programs. An asymmetric-top Hamiltonian with a Watson S reduction in the I^r representation was used.[4] The remaining constants were necessarily used as-is from the theoretical calculations. A simulated spectrum of C_3H^- at 22 K using this combined set of constants is displayed in Figure 2.7. A full CALPGM catalog for C_3H^- to 2 THz is also provided in Appendix B (see Table 2.5).

[4]Full details on the expressions and algorithms can be found in the CALPGM documentation and refs. therein. The interested reader may find that the analytical analysis presented in [90] provides a useful (and more approachable) approximation.

Table 2.5: CALPGM catalog simulation of C_3H^- format.

Column	Format	Description
1	F13.4	Frequency (MHz)
2	F8.4	Error of Freq (MHz)
3	F8.4	Base 10 log intensity (nm^2MHz at 300 K)
4	I2	Degrees of freedom in partition function
5	F10.4	Lower state energy (cm^{-1})
6	I3	Upper state degeneracy
7	I7	Species tag
8	I4	Quantum number format identifier
9	6I2	Upper state quantum numbers
10	6I2	Lower state quantum numbers

For a complete description of this file format,
see CALPGM documentation located at spec.jpl.nasa.gov.

Table 2.6: Rotational constants and dipole moments for l-C_3H^+ and C_3H^- .

Constant	l-C_3H^+	Ref.	C_3H^-	Ref.
A (MHz)	...	...	529 134	(3)
B (MHz)	11 244.9512(15)	(2)	11 355.3	(1)
C (MHz)	...	...	11 134.5	(1)
D (kHz)	7.766(40)	(2)	...	...
D_J (kHz)	...	...	4.63	(1)
D_{JK} (kHz)	...	...	702	(3)
D_K (MHz)	...	...	218	(3)
d_1 (Hz)	...	...	-112	(3)
d_2 (Hz)	...	...	-23	(3)
H (Hz)	0.56(19)	(2)	...	...
μ_a (Debye)	...	...	1.63	(1,3)
μ_b (Debye)	3	(2)	1.41	(1,3)

Refs. – (1) This work; (2) Pety et al. (2012); (3) Fortenberry et al. (2013).

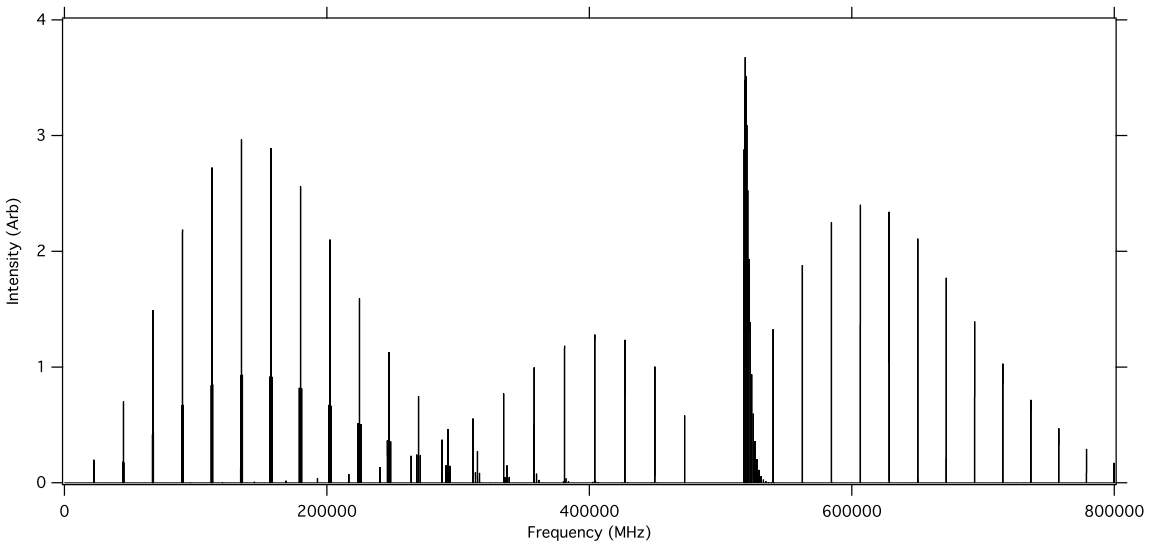

Figure 2.7: Simulated spectrum of C_3H^- at LTE, with an excitation temperature of $T_{ex} = 22$ K.

2.3.2 Observations

Sgr B2(N) - The data presented toward Sgr B2(N) were obtained as part of the PRIMOS project using the Robert C. Byrd 100 m Green Bank Telescope. The observed position was at (J2000) $\alpha = 17^{\rm h}47^{\rm m}19^{\rm s}.8$, $\delta = -28°22'17''$. An LSR source velocity of +64 km s^{-1} was assumed. Full observational details, including data reduction procedures and analysis, are given in [75].[5]

IRC+10216 - The observations presented toward IRC+10216 are part of the Barry E. Turner Legacy Survey using the NRAO 12 m Telescope on Kitt Peak. The observed position was at (J2000) $\alpha = 9^{\rm h}47^{\rm m}57^{\rm s}.3$, $\delta = +13°16'43''$. An LSR source velocity of -26 km s^{-1} was assumed. Full observational details are given in [76].[6]

TMC-1 - The observations presented toward the TMC-1 dark cloud were taken as part of the Kaifu et al. (2004) [78] survey using the Nobeyama Radio Observatory 45 m telescope. The observed position was at (J2000) $\alpha = 4^{\rm h}41^{\rm m}42^{\rm s}.5$, $\delta = +25°41'26.9''$. An LSR source velocity of +5.85 km s^{-1} was assumed. Full observational details are given in [78].

Horsehead PDR - The observations presented toward the Horsehead PDR were taken with the IRAM 30-m telescope as part of the Horsehead WHISPER project (PI: J. Pety). The observed position was at (J2000) $\alpha = 5^{\rm h}40^{\rm m}53^{\rm s}.936$, $\delta = -2°28'00''$. An LSR source velocity of +10.7 km s^{-1} was assumed. Full observational details are given in [48].

[5] Access to the entire PRIMOS dataset, specifics on the observing strategy, and overall frequency coverage information is available at http://www.cv.nrao.edu/∼aremijan/PRIMOS/.

[6] All observations from the PRIMOS project and Barry E. Turner Legacy Survey are accessible at http://www.cv.nrao.edu/∼aremijan/SLiSE.

2.3.3 Data Analysis

The column density of B11244 in each source, assuming local thermodynamic equilibrium (LTE), can be calculated using Equation 1.4. In the case of l-C_3H^+ , the partition function is well-approximated by the standard linear-molecule formula given by Eq. 2.6, with B expressed in Hz. For C_3H^- , Eq. 2.7, with $\sigma = 1$ and rotational constants with units of MHz, is appropriate [29]. The accuracy of Q_r for the anion is dependent on the accuracy of the rotational constants used. Thus, there is likely an uncertainty of a few percent in the value of Q_r used here. In any case, the partition function for the anion rapidly outpaces that of the cation above $T_{ex} \sim 8$ K.

$$Q_r\ (l\text{-}C_3H^+) \simeq \frac{kT}{hB} = 1.85(T) \tag{2.6}$$

$$Q_r\ (C_3H^-) \simeq \frac{5.34 \times 10^6}{\sigma} \left(\frac{T^3}{ABC}\right)^{1/2} = 0.65(T_{ex})^{3/2} \tag{2.7}$$

To calculate upper limits of l-C_3H^+ in IRC+10216, we use the molecule-specific parameters given in [45], and the upper limit ΔT_A^* and ΔV values given in Table 2.7. The line parameters and molecule-specific parameters used for all C_3H^- calculations are given in Table 2.7.

While the observed $K_a = 0$ transitions allow us to constrain B and C reasonably well, the lack of any confirmed detection of a $K_a = 1$ transition limits the overall accuracy in predicting the frequencies of these lines. However, the expected intensity of these lines, given a derived column density and temperature, is likely to be fairly accurate under LTE conditions. In the Horsehead PDR, these lines should have a peak intensity of $T_{mb} \sim 20 - 28$ mK for $J'' = 3$ to 6, using the derived conditions from the $K_a = 0$ transitions. In Sgr B2(N), the expected intensities are below detectable values in our observations.

We calculate a theoretical uncertainty in the center frequencies for these transitions of $\sigma \sim 370$ MHz for the $J = 4 - 3$ transition to as much as $\sigma \sim 650$ MHz for the $J = 7 - 6$ transition. At LTE, the strongest of these lines fall within the 3 mm window of the Pety et al. (2012) [48] survey. Due to the uncertainties in the line centers, we have searched a region equal to each transition's uncertainty on either side of each predicted line center. After identifying all known lines within this range, we find no detection of any signals which could be assigned to a $K_a = 1$ transition of C_3H^- at the RMS noise level of the observations ($\sim 5 - 10$ mK), despite peak predicted intensities of 20 - 28 mK at LTE. An example spectrum of the region searched around the predicted $4_{1,4} - 3_{1,3}$ transition is shown in Figure 2.8.

Table 2.7: Observed and targeted transitions of B11244, assuming it is C_3H^-. For simplicity, only those $K_a = 1$ transitions specifically searched for in our study are displayed.

Transition	ν		E_u	Horsehead		Sgr B2(N)		IRC+10216	
$J'_{K_a,K_c} - J''_{K_a,K_c}$	(MHz)	S_{ij}	(K)	ΔT_{mb}	ΔV	ΔT_A^*	ΔV	ΔT_A^*	ΔV
$1_{0,1} \rightarrow 0_{0,0}$	22 489.86	1	1.079	...	...	-27	13.4	...	...
$2_{1,2} \rightarrow 1_{1,1}$	44 755.94	1.5	28.07	...	...	[a]	14.7	...	...
$2_{0,2} \rightarrow 1_{0,1}$	44 979.50	2	3.237	...	...	-70	14.7	...	...
$2_{1,1} \rightarrow 1_{1,0}$	45 197.57	1.5	28.10	...	...	≤ 9	14.7	...	...
$4_{1,4} \rightarrow 3_{1,3}$	89 510.82	3.75	35.59	≤ 5.7	0.81	...	...	...	...
$4_{0,4} \rightarrow 3_{0,3}$	89 957.63	4	10.79	89	0.81	...	...	...	...
$4_{1,3} \rightarrow 3_{1,2}$	90 394.13	3.75	35.70	≤ 5.3	0.81	...	...	...	...
$5_{1,5} \rightarrow 4_{1,4}$	111 887.54	4.8	40.96	≤ 10.5	0.81	...	...	...	...
$5_{0,5} \rightarrow 4_{0,4}$	112 445.57	5	16.19	115	0.81	...	...	...	...
$5_{1,4} \rightarrow 4_{1,3}$	112 991.72	4.8	41.11	≤ 14.1	0.81	...	...	...	...
$6_{0,6} \rightarrow 5_{0,5}$	134 932.69	6	22.66	72	0.81	$\leq$52	13	$\leq$5	27.5
$7_{0,7} \rightarrow 6_{0,6}$	157 418.71	7	30.22	75	0.81	99[b]	13	$\leq$7	27.5
$9_{0,9} \rightarrow 8_{0,8}$	202 386.75	9	48.56	62	0.81	...	...	...	...
$10_{0,10} \rightarrow 9_{0,9}$	224 868.40	10	59.36	30	0.81	...	...	...	...
$11_{0,11} \rightarrow 10_{0,10}$	247 348.23	11	71.23	45	0.81	...	...	...	...
$12_{0,12} \rightarrow 11_{0,11}$	269 826.05	12	84.18	25	0.81	...	...	...	...

Note – ΔT_A^* and ΔT_{mb} given in units of mK, ΔV given in units of km s^{-1}. All upper limits are 1σ. Values for the Horsehead PDR and Sgr B2(N) are based on Gaussian fits to the lineshapes. The FWHM for IRC+10216 is based on a zeroth-order approximation from other observed transitions.

a) Completely obscured by blends.

b) Partially blended.

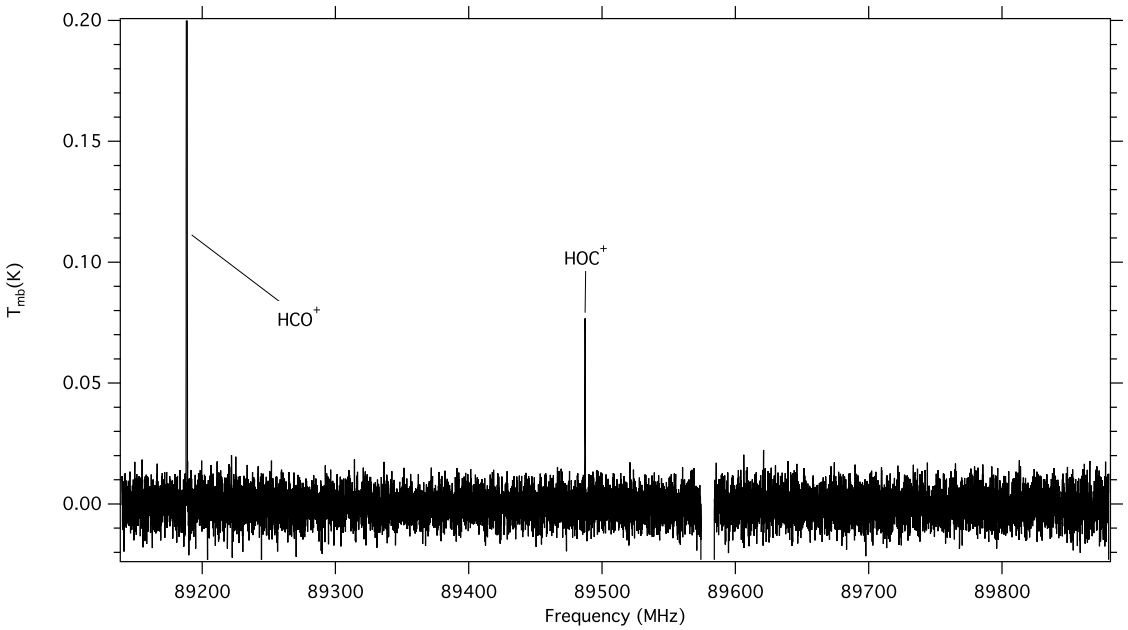

Figure 2.8: Targeted frequency window around the predicted $K_a = 1$, $4_{1,4} - 3_{1,3}$ transition of C_3H^- centered at 89535 MHz. The RMS noise level is 5.8 mK. Three features are observed – one each attributed to HCO^+ and HOC^+. A third, located at ∼89580 MHz, has been positively identified as belonging to a known interstellar species, but has been removed from the spectra for proprietary reasons. The identity of this line will be published in a forthcoming paper from Guzmán et al.

At higher frequencies ($\nu > 500$ GHz), additional branches of C_3H^- transitions are predicted, with slightly greater intensity. We have no spectral coverage at these frequencies. Additionally, these transitions are strongly dependent on the derived value for A, making any attempted search quite challenging.

2.3.4 Results & Discussion

In the following paragraphs, we discuss the results of our analysis in the context of determining the identity of B11244. We do not address topics that have been previously covered in the literature, and for which our analysis provides no further information; namely, the agreement (or lack thereof) between the fitted rotational and distortion constants for each species with those calculated by [57] and [58].

2.3.4.1 Anion/Neutral Abundance Ratio

The results of fits to column density and excitation temperature in the Horsehead PDR and Sgr B2(N), and upper limits in IRC+10216 and TMC-1, are displayed in Table 2.8 for l-C_3H^+ , C_3H^- ,

and C_6H^- as well as neutral C_3H and C_6H. In the Horsehead PDR and Sgr B2(N), the calculated column density for C_3H^- is ∼3 times that of the cation. This is due to an increase in the partition function and a decrease in the value of $S_{ij}\mu^2$ for the anion.

Among the reported carbon-chain anionic species detected to date in the interstellar medium (ISM) (C_4H^-, C_6H^-, C_8H^-), C_6H^- has been the most widely detected and characterized [91; 92]. The abundance fraction of C_6H^-, relative to the neutral, is remarkably consistent across observed sources, varying from ∼1.4% to 4.4% [92; 88]. The abundance ratio of C_3H^- to neutral C_3H, which is more than an order of magnitude greater than that of C_6H^- in observed sources, is therefore somewhat surprising. Additionally puzzling is that C_3H^- would appear to break the observed trend of increasing anion abundance fraction with increasing size, as well as the apparent trend for even-carbon molecular anions.

Fortenberry et al. (2013) [58] propose that the most likely route to efficient formation of C_3H^- is through a radiative attachment (RA) mechanism. Herbst & Osamura (2008) [93] calculate an exceptionally low radiative attachment rate for C_3H. At 300 K, they find an attachment rate for C_3H orders of magnitude lower than for C_4H, C_6H, and C_8H. Despite this, if B11244 is indeed C_3H^-, it would be the highest anion/neutral ratio detected in the ISM.[7]

As described in [58], C_3H^- possesses both dipole-bound and valence excited states of the same multiplicity, which provide the necessary states to allow for a RA mechanism to form the anion [94; 95]. Because the other detected anions possess only a dipole-bound state, Fortenberry et al. (2013) [58] propose that the presence of the valence excited state may cause an enhancement in the production of C_3H. The extent of this enhancement is difficult to quantify, and thus we cannot say whether this can offset the lower RA rate predicted in [93].

2.3.4.2 Detection in Sgr B2(N)

To our knowledge, no molecular anions have been detected in Sgr B2(N). An examination of both the PRIMOS cm-wave data and the 2 mm Turner Survey shows no indication of the presence of any of the known molecular anions. Of note, no such anions have been detected in the Horsehead PDR, either [96].

However, a re-examination of the PRIMOS data originally presented in McGuire et al. (2013) finds some evidence for B11244 absorption in lower-velocity ($V_{LSR} \sim +0 - 10$ km s^{-1} and $V_{LSR} \sim +18$ km s^{-1}) diffuse clouds along the line of sight to Sgr B2(N). For illustration, the $J = 1 - 0$ and

[7] Cernicharo et al. 2008 [73] find an abundance ratio of C_5N^-/C_5N in IRC+10216 of 57%, but suggest it may in fact be as low as 12.5%.

Table 2.8: Column densities and excitation temperatures for l-C_3H^+ and C_3H^- in our observations and from the literature, as well as ratios of these to their neutral counterparts. Literature values for the ratio of C_6H^- to neutral C_6H are also shown.

Source	l-C_3H^+ $N(10^{11}$ cm$^{-1})$	T_{ex}(K)	C_3H^- $N(10^{11}$ cm$^{-1})$	T_{ex}(K)	C_3H $N(10^{11}$ cm$^{-1})$	l-C_3H^+/C_3H (%)	C_3H^-/C_3H (%)	C_6H^-/C_6H (%)
Horsehead PDR	4.8(9)[1]	14(2)[1]	12(1)[a]	22(4)[a]	21(7)[1]	23(3)	57(16)	$\leq$9
Sgr B2(N)	240(30)[b]	8[b]	790(90)[b]	8[b]	3000 (300)[b]	8(1)	26(8)	...[c]
IRC+10216	$\leq$6	32	$\leq$40	32	560	$\leq$1.1	$\leq$7.1	3(2)[2]
TMC-1	$\leq$6[d]	9	$\leq$250[d]	9	90[3]	$\leq$7	$\leq$278	2.5(0.4)[4]

Note – Uncertainties are given in parentheses in units of the last significant digit, and are 1σ.
All values were calculated for this work unless otherwise noted.

Refs. – (1) [48] (2) [88] (3) [78] (4) [92]

a) To ensure consistency with the l-C_3H^+ values determined in [48], these values have been determined via a rotation diagram analysis. A least-squares fit analysis suggests that this column density may actually be a factor of 2 higher.

b) These values are slightly revised from those in [45]. While re-examining the data for this study, it became clear that the transition at 45 GHz, regardless of the carrier, is likely highly sub-thermal. We therefore base our figures here on the 22.5 GHz transition only, and assume the "standard" 8 K excitation temperatures for cold molecules in this source. We have extended this temperature to our previous analysis of C_3H in this source, as well.

c) There have been no reported detections of, and we see no evidence for, the presence of C_6H^- in Sgr B2(N).

d) Based on a tentative detection of the 45 GHz transition only, which, like H_2CO, displays anomalous absorption against the 2.7 K CMB in this source.

$J = 2 - 1$ transitions of B11244 are shown in Figure 2.9 in comparison to the known CH absorption spectra toward SgrB2(N)[8]. The strongest observed transition of l-C_3H is also shown and displays low-velocity absorption as well, although the $\sim$0 km s^{-1} component is blended with the +64 km s^{-1} main component of the l-C_3H, $J = 3/2 - 1/2$, f-parity, $F = 1 - 0$ transition.

While numerous cationic species have been detected in these diffuse clouds (see, e.g., [98; 99]), the possibility of anion chemistry in these regions is not well-understood. Indeed, no anions have previously been seen in these line-of-sight clouds. The indication of B11244 in these regions, presented here, will hopefully be a motivating factor that will drive future studies. Investigations of this diffuse gas, which displays chemistry distinct from regions such as IRC+10216 and Sgr B2(N), will certainly prove invaluable in furthering our understanding of gas-phase ion chemistry.

2.3.4.3 Non-Detection in IRC+10216

IRC+10216 has been the preeminent source for the detection of anionic species. The carbon-chain anions C_4H^-, C_6H^-, and C_8H^- have all detected in this source [100; 101; 88; 102], as well as the cyano-anions CN^-, C_3N^-, and C_5N^- [103; 104; 73]. As shown in Table 2.7, however, we see no signal from B11244 toward this source at an RMS of $\sim$5-7 mK. Given the known abundance of the neutral C_3H, we can determine upper limits to the anion fraction. We assume a rotational temperature of 32 K – similar to that of C_6H^- and C_8H^- in this source, and slightly higher than that of C_4H^-. This results in an upper limit abundance fraction of C_3H^-/C_3H of only $\sim$7% (see Table 2.8), about twice that of C_6H^- and less than half of the lower edge of our error bars in Sgr B2(N).

2.3.4.4 Anion Destruction via Photodetachment

Kumar et al. (2013) [105] have recently shown that UV photodetachment may be the dominant destruction mechanism of interstellar anions in IRC+10216. Their models assume the standard interstellar UV radiation field (c.f. [106]), and find that UV photodetachment is significant at these values. In the Horsehead PDR, however, the UV field is $\sim$60 times the standard UV value [107]. It is therefore contradictory that despite a far higher (destructive) UV field, C_3H^- would be present in the Horsehead PDR with an anion:neutral ratio 8 times higher than the upper limit for IRC+10216.

[8]The CH spectra shown are from the HEXOS survey of Sgr B2(N). Full observational, reduction, and analysis details are available in [75] and [97].

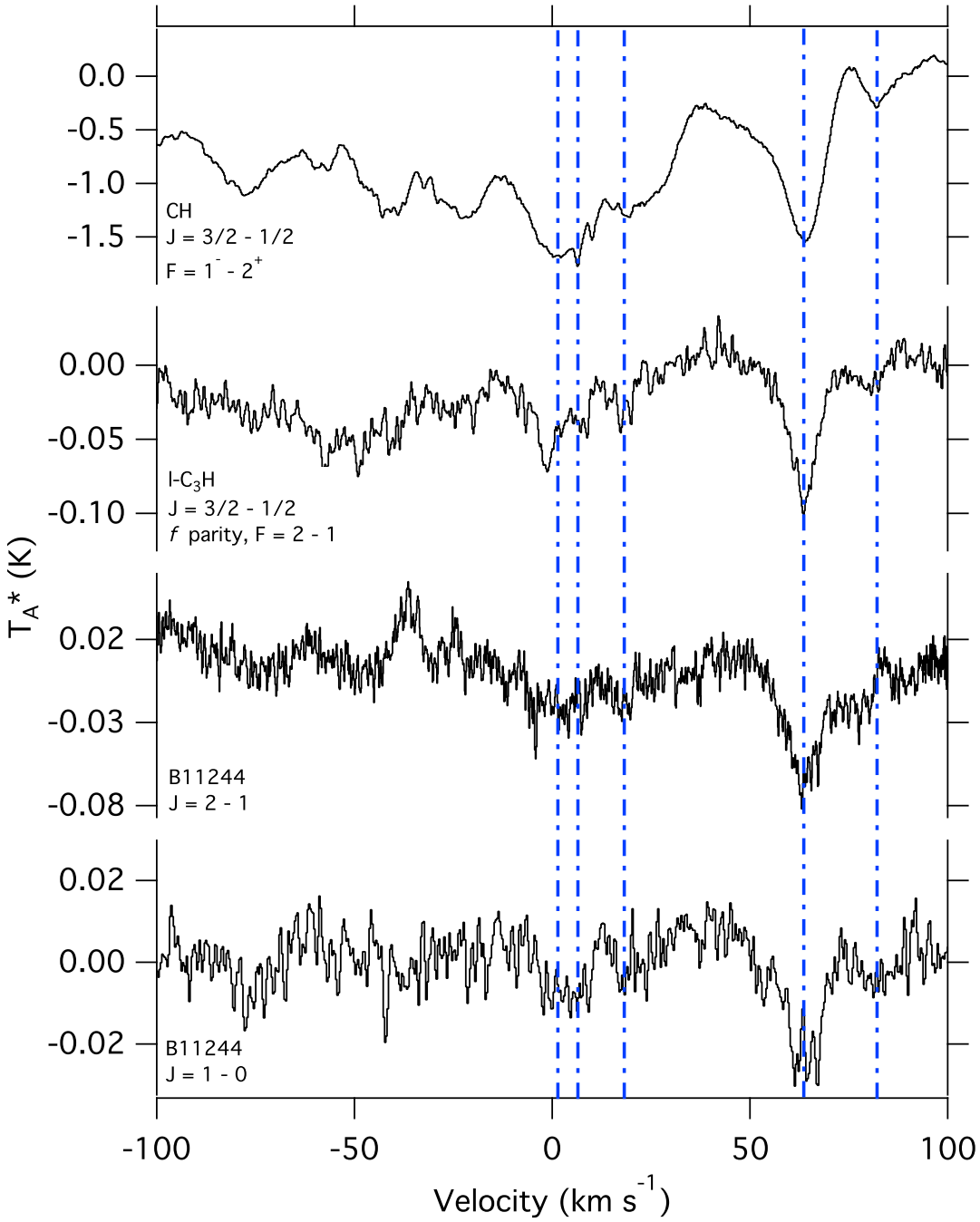

Figure 2.9: Observed transitions of B11244 and l-C_3H toward Sgr B2(N) from PRIMOS, and CH toward Sgr B2(N) from HEXOS. The blue vertical lines are provided to guide the eye to the diffuse cloud velocity components. The velocity axis is referenced to the rest frequency of each transition.

2.3.4.5 Non-Detection of $K_a = 1$ Transitions

The lack of detection of any signal that could reasonably be attributed to emission from $K_a = 1$ transitions strongly disfavors the assignment of B11244 to C_3H^-. In the Horsehead PDR, the $K_a = 0$ transitions of B11244 are well-modeled by LTE assumptions, and thus we do expect the intensity of the $K_a = 1$ transitions to be reasonably well-predicted. It should be noted, however, that a single molecule can display distinctly different excitation temperatures and column densities between two K ladders. Indeed, previous observations of HNCO toward OMC-1 show distinct differences between LTE column density and temperature measurements in high-K and low-K ladders [108]. The authors attribute this to radiative excitation of the higher-K, higher-energy states through strongly allowed b-type transitions at far-infrared (far-IR) wavelengths.

In the case of C_3H^- , we can examine three limiting cases that may apply in the Horsehead PDR: LTE conditions, the influence of a weak far-IR radiation field, and the influence of a strong far-IR radiation field.

LTE

As shown in §2.3.3, under LTE conditions, the $K_a = 1$ transitions of C_3H^- have predicted intensities of 20 - 28 mK. These are clearly not detected in our spectra at the RMS noise level of the observations ($\sim 5 - 10$ mK). Thus, we can say with some certainty that C_3H^- is not present in the Horsehead PDR under LTE conditions.

Weak far-IR radiation field

In the case of a weak far-IR radiation field, and assuming low to moderate H_2 densities in the region (i.e. non-LTE), the population of the $K_a = 1, 2, ...$ levels will be largely dominated by radiative selection rules. Any population driven into the $K_a = 1, 2, ...$ levels by collisions will rapidly decay back into the $K_a = 0$ states via radiative emission. For C_3H^- , this will result in a decrease in the observed intensity of the $K_a = 1$ transitions, relative to the $K_a = 0$ transitions, as compared to LTE. In this case, the lack of detected $K_a = 1$ transitions does not provide a constraint on the presence of C_3H^- .

Strong far-IR radiation field

We now examine the case of a strong far-IR radiation field, and low to moderate H_2 densities in the region (i.e. non-LTE). For transitions arising from low-energy states, the relative populations will be

determined by the rotational excitation temperature of the molecule (T_{ex} = 22 K). For transitions from higher-energy states connected by far-IR transitions, the relative populations of the energy levels will be determined by the color temperature of the dust radiation field at that frequency if that temperature is higher than T_{ex}. Thus, the K_a = 1, 2, ... transitions would be relatively more intense than predicted by LTE simulations at T_{ex}. This is the case for HNCO in OMC-1 [108], where the higher-K transitions are more intense than predicted from observations of the lower-K transitions.

In the Horsehead PDR, Goicoechea et al. (2009) [109] measure the millimeter dust continuum to have a temperature $T_d \simeq 30$ K. Under these circumstances, we would expect the $K_a = 1$ transitions to have intensities of $\sim 27 - 34$ mK. We can therefore conclude that assuming B11244 is subject to the radiation field measured in [109], C_3H^- is not the carrier.

It is clear from the two non-LTE cases discussed above that the location of B11244 within the Horsehead PDR region is critical. Interferometric mapping of the location of B11244, relative to the measured continuum levels in this region, will provide considerable insight into the mechanisms at work.

2.3.5 Conclusions

We have presented an analysis of observations of the Horsehead PDR, Sgr B2(N), IRC+10216, and TMC-1 with the goal of determining the identity of B11244. Our findings can be summarized as follows.

1. If B11244 is C_3H^- , it would display the highest anion:neutral ratio yet observed in the ISM (57% in the Horsehead PDR).

2. We find no evidence for C_3H^- emission in observations toward IRC+10216, and place an upper limit on the anion:neutral ratio in this source well below that found in the Horsehead PDR and Sgr B2(N).

3. Recent work has shown UV photodetachment is a dominant destruction pathway for molecular anions [105]. Despite a UV field more than 60 times that of IRC+10216, C_3H^- would be present in the Horsehead PDR with an anion:neutral ratio more than 8 times that of the upper limit in IRC+10216.

4. We find no evidence for the $K_a = 1$ lines of C_3H^- in observations of the Horsehead PDR. We examine three limiting cases for conditions within the Horsehead PDR, and find that a weak

far-IR radiation field can account for the lack of observed $K_a = 1$ transitions. LTE conditions or the presence of a strong far-IR radiation field, however, strongly disfavor the presence of C_3H^- . A significant far-IR radiation field has been reported for the Horsehead PDR, but it is unclear whether B11244 is subject to this radiation.

The observational evidence presented here, taken as a whole, casts doubt on the assignment of B11244 to C_3H^- , favoring instead the cation, l-C_3H^+ , as the most likely candidate. The evidence is, however, circumstantial; a definitive answer will almost certainly require laboratory confirmation. Indeed, K.N. Crabtree and co-workers at the Harvard-Smithsonian Center for Astrophysics have undertaken such work using Fourier-transform microwave spectroscopy. Preliminary evidence is suggestive of the cationic species. The full results of the laboratory investigation will be published in an upcoming paper (K.N. Crabtree, Private Communication).

Additional observations of the Horsehead PDR, with the aim of detecting the b-type transitions of C_3H^- , predicted to be strongest between 500 - 600 GHz, would also provide further evidence. Perhaps more insightful would be interferometric observations to discover the spatial correlation, or lack thereof, of B11244 with the previously-observed far-IR radiation field. Finally, further observations of the diffuse gas along the sightline to Sgr B2(N) would likely prove fruitful in understanding the possibility of anion chemistry in these regions.

2.4 A CSO Search for l-C_3H^+: Detection in the Orion Bar PDR

2.4.1 Introduction

While the question of identity has now been resolved, questions remain surrounding the formation conditions and chemical implications of l-C_3H^+ . Because l-C_3H^+ has been definitively detected in only two environments – the Horsehead PDR and Sgr B2(N) – efforts to explore these questions are hampered by a lack of information. In an attempt to address this deficiency, we have conducted a wide search of PDRs and complex molecular sources in search of l-C_3H^+ . Here, we present the results of a brief, targeted campaign of 14 astronomical sources with the Caltech Submillimeter Observatory (CSO) covering the $J = 10 - 9$ and $J = 12 - 11$ transitions of l-C_3H^+ . We also examine the $J = 10 - 9$ transition in broadband unbiased line surveys of a further 25 sources. The observational details are given in §2.4.2, resulting spectra are presented and data reduction strategies are outlined in §2.4.3, and a discussion follows in §2.4.4.

2.4.2 Observations and Data Reduction

Observations as part of the targeted campaign to detect l-C_3H^+ were conducted over the course of 4 nights in May 2013, 2 nights in October 2013, 2 nights in November 2013, and 2 nights in January 2014 as part of early remote observing trials using the CSO. The dataset of 25 unbiased molecular line surveys was obtained with the CSO between September 2007 and June 2013 in the frequency region of the $J = 10 - 9$ transition.

2.4.2.1 Targeted CSO Survey

Observations as part of the targeted campaign to detect l-C_3H^+ were conducted over the course of 4 nights in May 2013, 2 nights in October 2013, 2 nights in November 2013, and 2 nights in January 2014 as part of early remote observing trials using the CSO. The CSO 230/460 GHz double side band (DSB) heterodyne sidecab receiver, operating in its 210 - 290 GHz mode, was used in moderately good weather ($\tau \sim 0.07 - 0.12$) resulting in typical system temperatures of $T_{sys} \sim 250$ K. The backend consisted of two Fast Fourier Transform Spectrometers (FFTS): FFTS1 provided 1 GHz of DSB spectra at 122 kHz resolution while FFTS2 provided two, 2 GHz DSB spectral windows at 269 kHZ resolution. For the Orion Bar observations, the receiver was additionally used in its 170

Table 2.9: Sources, coordinates, V_{LSR}, and source type for the targeted search.

Source	α(J2000)	δ(J2000)	V_{LSR} (km s^{-1})	Notes
Sgr B2(OH)	17:47:20.8	-28:23:32	64	Galactic Center, Hot Core
Sgr A*	17:45:37.7	-29:00:58	20	Galactic Center, PDR
NGC 7023	21:01:33.9	+68:10:33	3	PDR
L 183	15:54:08.5	-02:52:48	2.5	Dark Cloud
IRC+10216	09:47:57.4	+13:16:44	-26	C-rich Circumstellar Envelope
M17-SW	18:20:25.1	-16:11:49	20	Star Forming Region, PDR
IRAS 16293	16:32:22.6	-24:28:33	3	Cold Core
S140 A	22:19:12.1	+63:18:06	-7.6	PDR
S140 B	22:19:17.3	+68:18:08	-7.6	PDR
CIT 6	10:16:02.3	+30:34:18	-2	C-rich Circumstellar Envelope
CB 228	20:51:20.5	+56:15:45	-1.6	Translucent Cloud
G+0.18-0.04	17:46:11.3	-28:48:22	72	Galactic Center, Molecular Cloud
W51e2	19:23:43.9	+14:30:35	55	Hot Core
Orion Bar	05:35:20.6	-05:25:14	10.4	PDR

- 210 GHz mode to observe the $J = 9 - 8$ transition at 202 GHz. The $J = 8 - 7$ transition at 180 GHz was not observed due to interference from the nearby water line.

Target sources and parameters are given in Table 2.9. For observations of sources with known extended structure, position switching observations were used. For more compact sources, a chopping secondary mirror with a throw of $2'$ was used – this resulted in lower overhead times than position switching observations. Details are given in Table 2.11. Pointing was performed every $\sim$2 hours, usually on a planetary source, with pointing corrections converging to within $\sim 1''$.

Spectra were obtained in DSB mode. For sources with no apparent emission in the observed DSB spectra, only a single IF setting was observed and averaged to produce the spectra. For W51e2 and the Orion Bar, where signal was observed near the expected l-C_3H^+ frequency, at least 3 IF frequency settings were observed to isolate the signal in either the signal or image side band. In the case of a further four sources – NGC 7023, IRC+10216, M17-SW, and IRAS 16293 – sufficient IF settings were obtained to perform a full deconvolution of the data. Details of the methods used for the deconvolution, as well as an example script, are given in Appendix A. In most cases, the expected linewidths were significantly broader than the resolution of the observations. In these cases, the data were Hanning-smoothed, normally to a resolution of $\sim$1.6 km s^{-1}. A summary is given in Table 2.11.

With the exception of the Sgr B2(N) observations, detailed baseline fitting and subtraction was performed for each observation. In some cases, extreme baseline structure was observed, necessitating the use of high-order polynomials to remove the ripple. In these cases, the frequency windows for

Table 2.10: Sources, coordinates, V_{LSR}, and source type for each observed source from the unbiased line surveys.

Source	α(J2000)	δ(J2000)	V_{LSR} (km s^{-1})	Notes
L1448 MM-1	03:25:38.80	+30:44:05.0	0.0	Class 0 + outflow
NGC 1333 IRAS 2A	03:28:55.40	+31:14:35.0	7.8	Hot Corino
NGC 1333 IRAS 4A	03:29:10.30	+31:13:31.0	6.8	Hot Corino
NGC 1333 IRAS 4B	03:29:11.99	+31:13:08.9	5.0	Hot Corino
Orion-KL	05:35:14.16	-05:22:21.5	8.0	Hot Core
NGC 2264	06:41:12.00	+09:29:09.0	7.6	Hot Core
NGC 6334-29	17:19:57.00	-35:57:51.0	-5.0	Class 0
NGC 6334-38	17:20:18.00	-35:54:42.0	-5.0	Class 0
NGC 6334-43	17:20:23.00	-35:54:55.0	-2.6	Class 0
NGC 6334-I(N)	17:20:55.00	-35:45:40.0	-2.6	Class 0
Sgr B2(N-LMH)	17:47:19.89	-28:22:19.3	64	Hot Core
GAL 10.47+0.03	18:08:38.40	-19:51:51.8	67.8	HII region
GAL 12.21-0.10	18:12:39.70	-18:24:20.9	24.0	HII region
GAL 12.91-00.26	18:14:39.00	-17:52:0.30	37.5	Hot Core
HH 80-81	18:19:12.30	-20:47:27.5	12.2	Outflow
GAL 19.61-0.23	18:27:37.99	-11:56:42.0	40.0	Hot Core
GAL 24.33+0.11 MM1	18:35:08.14	-07:35:01.1	113.4	Hot Core
GAL 24.78+0.08	18:36:12.60	-07:11:11.0	111.0	Hot Core
GAL 31.41+0.31	18:47:34.61	-01:12:42.8	97.0	Hot Core
GAL 34.3+0.20	18:53:18.54	+01:14:57.9	58.0	Hot Core
GAL 45.47+0.05	19:14:25.60	+11:09:26.0	62.0	Hot Core
GAL 75.78+0.34	20:21:44.09	+37:26:39.8	4.0	HII region
W75N	20:38:36.60	+42:37:32.0	10.0	Hot Core
DR21(OH)	20:39:01.10	+42:22:49.1	-3.0	Hot Core
L1157-MM	20:39:06.20	+68:02:16.0	2.7	Class 0 + outflow

the l-C_3H^+ transitions were carefully examined prior to the subtraction to ensure that no potential signal from l-C_3H^+ was affected by the subtraction. In the case of Sgr B2(N), where line confusion dominates the spectrum and little to no baseline is visible, a constant offset was corrected for by eye, resulting in absolute intensity uncertainties of ∼0.1 K - 0.2 K (see Appendix A for further details).[9]

2.4.2.2 Unbiased Line Surveys

The source positions and velocities used in the unbiased molecular line surveys are given in Table 2.10. System temperatures were generally <400 K during observations, with the maximum T_{sys} during high opacity being ∼1100 K.

Two receivers and spectrometers were used for these observations. First, a prototype 230 GHz wideband receiver [111; 112] was used with the facility acousto-optical spectrometer (AOS) to give spectra with 4 GHz bandwidth and ∼0.65 MHz channel width. Second, the facility 230 GHz wide-

[9]The Sgr B2(N) observations presented here are part of a broader line survey of Sgr B2(N) from 260 - 286 GHz presented in [110]. The complete preliminary reduction is accessible at http://www.cv.nrao.edu/∼aremijan/SLISE/.

band receiver [113] was used with the facility FFTS to give spectra with 4 GHz bandwidth and ∼0.27 MHz channel width. Rest frequencies of 223.192 – 251.192 GHz were used, with a 4 GHz separation between frequency settings. IF offsets of 4.254, 6.754, 5.268, and 7.795 GHz were applied to each rest frequency. Additional IF offsets of 6.283, 4.753, 5.767, and 7.269 GHz were applied to the two lowest rest frequency settings on each source to ensure a minimum frequency sampling redundancy of 6. Most frequencies were sampled by 8 separate frequency settings to enable deconvolution of the DSB spectra.

The raw data were intensity calibrated using the standard chopper wheel calibration method, which placed the intensities on the atmosphere-corrected temperature scale, T_A^*. A chopping frequency of 1.1 Hz was used with a chopper throw of either 70±8″ or 90±8″ . A noise level of ≤30 mK was achieved by adjusting integration times based on the T_{sys} value determined for each frequency setting. Pointing offsets were checked at a minimum of every two hours, and were consistent to ≤5″ each night. Each spectrum was also compared to previous spectra for intensity consistency as an independent verification of the pointing accuracy. The 230 GHz full-width-half-power beam size was 33.4″ for the prototype receiver, and 35.54″ for the facility receiver.

The CLASS software package included in the GILDAS suite of programs (Institut de Radioastronomie Millimétrique, Grenoble, France) was used for the data reduction and deconvolution. A first-degree baseline function was used to remove baselines from the DSB spectra. Spurious noise features were removed by blanking the affected channels prior to deconvolution. The cleaned and baseline subtracted spectra were resampled with a 1 MHz uniform channel spacing. The standard CLASS deconvolution routine was used to deconvolve the spectra. The initial deconvolution assumed no gain variations between the sidebands. A second deconvolution was then constrained using this first result, with the sideband gains being allowed to vary. The strong spectral features (i.e. those with intensities >2 K) were masked during deconvolution to prevent the introduction of spurious features. These features were added back into the spectrum after deconvolution. All intensities were then set to the main beam temperature scale, T_{mb}, where $T_{mb} = T_A^*/\eta_{mb}$; the main beam efficiency was determined through observations of planets to be $\eta_{mb} = 60 \pm 9\%$ for both receivers. The noise level in the final spectra is ≤25 mK on the T_{mb} scale. The deconvolved spectra in the frequency range covering the l-C_3H^+ lines are shown in Figures 2.14 – 2.16.

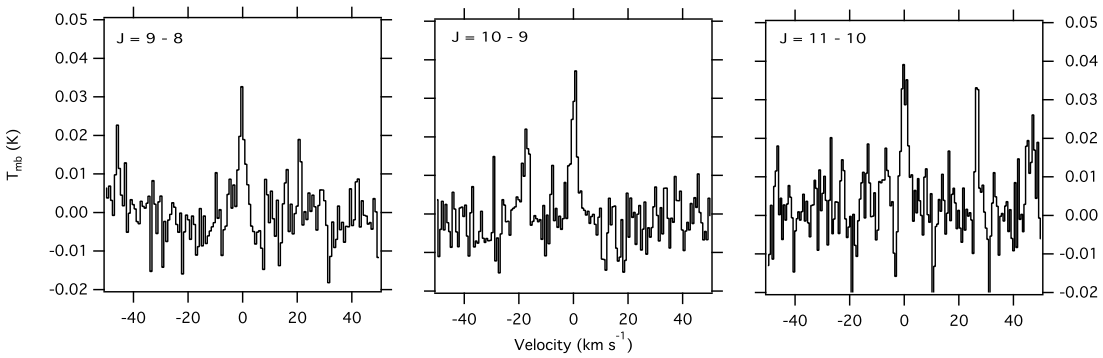

Figure 2.10: $J = 9 - 8$, $10 - 9$, and $11 - 10$ transitions of l-C_3H^+ observed toward the Orion Bar PDR. The spectra are corrected for an observed source LSR velocity of 10.4 km s^{-1}, and have been baseline-subtracted and Hanning-smoothed to a resolution of 488 kHz ($\sim$0.7 km s^{-1}).

2.4.3 Results and Data Analysis

Of the sources searched here, signal from l-C_3H^+ was observed only toward the Orion Bar PDR (see Figure 2.10). Gaussian fits to the emission lines show an average FWHM width of 3.6 km s^{-1}, with peak intensities of 28.5 mK ($J = 9 - 8$), 32.9 mK ($J = 10 - 9$), and 37.5 mK ($J = 11 - 10$), and signal-noise-ratios of 4.4, 5.2, and 5.0, respectively, with a $V_{LSR} = 10.4$ km s^{-1}. These values for linewidth and velocity are consistent with other molecules associated with the Orion Bar PDR [54]. A rotational diagram analysis indicates a rotational temperate of 178(13) K and a column density of $7(2) \times 10^{11}$ cm^{-2}. A detailed examination of the rotational diagram method, as well as the equation used to determine column densities (Equation 1.4), can be found in [31].

The spectra collected in the targeted search, other than in the Orion Bar PDR, are shown in Figure 2.11 ($J = 10 - 9$) and Figures 2.12 and 2.13 ($J = 12 - 11$). Spectra from the unbiased line surveys around the $J = 10 - 9$ transition are shown in Figures 2.14 - 2.16.

Upper limits to the column density in each source are calculated using Equation 1.4, following the convention of [30].

For all sources in the targeted search, ΔT_{mb} was taken as the RMS noise of the appropriately smoothed spectrum, and ΔV was typically determined by a Gaussian fit to the nearby $C^{17}O$ line. In some cases, such as the clearly masing Sgr A* signal or completely empty spectra, a literature value was used (see notes in Table 2.11). Partition functions were calculated using Equation 2.6 (cf. [29]) as described in [46].

To calculate upper limits, we use the molecule-specific parameters given in [48] and the upper limit ΔT_{mb} and ΔV values given in Table 2.11. For these frequency ranges at the CSO, η_b is

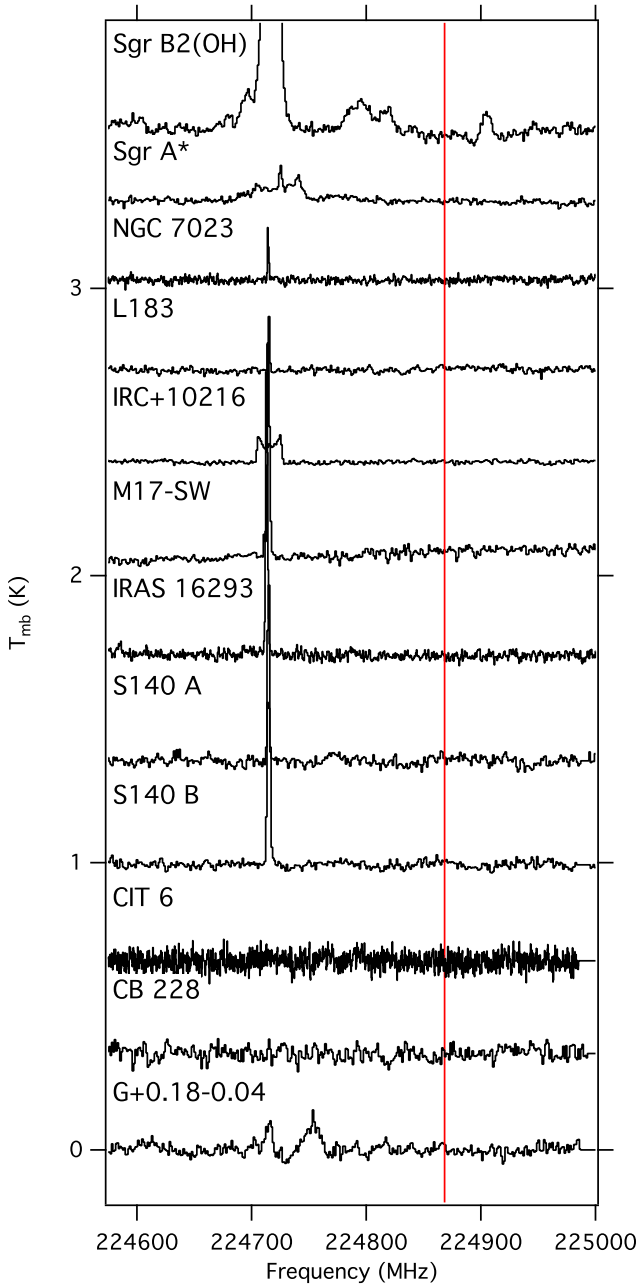

Figure 2.11: $J = 10 - 9$ spectral window toward target sources. All spectra are adjusted to the V_{LSR} indicated in Table 2.9, and are vertically offset for clarity. The feature at 224714 MHz is due to $C^{17}O$. The red vertical line indicates the frequency of the $J = 10 - 9$ transition.

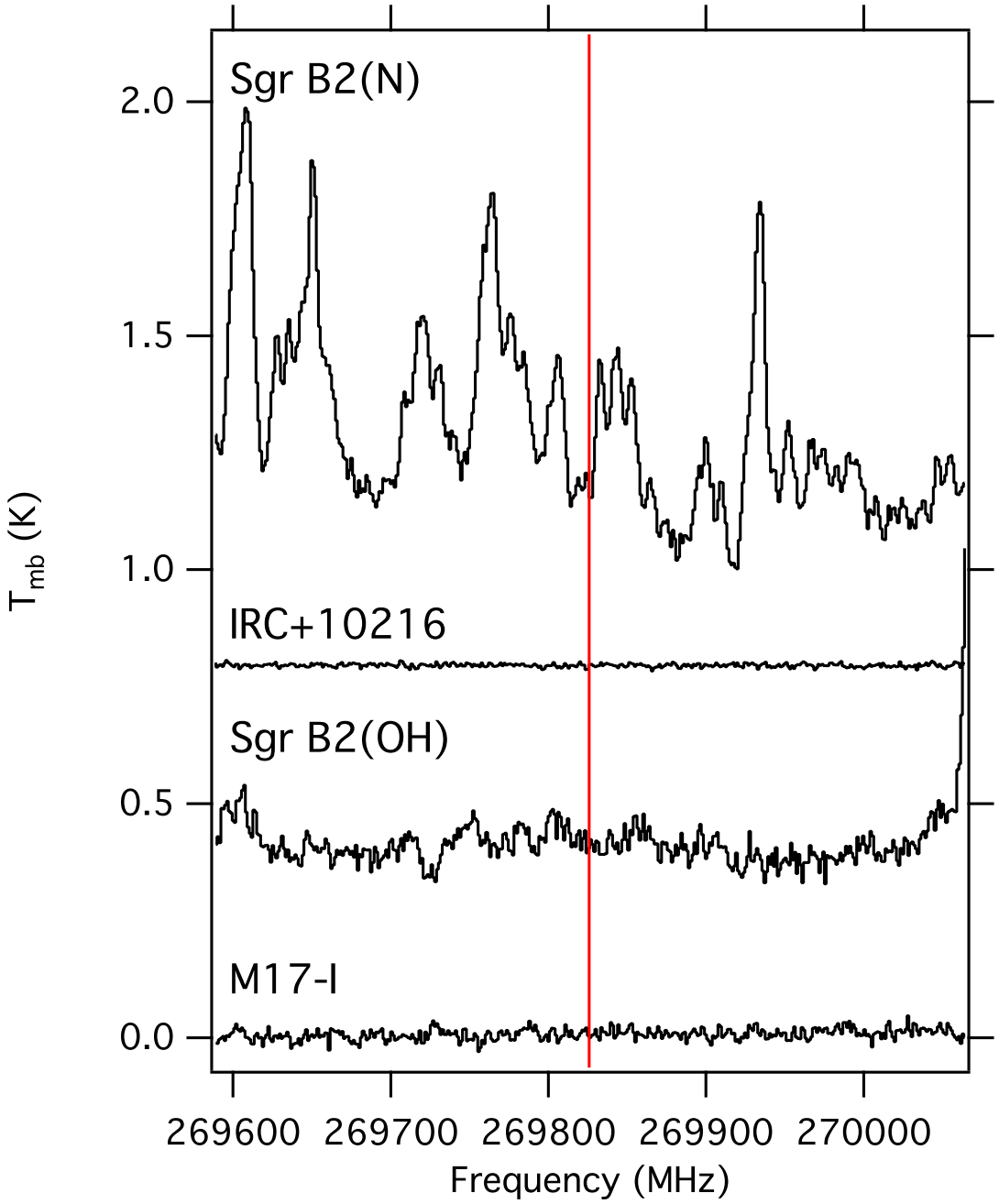

Figure 2.12: $J = 12 - 11$ spectral window toward target sources. All spectra are adjusted to the V_{LSR} indicated in Table 2.9, and are vertically offset for clarity. The red vertical line indicates the frequency of the $J = 12 - 11$ transition.

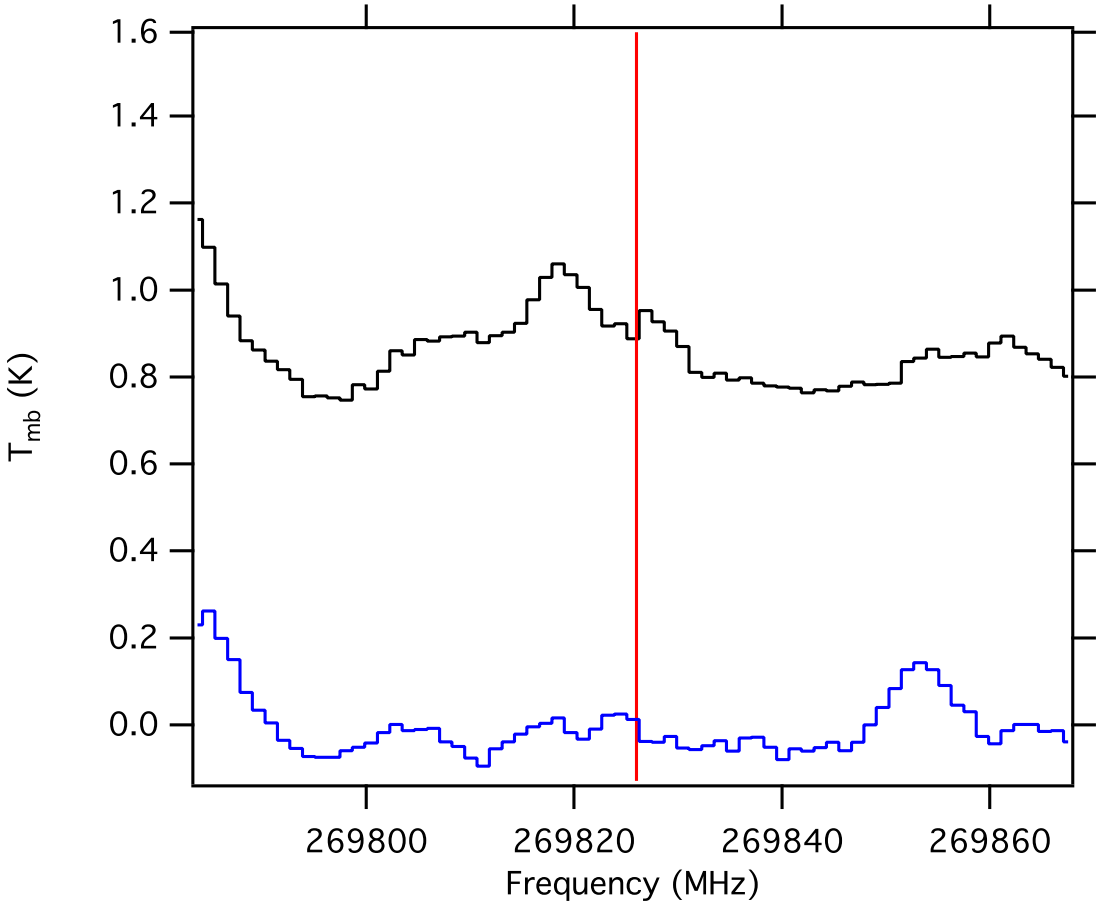

Figure 2.13: $J = 12 - 11$ spectral window toward W51e2 in two different IF settings. Spectra are DSB, adjusted to a $V_{LSR} = +55$ km s^{-1}, and are vertically offset for clarity. The red vertical line indicates the frequency of the $J = 12 - 11$ transition.

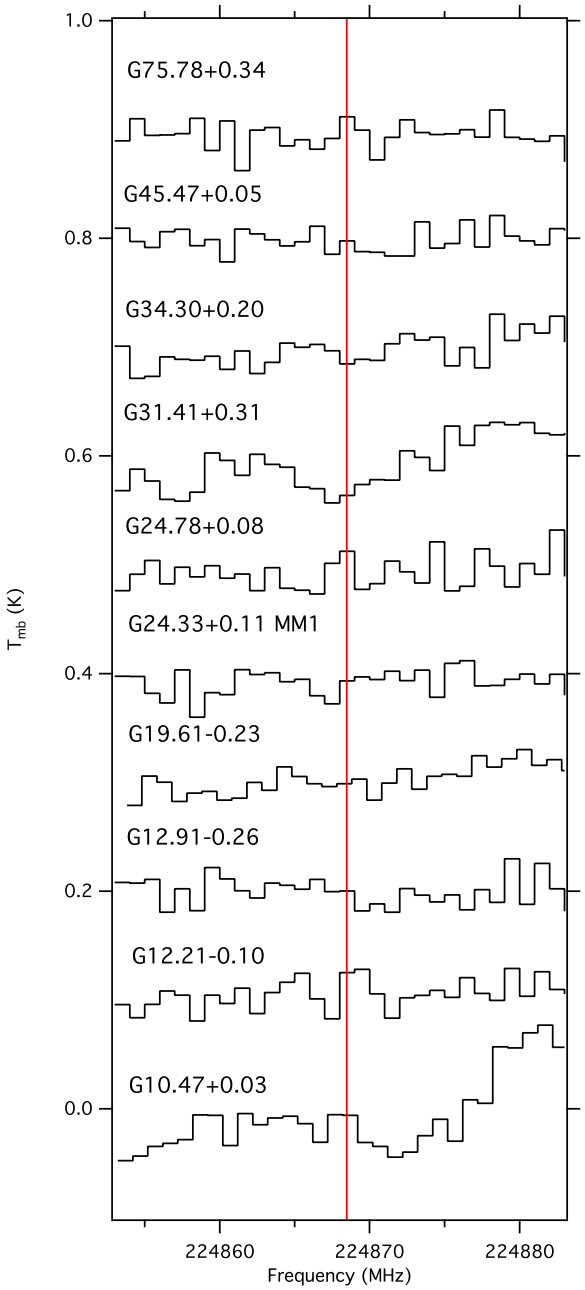

Figure 2.14: $J = 10 - 9$ spectral window toward unbiased line survey sources. All spectra are adjusted to the V_{LSR} indicated in Table 2.10, and are vertically offset for clarity. The red vertical line indicates the frequency of the $J = 10 - 9$ transition.

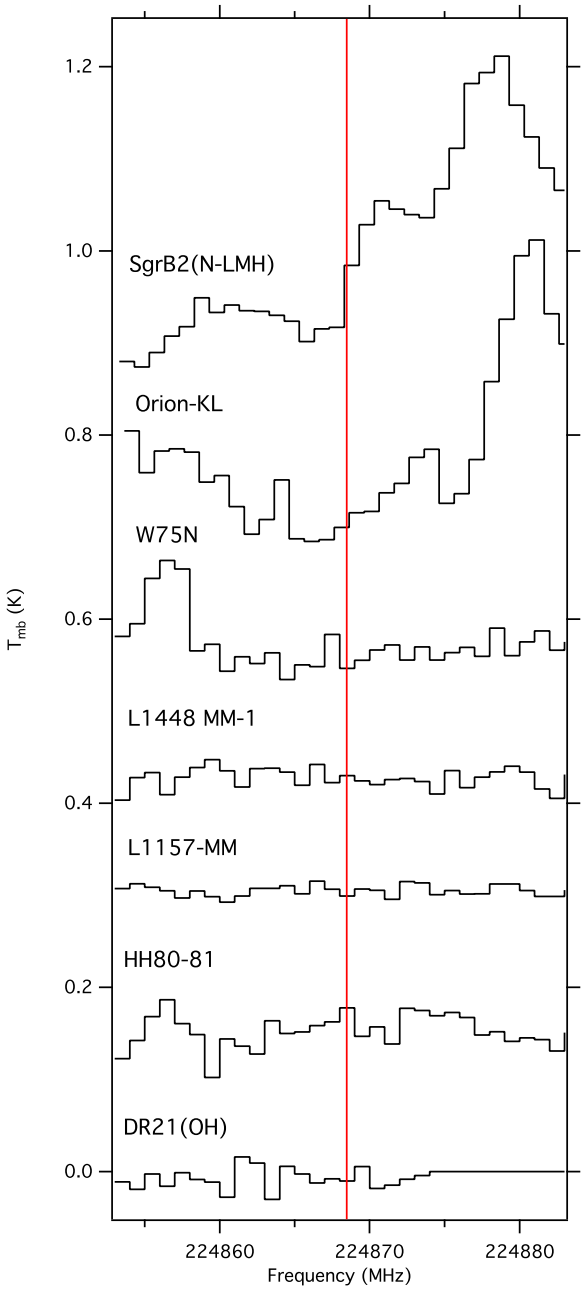

Figure 2.15: $J = 10 - 9$ spectral window toward unbiased line survey sources. All spectra are adjusted to the V_{LSR} indicated in Table 2.10, and are vertically offset for clarity. The red vertical line indicates the frequency of the $J = 10 - 9$ transition.

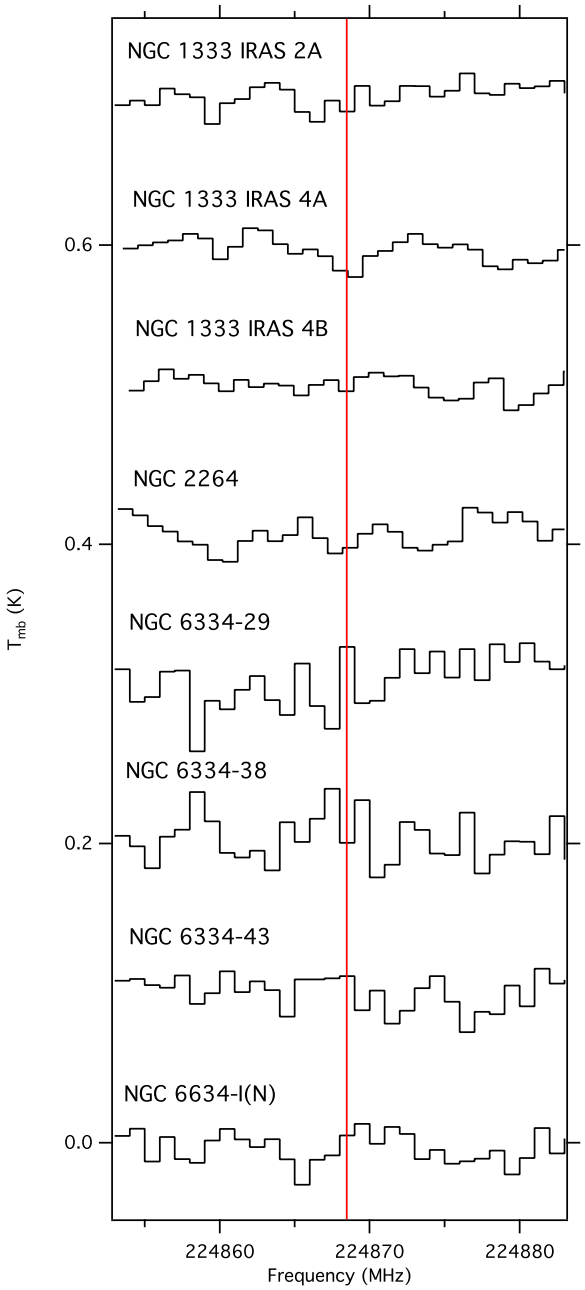

Figure 2.16: $J = 10 - 9$ spectral window toward unbiased line survey sources. All spectra are adjusted to the V_{LSR} indicated in Table 2.10, and are vertically offset for clarity. The red vertical line indicates the frequency of the $J = 10 - 9$ transition.

$\sim$0.70. Upper limits for each molecule in these sources, near the two extremes of temperature so far attributed to l-C_3H^+ , are shown in Table 2.12.

2.4.4 Discussion

Of the 39 sources observed in this work, l-C_3H^+ has been detected in a single one only: the Orion Bar PDR. This extends the list of environments in which l-C_3H^+ is known to be present to three: the Orion Bar PDR, the Horsehead PDR, and Sgr B2(N), with tenuous evidence for l-C_3H^+ in Sgr B2(OH) and TMC-1.

The lack of detection of l-C_3H^+ , in reasonably high-sensitivity observations, toward any molecularly-rich hot core source outside of Sgr B2(N), is initially puzzling. The detection in Sgr B2(N) by [45] may have been fortuitous; the highly sub-thermal nature of the observed absorption features may have allowed their observation despite an otherwise low abundance that would typically preclude detection. Perhaps more puzzling is the lack of detection in the majority of the PDR sources observed here. The answer is almost certainly one of temperature; with column densities similar to those found the Horsehead and Orion Bar PDRs, the observations presented here with the CSO are not sensitive to material cooler than $\sim$130 K. Thus, further high-sensitivity observations at 3 mm, where the Boltzmann peak for cold l-C_3H^+ falls, are warranted to fully explore the range of excitation conditions so far attributed to this molecule.

Further insight into likely sources in which l-C_3H^+ could be found may also be gained by comparing its formation and destruction pathways to that of HOC^+. As described by [48], the primary formation mechanism for l-C_3H^+ is through the reaction of acetylene with C^+. Destruction readily occurs via reaction with molecular hydrogen (see Eqs. 2.8 - 2.10).

$$C_2H_2 + C^+ \rightarrow C_3H^+ \tag{2.8}$$

$$C_3H^+ \xrightarrow{H_2} C_3H_2^+ \xrightarrow{e^-} C_3H \tag{2.9}$$

$$C_3H^+ \xrightarrow{H_2} C_3H_3^+ \xrightarrow{e^-} C_3H_2 \tag{2.10}$$

The detections of l-C_3H^+ in the Horsehead and Orion Bar PDRs support these formation and destruction mechanisms. Destruction via H_2 is expected to be rapid and thus dominate l-C_3H^+ populations under typical conditions. Within PDR sources, however, where the ultraviolet radiation field is greatly enhanced relative to the mean interstellar value, sufficient C^+ may be present to compete with this destruction pathway and lead to detectable abundances of l-C_3H^+ .

Table 2.11: Summary of observations of the $J = 10 - 9$ and $J = 12 - 11$ frequency windows.

	$J = 10 - 9$			$J = 12 - 11$					
	RMS	Resolution		RMS	Resolution		ΔV		
Source	(mK)	(MHz)	(km s^{-1})	(mK)	(MHz)	(km s^{-1})	(km s^{-1})	Switching	DSB/SSB
Sgr B2(OH)	27.5	1.2	1.6	32.0	1.2	1.3	25	PS	DSB
Sgr A*	6.0	1.2	1.6	...	...	...	20[a]	PS	DSB
NGC 7023	8.3	0.6	0.8	...	...	...	2	Chop	SSB
L 183	8.7	1.2	1.6	...	...	...	3	PS	DSB
IRC+10216	5.8	1.2	1.6	3.7	1.2	1.3	30	Chop†	SSB
M17-SW	10.9	1.2	1.6	13.0	1.3	1.4	5	PS‡	SSB
IRAS 16293	11.4	0.6	0.8	...	...	...	4	Chop	SSB
S140 A	14.1	1.2	1.6	...	...	...	4	Chop†	DSB
S140 B	11.5	1.2	1.6	...	...	...	5	PS	DSB
CIT 6	15.4	0.3	0.4	...	...	...	30[b]	PS	DSB
CB 228	21.9	1.2	1.6	...	...	...	1[c]	PS	DSB
G+0.18-0.04	15.4	1.2	1.6	...	...	...	27	PS	DSB
W51e2	...	...	...	46.2	1.2	1.3	13	PS	DSB⋆
Sgr B2(N)	...	...	...	15.0	1.2	1.3	13	PS	SSB
L1448 MM-1	10.9	1.0	1.3	...	...	...	1.4	Chop	SSB
NGC 1333 IRAS 2A	7.7	1.0	1.3	...	...	...	3.8	Chop	SSB
NGC 1333 IRAS 4A	8.5	1.0	1.3	...	...	...	5	Chop	SSB
NGC 1333 IRAS 4B	9.5	1.0	1.3	...	...	...	4.1	Chop	SSB
Orion-KL	36.9	1.0	1.3	...	...	...	6.5	Chop	SSB
NGC 2264	12	1.0	1.3	...	...	...	3.8	Chop	SSB
NGC 6334-29	19.4	1.0	1.3	...	...	...	4.5	Chop	SSB
NGC 6334-38	15.5	1.0	1.3	...	...	...	3.4	Chop	SSB
NGC 6334-43	10.9	1.0	1.3	...	...	...	3.2	Chop	SSB
NGC 6334-I(N)	10.6	1.0	1.3	...	...	...	4.8	Chop	SSB
Sgr B2(N-LMH)	32.3	1.0	1.3	...	...	...	18	Chop	SSB
GAL 10.47+0.03	34.4	1.0	1.3	...	...	...	8.7	Chop	SSB
GAL 12.21-0.10	14.2	1.0	1.3	...	...	...	7.4	Chop	SSB
GAL 12.91-00.26	12.9	1.0	1.3	...	...	...	4.2	Chop	SSB
HH 80-81	38.2	1.0	1.3	...	...	...	2.6	Chop	SSB
GAL 19.61-0.23	13.6	1.0	1.3	...	...	...	7.4	Chop	SSB
GAL 24.33+0.11 MM1	14.2	1.0	1.3	...	...	...	4	Chop	SSB
GAL 24.78+0.08	16.3	1.0	1.3	...	...	...	5.2	Chop	SSB
GAL 31.41+0.31	24.8	1.0	1.3	...	...	...	6.3	Chop	SSB
GAL 34.3+0.20	15.1	1.0	1.3	...	...	...	6.5	Chop	SSB
GAL 45.47+0.05	10.5	1.0	1.3	...	...	...	4.8	Chop	SSB
GAL 75.78+0.34	13.4	1.0	1.3	...	...	...	3.5	Chop	SSB
W75N	17.4	1.0	1.3	...	...	...	4	Chop	SSB
DR21(OH)	13.5	1.0	1.3	...	...	...	6.5	Chop	SSB
L1157-MM	6.2	1.0	1.3	...	...	...	5.5	Chop	SSB

† At least one observation was taken in position switched mode to determine whether extended structure was being chopped into with the secondary mirror. No difference was observed between the position switched and chopped off position.
‡ The throw for this source was 5′
⋆ Two IF settings were observed for this source.
References – (a) [114]; (b) [115]; [116]

Table 2.12: Upper limits for l-C_3H^+ in each source at 15 K and at 180 K.

	N_T (10^{12} cm^{-2})	
Source	15 K	180 K
Sgr B2(OH)	13	4.1
Sgr A*	2.2	0.7
NGC 7023	0.3	0.1
L 183	0.5	0.2
IRC+10216	3.3	1.0
M17-SW	1.0	0.3
IRAS 16293	0.9	0.3
S140 A	1.1	0.3
S140 B	1.1	0.3
CIT 6	8.7	2.7
CB 228	0.4	0.1
G+0.18-0.04	7.8	2.5
W51e2	41	2.8
Sgr B2(N)	13	0.9
L1448 MM-1	0.3	0.1
NGC 1333 IRAS 2A	0.5	0.2
NGC 1333 IRAS 4A	0.8	0.3
NGC 1333 IRAS 4B	0.7	0.2
Orion-KL	4.5	1.4
NGC 2264	0.9	0.3
NGC 6334-29	1.6	0.5
NGC 6334-38	1.0	0.3
NGC 6334-43	0.7	0.2
NGC 6334-I(N)	1.0	0.3
Sgr B2(N-LMH)	11	3.4
GAL 10.47+0.03	5.6	1.8
GAL 12.21-0.10	2.0	0.6
GAL 12.91-00.26	1.0	0.3
HH 80-81	1.9	0.6
GAL 19.61-0.23	1.9	0.6
GAL 24.33+0.11 MM1	1.1	0.3
GAL 24.78+0.08	1.6	0.5
GAL 31.41+0.31	2.9	0.9
GAL 34.3+0.20	1.8	0.6
GAL 45.47+0.05	0.9	0.3
GAL 75.78+0.34	0.9	0.3
W75N	1.3	0.4
DR21(OH)	1.6	0.5
L1157-MM	0.6	0.2

A comparison can be made with the chemistry of HOC^+, which is also formed, directly and indirectly, through reactions of C^+, and destroyed by reaction with H_2 to form HCO^+ (see Eqs. 2.11 - 2.13, c.f. [117; 54]). Thus, observations of a high HOC^+ abundance (or, alternatively, an enhanced $[HOC^+]/[HCO^+]$ ratio) may be indicative of chemical and physical conditions that will also favor the production of l-C_3H^+ , and act as a probe to guide future sources.

$$H_2O \xrightarrow{C^+} HOC^+ \tag{2.11}$$

$$OH \xrightarrow{C^+} CO^+ \xrightarrow{H_2} HOC^+ \tag{2.12}$$

$$HOC^+ \xrightarrow{H_2} HCO^+ \tag{2.13}$$

Indeed, such an enhanced HOC^+ abundance (and enhanced $[HOC^+]/[HCO^+]$ ratio) has already been detected toward both the Orion Bar PDR [54] and the Horsehead PDR [109], with these values peaking in the region of the PDR. A similarly enhanced presence of HOC^+ is detected by [54] in observations of the NGC 7023 PDR, for which l-C_3H^+ is not detected in these CSO observations. This suggests that perhaps l-C_3H^+ is simply too cold to be detected in our observations at this sensitivity, and that observations at lower frequencies may result in a detection.

Observations of HOC^+ in diffuse clouds by [118] find abundance ratios of $[HOC^+]/[HCO^+]$ comparable to that of the extreme cases of PDR enhancements in the Orion Bar and NGC 7023. This is consistent with the tentative detections of l-C_3H^+ absorption in diffuse, spiral arm clouds by [45] along the line of sight to Sgr B2(N), and suggests these sources may be intriguing targets for future observations.

Finally, detections of HOC^+ toward other regions with enhanced FUV flux provide other tantalizing sources for future study. A small list of these sources includes, for example, the Monocerous R2 ultracompact HII region [119] and the external galaxies NGC 253 [120] and M 82 [121].

2.4.5 Conclusions

We have examined the results of both a dedicated campaign targeting l-C_3H^+ in 14 sources, as well as 25 additional sources from unbiased molecular line surveys with frequency coverage coincident with l-C_3H^+ transitions. We detect the presence of l-C_3H^+ in only a single source: the Orion Bar PDR. These observations are only sensitive to relatively warm material, and follow-up observations at lower frequencies are necessary to obtain a complete picture of$l$-C_3H^+ in these sources. Finally, a comparison to the chemistry of HOC^+ has shown that HOC^+ has the potential to serve as a tracer

of l-C_3H^+ . Previous observations of HOC^+ can therefore be used as a guide to efficiently target new sources in additional searches for l-C_3H^+ .

Chapter 3

Carbodiimide (HNCNH)

The bulk of this chapter is reproduced from "Interstellar carbodiimide (HNCNH) - A new astronomical detection from the GBT PRIMOS survey via maser emission features," by B.A. McGuire et al., Astrophysical Journal Letters, 758, L33 (2012) [77].

3.1 Introduction

Historically, searches for new astronomical molecules resulted in the detection of favorable, high line strength transitions based on a thermal approximation to the excitation of these species in interstellar environments. At the temperatures of hot molecular cores inside molecular clouds, these transitions often reside at (sub)millimeter wavelengths. However, line confusion near the Boltzmann peak can lead to ambiguous identifications, and the peak intensities of low abundance, large organic molecules may never rise above the noise floor or the confusion limit. The success of molecule searches at centimeter wavelengths has shown that unique excitation conditions can lead to the unambiguous identification of very low abundance species with high accuracy.

Carbodiimide (HNCNH) is the second most stable isomer of cyanamide (NH_2CN), with NH_2CN being more stable by $\sim$4.0 kcal mol^{-1} [122; 123]. Since the detection of NH_2CN by Turner et al. (1975) [124] toward the high-mass star-forming region Sgr B2(N), HNCNH has been recognized as a candidate interstellar molecule. HNCNH is also a tautomer of NH_2CN, and can be formed via an isomerization reaction whereby a H atom can migrate along the molecular backbone from the amine group. At room temperature, HNCNH is in thermally-induced equilibrium with NH_2CN at a fraction of $\sim$1%. Given typical abundances of NH_2CN, and temperatures in many astrophysical environments of $<<$ 300 K, gas-phase tautomerization of NH_2CN is unlikely to produce HNCNH in appreciable abundance. Yet, HNCNH may exist in detectable abundance out of thermal equilibrium with NH_2CN

as in the case of interstellar hydrogen cyanide (HCN) and interstellar hydrogen isocyanide (HNC), in which HNC is in greater abundance in some clouds (see [125] and references therein).

Although tautomerization is likely inefficient in the gas phase under interstellar conditions, experimental studies have shown $NH_2CN \rightarrow$ HNCNH conversion in water ices and matrices is far more efficient ([126] and references therein). In the solid phase, the association of up to five water molecules with NH_2CN on an ice surface has been shown to significantly lower the activation barrier to tautomerization and promote the production of HNCNH [126]. In fact, HNCNH formation on a water-ice surface is shown to occur at temperatures as low as 70 K. The relative abundance of HNCNH formed from this process has been measured to range from 4% of NH_2CN at 80 K to as much as 13% at 140 K [126]. In the laboratory, HNCNH sublimation occurs between 80 - 170 K, with no additional desorption observed above 170 K [122]. In the ISM, non-thermal desorption via shocks is also a likely liberation mechanism. Assuming that tautomerization of NH_2CN on dust grain ice mantles is the dominant formation pathway for HNCNH, and that subsequent desorption occurs for both species, the gas phase abundance of HNCNH may be capped at $\sim$10% of NH_2CN.

NH_2CN has an estimated column density of $\sim 2\times10^{14}$ cm^{-2} towards Sgr B2(N) [25]; we therefore anticipate an HNCNH column density on the order of $\sim 10^{13}$ cm^{-2}. If thermal emission at hot core temperatures dominates the spectrum of HNCNH, the most favorable high line strength transitions are at millimeter and submillimeter wavelengths. Nevertheless, we have previously used the Robert C. Byrd Green Bank Telescope (GBT) to detect new molecular species including trans-methyl formate [75], and cyanoformaldehyde [81], which *only* had measurable astronomical line intensities detected at centimeter wavelengths. Encouraged by these results, we searched for centimeter wave transitions of HNCNH. All data were taken as part of the PRebiotic Interstellar MOlecular Survey (PRIMOS), and targeted rotation-torsion transitions of HNCNH selected from the Cologne Database for Molecular Spectroscopy[1,2] [18]. Our results are presented in §3.2. In §3.3, we evaluate the probability of mis-assigning these features to HNCNH, and discuss evidence that observed transitions are masing. Further, we explore the usefulness of our technique as a method for new molecule detection.

3.2 Observations and Results

All data used for this project were taken as part of the National Radio Astronomy Observatory's (NRAO) 100-m Robert C. Byrd Green Bank Telescope (GBT) PRebiotic Interstellar MOlecule

[1] Original laboratory data cataloged from Birk et al. (1980) [127], Wagener et al. (1995) [128], & Jabs et al. (1997) [129].

[2] Available at www.splatalogue.net [28].

Survey (PRIMOS) Legacy Project.[3] This NRAO key project started in January 2008, and concluded in July 2011. The PRIMOS project recorded a nearly frequency-continuous astronomical spectrum from 1 to 50 GHz towards the Sgr B2(N) molecular cloud, with the pointing position centered on the Large Molecule Heimat (LMH) at (J2000) α = 17h47m19.8s, δ = -28°22'17". An LSR source velocity of +64 km s^{-1} was assumed. Intensities are presented on the T_A^* scale [130]. See [75] for further details of the observations, full data reduction procedure, and analysis.

Targeted transitions of HNCNH are shown in Table 3.1. The table provides Gaussian fit parameters for peak intensity and line width for components at v_{LSR} = +64 km s^{-1} and +82 km s^{-1}. Molecular material at these two velocities is characteristic of clouds that lie within the GBT beam along the same line of sight (see e.g. [81] and references therein). Figure 3.2 shows the spectra for the observed passbands. The red and blue vertical lines indicate the location of the emission feature at LSR velocities of +64 km s^{-1} and +82 km s^{-1}, respectively. We find four unblended lines of HNCNH in this region (panels a) - c) and g)). One frequency range was unobservable by the GBT (16 GHz), while two spectral feature were contaminated by transitions of CH_3OH (panels d) & g)). Finally, one transition was not observed due to lack of frequency coverage (46.2 GHz). Of the observable transitions, we show clear detections of both the +64 km s^{-1} and +82 km s^{-1} components at 4.3, 4.8 and 25.8 GHz, and the +64 km s^{-1} component at 45.8 GHz (Figure 3.1). The four line detections and two non-detections are consistent with only masing lines being detectable, as discussed in §3.3.

3.3 Discussion

The initial identification of HNCNH was based on only the two lines at 4.3 and 4.8 GHz. In order to quantify the probability of coincidental overlap of features at these frequencies, which could lead to a possible mis-assignment, we used the method outlined in [75]. We find 37 observed transitions within a representative window of 200 MHz of PRIMOS at C-band (4 - 6 GHz), 14 of which are within ±50% of the intensity of the detected features. This line density is typical of the PRIMOS survey in this frequency range. Of these 14 features, 4 were in emission. If we then assume a conservative FWHM line width of 25 km s^{-1} (almost twice our measured FWHM), we calculate the probability of a single line falling coincidentally within one FWHM of our line to be 0.75%. For two detected lines, that probability drops to 0.002%. We find that this is both compelling evidence for

[3]Access to the entire PRIMOS dataset, and specifics on the observing strategy including the overall frequency coverage, is available at http://www.cv.nrao.edu/∼aremijan/PRIMOS/.

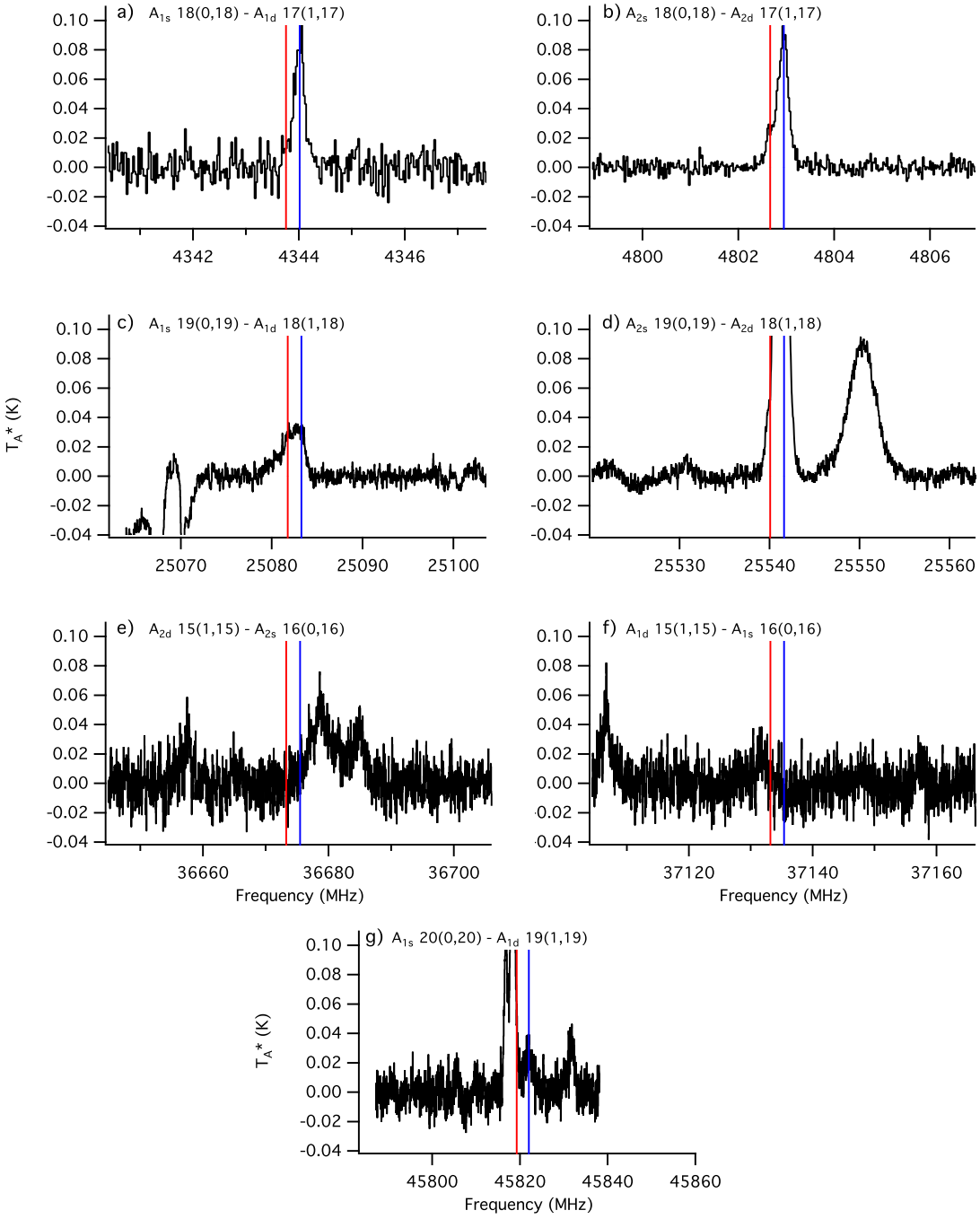

Figure 3.1: Carbodiimide (HNCNH) spectral passbands toward Sgr B2(N), recorded from the GBT PRIMOS Survey. Rotation-torsion doublet transition quantum numbers are shown in each panel. The passband width displayed is 500 km s^{-1} in each case. The spectra are plotted as a function of frequency (MHz), corrected for a LSR source velocity of +64 km s^{-1}. The blue and red vertical lines indicate the location of the transition rest frequency (see Table 3.1) at an assumed LSR source velocity of +64 km s^{-1} and +82 km s^{-1}, respectively. Data in all panels were Hanning-smoothed for display purposes.

Table 3.1: HNCNH Rotation-Torsion Doublets, Spectroscopic, and Observed Astronomical Parameters

				64 km s^{-1}		82 km s^{-1}	
Transition	Frequency[a]	$\log_{10}(A_{ij})$	E_u	Intensity[b]	FWHM[b]	Intensity[b]	FWHM[b]
Γ' J$'$(K$'_a$,K$'_c$) - Γ'' J$''$(K$''_a$,K$''_c$)	(MHz)		(cm^{-1})	(mK)	(km s^{-1})	(mK)	(km s^{-1})
A_{1s} 18(0,18) - A_{1d} 17(1,17)	4344.017	-9.10	118.2475	85(5)	16(1)	13(6)	8(5)
A_{1d} 16(1,16) - A_{1s} 17(0,17)	16395.527	-7.35	106.3484	... [c]	...	... [c]	...
A_{1s} 19(0,19) - A_{1d} 18(1,18)	25083.268	-6.81	131.3845	27(4)	14.0(0.5)	28(1)	22(2)
A_{1d} 15(1,15) - A_{1s} 16(0,16)	37135.396	-6.28	95.2854	≤ 12	...	≤ 12	...
A_{1s} 20(0,20) - A_{1d} 19(1,19)	45822.046	-6.03	145.2126	25(1)	13(2)	... [d]	...
A_{2s} 18(0,18) - A_{2d} 17(1,17)	4802.952	-8.97	118.2548	89(2)	15.9(0.4)	23(2)	12(1)
A_{2d} 16(1,16) - A_{2s} 17(0,17)	15936.094	-7.38	106.3405	... [c]	...	... [c]	...
A_{2s} 19(0,19) - A_{2d} 18(1,18)	25541.620	-6.79	131.3918	... [d]	...	(50)[f]	(12)[f]
A_{2d} 15(1,15) - A_{2s} 16(0,16)	36675.469	-6.30	95.2776	≤ 11	...	≤ 11	...
A_{2s} 20(0,20) - A_{2d} 19(1,19)	46279.903	-6.01	145.2199	... [c]	...	... [c]	...

a) All lines except those at 4 GHz have been experimentally measured with (Obs - Calc) frequency uncertainties ≤ 30 kHz. Uncertainties on the 4 GHz lines are calculated to be ≤ 30 kHz, type A, k = 2 (2σ) [85].
b) The uncertainties for the intensities and linewidths are type B, k = 1 (1σ) [85].
c) No data
d) Transition contaminated by CH_3OH emission.
f) Estimated based on a gaussian fit to the low-frequency shoulder of the CH_3OH emission at +82 km s^{-1}

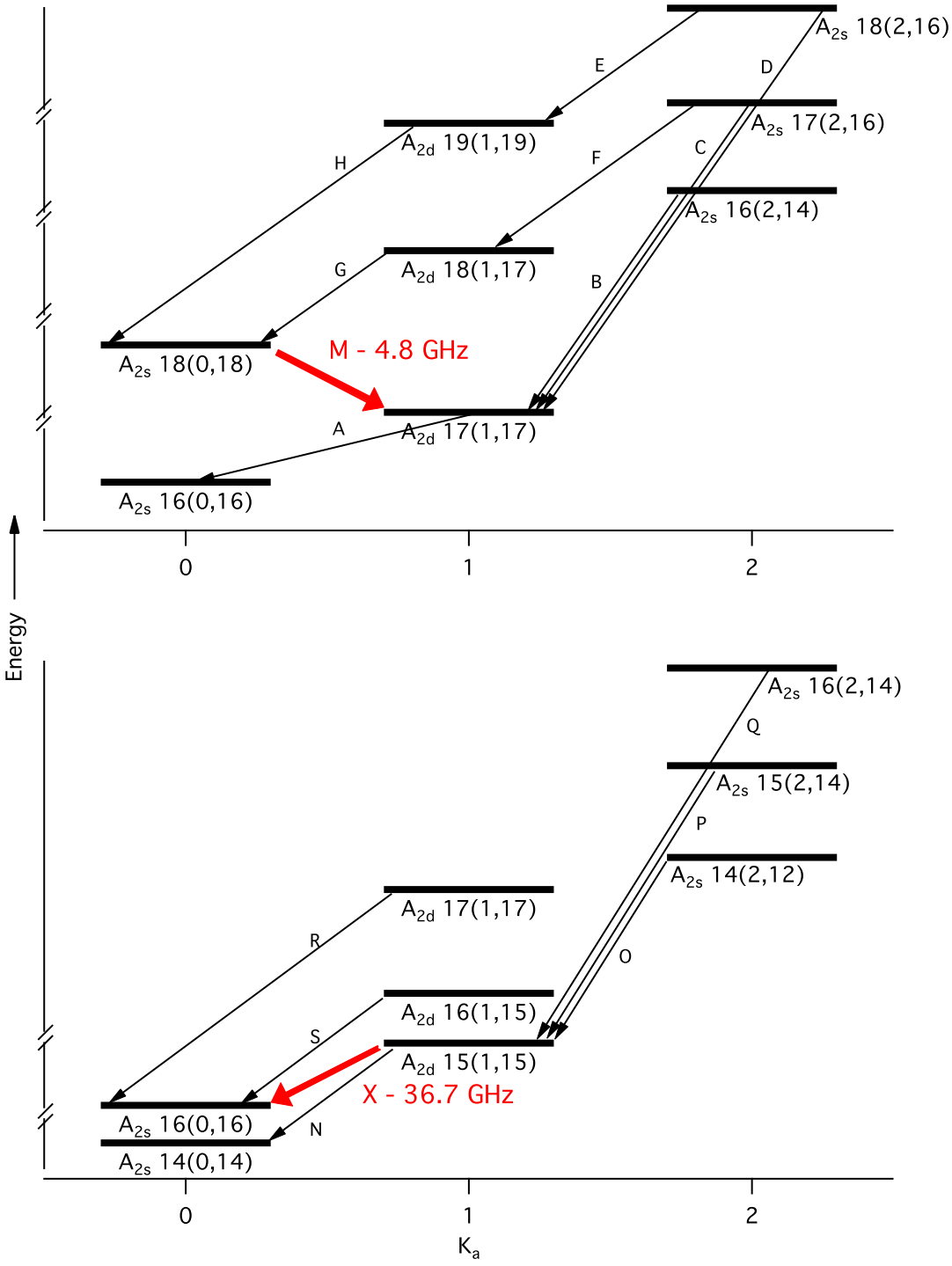

Figure 3.2: Energy level structure of the relevant transitions for the 4.8 GHz maser (top) and 36.6 GHz line (bottom). Energy levels are ordered by increasing energy, but are not drawn to scale. Allowed transitions are indicated by arrows.

a clear detection and an excellent example of the power of the GBT in new molecule detections at centimeter wavelengths, where line confusion is drastically reduced relative to the millimeter and sub-millimeter regimes.

Initially, the large beamwidths and high-energy nature of the observed lines pointed to emission arising from the hot, extended source that surrounds the cold LMH and couples well to the beam at these frequencies. An LTE analysis, however, showed excessively high column densities for thermal emission arising from these lines. In order to further verify the identification, and to understand the unusually high intensities of the lines, we examined higher frequency transitions. Unfortunately, the GBT has no receiver that operates between 15-16 GHz; we detected an emission feature at 25.0 GHz, but its doublet transition at 25.5 GHz is blended with the 9(2,7)-9(1,8) transition of CH_3OH at 25.541 GHz; we detected no emission features at 36.6 and 37.1 GHz; and a feature was identified at 45.8 GHz, the highest frequency line currently covered in the PRIMOS survey. The lack of observed transitions at 36.6 and 37.1 GHz was initially troubling, as there has been a firmly established series of requirements for an interstellar detection, including that no transition which should be of an observable intensity be "missing" [11]. However, an examination of the rotational energy level structure of HNCNH offers an explanation.

Figure 3.2 shows energy level diagrams containing transitions that are relevant to the observed masing lines at 4.8 GHz (labeled "M," Figure 3.2[a]) and 36.7 GHz (labeled "X," Figure 3.2[b]). The quantum mechanical parameters associated with transitions in Figure 3.2 are given in Table 3.1. In the case of the 4.8 GHz line "M," the upper energy level (A_{2s} 18(0,18)) is coupled to higher energy levels via fast millimeter and sub-millimeter transitions; the only downward transition out of this level is very slow, with an Einstein A coefficient of $\sim 10^{-9}$ s^{-1}. Downward and upward transitions out of the lower level (A_{2d} 17(1,17)), labeled "A - D," however, occur rapidly with Einstein A values between 0.2 - 2 x 10^{-2} s^{-1}. This creates a population inversion between the A_{2s} 18(0,18) and A_{2d} 17(1,17) levels, leading to the observed masing at 4.8 GHz. An analogous process occurs for the torsion doublet, causing masing at 4.3 GHz. A similar energy structure exists for the 25.5 GHz and 46.7 GHz transitions and their torsion doublets, leading to masing in these transitions as well.

For the 36.7 GHz line (labelled "X," Figure 3.2[b]), the upper state (A_{2d} 15(1,15)) is again coupled to higher energy levels via fast transitions, with the 36.7 GHz transition being the slow emission path to A_{2s} 16(0,16). In this case, however, a fast downward transition is allowed to the A_{2s} 14(0,14) state (transition labelled "N"). Population inversion is not achieved because of the presence of this drain, and the 36.7 GHz transition does not mase. A similar scenario holds for the

15.9 GHz transitions, as well as their torsion doublets. In summary, an analysis of the energy levels of HNCNH predicts a population inversion resulting in masing for the torsion doublets at 4, 25, and 46 GHz, with no masing by the doublets at 15 and 36 GHz. Furthermore, the 4 GHz doublets should show a greater degree of inversion due to the longer lifetime of the transitions (Table 3.1) than the 25 or 46 GHz transitions, resulting in more intense lines, which is in excellent agreement with our observations.

The observed maser emission is relatively weak and displays no line narrowing, suggesting that these are unsaturated maser lines. As collisional and radiative pumping rates for HNCNH are unknown, a full pumping model was not possible, and is beyond the scope of this work. A zeroth-order calculation of the critical density for the fast transitions connecting the maser transitions was, however, performed. Using collisional coefficients for similar transitions in HNCO, we find critical densities required to thermalize these transitions on the order of 10^8 - 10^{10} cm^{-3}, far higher than those typically associated with the region. Given this, and that the Sgr B2(N) region is known to contain a broad range of favorable radiative excitation conditions, a radiative excitation mechanism for these transitions is possible. The current observations, however, do not provide a definitive answer to the excitation question, and further investigation is warranted. A mapping study of the 4 GHz lines in Sgr B2(N) would be extremely beneficial to elucidating the environment these signals are arising from, including their spatial correlation with other known maser such as CH_3OH, and therefore the most likely excitation mechanisms.

We have also carried out an analysis of the expected intensity of HNCNH lines in this frequency region based on a thermal population of HNCNH. Assuming local thermodynamic equilibrium (LTE) conditions, we calculate a column density of HNCNH giving rise to the 4 GHz maser lines of $\sim$2 x 10^{16} cm^{-2} at 150 K, although this value is largely invariant over temperatures from 80 - 500 K. Given this column density, the expected intensity of the 36.7 GHz transition would be $\sim$740 mK. Further, at a column density of $\sim$2 x 10^{13} cm^{-2} ($\sim$10% of NH_2CN in this source [25]), we would expect the most intense lines in this region to be less than 1 mK for rotational temperatures above 80 K. Given this, and the lack of any detection at 36.7 GHz with an RMS noise level of $\sim$10 mK, we conclude that these transitions are not arising from a thermal population.

This is consistent with our non-detection of transitions that are not masing. In gas above 80 K, the most intense lines of HNCNH at LTE would fall at millimeter and sub-millimeter wavelengths. Numerous high-resolution, high-sensitivity spectral line surveys of this region have been carried out (see [131; 132; 25] and refs. therein) covering the these transitions up to $\sim$1.8 THz. With an

abundance of 10% NH_2CN, the strongest transitions under LTE emission at 80 K would be on the order of the RMS noise level of the survey observations. With increasing temperature, the expected line strengths decrease rapidly. Thus, at these column densities, a thermal population of HNCNH would likely not be detectable in even the most sensitive line surveys to date.

This is in itself remarkable. A heroic effort has been performed in recent years in compiling molecular inventories and facilitating new molecule detections using state-of-the-art millimeter and sub-millimeter observatories and molecular line surveys. These surveys have provided invaluable information on the physical and chemical conditions present in the ISM, and their high scientific value is unquestionable. They suffer, however, from extremely high line densities and long integration times relative to lower-frequency telescopes. Because of this, identifications of new molecular species, especially those in low abundance, can be difficult due to the line confusion at the noise floor and the degree of coincidental overlap of target lines with other molecular transitions.

In this work, we have shown that a molecule that would be undetectable via transitions arising from a thermal population can be identified via maser transitions at centimeter wavelengths. This detection was possible only through low-frequency surveys of a chemically-rich region by the GBT through a dedicated project (PRIMOS). The number of transitions that display significant maser activity in any given molecule is likely to be small, but weak masing behavior has been observed in a number of molecules, such as H_2CO and NH_3 [133; 134]. In addition, at centimeter wavelengths, the lack of line confusion makes definitive identification of a species possible with only a small number of observed transitions. This may represent a new strategy for searches for key molecules of interest to the astrochemistry and astrobiology communities that have not yet been detected due to their low abundances.

In summary, we have detected four transitions of carbodiimide (HNCNH) towards Sgr B2(N) with very high confidence. All four signals have been found to be the result of maser activity. We also report two transitions that were not detected, consistent with HNCNH only being detectable towards Sgr B2(N) through maser lines. This detection presents a new methodology for searches for interstellar molecular candidates that may be too low in abundance to be detected in thermal emission by modern radio observatories.

Part III

Time-Domain TeraHertz Spectroscopy of Interstellar Ice Analogs

Portions of this Part have been reproduced from "THz and mid-IR spectroscopy of interstellar ice analogs: methyl and carboxylic acid groups," by S. Ioppolo, B.A. McGuire, M.A. Allodi, and G.A. Blake, Faraday Discussions 168, in press (2014) [135] and "The structure and dynamics of carbon dioxide and water containing ices investigated via THz and mid-IR spectroscopy," by M.A. Allodi, S. Ioppolo, M.J. Kelley, B.A. McGuire, and G.A. Blake, Phys. Chem. Chem. Phys., 16, 3442 (2014) [136].

Chapter 4

The Power of THz Spectroscopy

While the number of known molecules identified in the gas phase continues to increase (see Figure 4.1), identification of solid-phase molecules has been remarkably slower. The majority of these are simple, abundant ice constituents - H_2O, CH_3OH, CO, CO_2, H_2CO, CH_4, and HCOOH [137]. Identification of complex species, such as methyl formate (CH_3OCHO), which are widely observed in high abundance in the gas phase but must be formed primarily in the solid-phase [7; 9], is so far lacking. Additionally, the number of sources in which *any* measurements of ices have been made is limited. This is likely due to several complicating factors.

First, the features arising from these solid-phase species in the infrared are often relatively broad, resulting in overlapping and confused signals in observations. Second, the sample set of sources from which we may observe these species in ices is limited, relative to gas-phase species, as we can observe these species only in absorption, rather than emission. At thermal equilibrium, detectable emission requires that the energy of the observed transition be much less than the populated energy levels – i.e. $h\nu \ll kT$. In the infrared, this generally requires temperatures in excess of 500 K, far too hot to sustain an ice. Additionally, absorption measurements in the infrared (see Figure 4.2) must be made against a background radiation source (background star or embedded protostar), as the continuum radiation field in these regions is not sufficiently high at temperatures required to maintain an ice.

Observations in the THz region of the spectrum will resolve both of these issues. Here, $h\nu$ is sufficiently small that temperatures less than $\sim$150 K can provide detectable emission, and background black- and gray-body continuum levels are often sufficient to allow for absorption measurements without the need of a background star or embedded radiation source. The combination of these factors vastly increases the number of target sources available for observation. Preliminary indications are that the spectra of solid-phase molecules in the THz are more distinctive than those in the infrared, and provide information on the structure, temperature, and thermal history of the ice. While some

2 Atoms

H_2 AlF AlCl C_2 CH CH^+ CN CO CO^+ CP SiC HCl KCl NH NO NS NaCl OH PN SO SO^+ SiN SiO SiS CS HF HD FeO O_2 CF^+ SiH PO AlO OH^+ CN^- SH^+ SH HCl^+ TiO ArH^+

3 Atoms

C_3 C_2H C_2O C_2S CH_2 HCN HCO HCO^+ HCS^+ HOC^+ H_2O H_2S HNC HNO MgCN MgNC N_2H^+ N_2O NaCN OCS SO_2 *c*-SiC_2 CO_2 NH_2 H_3^+ SiCN AlNC SiNC HCP CCP AlOH H_2O^+ H_2Cl^+ KCN FeCN HO_2 TiO_2

4 Atoms

c-C_3H *l*-C_3H C_3N C_3O C_3S C_2H_2 NH_3 HCCN $HCNH^+$ HNCO HNCS $HOCO^+$ H_2CO H_2CN H_2CS H_3O^+ *c*-SiC_3 CH_3 C_3N^- PH_3 HCNO HOCN HSCN H_2O_2 C_3H^+ HMgNC

5 Atoms

C_5 C_4H C_4Si *l*-$C3H_2$ *c*-C_3H_2 H_2CCN CH_4 HC_3N HC_2NC HCOOH H_2CNH H_2C_2O H_2NCN HNC_3 SiH_4 H_2COH^+ C_4H^- HC(O)CN HNCNH CH_3O NH_4^+ H_2NCO^+

6 Atoms

C_5H *l*-H_2C_4 C_3H_4 CH_3CN CH_3NC CH_3OH CH_3SH HC_3NH^+ HC_2CHO NH_2CHO C_5N *l*-HC_4H *l*-HC_4N *c*-H_2C_3O H_2CCNH C_5N^- HNCHCN

7 Atoms

C_6H CH_2CHC N CH_3C_2H HC_5N CH_3CHO CH_3NH_2 *c*-C_2H_4O H_2CCHO H C_6H^-

8 Atoms

CH_3C_3N $HC(O)OCH_3$ CH_3COOH C_7H C_6H_2 CH_2OHCHO *l*-HC_6H CH_2CHCHO CH_2CCHCN H_2NCH_2CN CH_3CHNH

9 Atoms

CH_3C_4H CH_3CH_2CN $(CH_3)_2O$ CH_3CH_2OH HC_7N C_8H $CH_3C(O)NH_2$ C_8H^- C_3H_6

10 Atoms

CH_3C_5N $(CH_3)_2CO$ $(CH_2OH)_2$ CH_3CH_2CHO

11 Atoms

HC_9N CH_3C_6H C_2H_5OCHO $CH_3OC(O)CH_3$

12 Atoms

c-C_6H_6 $C_2H_5OCH_3$ *n*-C_3H_7CN

>12 Atoms

$HC_{11}N$ C_{60} C_{70}

Figure 4.1: List of molecules that have been detected in the ISM as of April 2014 from https://www.astro.uni-koeln.de/cdms/molecules.

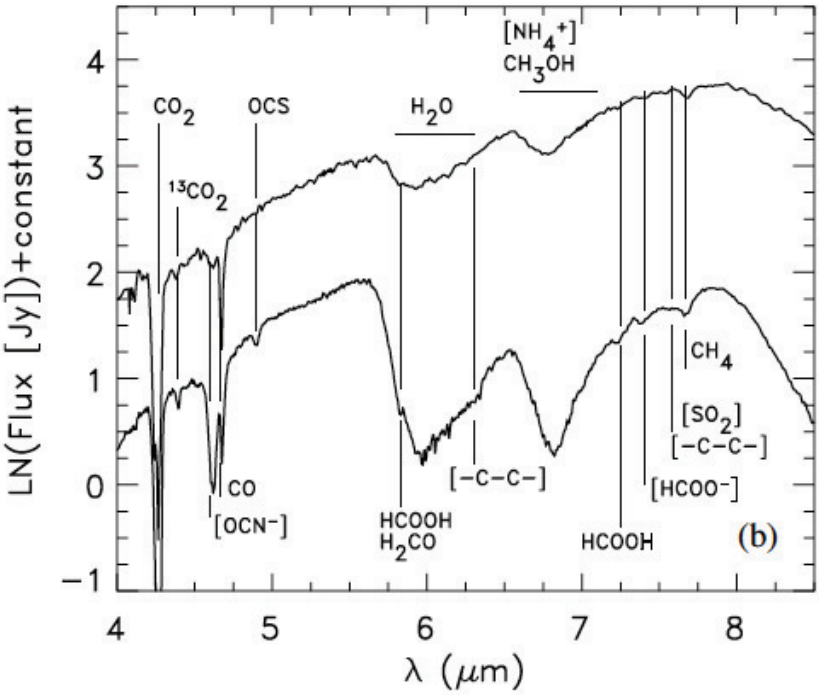

Figure 4.2: Example infrared ice spectra: Fig. 2 from [137] showing absorption from major ice constituents in mid-infrared ISO/SWS observations of NGC 7538 IRS 9 (top) and W33 A (bottom)

limited work has been conducted in this frequency region already (see, e.g. [138; 139; 140; 141; 142]), the vast majority of molecules of interest are unexplored.

To take full advantage of the enormous amount of available THz observations (e.g., *Herschel*, SOFIA, and ALMA), laboratory analogs must be studied systematically. Here, we present the THz and mid-IR spectra of perhaps the simplest series of astrophysically-relevant molecules that share common, and progressively more complex, functional groups, as well as methyl formate and the simpler ice species H_2O, D_2O, CO_2, and CH_3OH.

Chapter 5

Experimental Design

5.1 Spectrometer Overview

The details of the TeraHertz Time-Domain Spectrometer (THz-TDS) have been published previously [136; 135], and recent improvements will be covered in full in the thesis by M. A. Allodi (2015). An overview of the instrument is presented here to provide context for the spectroscopic details presented in Chapter 6.

A diagram of the instrument is provided in Figure 5.1 as a reference to the reader. Briefly, pulsed (∼320 fs full width at zero crossing) THz radiation is generated via plasma filamentation using the output of a pulsed (∼35 fs) 800 nm regenerative amplifier coupled with an optical parametric amplifier producing light at 1745 nm (see §5.2). The THz pulse is focused onto a 1" high-resistivity intrinsic-silicon substrate upon which an ice of interest has been generated via vapor deposition (see §5.3). Finally, the remaining THz signal is focused onto a non-linear gallium phosphide (GaP) crystal and detected via electro-optic (EO) sampling (§5.4).

In addition to the THz spectrometer, a mid-IR Fourier-transform infrared (FTIR) spectrometer (Nicolet 6700) is coupled into the system. The THz and mid-IR radiation are aligned with the cryostat such that they probe the same region of the sample/substrate. The FTIR spectrometer provides spectra with 1 cm^{-1} resolution over a range of 400 cm^{-1} to 4000 cm^{-1}, and is used for diagnostic purposes and monitoring of the ices during deposition and spectral acquisition. Spectra of the ices discussed in §6 obtained with the FTIR are provided in Appendix C.

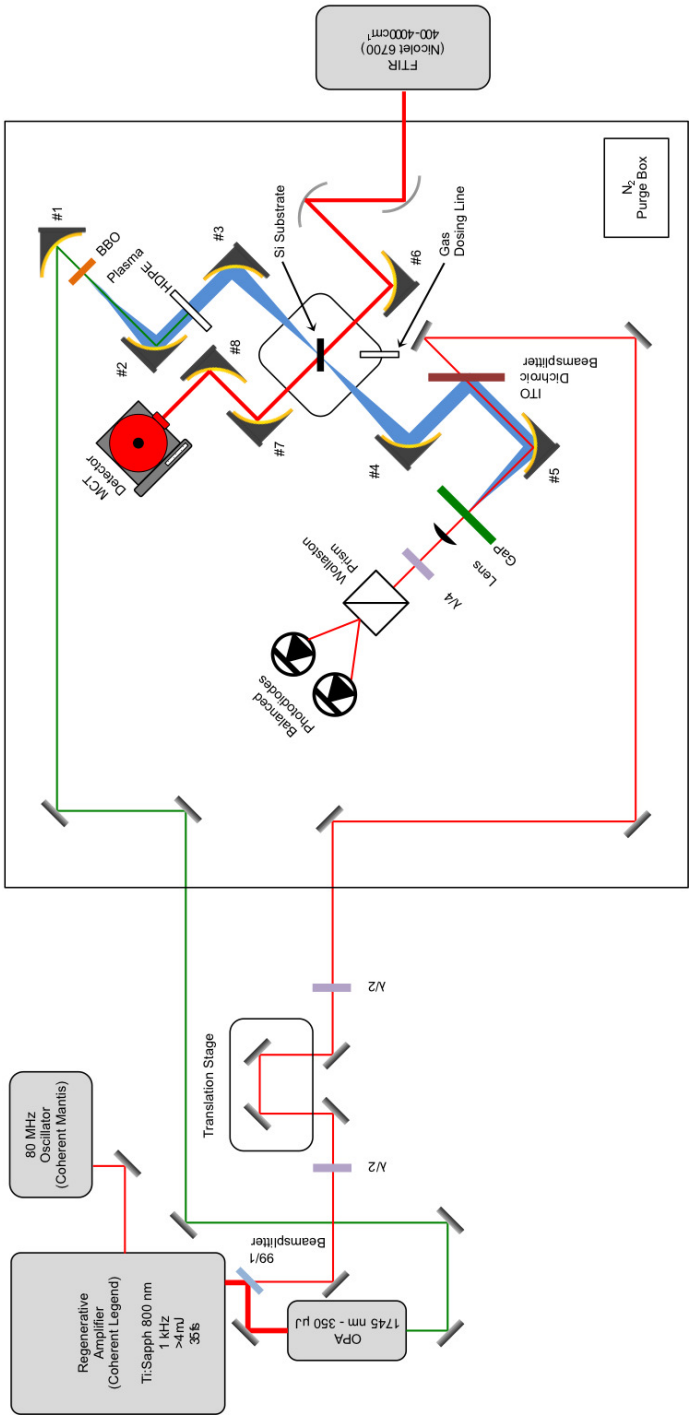

Figure 5.1: Schematic of the TD-THz system.

5.2 THz Generation

Pulsed THz radiation is generated through plasma filamentation in air (or the dry N_2-purge gas). First, 85% of the the 35 fs, 4 mJ/pulse output of a Titanium:sapphire Regenerative Amplifier (Coherent Inc. *Legend Elite*) at 800 nm is passed through an optical parametric amplifier (OPA) (Lighy Conversion Inc. *TOPAS-C*). The idler output of the OPA at 1745 nm then interacts with a beta-barium borate (BBO) crystal (Eksma Optics) which frequency doubles a small portion of the light. Both colors of light are then focused with either an off-axis parabolic mirror (OAPM) or, in later configurations of the system, an achromatic lens. At the focus, the 1745 nm light sparks a plasma filament in the air (or the dry N_2-purge gas), while the doubled light induces THz generation. An optical chopper placed before the BBO crystal modulates the signal at 500 Hz for lock-in amplification.

This plasma generates THz pulses in a similar manner to the two-color plasma created with an 800 nm pulse and its second harmonic [143; 144; 145; 146]; however, the THz generation mechanism in plasma is more efficient at longer wavelengths [147]. In the first generation of this spectrometer, pulses with roughly 3.5 mJ of energy at 800 nm created a plasma to generate THz pulses. Now, pulses with roughly 350 μJ of energy at 1745 nm generate a plasma that produces THz pulses with a power comparable to the previous plasma at 800 nm. The wavelength of 1745 nm was chosen because it provided the largest peak THz electric fields for the current optical alignment of the spectrometer.

5.3 Cryostat Design, Sample Preparation, and Deposition

5.3.1 Cryostat Design

The ice sample is prepared on a substrate housed in a high vacuum enclosure (R. C. Janis) connected to the cold finger of a closed-cycle, helium-cooled cryostat (CTI Cryogenics) that is capable of cooling the substrate to $\sim$8 K (see Figure 5.3). The substrate itself is a 1" diameter, high-resistivity, intrinsic silicon wafer. A thermocouple connected to the cryostat allows real-time monitoring of the temperature, which is precisely controllable in the range of $\sim$8 K to 300 K using a heating element in the cryostat. The chamber is evacuated through a 1.5" diameter, flexible stainless steel bellows connected to a turbomolecular pump (Turbo V 250 Varian Inc.). Room-temperature base pressures below 10^{-8} Torr are routinely observed.

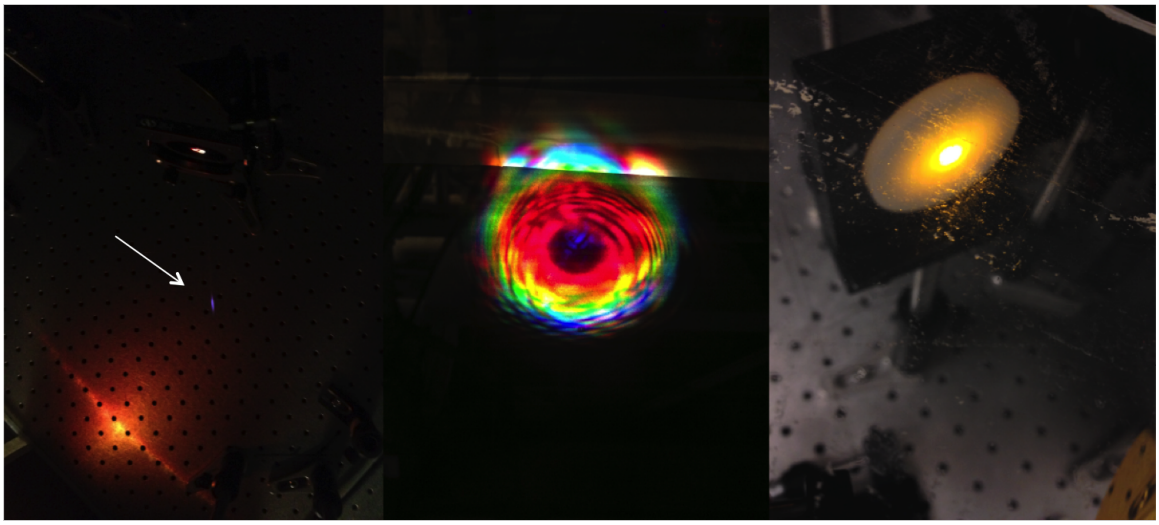

Figure 5.2: Photographs showing the plasma filament, indicated with a white arrow (left panel), visible light scattering from the beam block using 800 nm generation (center panel), and visible light scattering from the beam block using 1745 nm generation (right panel).

For the bulk of the work presented here, the THz radiation entered the chamber through a pair of 2" diameter, high-resistivity, intrinsic silicon windows. The index of refraction of silicon in the THz is large (n >3), and only ~40% transmission is seen through each piece of silicon (~10% total transmission through two windows and the substrate). In the latest iteration of the cryostat design, the two windows were replaced with 2" diameter TOPAS polymer windows (TOPAS Advanced Polymers) that have >90% transmission in the THz region. While these windows favorably enhanced the THz signal in the system, they are less robust than the silicon windows, are prone to cracking under vacuum conditions, and are difficult to machine from raw stock. A TOPAS substrate was tested for use; however, TOPAS was found to be nearly completely opaque in the mid-IR, making the incorporated diagnostic FTIR unusable, and thus, the original silicon substrate is still in use. Under ideal conditions, a single-crystal CVD diamond substrate, with matching windows, would provide optimum THZ transmission and also be transparent in the mid-IR, but is cost-prohibitive.

A 1/8" diameter stainless steel pipe connects the cryostat to the sample preparation dosing line through an all-metal leak valve (Lesker). The pipe is oriented normal to the surface of the substrate, about 1" away, and is capped with a metal mesh with a 38 μm hole size (McMaster-Carr 85385T117). This configuration ensures a uniform, homogenous ice deposition strongly favoring the side of the substrate facing the dosing line.

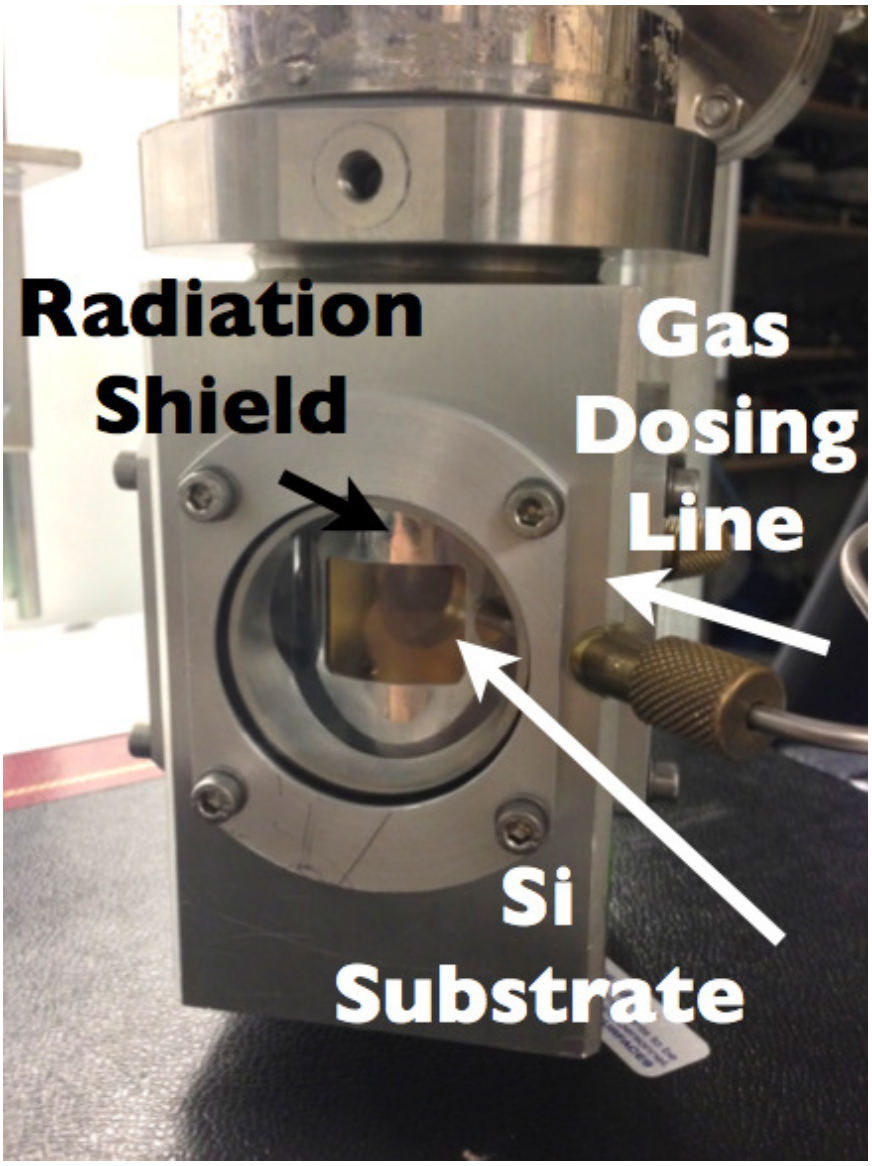

Figure 5.3: Photograph of the high vacuum cryostat showing the cold finger and silicon substrate, radiation shield, gas dosing line, and TOPAS windows.

5.3.2 Sample Preparation and Deposition

Samples are prepared in a dosing line system prior to deposition (Figure 5.4). For liquid samples, a small volume of sample (< 10 mL) is placed into a glass sample finger and evacuated with a rough pump for initial degassing, followed by one or more freeze-pump-thaw cycles with liquid nitrogen. The pump is then closed off, and the line fills with sample gas that evolves from the liquid. This initial gas is then used to flush the line, which is once again pumped with the rough pump, followed by the turbomolecular pump, removing as many contaminants as possible from the line. The line is then once again filled with sample to a desired pressure, after which the sample is introduced to the chamber through the leak valve, typically at a rate of ∼10 mTorr per second. For gaseous samples, the glass sample finger is removed and gasses are introduced through the valve from a cylinder or lecture bottle. In general, the ices grown for this work were ∼10 μm thick.

The sample mixtures discussed here were prepared by first filling the dosing line, including the large glass mixture bulb, with gas from the first sample species. The mixture bulb is then closed off from the rest of the line, and the first gas is evacuated from the line. The second species is then allowed to fill the line to a pressure appropriate for the desired mixing ratio, and the mixture bulb is opened, allowing the gasses to mix. The mixture is then introduced to the cryostat through the leak valve.

A simpler method is to first fill the large glass bulb with the first species to a desired pressure. The bulb is then closed off, and the first species is frozen out into the solid phase by the application of a liquid-nitrogen bath. The bulb is then opened to the line once more, and quickly filled with the second species in the desired mixing ratio. After closing the bulb off, the first species is allowed to boil and mix with the second. These are then deposited together through the leak valve.

5.4 THz Detection

The THz radiation is detected through free-space electro-optic (EO) sampling [148; 149]. The remaining 15% of the original 800 nm pulse is routed through a mechanical delay line (Newport ISL 150 with ESP300 controller) and a half-wave plate (Newport 10RP02-46), which allows for precise control of the linear polarization of this probe pulse. The probe beam is then made co-linear with the THz signal beam by passing the 800 nm probe through a thin indium-tin oxide (ITO) plate that is transparent at 800 nm and reflective at THz frequencies. The two beams are then focused using an OAPM onto a thin piece of optically-contacted gallium phosphide (GaP) crystal (Del Mar

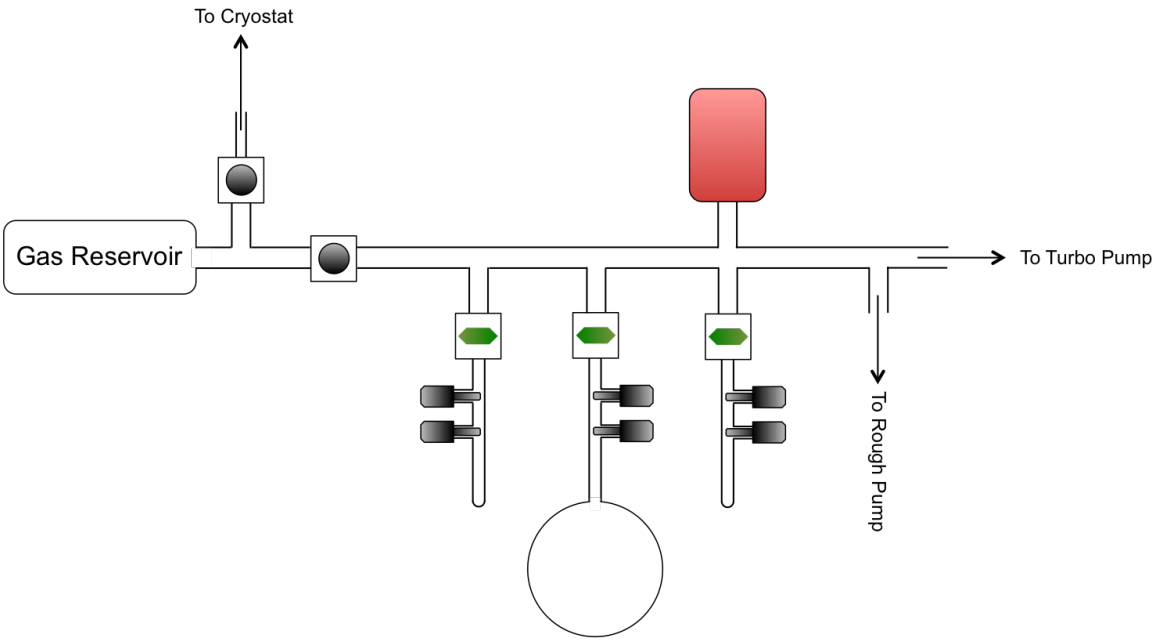

Figure 5.4: Schematic drawing of the sample preparation dosing line. The line can be evacuated either via a rough pump or through the turbomolecular pump, and pressures are monitored via a mass-independent, active capacitance transmitter pressure gauge (MKS Baratron, Red) between 0.01 Torr and 1100 Torr. Samples are prepared in glass fingers and mixed in the large glass bulb. A separate gas mixture reservoir is also available to contain samples for long periods prior to deposition, or to allow the facile deposition of two mixtures in rapid succession.

Photonics, Inc.). This crystal is different from the one used by [136], because it has a thin EO active layer optically contacted to a thicker inactive layer. A GaP (110) layer 200 μm thick, and capable of EO sampling, is optically contacted to a GaP (100) layer 4 mm thick that is EO inactive. This provides the advantage of pushing etalon features, or recurrences of the pulse in the time domain, outside of the window being scanned. As a result, the signal-to-noise of the data as a whole improves because the etalon features are not efficiently removed by the background subtraction in parts of the spectrum where the signal-to-noise is low.

When focused onto the crystal together, the electric field of the THz pulse (10s of ps in length after passing through the cryostat and sample) acts as a DC-bias on the crystal, as seen by the 35 fs 800 nm pulse. The THz light generates a transient birefringence in the GaP via the Pockels effect, which rotates the polarization of the 800 nm pulses. The magnitude of this change is linearly proportion to the intensity of the THz electric field applied at the time of interaction, in the small THz field limit. By varying the length of the probe line via the mechanical delay line, the timing of arrival of the 800 nm pulse with respect to the THz pulse can be controlled. In this way, the probe pulse can be made to fully sample the THz pulse out to a delay of >100 ps.

After passing through the GaP crystal, the 800 nm probe beam is focused, and propagates through a quarter-wave plate (Newport 10RP04-46) to create a circularly-polarized beam, which is then split into orthogonal polarizations by a Wollaston Prism (Thorlabs WP20). The signal is then measured as a difference signal on a pair of balanced, bare photodiodes. When no THz light is present, no difference signal is observed. Under the applied electric field of a THz pulse, a difference in the two polarizations is observed by the photodiodes, corresponding to the intensity of the THz electric field at the time of interaction of the pulses. This signal is then sent to a lock-in amplifier (Stanford Research Systems SR830) that records the spectrum as a function of delay.

A representative time-domain trace acquired with the spectrometer is shown in Figure 5.5. For the majority of the results shown in §6, only ∼12 ps of the pulse were collected and used, as the original beam block caused an etalon feature that arose shortly thereafter and made the data past that point unusable. The resolution of the spectra collected is approximately equal to the inverse of the length of scan in the time domain. For these experiments, this yields a ∼90 GHz resolution in the frequency domain. Recently, a thicker beam block was obtained that pushed the etalon out beyond the range of the scan, and as a result, ∼35 ps of the pulse were collected for the crystalline H_2O, D_2O, CO_2, and methyl formate shown in §6. The duration of the scan is now limited by the substrate etalon at ∼37 ps. This has resulted in a resolution of ∼30 GHz in the frequency domain.

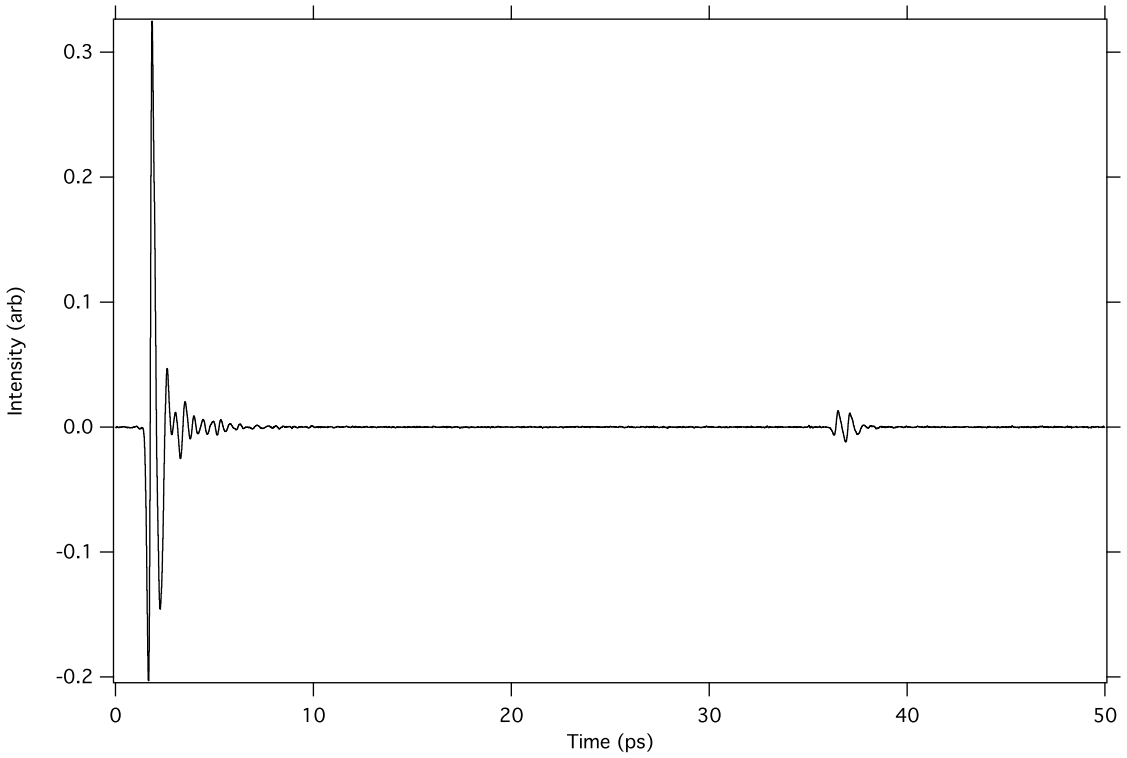

Figure 5.5: Representative time-domain pulse acquired with the THz-TDS. The feature at ∼37 ps is an etalon arising from the silicon substrate.

Frequency-domain spectra are obtained from the time-domain pulse by taking a fast Fourier transform (FFT) of the data and dividing by a reference scan of the bare silicon substrate. Apodization is a necessary element of the data analysis to prevent spectral leakage. All the data in this paper are processed using an asymmetric Hann window peaked at the maximum of the THz signal. The Hann window [150] provides a good balance between sidelobe suppression and lineshape concerns. After apodization, zeros were added to the apodized data to both interpolate between points in the frequency domain and ensure that the length of the data set equals a power of two. Zero padding in the time domain before taking an FFT is mathematically identical to interpolation in the frequency domain [151]. In addition to interpolation, zero padding to create a data set of length 2^N, where N is a positive integer, maximizes the speed of the FFT calculation.

THz generation via plasma filamentation produces extremely broadband THz pulses. At the point of generation, the 1745 nm pulses are at most of the order a few hundred fs in length, and thus result in THz pulses containing bandwidth out to at least 20 THz. In our system, the effective useable bandwidth is limited not by this production, but by the EO detection in GaP. A power spectrum plot of the detectable bandwidth of the system is shown in Figure 5.6, along with the frequency coverage of several key astronomical observatories operating in this frequency region, for reference.

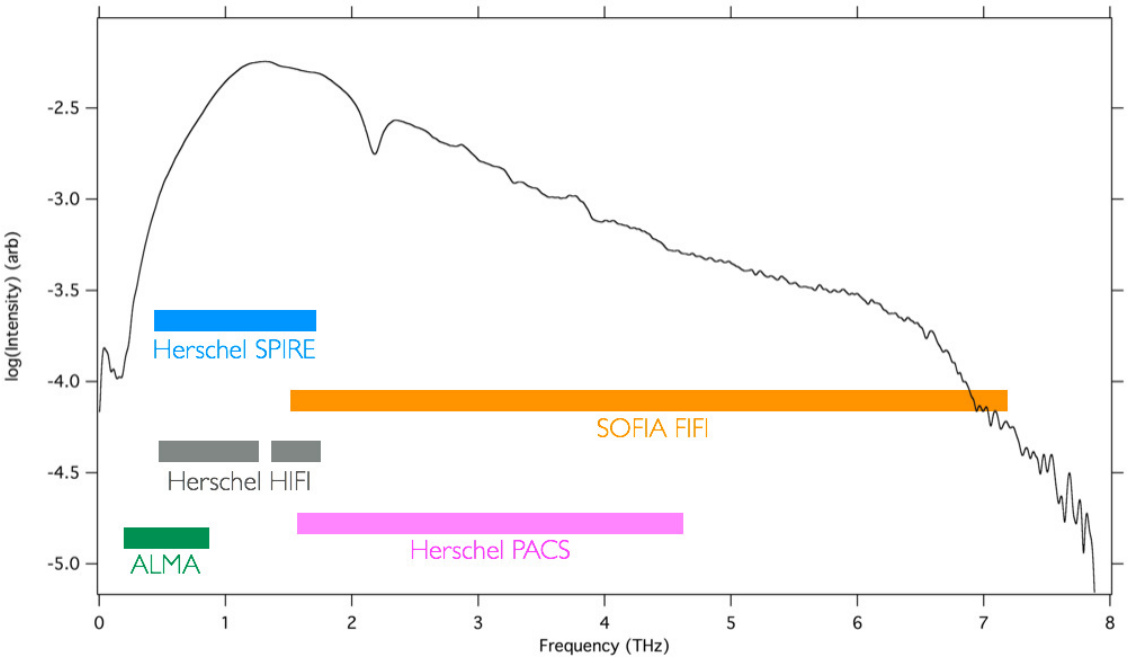

Figure 5.6: Cartoon depicting the approximate bandwidth ranges covered by receivers on the Herschel Space Telescope, Atacama Large Millimeter Array, and Stratospheric Observatory for Infrared Astronomy. They are overlaid on a THz power spectrum from the THz-TDS instrument generated from the FFT of the first 35 ps of the pulse shown in Figure 5.5. The vertical positions of the telescope coverage are arbitrary.

Chapter 6

Results

A comparison of the ices studied presented here is shown in Figure 6.1. Spectra of each individual species is presented and discussed in detail in the following sections.

6.1 Water (H_2O)

Crystalline water was formed through the deposition of 5 Torr of gaseous water over a period of 5 minutes at 150 K. Amorphous water was formed through the deposition of 4 Torr of gaseous water over a period of 7 minutes at 10 K.

Crystalline water (Figure 6.3) shows a single sharp band at 6.9 THz (H-bond stretching between hydrogen-bonded bilayers), 5.7 THz (out-of-phase vibration within a bilayer), 4.9 THz (proton disordered motion), 4.3 THz, and 1.9 THz (O-O-O bending motion) [152; 153]. The features at 4.9 THz and 6.9 THz display a narrowing and blue shift with decreasing temperature. Amorphous water (Figure 6.4) ice displays strong, broad absorption bands at 4.6 THz and 6.2 THz. Crystalline water is the most well-studied in the literature in this frequency region (see, e.g. [154; 140]). A qualitative comparison of the spectrum of crystalline water ice obtained in our instrument to that of [154] is shown in Figure 6.2.

Amorphous water that has been annealed to 175 K for a period of 10 minutes presents a set of features that appear to be a blending of both amorphous and purely crystalline water ice (Figure 6.5). The peak at 6.9 THz appears to shift somewhat, and to grow in on top of the amorphous features.

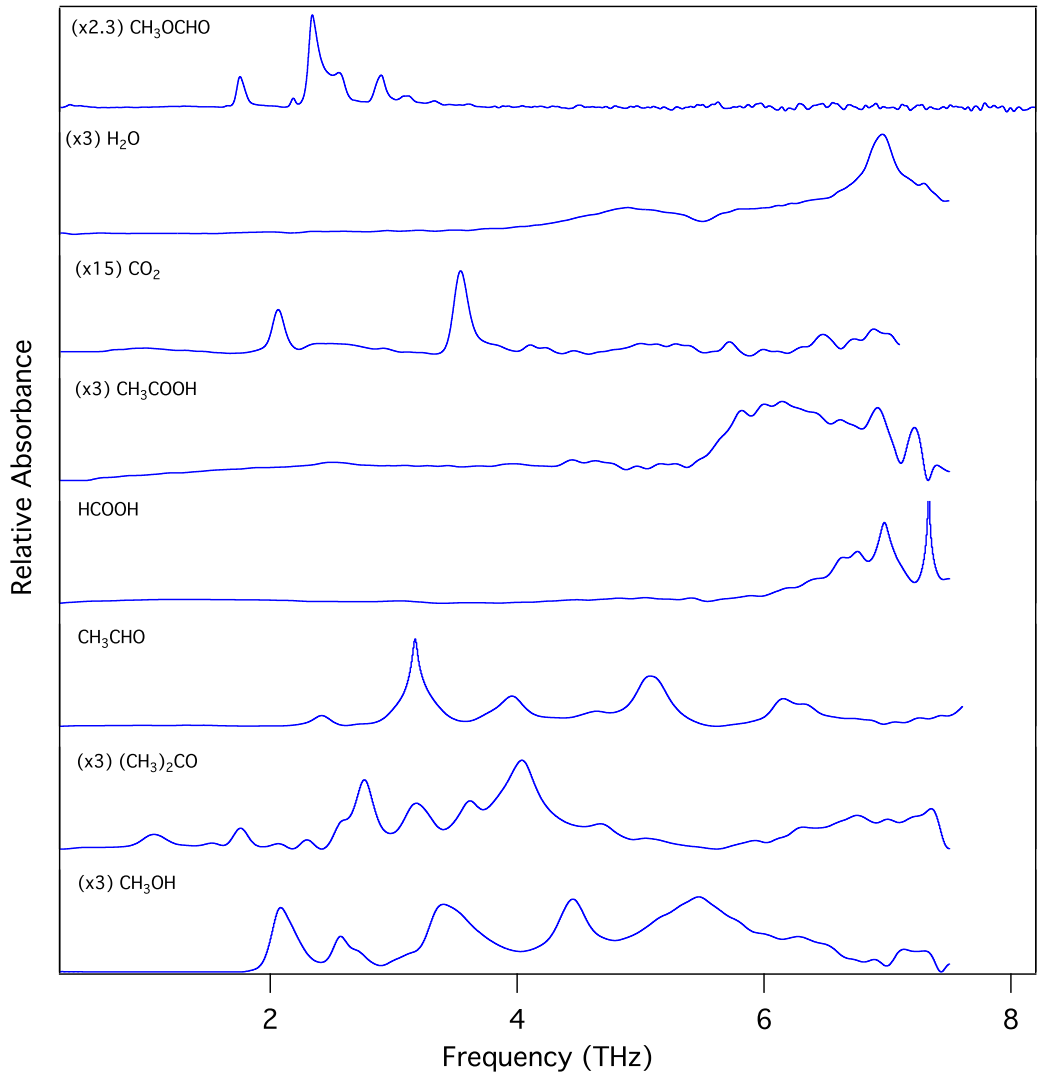

Figure 6.1: Comparison of THz spectra of crystalline ices studied in the laboratory, all at 10 K. Traces are vertically offset for clarity, and scaled to show detail.

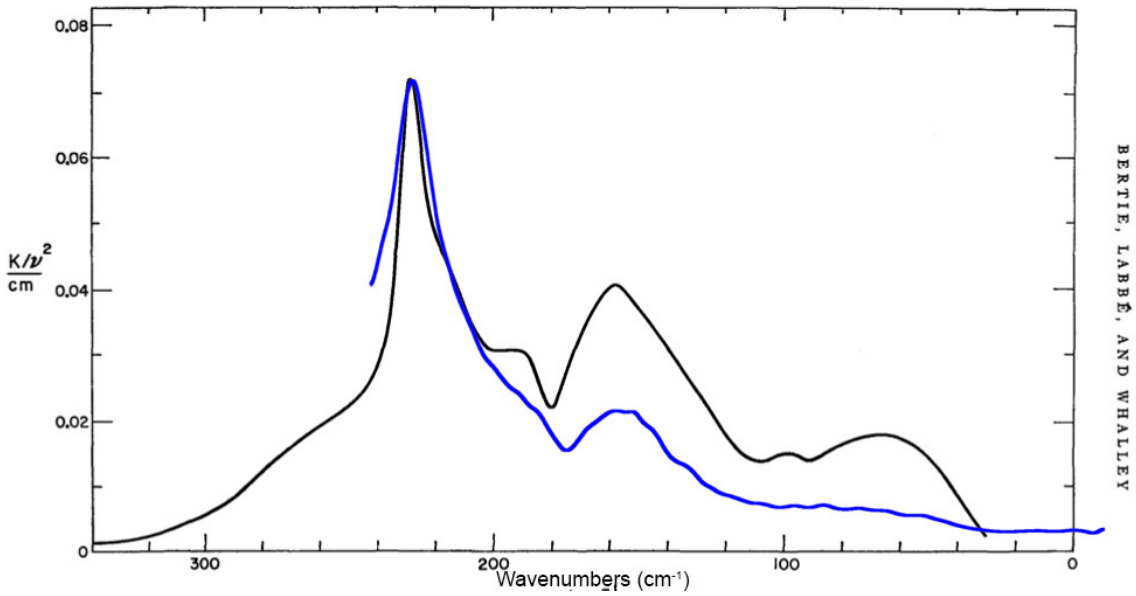

Figure 6.2: Qualitative comparison of the spectrum of crystalline water at 10 K (blue) obtained with the Blake Group THz-TDS system to that of [154]. Adapted from Figure 11 of [154]. Traces are on equivalent frequency scale; the intensity of the blue trace has been normalized to that of the peak of the literature trace.

6.2 Deuterated Water (D_2O)

Crystalline D_2O was formed through the deposition of 5.5 Torr of gaseous D_2O over a period of 9 minutes at 150 K. At 150 K, crystalline D_2O displays a sharp peak at 6.7 THz, a broader peak at 4.7 THz, and a broad shoulder centered at ∼5.7 THz. All distinct peaks show a narrowing and blue shift with decreasing temperature. Compared to H_2O, the features at 6.7 THz and 4.7 THz are noticeably red-shifted, while the broad shoulder at 5.9 THz is relatively unchanged. The red shift in the modes at 6.7 THz and 4.7 THz agrees well with the model of heavier molecules shifting vibrations to lower frequencies.

6.3 Methanol (CH_3OH)

Crystalline methanol was formed through the deposition of 8 Torr of gaseous methanol over a period of 10 minutes at 140 K. Amorphous methanol was formed through the deposition of 8 Torr of gaseous methanol over a period of 18.5 minutes at 10 K.

Crystalline methanol (Figure 6.7) presents narrow, strong peaks at 5.4 THz, 4.4 THz, 3.4 THz, 2.6 THz, and 2.1 THz. The peaks above 3 THz have been previously observed and documented in the literature [140] and agree with our data. The peaks at 2.6 THz and 2.1 THz have not been

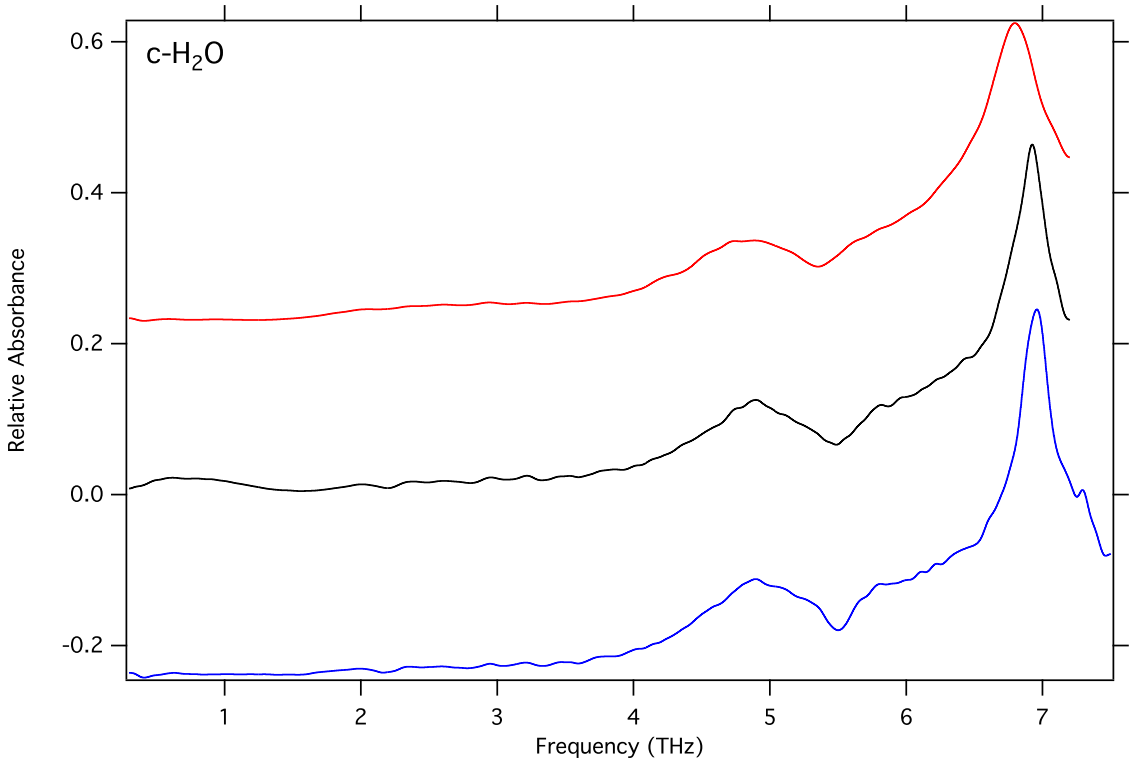

Figure 6.3: Spectra of crystalline water, deposited at 150 K, at 150 K (red), 75 K (black), and 10 K (blue). Traces have been vertically offset for clarity.

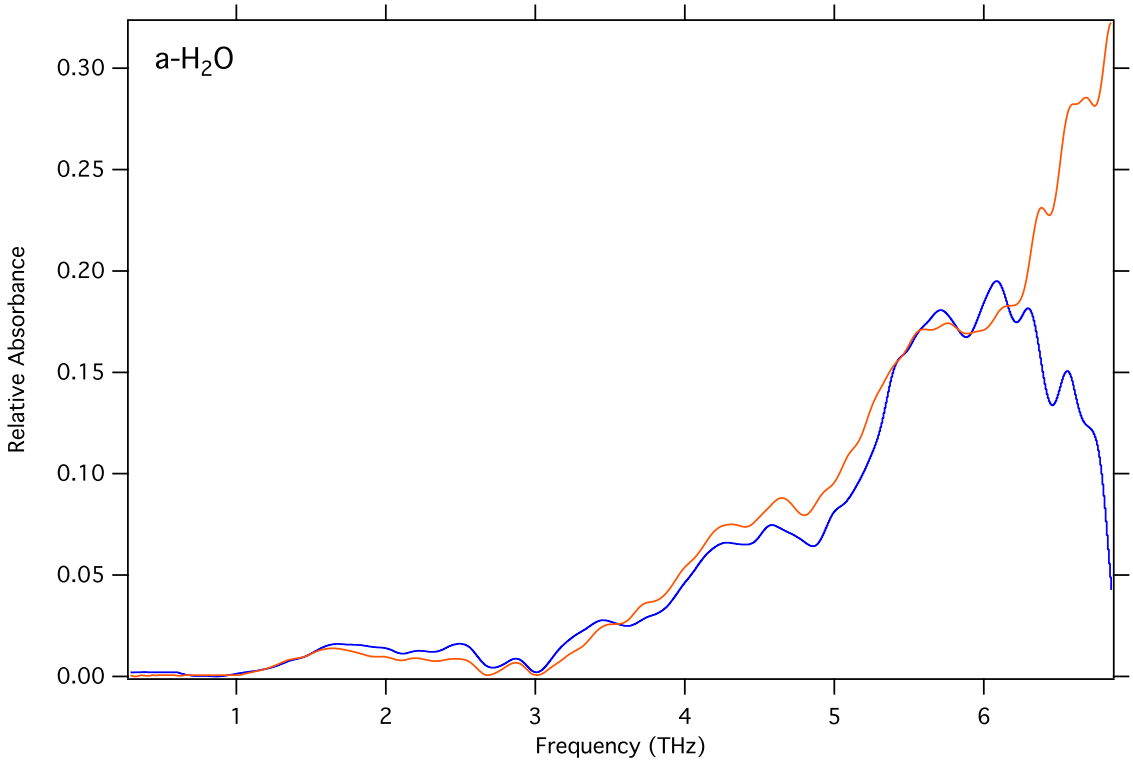

Figure 6.4: Spectra of amorphous water, deposited at 10 K, at 125 K (orange) and 10 K (blue).

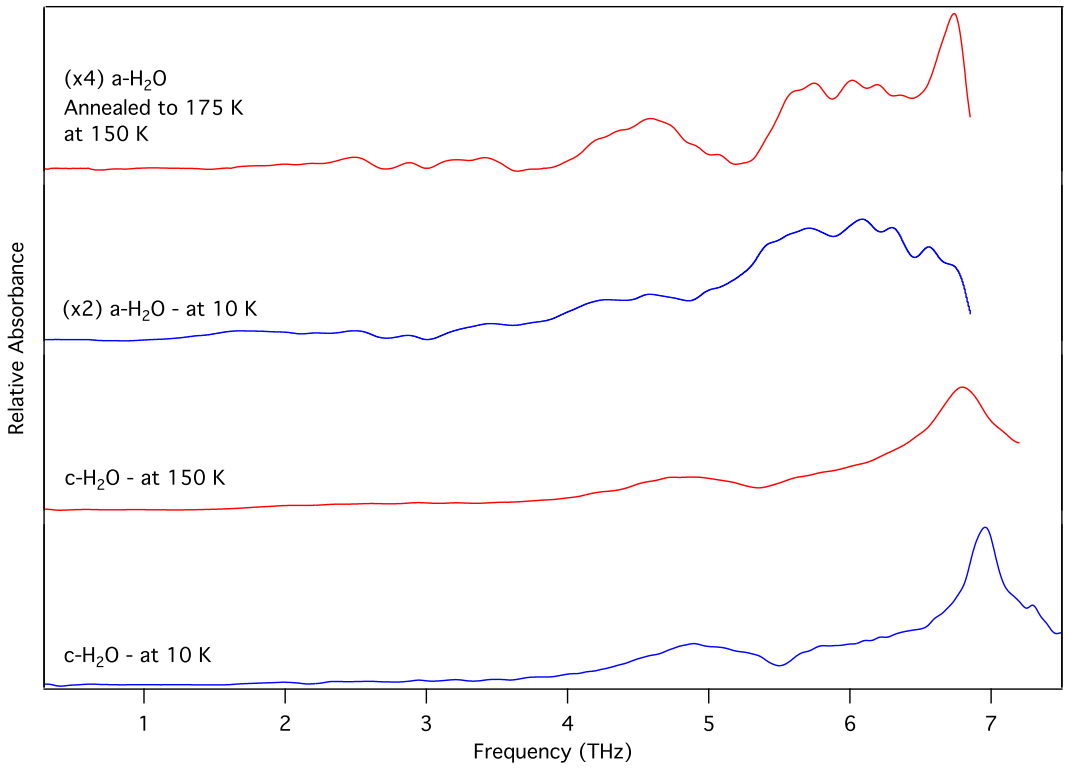

Figure 6.5: Comparison of crystalline water, deposited at 150 K, at 150 K (red) and 10 K (blue) to amorphous water deposited at 10 K at 10 K (blue) and at 150 K after being annealed to 175 K for 10 minutes (red). Traces have been scaled as indicated to show detail, and offset vertically for clarity. The annealed ice clearly displays profiles distinct from both amorphous water and water that was deposited crystalline, indicating that these THz features are sensitive to the thermal history of the ice.

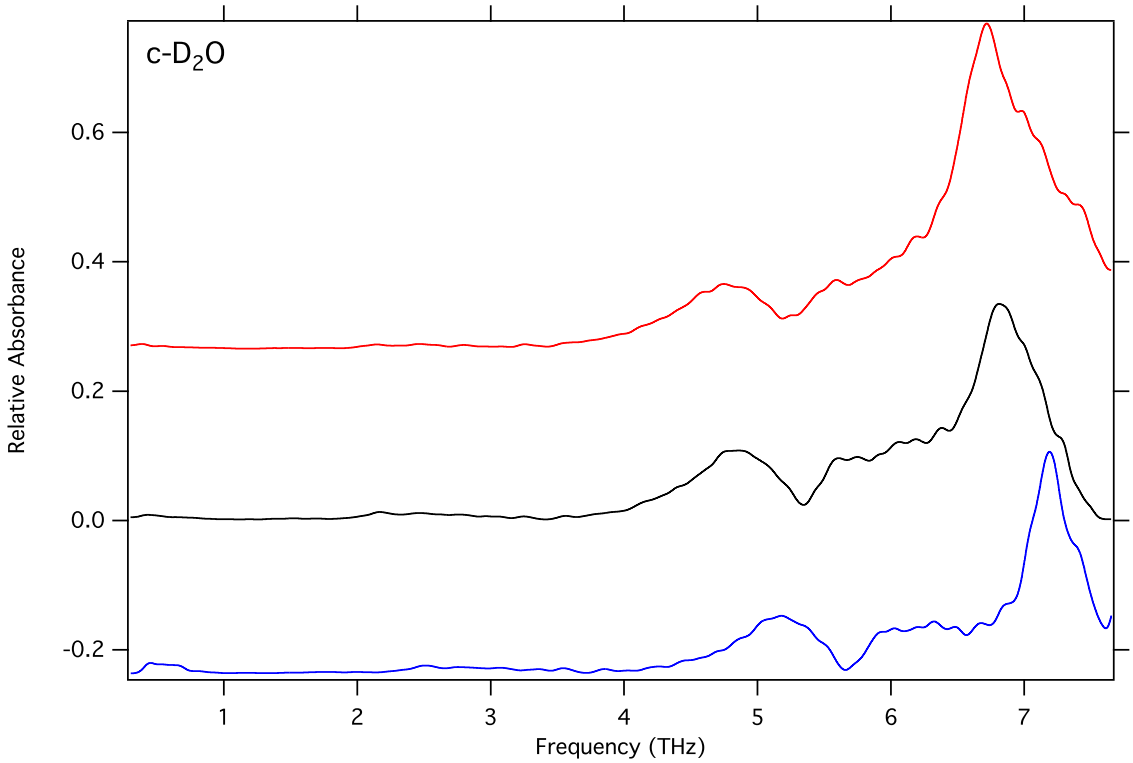

Figure 6.6: Spectra of crystalline D_2O, deposited at 150 K, at 150 K (red), 75 K (black), and 10 K (blue). Traces have been vertically offset for clarity.

previously reported. All distinct peaks show a narrowing and blue shift with decreasing temperature. Amorphous methanol (Figure 6.8) shows a broad feature at 4.4 THz and potentially a second feature at 6.8 THz, though this is reaching the limit of our noise floor in these data. These features have been previously observed, as well [140].

Amorphous methanol that has been annealed to 140 K for a period of 10 minutes shows a set of features that is clearly distinct from those displayed by amorphous and purely crystalline methanol (Figure 6.9). In particular, the sharp mode at 5.4 THz is significantly broadened and weaker.

6.4 Water-Methanol Mixtures

Three mixtures of water and methanol were prepared in ratios of 2:1, 1:1, and 1:2 water:methanol and deposited crystalline at 140 K over a period of 20 minutes, 17.5 minutes, and 15 minutes, respectively, before being cooled to 10 K (Figure 6.10). In the case of the 2:1 water:methanol mixture, the spectra are dominated by crystalline water features, displaying few disruptions from the presence of the methanol. The 1:1 mixture displays a spectrum that strongly resembles that of amorphous water ice, while the 2:1 mixture displays a spectrum that shows significant disruptions to the amorphous water profile.

6.5 Methyl Formate (CH_3OCHO)

Crystalline methyl formate was formed through the deposition of 6 Torr of gaseous methyl formate over a period of 4.5 minutes at 135 K. Crystalline methyl formate presents narrow features at 1.75 THz, 2.2 THz, 2.3 THz, 2.5 THz, 2.9 THz, and 3.3 THz. A broader peak at 3.1 THz shows indications that it may be a blend of two narrower features. Several smaller features are possibly visible up to 4 THz, and a pair of weak features may be present at 370 GHz and 470 GHz. All distinct peaks show a narrowing and blue shift with decreasing temperature.

6.6 Carbon Dioxide (CO_2)

Crystalline carbon dioxide was formed through the deposition of 6 Torr of gaseous carbon dioxide over a period of 2 minutes at 75 K. The spectrum of crystalline carbon dioxide (Figure 6.12) shows only two weak, but distinct and narrow transitions at 2.1 THz and 3.5 THz. Both of these features display a narrowing and blue shift with decreasing temperature (see inset of Figure 6.12 for detail).

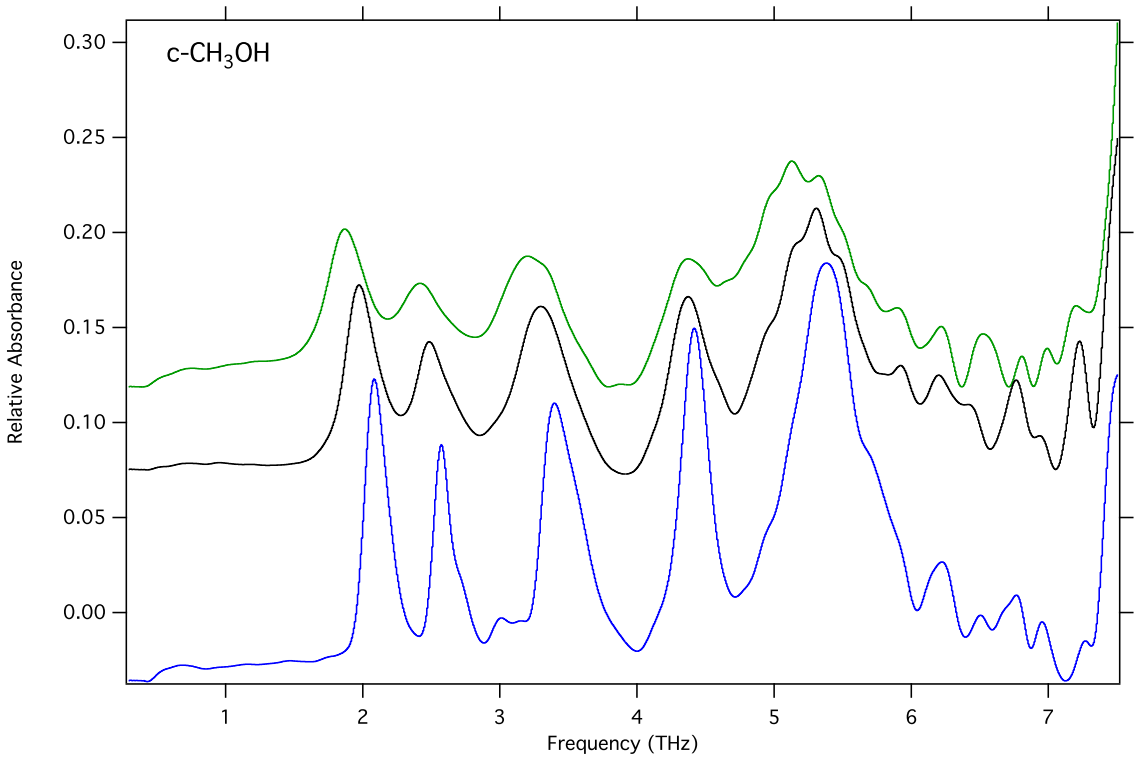

Figure 6.7: Spectra of crystalline methanol, deposited at 140 K, at 100 K (green), 75 K (black), and 10 K (blue). Traces have been vertically offset for clarity.

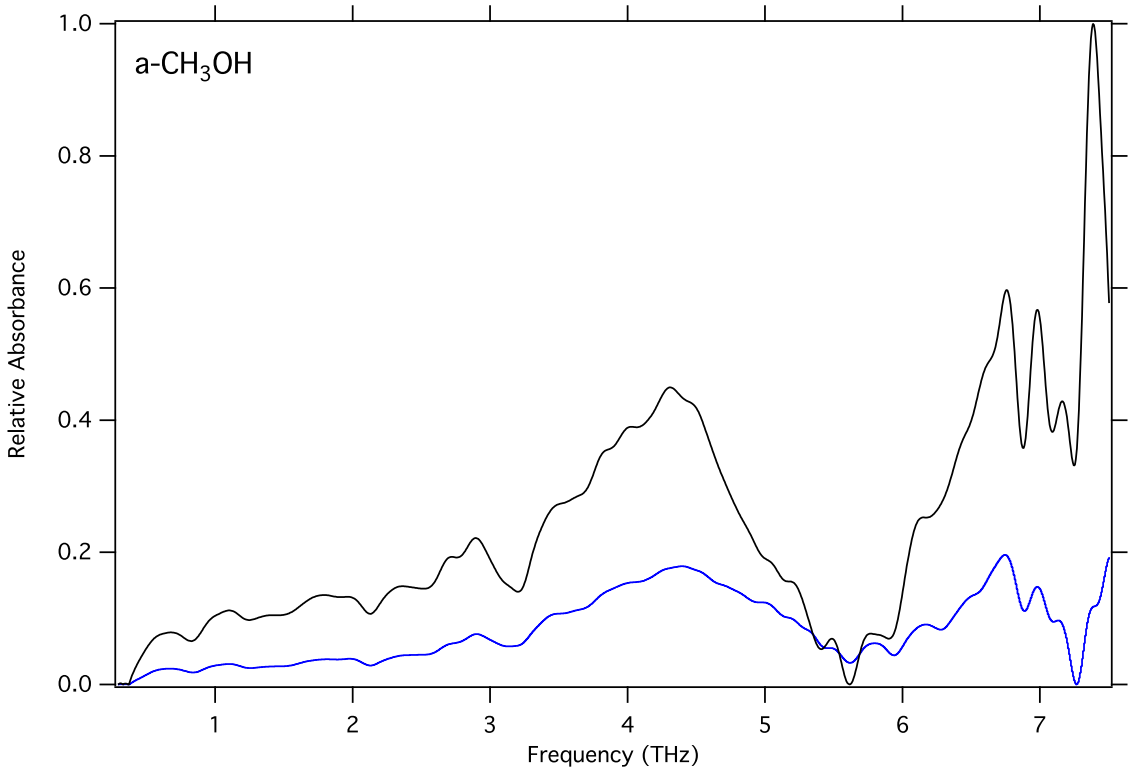

Figure 6.8: Spectra of amorphous methanol, deposited at 10 K, at 75 K (black) and 10 K (blue).

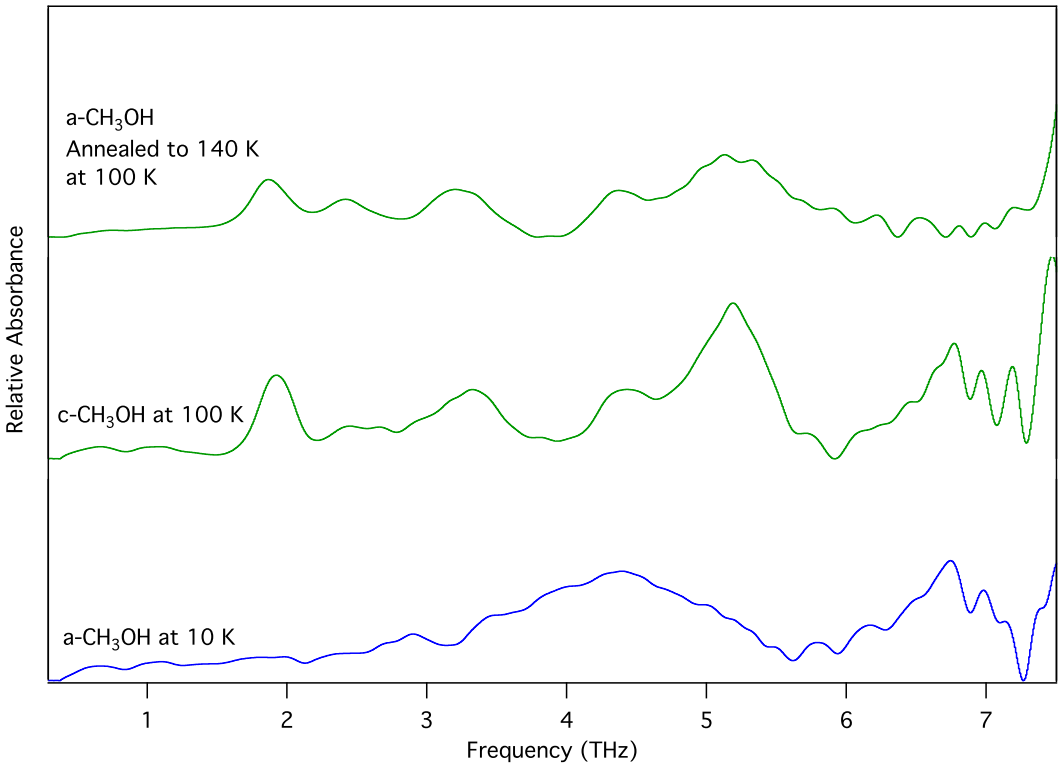

Figure 6.9: Comparison of crystalline methanol, deposited at 140 K, at 100 K (green) to amorphous methanol deposited at 10 K at 10 K (blue) and at 100 K after being annealed to 140 K for 10 minutes (red). Traces have been offset vertically for clarity. The annealed ice clearly displays profiles distinct from both amorphous methanol and methanol that was deposited crystalline, indicating that these THz features are sensitive to the thermal history of the ice.

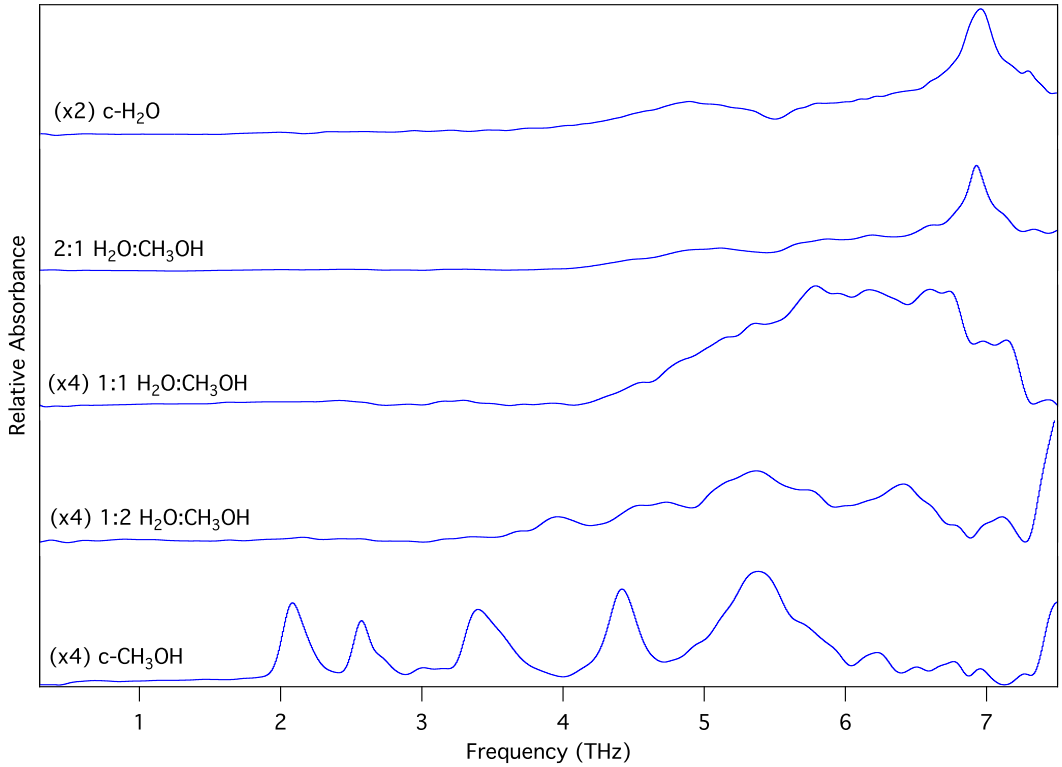

Figure 6.10: Spectra of purely crystalline water, purely crystalline methanol, and mixtures of water:methanol in ratios of 2:1, 1:1, and 1:2, all deposited crystalline and cooled to 10 K. Traces are scaled to show detail, and vertically offset for clarity.

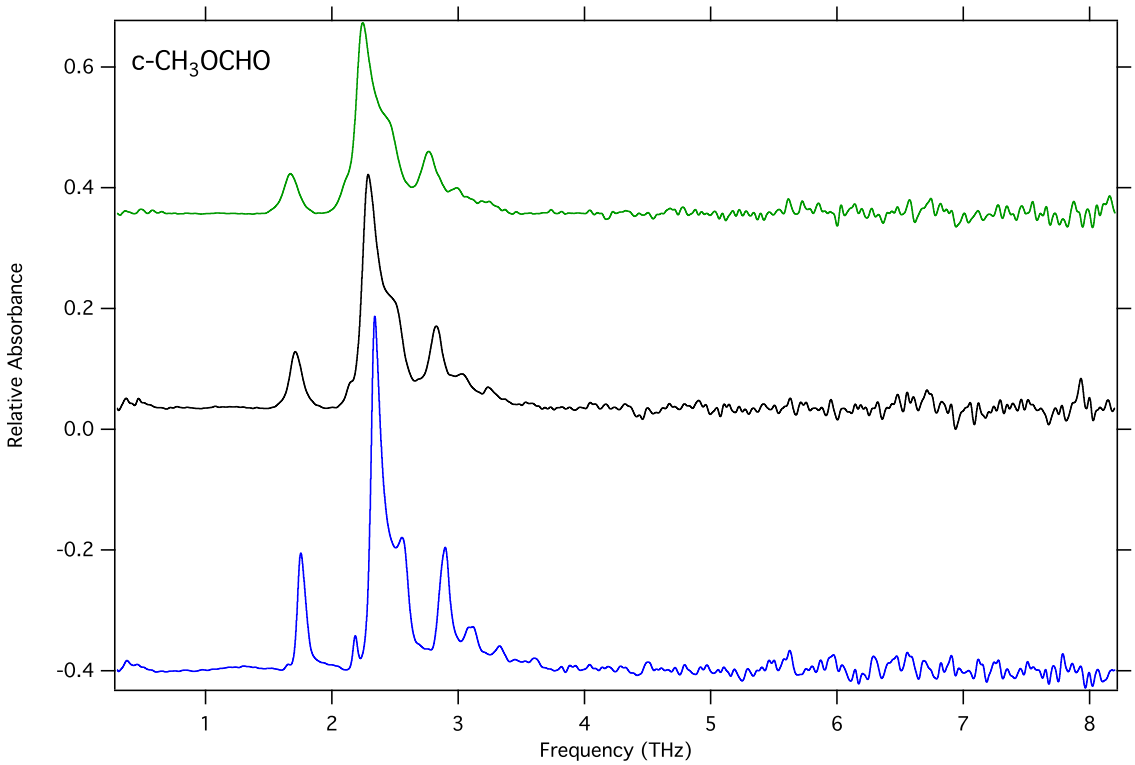

Figure 6.11: Spectra of crystalline methyl formate, deposited at 135 K, at 100 K (green), 75 K (black), and 10 K (blue). Traces have been vertically offset for clarity.

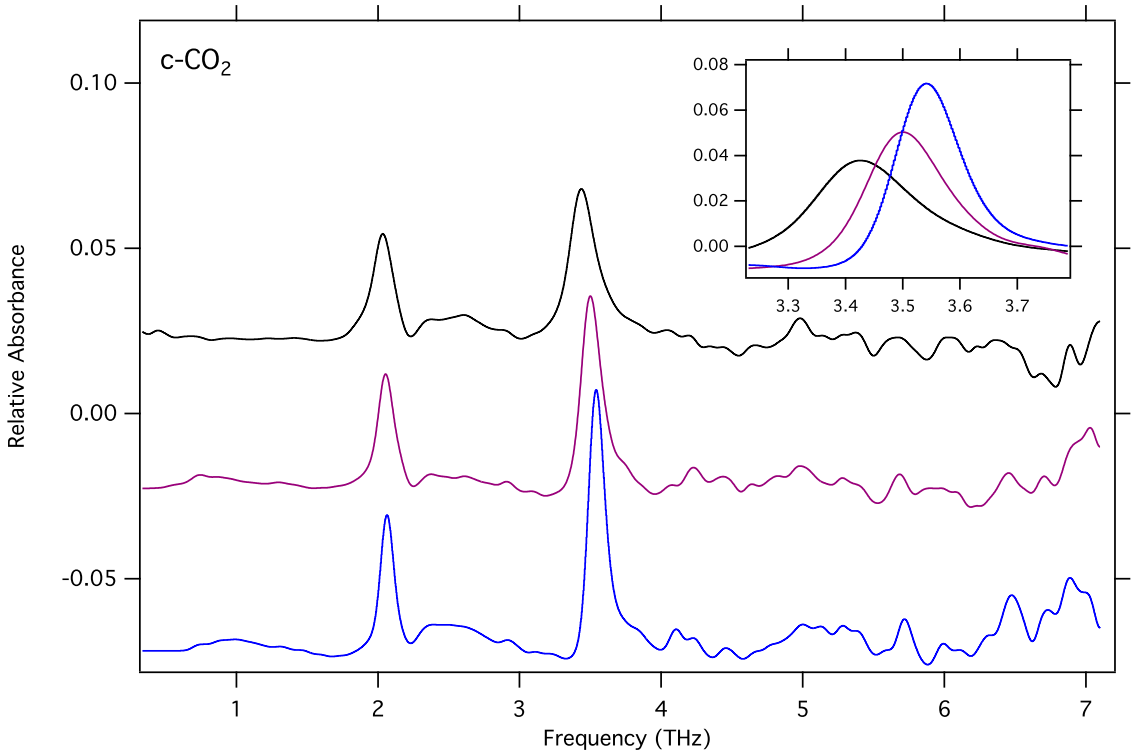

Figure 6.12: Spectra of crystalline carbon dioxide, deposited at 75 K, at 75 K (black), 50 K (violet), and 10 K (blue). Traces have been vertically offset for clarity. Inset shows detail on the narrowing and blue-shift of the 3.5 THz transition of CO_2 with decreasing temperature.

The feature at 3.5 THz has been previously observed in the literature [140], while both features have been predicted by theory [155] at high pressures. A predicted spectrum of crystalline carbon dioxide at ambient pressure was generated using Crystal 09, and is shown as red sticks in Figure 6.13 for comparison.

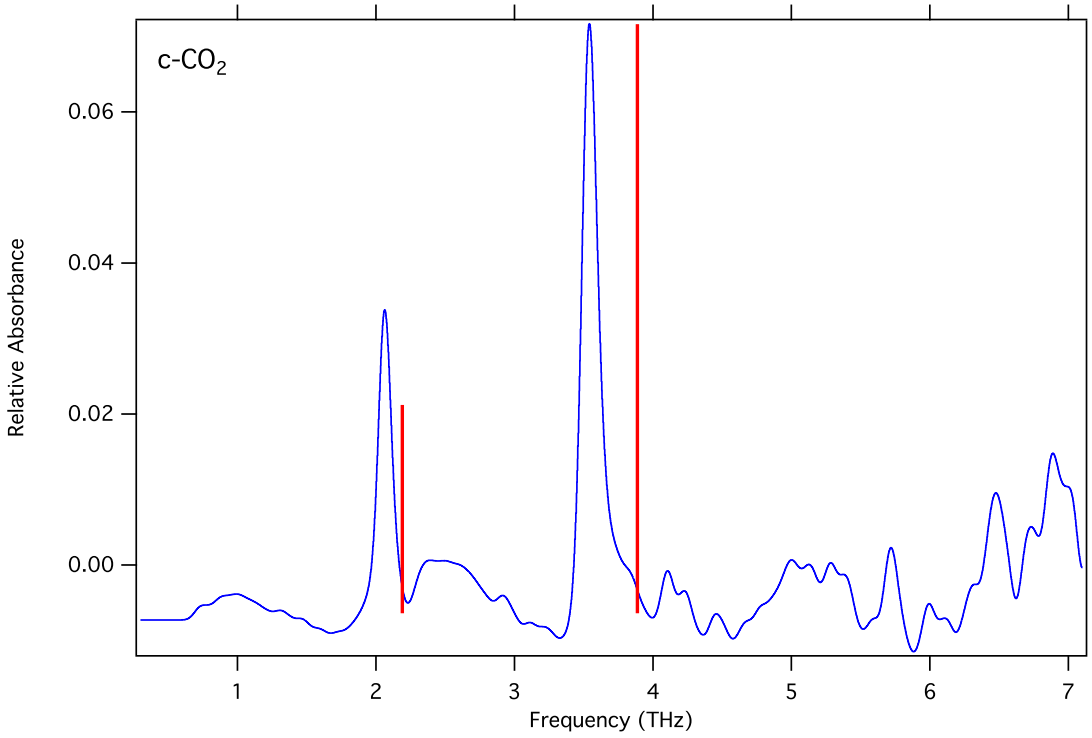

Figure 6.13: Spectra of crystalline carbon dioxide at 10 K (blue), with theoretical predictions from Crystal 09 overlaid in red based on the crystal structure at ambient pressures.

6.7 Formaldehyde Functionalization: Formic Acid, Acetic Acid, Acetaldehyde, and Acetone

To take full advantage of the enormous amount of available THz observations (e.g., *Herschel*, SOFIA, and ALMA), laboratory analogs must be studied systematically. Here, we present the THz spectra of perhaps the simplest series of astrophysically-relevant molecules that share common, and progressively more complex, functional groups (see Figure 6.14).

6.8 Acetaldehyde (CH_3CHO)

Crystalline acetaldehyde was formed through the deposition of 8 Torr of gaseous acetaldehyde over a period of 15 minutes. When preparing the sample, it was noted that acetaldehyde rapidly boils when exposed to vacuum, resulting in significant sample loss. Thus, care must be taken to ensure adequate sample remains after the initial vacuum exposure and the ensuing freeze-pump-thaw cycle. Initial attempts to deposit at 140 K were unsuccessful. The deposition temperature was gradually lowered until signal from acetaldehyde was observed in the FTIR spectra, which occurred at ∼125

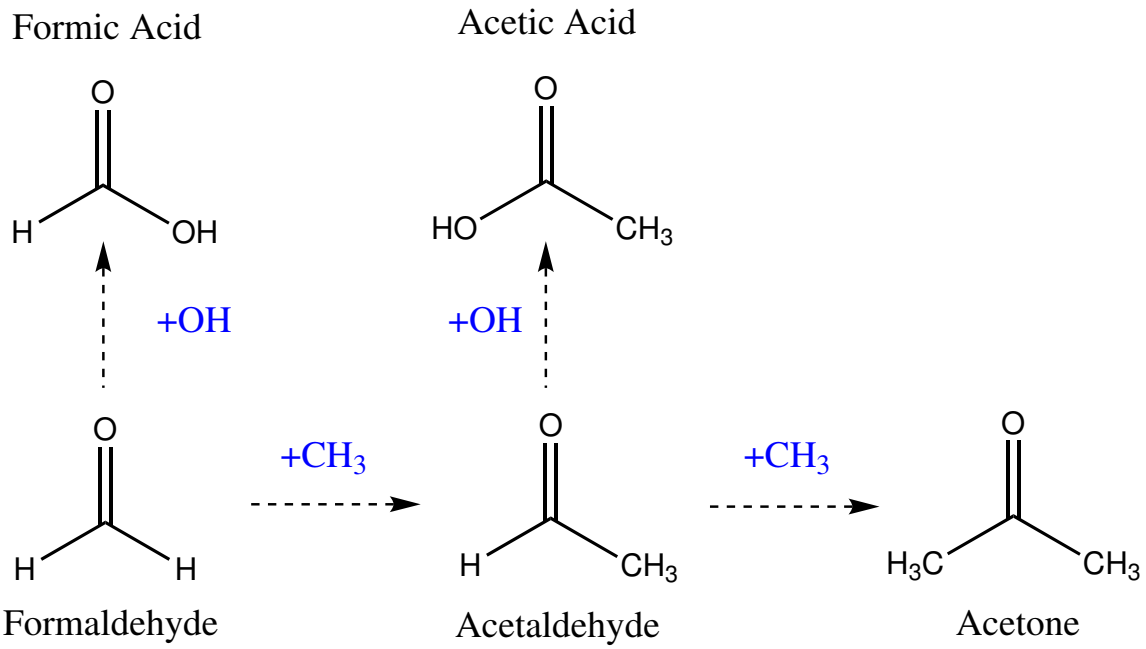

Figure 6.14: Cartoon demonstrating the increasing complexity achievable with the addition of a single functional group (in this case OH or CH_3 radicals) to a simpler, neutral species. Arrows do not represent reaction pathways or mechanisms.

K. Amorphous acetaldehyde was formed through the deposition of 4 Torr of gaseous acetaldehyde over a period of 5.5 minutes at 10 K.

Crystalline acetaldehyde (Figure 6.15) displays a dense set of spectral features with prominent peaks at 6.2 THz, 5.1 THz, 4.0 THz, 3.2 THz, and 2.4 THz. All of these peaks show both a narrowing and a blue shift with decreasing temperature. Amorphous acetaldehyde displays a single broad feature centered around 2.5 THz.

Amorphous acetaldehyde is unstable, and crystallized rapidly when heated to 75 K, well below the deposition (and intended annealing temperature) of 125 K, as seen in Figure 6.16. Amorphous acetaldehyde, that is annealed to 125 K and then cooled to 100 K (Figure 6.17), displays peaks that are broader than their counterparts in crystalline acetaldehyde at 100 K. This may indicate that although amorphous acetaldehyde is unstable and rapidly converts to a more crystalline structure, the formation of a fully crystalline lattice is not efficient under these conditions. It should be noted, however, that the spectral difference between annealed and fully crystalline acetaldehyde is markedly more subtle than similar comparisons in other species in this study.

Acetaldehyde was difficult to fully purge from the system after study. For several days afterward, despite allowing the substrate to warm to room temperature overnight every night, weak absorption was seen at the frequency of the strong, sharp transition from crystalline acetaldehyde at 3.2 THz. The most likely explanation is that the acetaldehyde desorbed to the walls of the vacuum chamber and subsequently deposited, crystalline, as soon as the substrate was cooled down from room temperature the next day for experiments. After the chamber was opened and thoroughly cleaned with 200-proof ethanol, the signal at 3.2 THz no longer appeared in subsequent scans.

6.9 Water-Acetaldehyde Mixtures

Three mixtures of water and acetaldehyde were prepared in ratios of 2:1, 1:1, and 1:2 water:acetaldehyde and deposited crystalline at 125 K over a period of 21 minutes, 14 minutes, and 17.5 minutes, respectively, before being cooled to 10 K (Figure 6.10). In the case of the 2:1 water:acetaldehyde mixture, the spectrum is appears to mostly resemble amorphous water, with a small peak at the 6.9 THz sharp feature of crystalline water. The 1:1 mixture displays a spectrum that resembles quite strongly that of amorphous water ice, however, with the addition of several crystalline acetaldehyde peaks at 2.4 THz, 3.2 THz, 4.0 THz, and 5.1 THz. The 2:1 mixture displays a spectrum that shows significant disruptions to the amorphous water profile, resembling more the crystalline acetaldehyde with a single broad component interfering at the higher frequencies.

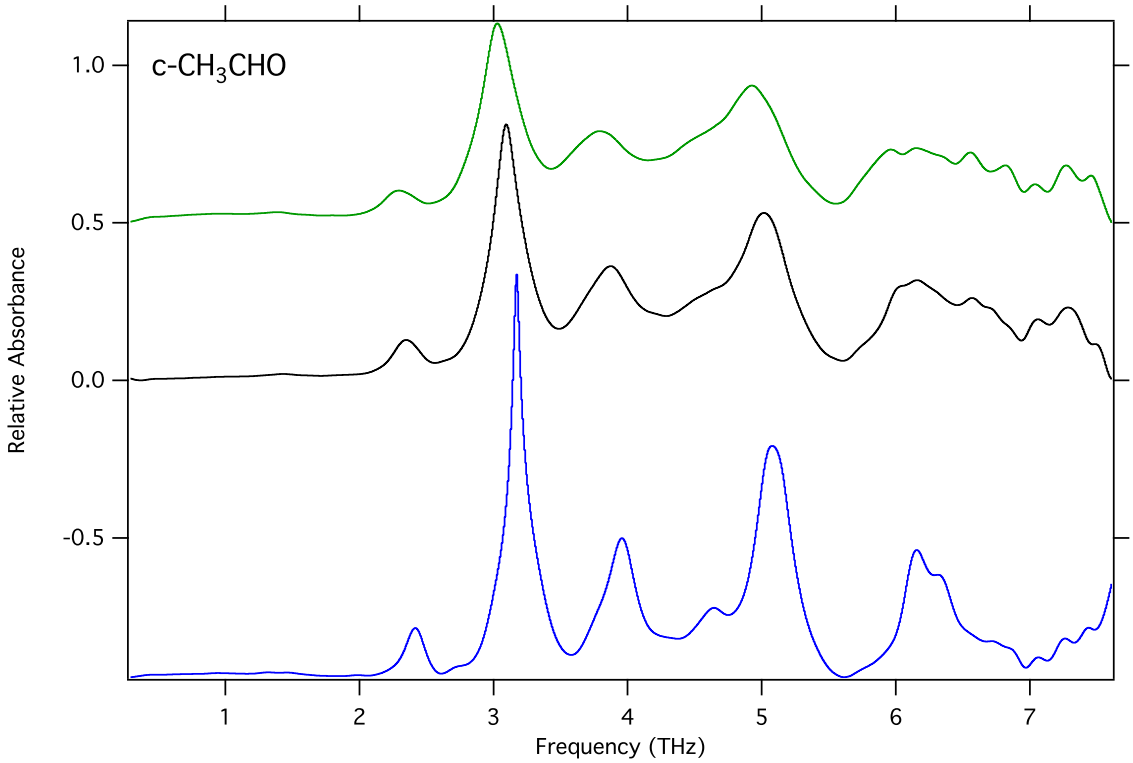

Figure 6.15: Spectra of crystalline acetaldehyde, deposited at 125 K, at 100 K (green), 75 K (black), and 10 K (blue). Traces have been vertically offset for clarity.

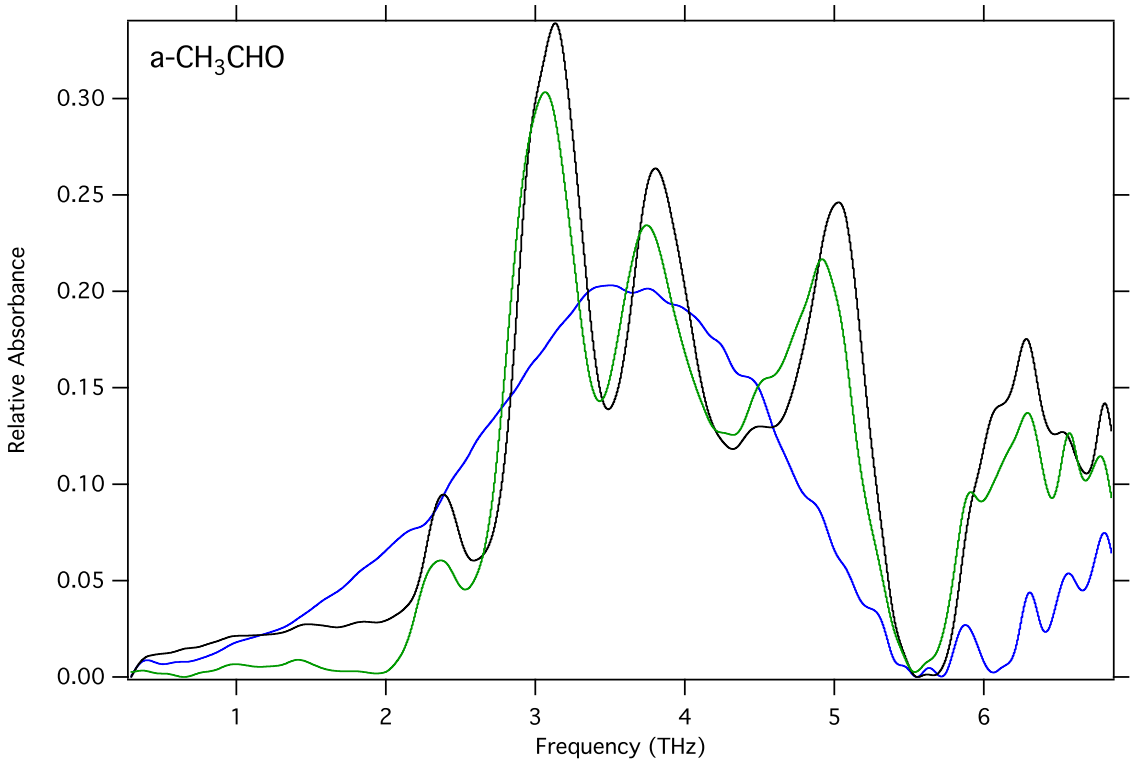

Figure 6.16: Spectra of amorphous acetaldehyde, deposited at 10 K, at 100 K (green), 75 K (black), and 10 K (blue).

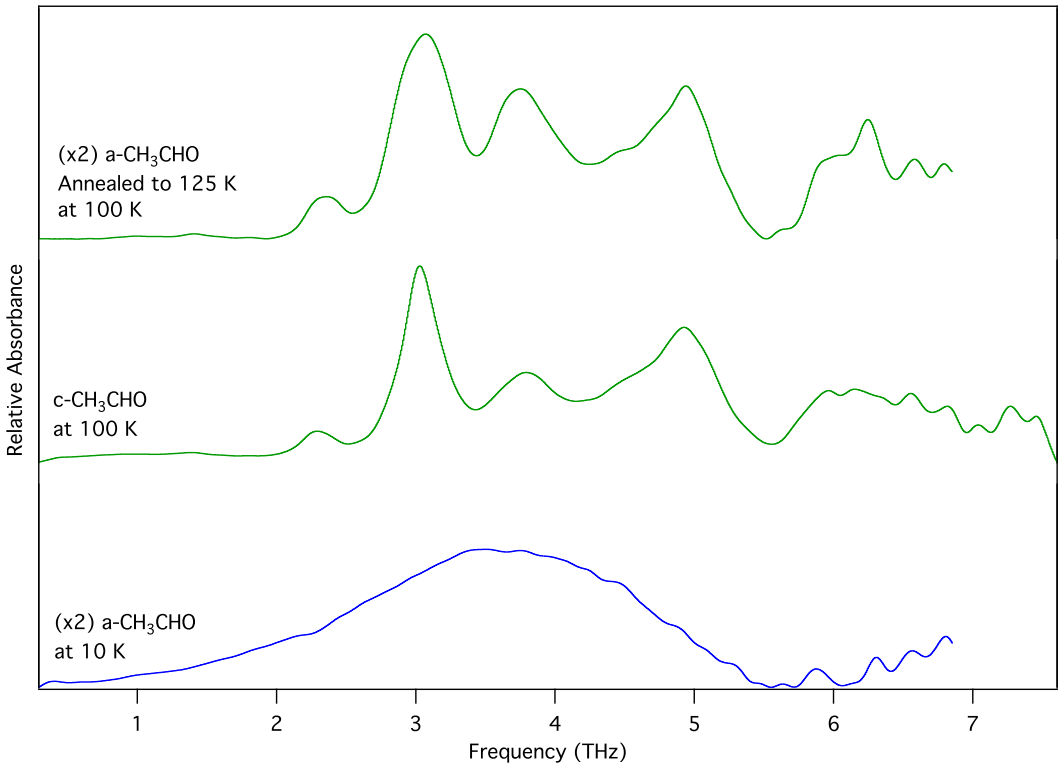

Figure 6.17: Comparison of crystalline acetaldehyde, deposited at 125 K, at 100 K (green) to amorphous acetaldehyde deposited at 10 K at 10 K (blue) and at 100 K after being annealed to 125 K for 5 minutes (green). Traces have been scaled as indicated, and offset vertically for clarity. The annealed ice clearly displays profiles distinct from both amorphous acetaldehyde and acetaldehyde that was deposited crystalline, indicating that these THz features are sensitive to the thermal history of the ice.

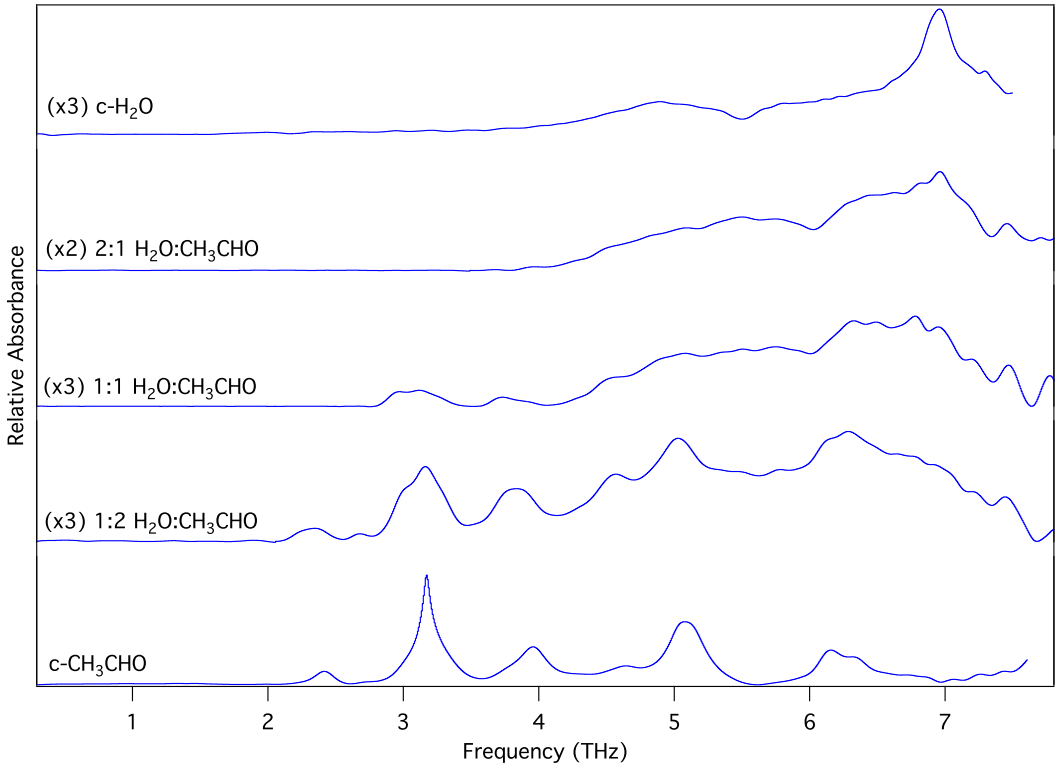

Figure 6.18: Spectra of purely crystalline water, purely crystalline acetaldehyde, and mixtures of water:acetaldehyde in ratios of 2:1, 1:1, and 1:2, all deposited crystalline and cooled to 10 K. Traces are scaled to show detail, and vertically offset for clarity.

6.10 Acetone ($(CH_3)_2CO$)

Crystalline acetone was formed through the deposition of 8 Torr of gaseous acetone over a period of 9 minutes at 150 K. Amorphous acetone was formed through the deposition of 8 Torr of gaseous acetone over a period of 11 minutes at 10 K. The appropriate annealing temperature for this ice was not known *a priori*, and attempts were made at 150 K, 160 K, and 170 K. The ice was observed to completely and rapidly desorb at a temperature of 170 K. To study the annealed ice, a second sample of amorphous acetone was prepared under the same deposition conditions and annealed to 150 K for 10 minutes.

Crystalline acetone (Figure 6.19) displays a rich absorption profile in the THz, comparable to that of crystalline methanol, but with peaks that are often narrower. Further, crystalline acetone is the only molecule studied here to show distinct, narrow signals below 2 THz. The strongest transitions arise at 2.8 and 4.0 THz. Some peaks, such as the strong signal at 4.0 THz, display the narrowing and blue shift with decreasing temperature. Others, however, like the feature at 1.8 THz, show very little shift relative to the other signals.

Like amorphous acetaldehyde, amorphous acetone (Figure 6.20) is relatively unstable, and will begin to crystallize at temperatures well below the crystalline deposition temperature. Fully amorphous acetone shows two strong, broad absorption bands centered at 3.5 and 7.0 THz. At 100 K, the band at 3.5 THz begins to resolve into the strong crystalline features at 2.8 and 4.0 THz, and the smaller, sharper features below 2 THz also become visible. Amorphous acetone that is annealed to 150 K for 10 minutes before being cooled to 100 K (Figure 6.21) displays a spectrum which is similar to fully crystalline acetone at this temperature. While the peak centers are mostly reproduced, the lineshapes presented are subtly different.

6.11 Formic Acid (HCOOH)

Crystalline formic acid was formed through the deposition of 4 Torr of gaseous formic acid over a period of 5.5 minutes at 150 K. Amorphous formic acid was formed through the deposition of 2 Torr of gaseous formic acid over a period of 8 minutes at a temperature of 10 K.

Crystalline formic acid (Figure 6.22) and amorphous formic acid (Figure 6.23) display remarkably similar spectral profiles, with intense, broad absorption centered around 6.8 THz. The features from amorphous formic acid are perhaps slightly broader, while crystalline formic acid may display sharper features on top of the broad absorption profile. In general, these features do not show a consistent or

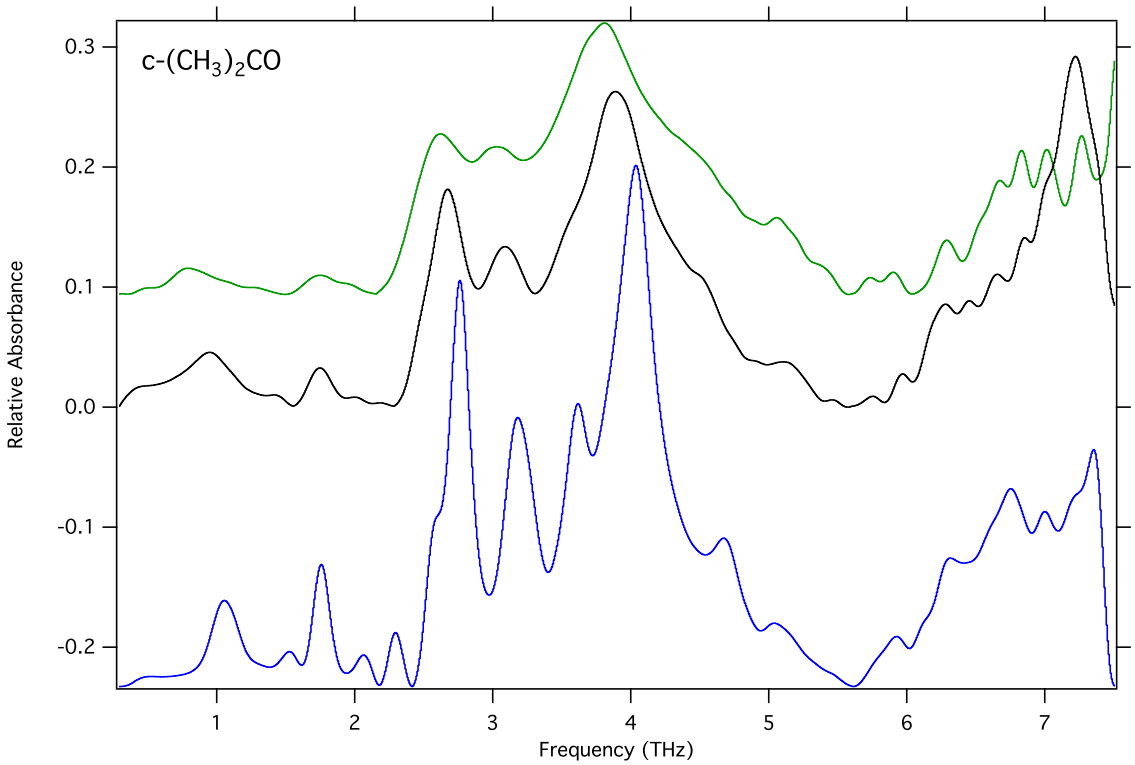

Figure 6.19: Spectra of crystalline acetone, deposited at 150 K, at 100 K (green), 75 K (black), and 10 K (blue). Traces have been vertically offset for clarity.

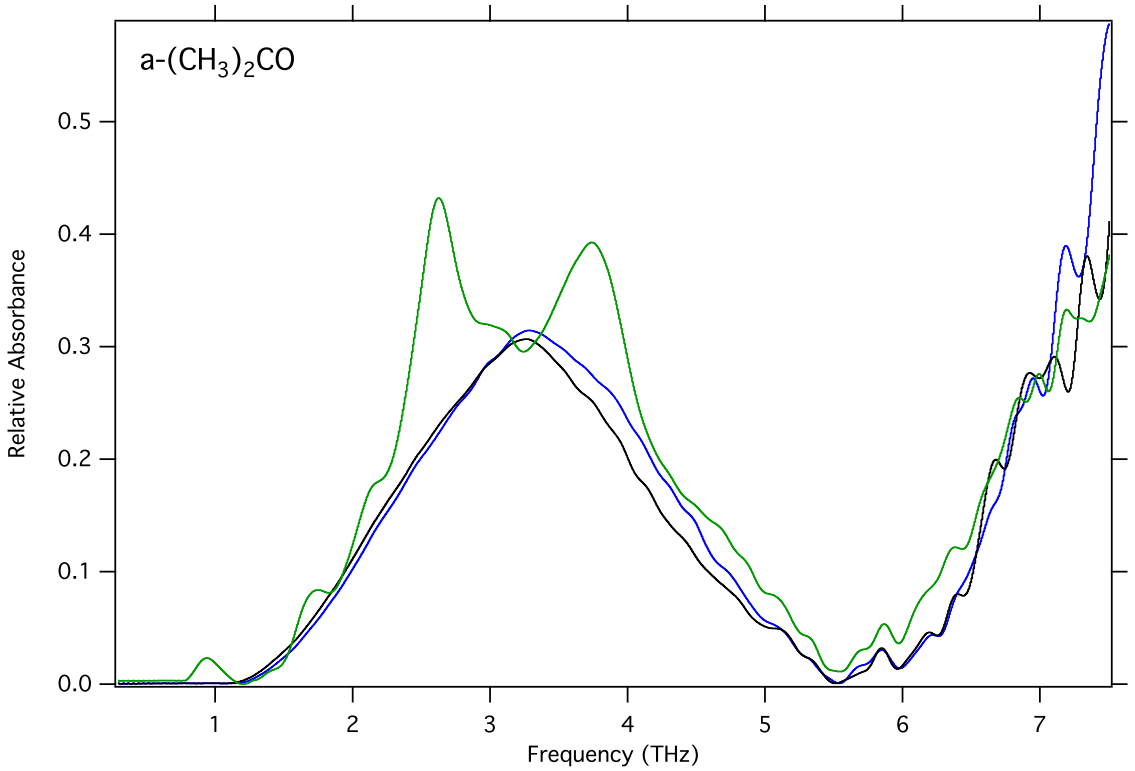

Figure 6.20: Spectra of amorphous acetone, deposited at 10 K, at 100 K (green), 75 K (black), and 10 K (blue).

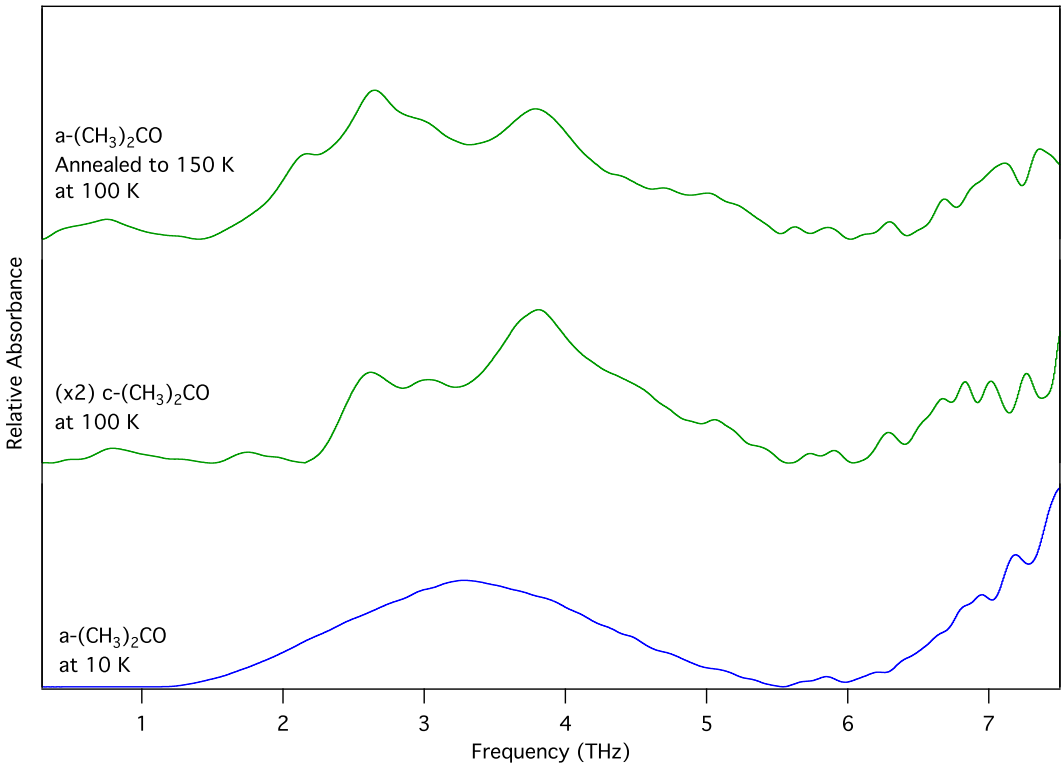

Figure 6.21: Comparison of crystalline acetone, deposited at 150 K, at 100 K (green) to amorphous acetone deposited at 10 K at 10 K (blue) and at 100 K after being annealed to 150 K for 10 minutes (green). Traces have been scaled as indicated, and offset vertically for clarity. The annealed ice clearly displays profiles distinct from both amorphous acetone and acetone which was deposited crystalline, indicating that these THz features are sensitive to the thermal history of the ice.

easily discernible narrowing or blue shift with decreasing temperature, as has been widely observed in other species.

Annealed formic acid (Figure 6.24) displays a spectral profile that appears distinct from amorphous and fully crystalline formic acid. The uncertainty in the origin of the structure observed over the broad feature, however, makes any attempt at a more rigorous comparison difficult.

6.12 Acetic Acid (CH_3COOH)

Crystalline acetic acid was formed through the deposition of 4 Torr of gaseous acetic acid over a period of 3 minutes at 150 K. It was noted that the acetic acid froze more rapidly than most species during the freeze-pump-thaw cycle. After freezing, the sample was exposed to vacuum for a significant amount of time, but no melting was observed. Despite this, when the line was allowed to fill with gas, the pressure rose rapidly to 13 Torr. At this point, the sample appeared to remain solid, but had formed a hollow tube structure in the sample finger, and was no longer cold to the touch. After some time, the sample did eventually melt. The FTIR clearly indicated the presence of pure, crystalline acetic acid. Amorphous acetic acid was formed through the deposition of 2 Torr of gaseous acetic acid over a period of 3 minutes at 10 K. In this case, a warm water bath was introduced after the sample was frozen and exposed to vacuum. The sample melted more rapidly.

As with formic acid, crystalline acetic acid (Figure 6.25) and amorphous acetic acid (Figure 6.26) display markedly similar profiles, with broad absorption centered around 6.0 THz. Unlike formic acid, however, crystalline acetic acid displays an additional, albeit weak absorption feature at 2.6 THz that is not seen in amorphous formic acid. By monitoring the signal from acetic acid with the FTIR, we experimentally determined that all acetic acid desorbed from the substrate at around 220 K. An annealing temperature of 200 K was therefore chosen. After annealing to 200 K for 5 minutes and cooling back to 100 K, the annealed acetic acid shows the feature at 2.6 THz, as well as displaying a narrowing in the band at 6.0 THz, relative to both crystalline and amorphous acetic acid.

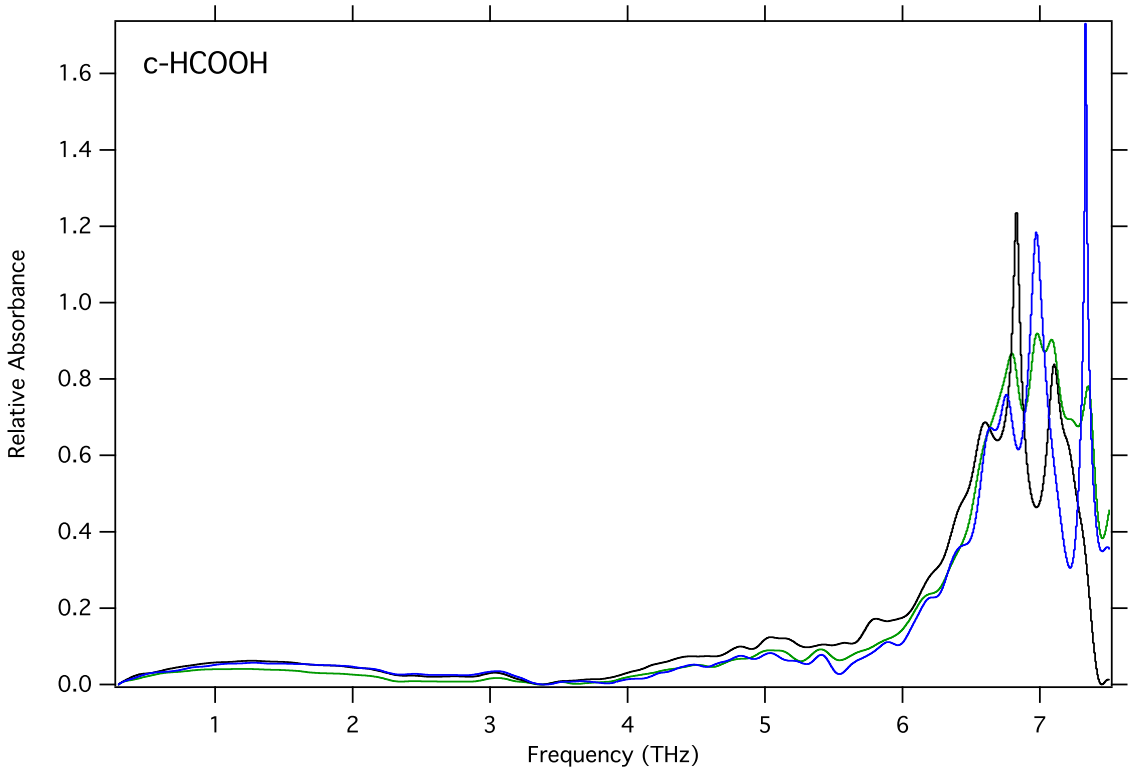

Figure 6.22: Spectra of crystalline formic acid, deposited at 150 K, at 100 K (green), 75 K (black), and 10 K (blue).

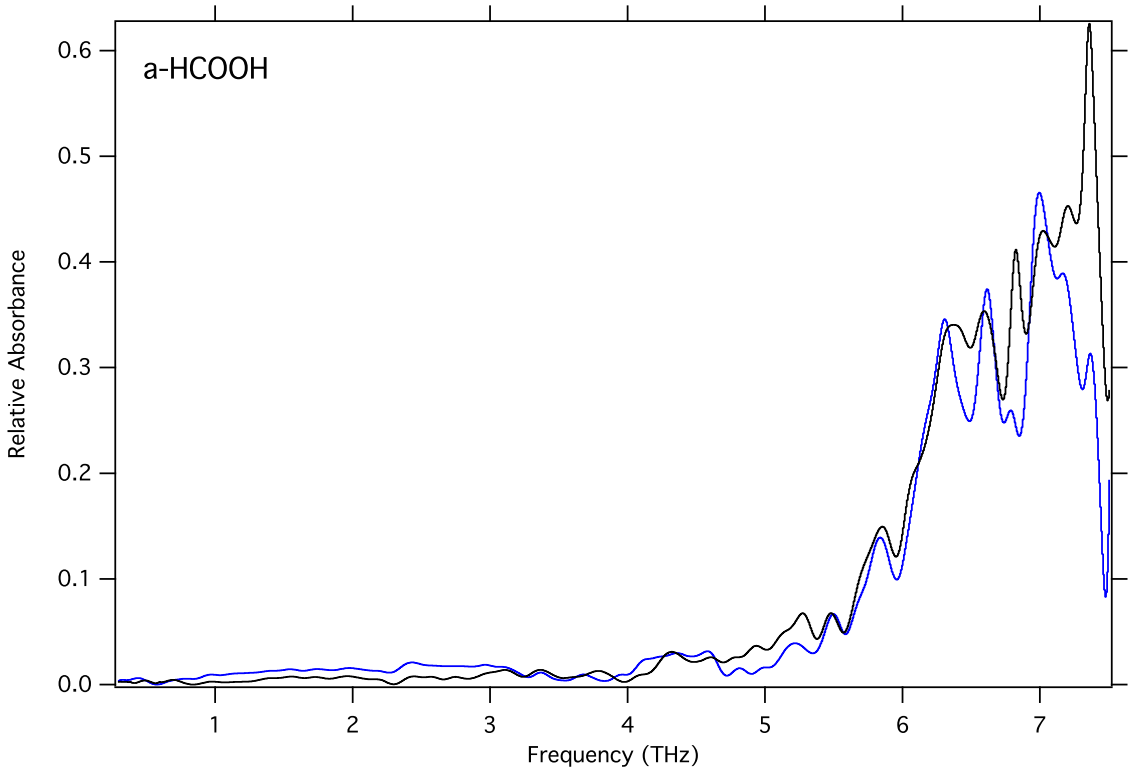

Figure 6.23: Spectra of amorphous formic acid, deposited at 10 K, at 75 K (black), and 10 K (blue).

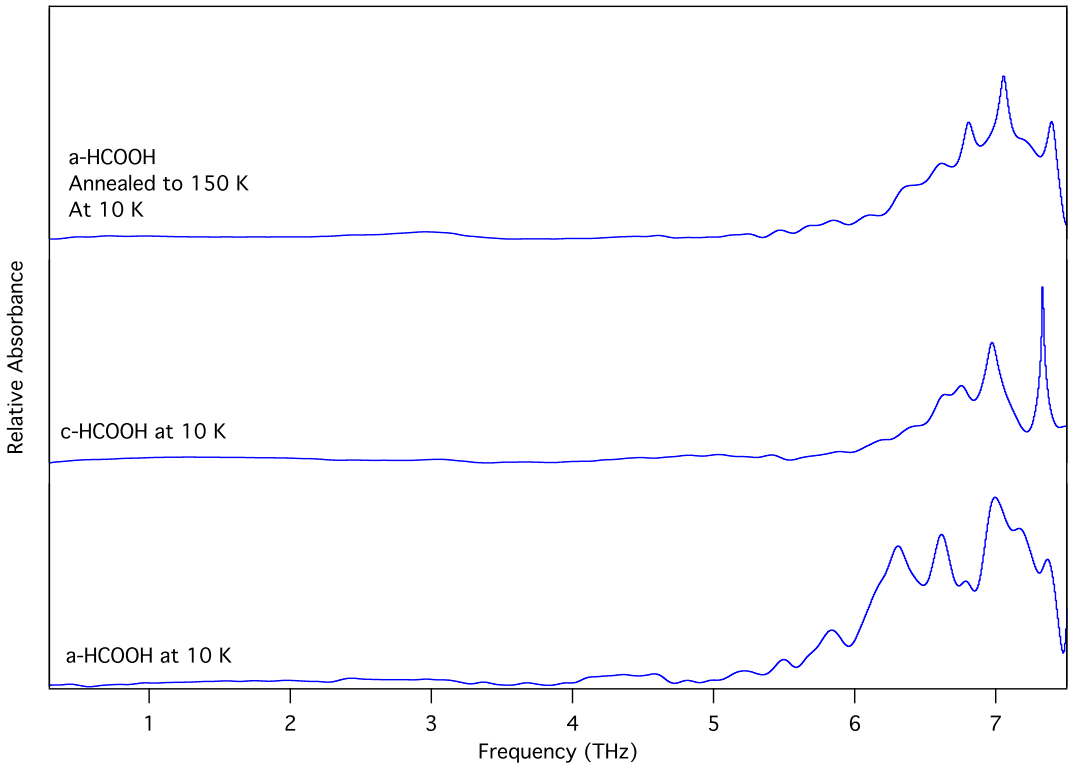

Figure 6.24: Comparison of crystalline formic acid, deposited at 150 K, at 10 K (blue) to amorphous formic acid deposited at 10 K at 10 K (blue) and at 10 K after being annealed to 150 K (blue). Traces have been scaled as indicated, and offset vertically for clarity. While the annealed ice clearly displays profiles distinct from both amorphous formic acid and formic acid that was deposited crystalline, the overall profile of the absorption has remained the same. This is consistent with a strongly-bound dimer structure that largely prevents reorganization into a wider lattice.

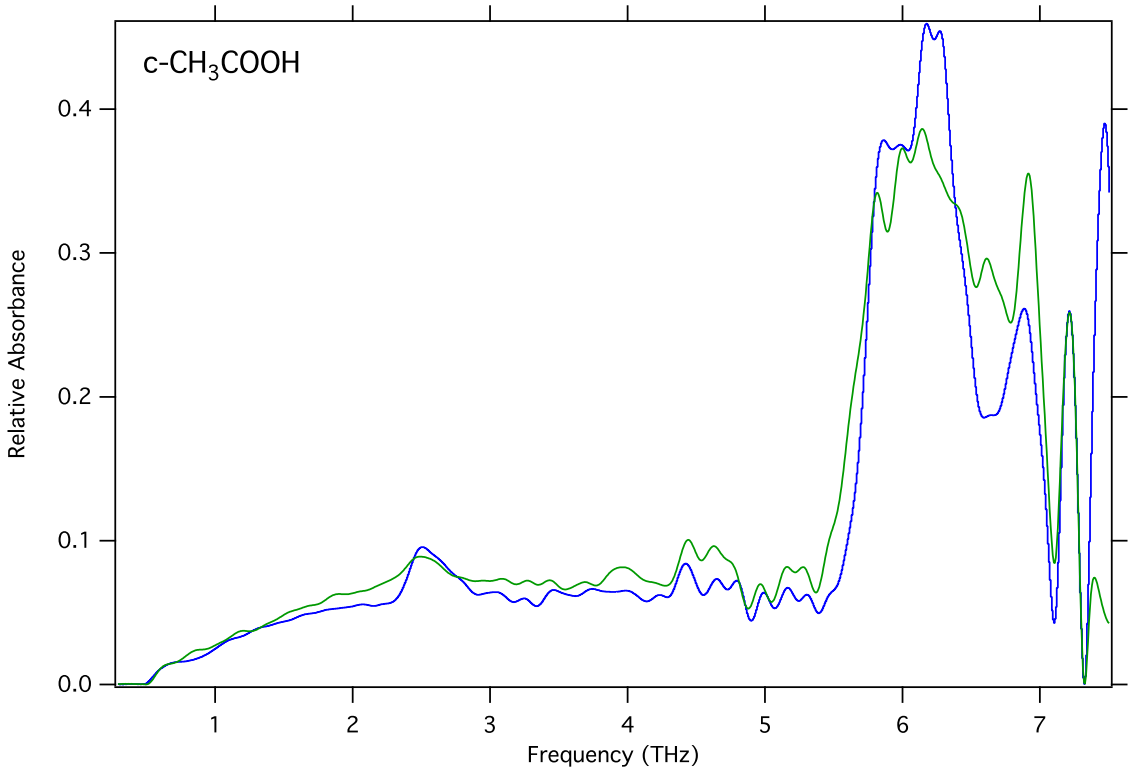

Figure 6.25: Spectra of crystalline acetic acid, deposited at 150 K, at 100 K (green) and 10 K (blue).

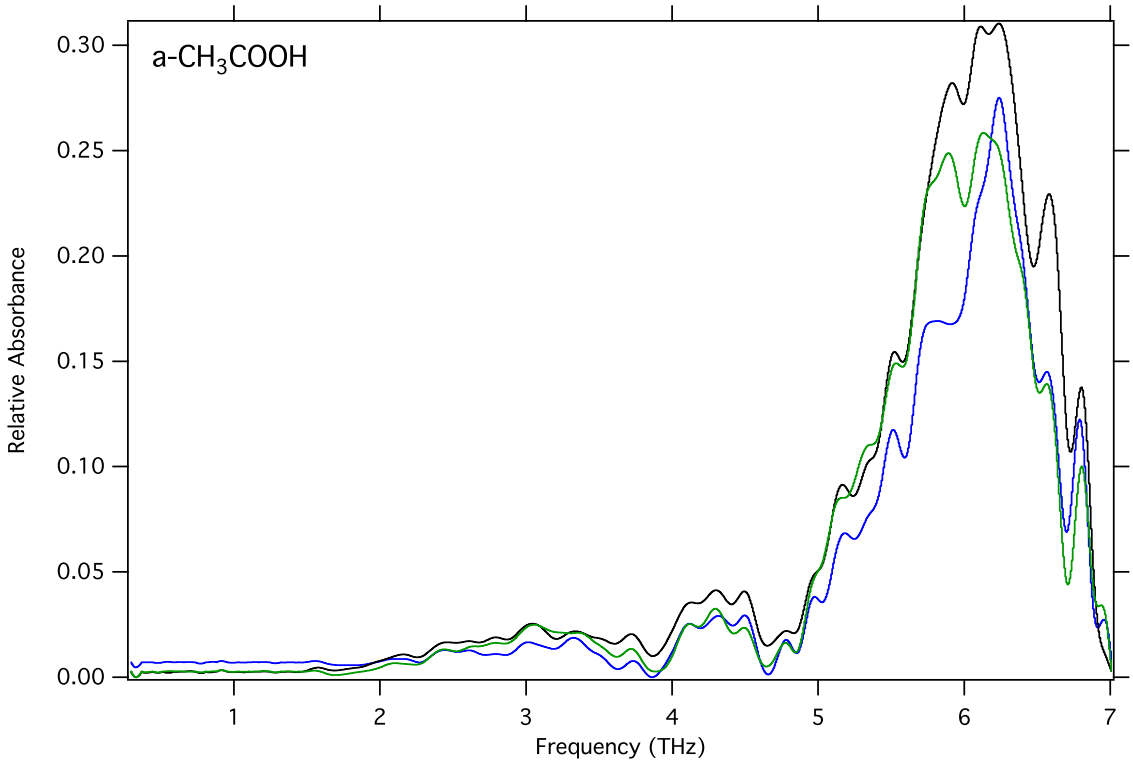

Figure 6.26: Spectra of amorphous acetic acid, deposited at 10 K, at 100 K (green), 75 K (black), and 10 K (blue).

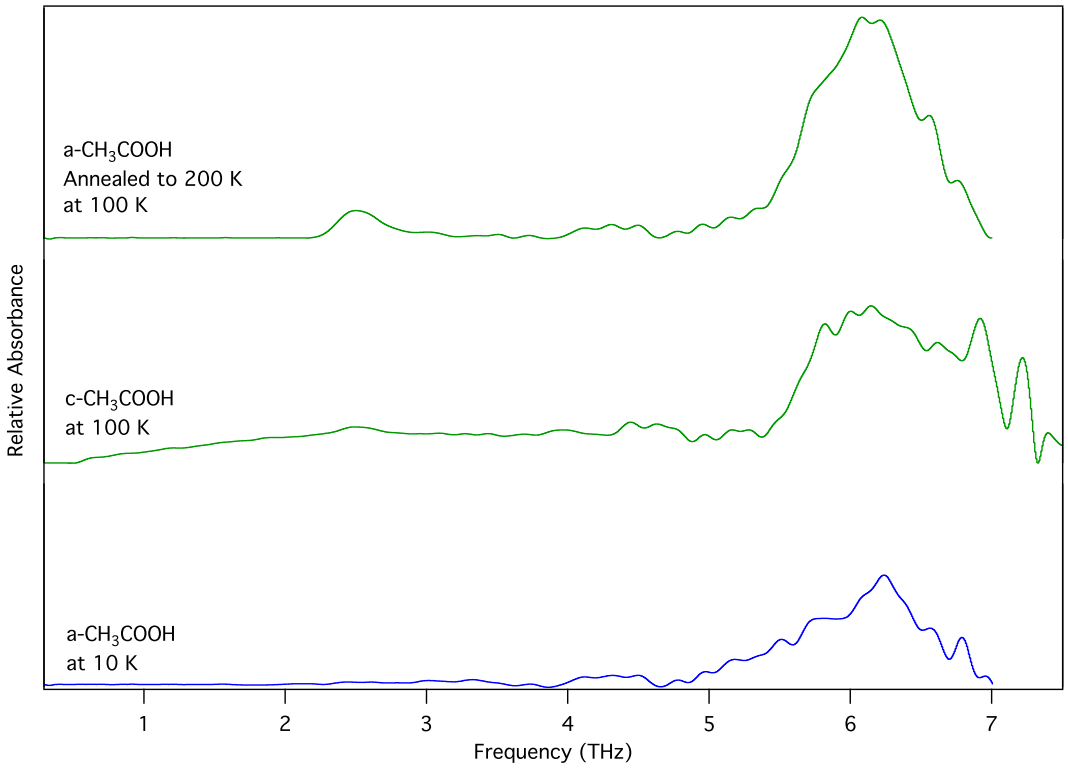

Figure 6.27: Comparison of crystalline acetic acid acid, deposited at 150 K, at 100 K (green) to amorphous acetic acid deposited at 10 K at 10 K (blue) and at 100 K after being annealed to 200 K (green). Traces have been offset vertically for clarity. While the annealed ice clearly displays an additional small absorption at 2.5 THz, the primary absorption feature remains largely unchanged. This is may indicate a strongly-bound dimer structure, similar to formic acid, that largely prevents reorganization into a wider lattice.

Chapter 7

Discussion

7.1 Molecular Motions

The THz spectra presented here probe a set of molecular motions that is distinct from those at both higher and lower frequencies. Generally speaking, transitions in the infrared (like those in Appendix C) arise from the intramolecular motions of molecules – the bending and stretching of bonds within a single molecule, perhaps perturbed somewhat by interactions with surrounding species (solids, neat liquids) or solvents – while transitions in the microwave arise from the pure rotational or torsional motions of a single molecule (see Figure 7.1). Signals arising in the THz region of the spectrum, however, probe a distinctly different regime.

The pure rotational motion of some lighter molecules, and the torsional motion of complex species such as methanol, has transitions from intramolecular motion in the range of 1 to a few THz. However, the bulk of the transitions observed in the THz arise from the intermolecular motion of molecules. In particular, the long-range, bulk motion (i.e. lattice modes) of hydrogen-bonded structures seems to dominate this spectral region. The most-studied of these is the case of crystalline water, which shows transitions arising from the bulk motion of hydrogen-bonded bilayers with respect to one another [152; 153] (see Figure 7.2). It is therefore of little surprise that the THz spectra collected with our instrument for crystalline ices present both more numerous and more distinct features than those from amorphous ices. This also offers the ability to probe the effects of impurities on the large-scale structure (i.e. hydrogen-bonding networks) in these crystalline ices.

Indeed, the THz spectra of these ices appear to be exquisitely sensitive to this structure, and to any disruption in the crystalline network. Perhaps the most extreme example of this is shown in Figure 6.17. Amorphous acetaldehyde appears to require very little thermal energy to reorganize into a crystalline structure, with distinctly crystalline features arising in samples that are heated to

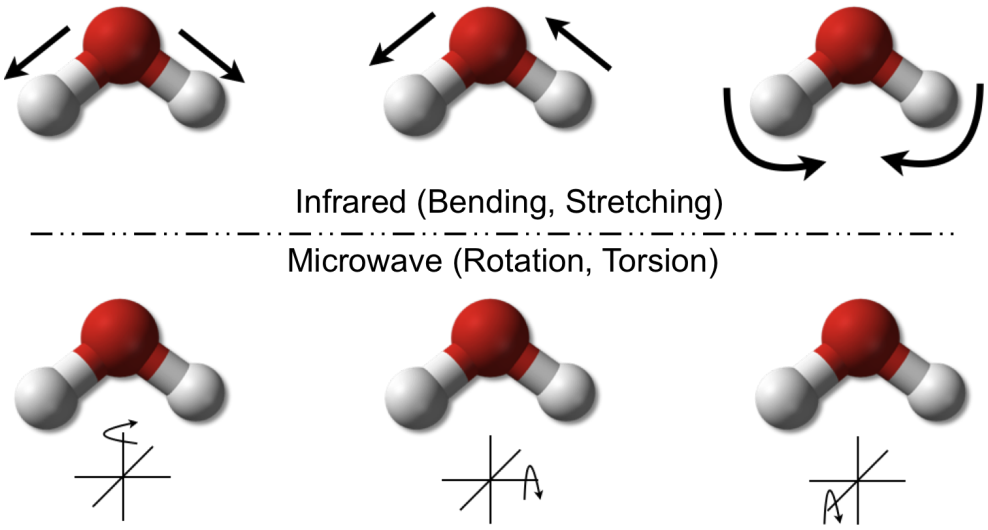

Figure 7.1: Cartoon depicting the molecular motions that generally lead to transitions arising in the infrared – intramolecular vibrations – and in the microwave – rotational and torsional motion.

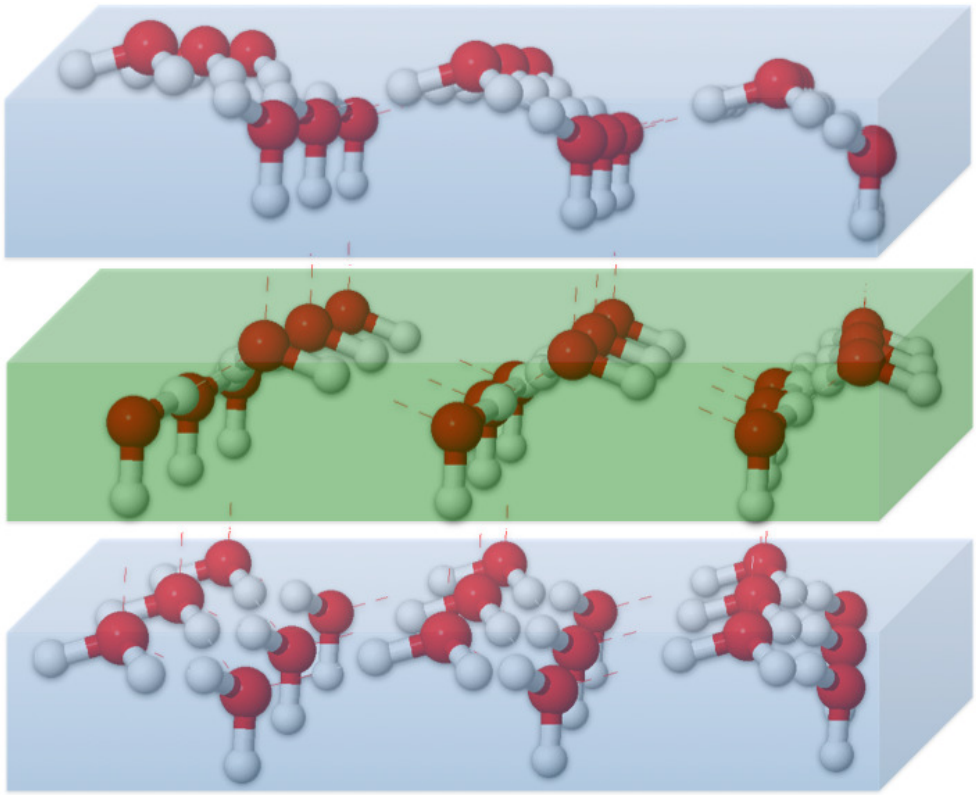

Figure 7.2: Cartoon depicting the hydrogen-bonded bilayers formed in crystalline water ice. THz spectroscopy is sensitive to the large-scale, bulk stretching and bending of hydrogen bonds between and among these bilayers.

as little as 75 K (50 K below the deposition temperature for purely crystalline acetaldehyde). In these experiments, the samples are held at the temperatures reported for each spectra for at least 2 hours to complete the scans. In this case, the amorphous acetaldehyde was kept at 75 K and then 100 K for more than 4 hours, before being briefly annealed to 125 K for 5 minutes and cooled back down to 100 K for stability. Despite this large thermal bath, and long exposure times, the amorphous sample does not present the same spectrum as purely crystalline acetaldehyde. Thus, these THz spectra provide insight into the *thermal history* of the ices, and not just their current configuration.

This seems to hold, to greater or lesser extent, for the large majority of the species studied. Perhaps the most important of these is water, which clearly shows evidence of a mix of amorphous and crystalline forms after annealing (Figure 6.5). Of the ices studied here, this has the greatest potential to provide direct insight from observations of protoplanetary disks, hot cores around young protostars, or other regions where a large temperature gradient exists. If this incomplete crystallization holds over astronomical timescales, it is easy to imagine being able to distinguish between a crystalline ice that was formed from water that has cooled from higher temperatures, and one which was initially amorphous, but has been warmed, either through the ignition of a young star or through migration toward a source of thermal energy. Thus, observations of water ice in the THz hold the possibility to elucidate pathways of volatile transport in protoplanetary disks, and in the thermal evolution of complex organic molecules.

7.2 A Lattice-Mode Exception: Formic and Acetic Acid

Notable exceptions to this are the cases of formic and acetic acid. In these cases (see Figures 6.22, 6.23, 6.25, and 6.26) both the crystalline and amorphous ices appear to present almost indistinguishable spectra, with a single strong, broad feature arising at ∼7 THz and ∼6 THz in formic and acetic acid, respectively.[1] The likeliest explanation is that neither formic nor acetic acid form long-range structures at energies low-enough to maintain an ice. Instead, the signal may be arising from the hydrogen-bond stretching between dimers of the molecules that have formed in the gas phase in the deposition line and deposited as dimers onto the surface where the thermal bath is not sufficient to cause a reorganization (see Figure 7.3).

[1]Some structure is visible on top of these broad peaks, but it is unclear whether or not this structure is arising due to the very low transmission at the peak of these transitions. Follow-up scans at higher resolution should be conducted to elucidate the details of the spectra profile.

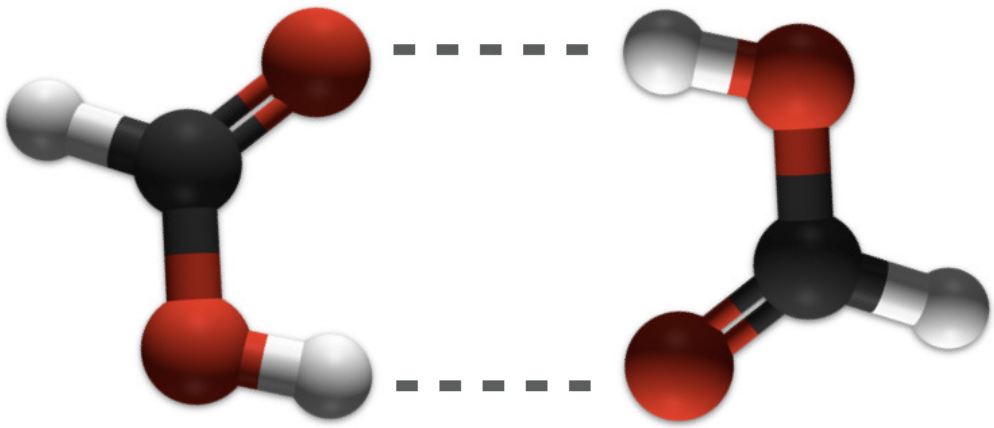

Figure 7.3: Cartoon depicting the gas-phase hydrogen-bonding arrangement of the formic acid dimer (not to scale).

To test this theory, we performed a modest computational analysis of the vibrational modes of the formic and acetic acid dimers. All calculations were performed using the MP2/6-311+G(d,p) level of theory and basis set to adequately model the hydrogen bonding interactions between molecules, and were carried out using Gaussian 09 [156]. Since harmonic frequencies calculated with MP2 are known to be systematically biased toward higher frequencies than observed [157], the calculated frequencies in wavenumbers were scaled by a value of 0.9646 as used by [158].

While these calculations are for gas-phase dimers, they can provide some insight into solid-phase structures as well. The hydrogen-bonded interaction that forms a dimer is indeed strong, and dimers can therefore dominate the structure of pure ices. Our calculations provide evidence in support of this. In the case of the formic acid dimer, the calculations reveal a strong mode corresponding to a rocking of the two molecules, which stretches their hydrogen bonds, at 235 cm^{-1} (7.0 THz). This is in good agreement with the formic acid mode observed in the experimental spectrum at ∼7 THz. A similar mode is found in the calculated vibrations for the acetic acid dimer at 160 cm^{-1} (4.8 THz). According to our experimental data, however, the strongest mode of acetic acid peaks at ∼6 THz. Differences between these MP2 simulations and the THz laboratory results can be explained by the

more constrained nature of the molecules in the ice that can cause the frequency of this rocking vibration to be higher in energy in the solid phase than in the gas phase.

Overall, while the predicted mode of acetic acid does not agree perfectly with the experimentally-measured transition, the calculations produce the same red shift in frequency, relative to the formic acid mode, as observed in the experiments. This offers evidence to support our assignments of these transitions, as a model of harmonic vibrations predicts a decrease in frequency when mass is increased, as is the case when a heavier functional group is added (-CH_3 vs H). Therefore, similarities between THz spectra of amorphous and crystalline acidic ices can be explained by the direct deposition of acidic dimers onto the substrate. As a result of the strong hydrogen-bonding interaction between dimers, the features around 6 and 7 THz remain largely unchanged when the molecules are deposited at high temperatures or when amorphous ices are annealed.

7.3 Mixtures

Although there are some mixed binary and more complex ices reported in literature in the far-IR region of the electromagnetic spectrum, there are no data available at low frequencies (between 0.3 and 3 THz). For instance, Moore and Hudson [140] mixed water with other interstellar relevant species with a ratio of 10:1 and 2:1. All of their amorphous ices were deposited at 13 K, while the crystalline mixtures were obtained by annealing amorphous ices to 155 K and cooling them back to 13 K. This procedure may lead to some desorption, diffusion, and reorganization. However, we showed that annealed ices are hardly fully crystalline unless the ice is annealed to temperatures close to their desorption temperature for several minutes. This can also cause desorption of part of the ice. Allodi et al. [136] showed that CO_2 mixed in water ice segregates at higher temperatures between the bilayers of water ice, disrupting the crystalline structure of water ice. Spectra of these mixtures are hard to interpret if not supported by proper THz ice-database that includes spectra of pure ices at different temperatures and different mixtures deposited at high temperatures. Therefore, our goal here is the investigation of the spectral changes of crystalline ice when binary mixtures are deposited at different ratios and high temperature.

Figure 6.10 shows mixtures of water with methanol in ratios of 2:1, 1:1, and 1:2 deposited fully crystalline at 140 K. The mixture at 2:1 H_2O:CH_3OH shows little change from that of purely crystalline H_2O. This is in sharp contrast to the study of CO_2 and H_2O mixtures in [136], where even with dilutions as high as 10:1 H_2O:CO_2, severe disruption of the H_2O hydrogen-bonding network is seen (see Figure 8 of [136]). Indeed, at a mixture ratio of 5:1 H_2O:CO_2, there is no evidence for

crystalline structure at all, with the ice appearing fully amorphous. At the 10:1 H_2O:CO_2 dilution, a hint of the crystalline H_2O feature around 7.2 THz can be seen, but is barely above the noise level. This is in sharp contrast to the 2:1 H_2O:CH_3OH mixture studied here. In this case, the ice appears nearly fully crystalline, with all features still clearly visible. This is likely due to the ability for CH_3OH to substitute in to the hydrogen-bonding network of H_2O without largely disrupting the long-range motion.

At an even ratio of 1:1 H_2O:CH_3OH, the ice appears fully amorphous, which is perhaps unsurprising, as despite the ability of both species to form hydrogen bonds, the lack of a dominant member prevents an overall ordered structure from forming. This conclusion seems to be supported by the 1:2 H_2O:CH_3OH mixture where modes of crystalline CH_3OH have clearly begun to be visible. This indicates that the ice has formed an ordered structure similar to that of purely crystalline CH_3OH, with H_2O impurities participating in the hydrogen-bonding lattice.

A similar, but subtly different effect is seen when the mixture partner is acetaldehyde (see Figure 6.18). In this case, the CH_3CHO, while a better hydrogen-bonding impurity than CO_2, does not appear to participate as fully in the network as CH_3OH. As a result, the spectra of 2:1 H_2O:CH_3CHO appears nearly fully amorphous, with only a small crystalline H_2O feature still visible. The CH_3CHO, however, appears to be much more tolerant of H_2O impurities than CH_3OH, with purely crystalline CH_3CHO features clearly appearing in the 1:1 mixture. At an enrichment of 1:2 H_2O:CH_3CHO, the ice appears nearly fully crystalline CH_3CHO. Another possibility is that the H_2O and CH_3CHO are porous enough that the dopant species has segregated, and has crystallized within the pores of the primary constituent.

Part IV

Conclusions

The work presented here attacks the issue of understanding the chemical evolution of prebiotic and biotic materials, such as amino acids, from multiple fronts. From an observational standpoint, the identification of carbodiimide in the ISM for the first time has added a new molecule to the known molecular inventory. Beyond this result, and perhaps more importantly, it has hopefully opened others up to the possibility that searches for molecules that should be undetectable under LTE conditions may yet be fruitful. With the thoughtful exploitation of phenomena such as masing, important transient or intermediate species, which have a non-negligible effect on the overall chemical and physical evolution of a system, may yet be detected.

Through the studies of l-C_3H^+ presented here, it has been shown that careful examination of the chemistry and chemical environments probed by the observations can provide a robust and deep insight into the mechanisms at work and the species present. Without any laboratory work having been conducted, and examining only archival observational data, C_3H^- was dismissed as the carrier of B11244 based on an analysis of the *chemistry* at work in the environments where it had been detected. This work now expands, seeking to explore how l-C_3H^+ can probe the environments, and the thus-far rare conditions in which it is present in detectable abundance.

Again, using only archival observational data, a serious gap in the completeness of state-of-the-art gas-grain astrochemical models was closed by the report of a *non-detection* of hydroxylamine in a number of complex molecular sources. As a result of this work, what is perhaps the last efficient route to the formation of glycine in the gas phase has been challenged, and new astrochemical models now turn to reactions on and within the icy mantles of dust grains to form this important species.

While the primary composition of these icy environments is relatively well-understood, there has been no definitive observational evidence for the presence of any molecules more complex than methanol in the solid phase. The construction of a THz-TDS system to study astrophysical ices has begun to open up a region of the electromagnetic spectrum that has been almost completely unexplored in terms of observing solid-phase species in the ISM. This work has revealed not only the richness of spectral features in the THz region, but the exquisite sensitivity of these spectra on the long-range structure of the ices as well. While traditional observations in the mid-IR offer a somewhat comparable insight into this structure, the THz has, at least preliminarily, demonstrated an unparalleled and exciting ability to probe the *thermal history* of the ices. Should such a history be observable in observational spectra in the THz, the potential insight gained into the physical evolution, dynamics, and mass transport within protostellar cores and protoplanetary systems is remarkable.

These initial studies of ices in the THz-TDS instrument, and the conclusions drawn from them, are largely based on a qualitative assessment of the relative positions, intensities, and profiles of the signals observed. This is a natural and expected consequence of the foundational work being done with this system; there is essentially no prior body of knowledge from which to build on, and thus, this work must necessarily begin from the most basic of analyses, and yet, such efforts can only achieve so much. The full potential of these endeavors cannot be realized until the basic forces at work are quantified, and the underlying physical phenomena elucidated. The use of the relatively basic theoretical simulations of dimers to understand the behavior of formic and acetic acids, and to predict, with surprising accuracy, the observed modes of CO_2 using periodic boundary condition-constrained solid-state calculations, represent a first step into a larger world. The sensitivity of these observations to ordered structure demands deeper theoretical investigations into the long-range lattice structures present in these ices. For example, mixtures of methanol and acetaldehyde with water generate an immediate awareness that understanding the interplay and transitions between these distinctly separate ordered domains will be a complex undertaking that will rely on both computational and laboratory efforts. The inherently time-domain nature of these studies extends their utility by offering the opportunity to probe directly the optical constants of a species of interest, without the need for approximate treatments of indirect data.

These studies illuminate both the early (i.e. the formative, complex molecular nebulae) and the late (i.e. the incorporation into, or formation of amino acids in cometary ices) stages of complex prebiotic organic chemistry along the pathway to the formation of primitive life on Earth. They examine the two disparate, yet intricately interconnected phases of chemical evolution in the ISM by probing, or offering the means to probe, the composition and the chemistry of both the gas and solid phases of organic matter. In the end, it is not enough that we know what is out there, between the stars; rather, it is our goal to understand how it all fit together, sometime in the last 13.7 billion years (give or take), to make us.

Bibliography

[1] S. L. Miller and H. C. Urey, "Organic Compound Synthesis on the Primitive Earth," *Science*, **130**, 245–251 (1959).

[2] O. Botta and J. L. Bada, "Extraterrestrial organic compounds in meteorites," *Surveys in Geophysics*, **23**, 411–467 (2002).

[3] J. E. Elsila, D. P. Glavin, and J. P. Dworkin, "Cometary glycine detected in samples returned by Stardust," *Meteoritics & Planetary Science*, **44**, 1323–1330 (2009).

[4] R. L. Pulliam, B. A. McGuire, and A. J. Remijan, "A search for hydroxylamine (NH_2OH) toward select astronomical sources," *The Astrophysical Journal*, **751**, 1 (2012).

[5] V. Blagojevic, S. Petrie, and D. K. Bohme, "Gasphase syntheses for interstellar carboxylic and amino acids," *Monthly Notices of the Royal Astronomical Society*, **339**, L7–L11 (2003).

[6] J. L. Snow, G. Orlova, V. Blagojevic, and D. K. Bohme, "Gas-phase ionic syntheses of amino acids: β versus α," *Journal of the American Chemical Society*, **129**, 9910–9917 (2007).

[7] R. T. Garrod, S. L. W. Weaver, and E. Herbst, "Complex Chemistry in Star-forming Regions: An Expanded Gas-Grain Warm-up Chemical Model," *Astrophys. J.*, **682**, 283 (2008).

[8] E. Congiu, G. Fedoseev, S. Ioppolo, F. Dulieu, H. Chaabouni et al., "NO ice hydrogenation: a solid pathway to NH_2OH formation in space," *The Astrophysical Journal*, **750**, L12 (2012).

[9] R. T. Garrod, "A three-phase chemical model of hot cores: the formation of glycine," *The Astrophysical Journal*, **765**, 60 (2013).

[10] Y.-J. Kuan, S. B. Charnley, H.-C. Huang, W.-L. Tseng, and Z. Kisiel, "Interstellar Glycine," *The Astrophysical Journal*, **593**, 848–867 (2003).

[11] L. Snyder, F. Lovas, J. Hollis, D. Friedel, P. Jewell et al., "A rigorous attempt to verify interstellar glycine," *Astrophys. J.*, **619**, 914–930 (2005).

[12] Y. S. J. Shiao, L. W. Looney, A. J. Remijan, L. E. Snyder, and D. N. Friedel, "First acetic acid survey with CARMA in hot molecular cores," *The Astrophysical Journal Letters*, **716**, 286–298 (2010).

[13] N. Nishi, H. Shinohara, and T. Okuyama, "Photodetachment, photodissociation, and photochemistry of surface molecules of icy solids containing NH_3 and pure H_2O ices," *The Journal of chemical physics*, **80**, 3898 (1984).

[14] W. Zheng and R. I. Kaiser, "Formation of hydroxylamine (NH_2OH) in electron-irradiated ammonia-water ices," *Journal of Physical Chemistry*, **114**, 5251–5255 (2010).

[15] S. B. Charnley, S. D. Rodgers, and P. Ehrenfreund, "Gas-grain chemical models of star-forming molecular clouds as constrained by ISO and SWAS observations," *A&A*, **378**, 1024–1036 (2001).

[16] L. J. Allamandola and C. A. Norman, "Infra-red emission lines from molecules in grain mantles," *Astronomy & Astrophysics*, **63**, L23–L26 (1978).

[17] M. Akyilmaz, D. R. Flower, P. Hily-Blant, G. Pineau des Forêts, and C. M. Walmsley, "The depletion of NO in pre-protostellar cores," *A&A*, **462**, 221–230 (2007).

[18] H. S. P. Müller, F. Schlöder, J. Stutzki, and G. Winnewisser, "The Cologne Database for Molecular Spectroscopy, CDMS: a useful tool for astronomers and spectroscopists," *Journal of Molecular Structure*, **742**, 215–227 (2005).

[19] I. Morino, K. M. T. Yamada, H. Klein, S. P. Belov, G. Winnewisser et al., "Terahertz rotational spectra of NH_2OH in the ground and some low excited vibrational states," *Journal of Molecular Structure*, **517**, 367–373 (2000).

[20] S. Tsunekawa, "Microwave Spectrum of Hydroxylamine," *Journal of the Physical Society of Japan*, **33**, 167 (1972).

[21] L. M. Ziurys and D. McGonagle, "The spectrum of Orion-KL at 2 millimeters (150-160 GHz)," *The Astrophysical Journal Supplement Series (ISSN 0067-0049)*, **89**, 155–187 (1993).

[22] K. M. Menten, C. M. Walmsley, C. Henkel, and T. L. Wilson, "Methanol in the Orion region. I - Millimeter-wave observations. II - The 25 GHz masers revisited," *Astronomy and Astrophysics (ISSN 0004-6361)*, **198**, 253–273 (1988).

[23] W. B. Latter and S. B. Charnley, "Methanol in the Circumstellar Envelope of IRC+ 10216," *The Astrophysical Journal Letters*, **463**, L37 (1996).

[24] B. E. Turner, "A molecular line survey of Sagittarius B2 and Orion-KL from 70 to 115 GHz. II-Analysis of the data." *The Astrophysical Journal Supplement Series*, **76**, 617–686 (1991).

[25] A. Nummelin, P. Bergman, Å. Hjalmarson, P. Friberg, W. Irvine et al., "A three-position spectral line survey of sagittarius B2 between 218 and 263 GHz. II. Data analysis," *Astrophysical Journal Supplement Series*, **128**, 213–243 (2000).

[26] T. J. Millar, P. D. Brown, H. Olofsson, and Å. Hjalmarson, "The detection of ethanol in W51M," *Astronomy and Astrophysics (ISSN 0004-6361)*, **205**, L5–L7 (1988).

[27] F. P. Helmich, D. J. Jansen, T. de Graauw, T. D. Groesbeck, and E. F. van Dishoeck, "Physical and chemical variations within the W3 star-forming region. 1: SO2, CH3OH, and H2CO," *Astronomy and Astrophysics (ISSN 0004-6361)*, **283**, 626–634 (1994).

[28] A. J. Remijan, A. Markwick-Kemper, and ALMA Working Group on Spectral Line Frequencies, "Splatalogue: Database for Astronomical Spectroscopy," in "American Astronomical Society Meeting Abstracts," #132.11 (2007).

[29] W. Gordy and R. L. Cook, *Microwave Molecular Spectra*, New York, NY: Wiley, 3 ed. (1984).

[30] J. M. Hollis, P. R. Jewell, F. J. Lovas, and A. Remijan, "Green bank telescope observations of interstellar glycolaldehyde: low-temperature sugar," *The Astrophysical Journal*, **613**, L45 (2004).

[31] P. F. Goldsmith and W. D. Langer, "Population diagram analysis of molecular line emission," *Astrophys. J.*, **517**, 209 (1999).

[32] M. Womack, L. M. Ziurys, and S. Wyckoff, "Estimates of N_2 abundances in dense molecular clouds," *Astrophysical Journal*, **393**, 188–192 (1992).

[33] N. A. Patel, K. H. Young, C. A. Gottlieb, P. Thaddeus, R. W. Wilson et al., "An Interferometric Spectral-line Survey of IRC+10216 in the 345 GHz Band," *The Astrophysical Journal Supplement Series*, **193**, 17 (2011).

[34] J. Cernicharo, L. B. F. M. Waters, L. Decin, P. Encrenaz, A. G. G. M. Tielens et al., "A high-resolution line survey of IRC+10216 with Herschel/HIFI," *A&A*, **521**, L8 (2010).

[35] S. G. Lias, J. E. Bartmess, J. F. Liebman, J. L. Holmes, R. D. Levin et al., "Gas-phase ion and neutral thermochemistry," *JOURNAL OF PHYSICAL AND CHEMICAL REFERENCE DATA*, **17**, 1–861 (1988).

[36] D. E. Woon, "Modeling gas-grain chemistry with quantum chemical cluster calculations. I. Heterogeneous hydrogenation of CO and H_2CO on icy grain mantles," *Astrophys. J.*, **569**, 541 (2002).

[37] O. Schnepp and K. Dressler, "Photolysis of Ammonia in a Solid Matrix at Low Temperatures," *The Journal of chemical physics*, **32**, 1682 (1960).

[38] Y. Miao, D. M. Mehringer, Y.-J. Kuan, and L. E. Snyder, "Complex molecules in Sagittarius B2(N): The importance of grain chemistry," *Astrophysical Journal*, **445**, L59–L62 (1995).

[39] M. A. Requena-Torres, J. Martin-Pintado, A. Rodríguez-Franco, S. Martín, N. J. Rodríguez-Fernández et al., "Organic molecules in the Galactic center," *A&A*, **455**, 971–985 (2006).

[40] P. Boulet, F. Gilardoni, J. Weber, H. Chermette, and Y. Ellinger, "Theoretical study of interstellar hydroxylamine chemistry: protonation and proton transfer mediated by H3+." *Chemical Physics*, **244**, 163–174 (1999).

[41] F. Angelelli, M. Aschi, F. Cacace, F. Pepi, and G. de Petris, "Gas-Phase Reactivity of Hydroxylamine toward Charged Electrophiles. A Mass Spectrometric and Computational Study of the Protonation and Methylation of H2NOH," *The Journal of Physical Chemistry*, **99**, 6551–6556 (1995).

[42] P. Pérez and R. Contreras, "A theoretical analysis of the gas-phase protonation of hydroxylamine, methyl-derivatives and aliphatic amino acids," *Chemical Physics Letters*, **293**, 239–244 (1998).

[43] L. Largo, V. M. Rayon, C. Barrientos, A. Largo, and P. Redondo, "Chemical Physics Letters," *Chemical Physics Letters*, **476**, 174–177 (2009).

[44] D. M. Mehringer, L. E. Snyder, Y. Miao, and F. J. Lovas, "Detection and confirmation of interstellar acetic acid," *The Astrophysical Journal Letters*, **480**, L71 (1997).

[45] B. A. McGuire, P. B. Carroll, R. A. Loomis, G. A. Blake, J. M. Hollis et al., "A search for l-C_3H^+ and l-C_3H in Sgr B2(N), Sgr B2(OH), and the dark cloud TMC-1," *The Astrophysical Journal*, **774**, 56 (2013).

[46] B. A. McGuire, P. B. Carroll, P. Gratier, V. Guzmán, J. Pety et al., "An observational investigation of the identity of B11244 (l-C_3H^+/C_3H^-)," *The Astrophysical Journal*, **783**, 36 (2014).

[47] B. A. McGuire, P. B. Carroll, J. L. I. Sanders, S. L. Widicus Weaver, G. A. Blake et al., "A CSO search for l-C_3H^+: detection in the Orion Bar PDR," *Monthly Notices of the Royal Astronomical Society*, **442**, 2901–2908 (2014).

[48] J. Pety, P. Gratier, V. Guzmán, E. Roueff, M. Gerin et al., "The IRAM-30 m line survey of the Horsehead PDR," *A&A*, **548**, A68 (2012).

[49] S. Ikuta, "An ab initio MO study on structures and energetics of C_3H^-, C_3H, and C_3H^+," *The Journal of chemical physics*, **106**, 4536 (1997).

[50] J. Le Bourlot, F. Le Petit, C. Pinto, E. Roueff, and F. Roy, "Surface chemistry in the interstellar medium," *A&A*, **541**, A76 (2012).

[51] F. Le Petit, C. Nehmé, J. Le Bourlot, and E. Roueff, "A model for atomic and molecular interstellar gas: The Meudon PDR code," *The Astrophysical Journal Supplement Series*, **164**, 506 (2006).

[52] B. E. Turner, E. Herbst, and R. Terzieva, "The physics and chemistry of small translucent molecular clouds. XIII. The basic hydrocarbon chemistry," *The Astrophysical Journal Supplement Series*, **126**, 427 (2000).

[53] V. Wakelam, I. W. M. Smith, E. Herbst, J. Troe, W. Geppert et al., "Reaction Networks for Interstellar Chemical Modelling: Improvements and Challenges," *Space Science Reviews*, **156**, 13–72 (2010).

[54] A. Fuente, A. Rodr guez Franco, S. Garc a Burillo, J. Mart n Pintado, and J. H. Black, "Observational study of reactive ions and radicals in PDRs," *A&A*, **406**, 899–913 (2003).

[55] D. Teyssier, D. Foss, M. Gerin, J. Pety, A. Abergel et al., "Carbon budget and carbon chemistry in Photon Dominated Regions," *A&A*, **417**, 135–149 (2004).

[56] J. Pety, D. Teyssier, D. Fossé, M. Gerin, E. Roueff et al., "Are PAHs precursors of small hydrocarbons in photo-dissociation regions? The Horsehead case," *A&A*, **435**, 885–899 (2005).

[57] X. Huang, R. C. Fortenberry, and T. J. Lee, "Spectroscopic constants and vibrational frequencies for l-C_3H^+ and isotopologues from highly accurate quartic force fields: the detection of l-C_3H^+in the Horsehead Nebula PDR questioned," *The Astrophysical Journal*, **768**, L25 (2013).

[58] R. C. Fortenberry, X. Huang, T. D. Crawford, and T. J. Lee, "High-accuracy quartic force field calculations for the spectroscopic constants and vibrational frequencies of 1_1A l-C_3H^-: A possible link to lines observed in the Horsehead Nebula photodissociation region," *The Astrophysical Journal*, **772**, 39 (2013).

[59] T. Pino, M. Tulej, F. Guthe, M. Pachkov, and J. P. Maier, "Photodetachment spectroscopy of the C2nH-(n= 2-4) anions in the vicinity of their electron detachment threshold," *Journal of Chemical Physics*, **116**, 6126–6131 (2002).

[60] S. Brünken, L. Kluge, A. Stoffels, O. Asvany, and S. Schlemmer, "Laboratory rotational spectrum of l-C_3H^+ and confirmation of its astronomical detection," *The Astrophysical Journal*, **783**, L4 (2014).

[61] P. Botschwina, C. Stein, P. Sebald, B. Schröder, and R. Oswald, "Strong theoretical support for the assignment of B11244 to l-C_3H^+," *Astrophysical Journal*, **787**, 72 (2014).

[62] D. Buhl and L. E. Snyder, "Unidentified Interstellar Microwave Line," *Nature*, **228**, 267–269 (1970).

[63] R. C. Woods, T. A. Dixon, R. J. Saykally, and P. G. Szanto, "Laboratory microwave spectrum of HCO^+," *Physical Review Letters*, **35**, 1269–1272 (1975).

[64] W. Klemperer, "Carrier of the interstellar 89.190 GHz line," *Nautre*, **227**, 1230 (1970).

[65] S. Green, J. A. J. Montgomery, and P. Thaddeus, "Tentative identification of U93.174 as the molecular ion N_2H^+," *Astrophysical Journal*, **193**, L89–L91 (1974).

[66] P. Thaddeus and B. E. Turner, "Confirmation of interstellar N_2H^+," *Astrophysical Journal*, **201**, L25–L26 (1975).

[67] B. E. Turner, "U93.174 - A new interstellar line with quadrupole hyperfine splitting," *Astrophysical Journal*, **193**, L83–L87 (1974).

[68] R. J. Saykally, T. A. Dixon, T. G. Anderson, P. G. Szanto, and R. C. Woods, "Laboratory microwave spectrum and rest frequencies of the N_2H^+ ion," *Astrophysical Journal Letters v.205*, **205**, L101 (1976).

[69] M. Guélin and P. Thaddeus, "Tentative detection of the C_3N radical," *Astrophysical Journal Letters*, **212**, L81 (1977).

[70] M. Guélin, S. Green, and P. Thaddeus, "Detection of the C_4H radical toward IRC+10216," *Astrophysical Journal*, **224**, L27–L30 (1978).

[71] S. Wilson and S. Green, "Theoretical study of the butadiynyl and cyanoethynyl radicals - Support for the identification of C_3N in IRC+10216," *Astrophysical Journal*, **212**, L87–L90 (1977).

[72] C. A. Gottlieb, E. W. Gottlieb, P. Thaddeus, and H. Kawamura, "Laboratory detection of the C_3N an C_4H free radicals," *Astrophysical Journal*, **275**, 916–921 (1983).

[73] J. Cernicharo, M. Guélin, M. Agúndez, M. C. McCarthy, and P. Thaddeus, "Detection of C_5N and vibrationally excited C_6H in IRC+10216," *The Astrophysical Journal*, **688**, L83 (2008).

[74] P. Botschwina and R. Oswald, "Carbon chains of type $C_{2n+1}N$ (n=2–6): A theoretical study of potential interstellar anions," *The Journal of chemical physics*, **129**, 044305 (2008).

[75] J. L. Neill, M. T. Muckle, D. P. Zaleski, A. L. Steber, B. H. Pate et al., "Laboratory and tentative interstellar detection of *trans*-methyl formate using the publicly available Green Bank Telescope PRIMOS Survey," *The Astrophysical Journal*, **755**, 153 (2012).

[76] A. J. Remijan, D. P. Leigh, A. J. Markwick-Kemper, and B. E. Turner, "Complete 2mm Spectral Line Survey (130-170 GHz) of Sgr B2N, Sgr B2OH, IRC +10216, Orion (KL), Orion-S, W51M, and W3(IRS5)," *ArXiv e-prints* (2008).

[77] B. A. McGuire, R. A. Loomis, C. M. Charness, J. F. Corby, G. A. Blake et al., "Interstellar carbodiimide (HNCNH): a new astronomical detection from the GBT PRIMOS survey via maser emission features," *The Astrophysical Journal*, **758**, L33 (2012).

[78] N. Kaifu, M. Ohishi, K. Kawaguchi, S. Saito, S. Yamamoto et al., "A 8.8–50GHz Complete Spectral Line Survey toward TMC-1 I. Survey Data," *Publications of the Astronomical Society of Japan*, **56**, 69–173 (2004).

[79] P. Thaddeus, C. A. Gottlieb, Å. Hjalmarson, L. Johansson, W. M. Irvine et al., "Astronomical identification of the C_3H radical," *Astrophys. J.*, **294**, L49–L53 (1985).

[80] C. A. Gottlieb, E. W. Gottlieb, P. Thaddeus, and J. M. Vrtilek, "The rotational spectrum of the C_3H radical," *Astrophys. J.*, **303**, 446–450 (1986).

[81] A. J. Remijan, J. M. Hollis, F. J. Lovas, W. D. Stork, P. R. Jewell et al., "Detection of interstellar cyanoformaldehyde (CNCHO)," *Astrophysical Journal Letters*, **675**, L85–L88 (2008).

[82] J. M. Hollis, A. J. Remijan, P. R. Jewell, and F. J. Lovas, "Cyclopropenone ($c$$H_2C_3O$): a new interstellar ring molecule," *The Astrophysical Journal*, **642**, 933–939 (2006).

[83] S. V. Kalenskii, V. I. Slysh, P. F. Goldsmith, and L. E. Johansson, "A 4-6 GHz Spectral Scan and 8-10 GHz Observations of the Dark Cloud TMC-1," *Astrophys. J.*, **610**, 329 (2004).

[84] H. M. Pickett, "The fitting and prediction of vibration-rotation spectra with spin interactions," *Journal of Molecular Spectroscopy*, **148**, 371–377 (1991).

[85] B. N. Taylor and C. E. Kuyatt, "Guidelines for Evaluating and Expressing the Uncertainty of NIST Measurement Results," *NIST Technical Note 1297* (1994).

[86] V. G. Anicich and W. T. J. Huntress, "A survey of bimolecular ion-molecule reactions for use in modeling the chemistry of planetary atmospheres, cometary comae, and interstellar clouds," *Astrophysical Journal Supplement Series*, **62**, 553–672 (1986).

[87] I. Savić and D. Gerlich, "Temperature variable ion trap studies of $C_3H_n{}^+$ with H_2 and HD," *Phys. Chem. Chem. Phys.*, **7**, 1026 (2005).

[88] M. C. McCarthy, C. A. Gottlieb, H. Gupta, and P. Thaddeus, "Laboratory and astronomical identification of the negative molecular ion C_6H^{--}," *The Astrophysical Journal*, **652**, L141 (2006).

[89] M. Bogey, C. Demuynck, and J. L. Destombes, "Laboratory detection of the protonated carbon dioxide by submillimeter wave spectroscopy," *Astronomy & Astrophysics*, **138**, L11 (1984).

[90] S. R. Polo, "Energy Levels of Slightly Asymmetric Top Molecules," *Canadian Journal of Physics*, **35**, 880–885 (1957).

[91] H. Gupta, C. A. Gottlieb, M. C. McCarthy, and P. Thaddeus, "A survey of C_4H, C_6H, and C_6H^{--} with the Green Bank Telescope," *The Astrophysical Journal*, **691**, 1494–1500 (2009).

[92] M. A. Cordiner, J. V. Buckle, E. S. Wirström, A. O. H. Olofsson, and S. B. Charnley, "On the ubiquity of molecular anions in the dense interstellar medium," *The Astrophysical Journal*, **770**, 48 (2013).

[93] E. Herbst and Y. Osamura, "Calculations on the formation rates and mechanisms for CnH anions in interstellar and circumstellar media," *Astrophys. J.*, **679**, 1670 (2008).

[94] F. Güthe, M. Tulej, M. V. Pachkov, and J. P. Maier, "Photodetachment spectrum of l-$C_3H_2{}^-$: The role of dipole bound states for electron attachment in interstellar clouds," *Astrophys. J.*, **555**, 466 (2001).

[95] F. Carelli, M. Satta, T. Grassi, and F. A. Gianturco, "Carbon-rich molecular chains in protoplanetary and planetary atmospheres: Quantum mechanisms and electron attachment rates for anion formation," *The Astrophysical Journal*, **774**, 97 (2013).

[96] M. Agúndez, J. Cernicharo, M. Guélin, M. Gerin, M. C. McCarthy et al., "Search for anions in molecular sources: C 4H -detection in L1527," *A&A*, **478**, L19–L22 (2008).

[97] J. L. Neill, E. A. Bergin, D. C. Lis, P. Schilke, N. R. Crockett et al., "Herschel observations of EXtraordinary Sources: Analysis of the full Herschel/HIFI molecular line survey of Sagittarius B2(N)," *Astrophysical Journal*, **In Revision** (2014).

[98] M. Gerin, M. De Luca, J. Black, J. R. Goicoechea, E. Herbst et al., "Interstellar OH^+, H_2O^+ and H_3O^+ along the sight-line to G10.6–0.4," *A&A*, **518**, L110 (2010).

[99] B. Godard, E. Falgarone, M. Gerin, P. Hily-Blant, and M. De Luca, "Molecular absorption lines toward star-forming regions: a comparative study of HCO^+, HNC, HCN, and CN," *A&A*, **520**, A20 (2010).

[100] H. Gupta, S. Brünken, F. Tamassia, C. A. Gottlieb, M. C. McCarthy et al., "Totational spectra of the carbon chain negative ions C_4H^{--} and C_8H^{--}," *The Astrophysical Journal*, **655**, L57 (2007).

[101] J. Cernicharo, M. Guélin, M. Agúndez, K. Kawaguchi, M. McCarthy et al., "Astronomical detection of C_4H^-, the second interstellar anion," *A&A*, **467**, L37–L40 (2007).

[102] A. J. Remijan, J. M. Hollis, F. J. Lovas, M. A. Cordiner, T. J. Millar et al., "Detection of $C_8H^{--}$and comparison with C_8H toward IRC+10216," *The Astrophysical Journal*, **664**, L47 (2007).

[103] M. Agúndez, J. Cernicharo, M. Guélin, C. Kahane, E. Roueff et al., "Astronomical identification of CN^-, the smallest observed molecular anion," *A&A*, **517**, L2 (2010).

[104] P. Thaddeus, C. A. Gottlieb, H. Gupta, S. Brünken, M. C. McCarthy et al., "Laboratory and astronomical detection of the negative molecular ion C_3N," *Astrophys. J.*, **677**, 1132 (2008).

[105] S. S. Kumar, D. Hauser, R. Jindra, T. Best, Š. Roučka et al., "Photodetachment as a destruction mechanism for CN^- and C_3N^- anions in circumstellar envelopes," *The Astrophysical Journal*, **776**, 25 (2013).

[106] B. T. Draine, "Photoelectric heating of interstellar gas," *The Astrophysical Journal Supplement Series*, **36**, 595 (1978).

[107] E. Habart, A. Abergel, C. M. Walmsley, D. Teyssier, and J. Pety, "Density structure of the Horsehead nebula photo-dissociation region," *A&A*, **437**, 177–188 (2005).

[108] G. A. Blake, E. C. Sutton, C. R. Masson, and T. G. Phillips, "Molecular abundances in OMC-1 - The chemical composition of interstellar molecular clouds and the influence of massive star formation," *Astrophys. J.*, **315**, 621–645 (1987).

[109] J. R. Goicoechea, J. Pety, M. Gerin, P. Hily-Blant, and J. Le Bourlot, "The ionization fraction gradient across the Horsehead edge: an archetype for molecular clouds," *A&A*, **498**, 771–783 (2009).

[110] B. A. McGuire, P. B. Carroll, and A. J. Remijan, "A CSO broadband spectral line survey of Sgr B2(N)-LMH from 260 - 286 GHz," *ArXiv e-prints*, **astro-ph.GA** (2013).

[111] A. B. Kaul, B. Bumble, K. A. Lee, H. G. LeDuc, F. Rice et al., "Fabrication of wide-IF 200–300GHz superconductor–insulator–superconductor mixers with suspended metal beam leads formed on silicon-on-insulator," *Journal of Vacuum Science & Technology B: Microelectronics and Nanometer Structures*, **22**, 2417 (2004).

[112] F. Rice, M. Sumner, J. Zmuidzinas, R. Hu, H. G. LeDuc et al., "SIS mixer design for a broadband millimeter spectrometer suitable for rapid line surveys and redshift determinations," **4855**, 301–311 (2003).

[113] J. W. Kooi, A. Kovacs, M. C. Sumner, G. Chattopadhyay, R. Ceria et al., "A 275-425-GHz tunerless waveguide receiver based on AlN-Barrier SIS technology," *IEEE Transactions on Microwave Theory and Techniques*, **55**, 2086–2096.

[114] S. Martín, J. Martin-Pintado, M. Montero-Castaño, P. T. P. Ho, and R. Blundell, "Surviving the hole," *A&A*, **539**, A29 (2012).

[115] W. Chau, Y. Zhang, J.-i. Nakashima, S. Deguchi, and S. Kwok, "Molecular line observations of the carbon-rich circumstellar envelope CIT 6 at 7 mm wavelengths," *The Astrophysical Journal*, **760**, 66 (2012).

[116] Y. Morisawa, H. Hoshina, Y. Kato, Z. Simizu, S. Kuma et al., "Search for CCH^-, NCO^-, and NCS^-negative ions in molecular clouds," *Publications of the Astronomical Society of Japan*, **57**, 325–334 (2005).

[117] M. A. Smith, S. v. Schlemmer, J. von Richthofen, and D. Gerlich, "$HOC^+ + H_2$ isomerization rate at 25 K: Implications for the observed $[HCO^+]/[HOC^+]$ ratios in the interstellar medium," *The Astrophysical Journal Letters*, **578**, L87 (2002).

[118] H. Liszt, R. Lucas, and J. H. Black, "The abundance of HOC^+ in diffuse clouds," *A&A*, **428**, 117–120 (2004).

[119] D. Ginard, M. González García, A. Fuente, J. Cernicharo, T. Alonso-Albi et al., "Spectral line survey of the ultracompact HII region Monoceros R2," *A&A*, **543**, A27 (2012).

[120] S. Martín, J. Martin-Pintado, and S. Viti, "Photodissociation chemistry footprints in the starburst galaxy NGC 253," *The Astrophysical Journal Letters*, **706**, 1323–1330 (2009).

[121] A. Fuente, S. García-Burillo, M. Gerin, D. Teyssier, A. Usero et al., "Photon-dominated chemistry in the nucleus of M82: Widespread HOC^+ emission in the inner 650 parsec disk," *The Astrophysical Journal Letters*, **619**, L155 (2005).

[122] F. Duvernay, T. Chiavassa, F. Borget, and J.-P. Aycard, "Experimental Study of WaterIce Catalyzed Thermal Isomerization of Cyanamide into Carbodiimide: Implication for Prebiotic Chemistry," *Journal of the American Chemical Society*, **126**, 7772–7773 (2004).

[123] F. Tordini, A. Bencini, M. Bruschi, L. De Gioia, G. Zampella et al., "Theoretical study of hydration of cyanamide and carbodiimide," *The Journal of Physical Chemistry A*, **107**, 1188–1196 (2003).

[124] B. E. Turner, H. S. Liszt, N. Kaifu, and A. G. Kisliakov, "Microwave detection of interstellar cyanamide," *Astrophysical Journal*, **201**, L149–L152 (1975).

[125] T. L. Allen, J. D. Goddard, and H. F. Schaefer, "A possible role for triplet H2CN+ isomers in the formation of HCN and HNC in interstellar clouds," *The Journal of chemical physics*, **73**, 3255 (1980).

[126] F. Duvernay, T. Chiavassa, F. Borget, and J.-P. Aycard, "Carbodiimide production from cyanamide by UV irradiation and thermal reaction on amorphous water ice," *Journal of Physical Chemistry*, **109**, 603–608 (2005).

[127] M. Birk, M. Winnewisser, and E. A. Cohen, "The rotational-torsional spectrum of carbodiimide - a probe for the unusual dynamics," *Journal of Molecular Spectroscopy*, **136**, 402–445 (1989).

[128] V. Wagener, M. Winnewisser, and M. Bellini, "The $^R\mathrm{Q}_{Ka}$, branches of carbodiimide, HNCNH, between 1.8 and 3.3 THz," *Journal of Molecular Spectroscopy*, **170**, 323–334 (1995).

[129] W. Jabs, M. Winnewisser, S. Belov, T. Klaus, and G. Winnewisser, "The $^r\mathrm{Q}_1$ branch of carbodiimide, HNCNH, at 1.1 THz," *Chemical Physics*, **225**, 77–91 (1997).

[130] B. L. Ulich and R. W. Haas, "Absolute calibration of millimeter-wavelength spectral lines." *Astrophysical Journal*, **30**, 247–258 (1976).

[131] S. Wang, E. A. Bergin, N. R. Crockett, P. F. Goldsmith, D. C. Lis et al., "Herschelobservations of EXtra-Ordinary Sources (HEXOS): Methanol as a probe of physical conditions in Orion KL," *A&A*, **527**, A95 (2011).

[132] B. Tercero, J. Cernicharo, J. R. Pardo, and J. R. Goicoechea, "A line confusion limited millimeter survey of OrionKL I. Sulfur carbon chains," *A&A*, **517**, A96 (2010).

[133] J. R. Forster, W. M. Goss, T. L. Wilson, D. Downes, and H. R. Dickel, "A formaldehyde maser in NGC 7538," *Astronomy & Astrophysics*, **84**, L1–L3 (1980).

[134] R. A. Gaume, K. J. Johnston, H. A. Nguyen, T. L. Wilson, H. R. Dickel et al., "NGC 7538 IRS 1 - Subarcsecond resolution recombination line and (N-15)H3 maser observations," *Astrophysical Journal*, **376**, 608–614 (1991).

[135] S. Ioppolo, B. A. McGuire, M. A. Allodi, and G. A. Blake, "THz and mid-IR spectroscopy of interstellar ice analogs: methyl and carboxylic acid groups," *Faraday Discussions*, – (2014).

[136] M. A. Allodi, S. Ioppolo, M. J. Kelley, B. A. McGuire, and G. A. Blake, "The structure and dynamics of carbon dioxide and water containing ices investigated via THz and mid-IR spectroscopy," *Phys. Chem. Chem. Phys.*, **16**, 3442 (2014).

[137] A. C. Boogert and P. Ehrenfreund, "Interstellar ices," *arXiv preprint astro-ph/0311163* (2003).

[138] J. E. Bertie, "Far-Infrared Spectra of the Ices," *Applied Spectroscopy*, **22**, 634–640 (1968).

[139] J. E. Bertie and S. M. Jacobs, "Far-infrared absorption by ices Ih and Ic at 4.3 °K and the powder diffraction pattern of ice Ic," *Journal of Chemical Physics*, **67**, 2445–2448 (1977).

[140] M. H. Moore and R. L. Hudson, "Far-infrared spectra of cosmic-type pure and mixed ices," *Astronomy and Astrophysics Suppl. 103*, **103**, 45–56 (1994).

[141] M. H. Moore and R. L. Hudson, "Far-infrared spectral studies of phase changes in water ice induced by proton irradiation," *Astrophysical Journal*, **401**, 353–360 (1992).

[142] R. L. Hudson and M. H. Moore, "FAR-IR spectral changes accompanying proton irradiation of solids of astrochemical interest," *Radiation Physics and Chemistry*, **45**, 779–789 (1995).

[143] D. J. Cook and R. M. Hochstrasser, "Intense terahertz pulses by four-wave rectification in air," *Optics letters*, **25**, 1210–1212 (2000).

[144] X. Xie, J. Dai, and X. C. Zhang, "Coherent Control of THz Wave Generation in Ambient Air," *Physical Review Letters*, **96**, 075005 (2006).

[145] K.-Y. Kim, J. H. Glownia, A. J. Taylor, and G. Rodriguez, "Terahertz emission from ultrafast ionizing air in symmetry-broken laser fields," *Optics Express*, **15**, 4577–4584 (2007).

[146] K. Y. Kim, A. J. Taylor, J. H. Glownia, and G. Rodriguez, "Coherent control of terahertz supercontinuum generation in ultrafast laser–gas interactions," *Nat Photon*, **2**, 605–609 (2008).

[147] M. Clerici, M. Peccianti, B. E. Schmidt, L. Caspani, M. Shalaby et al., "Wavelength Scaling of Terahertz Generation by Gas Ionization," *Physical Review Letters*, **110**, 253901 (2013).

[148] D. H. Auston, A. M. Johnson, P. R. Smith, and J. C. Bean, "Picosecond optoelectronic detection, sampling, and correlation measurements in amorphous semiconductors," *Applied Physics Letters*, **37**, 371 (1980).

[149] Q. Wu and X. C. Zhang, "Free-space electro-optic sampling of terahertz beams," *Applied Physics Letters*, **67**, 3523 (1995).

[150] R. B. Blackman and J. W. Tukey, *The Measurement of Power Spectra, from the Point of View of Communications Engineerings*, Dover (1959).

[151] J. O. Smith, *Mathematics of the Discrete Fourier Transform (DFT), with Audio Applications*, W3K Publishing, 2 ed. (2007).

[152] S. Krishnamurthy, R. Bansil, and J. Wiafe-Akenten, "Low-frequency Raman spectrum of supercooled water," *The Journal of chemical physics*, **79**, 5863 (1983).

[153] G. Profeta and S. Scandolo, "Far-infrared spectrum of ice Ih: A first-principles study," *Physical Review B*, **84**, 024103 (2011).

[154] J. E. Bertie, "Absorptivity of ice I in the range 4000–30 cm^1," *The Journal of chemical physics*, **50**, 4501 (1969).

[155] K. Kobashi and T. Kihara, "Molecular librations of solid CO2 under high pressure based on Kihara core potentials," *The Journal of chemical physics*, **72**, 3216 (1980).

[156] M. J. Frisch, G. W. Trucks, H. B. Schlegel, G. E. Scuseria, M. A. Robb et al., "Gaussian 09 Revision D.01," .

[157] C. J. Cramer, *Essentials of Computational Chemistry*, Wiley, 2 ed. (2004).

[158] J. A. Pople, A. P. Scott, M. W. Wong, and L. Radom, "scaling factors for obtaining fundamental vibrational frequencies and zero-point energies from HF/6–31G* and MP2/6–31G* harmonic frequencies," *Israel Journal of Chemistry*, **33**, 345–350 (1993).

[159] A. Belloche, K. M. Menten, C. Comito, H. S. P. Müller, P. Schilke et al., "Detection of amino acetonitrile in Sgr B2(N)," *A&A*, **482**, 179–196 (2008).

[160] D. N. Friedel, L. E. Snyder, B. E. Turner, and A. Remijan, "A Spectral Line Survey of Selected 3 Millimeter Bands toward Sagittarius B2(N-LMH) Using the National Radio Astronomy Observatory 12 Meter Radio Telescope and the Berkeley-Illinois-Maryland Association Array. I. The Observational Data," *The Astrophysical Journal*, **600**, 234–253 (2004).

[161] A. Nummelin, P. Bergman, Å. Hjalmarson, P. Friberg, W. M. Irvine et al., "A three-position spectral line survey of Sagittarius B2 between 218 and 263 GHz. I. The observational data," *The Astrophysical Journal Supplement Series*, **117**, 427 (1998).

[162] J. L. Neill, E. A. Bergin, D. C. Lis, T. G. Phillips, M. Emprechtinger et al., "Broadband analysis techniques for Herschel/HIFI spectral surveys of chemically rich star-forming regions," *Journal of Molecular Spectroscopy*, **280**, 150–154 (2012).

Appendix A

A CSO Broadband Spectral Line Survey of Sgr B2(N)-LMH from 260 - 286 GHz

The entirety of this appendix is reproduced from "A CSO broadband spectral line survey of Sgr B2(N)-LMH from 260 - 286 GHz," by B.A. McGuire et al., arXiv:1306.0927 (2013).

A.1 Abstract

Presented here are the results of a broadband spectral line survey of the Sgr B2(N) - LMH region from 260 - 286 GHz using the Caltech Submillimeter Observatory. The data were taken over the course of a single night (May 26, 2013) during the course of science testing of the remote observational capabilities of the facility. The data are freely available to public both as raw, double-side band observational data and as a minimally-reduced ascii spectrum. The procedural scripts used for the preliminary data reduction using CLASS are provided as well. The observational parameters and preliminary data reduction procedures are detailed. Finally, we provide instructions for accessing the data, as well as comment on the robustness of the preliminary reduction.

A.2 Introduction

Advances in the state-of-the-art during the last decade have made the acquisition of broadband, high-resolution, and high-sensitivity spectral line surveys a time-efficient process. These surveys have great staying power. By collecting data over a wide range in frequency space, rather than focusing on small windows around molecular transitions of interest, the data can be mined repeatedly for

Table A.1: Summary of spectral line surveys of Sgr B2(N)

Covered Frequencies	Facility	Reference
0.3 - 50 GHz	GBT	(see, e.g. [77])
80 - 116 GHz	IRAM 30-m	[159]
86 - 90 GHz 106 - 110 GHz	BIMA & NRAO 12-m	[160]
140 - 170 GHz	NRAO 12-m	[24][a]
202 - 218 GHz	IRAM 30-m	[159]
218 - 265 GHz	SEST	[161]
260 - 286 GHz	CSO	(This work)
480 - 1910 GHz	Herschel Space Telescope	[162]

a) Details of the observations and motivations can be found in [76]

GBT - Robert C. Byrd 100-m Green Bank Telescope
IRAM - Institut de Radioastronomique Millimétrique
BIMA - Berkeley-Illinois-Maryland Array
SEST - Swedish-ESO Submillimeter Telescope
CSO - Caltech Submillimeter Observatory

new molecular information as laboratory spectra become available. Perhaps the most studied target of these surveys is the galactic center source Sagittarius B2(N) (see Table A.1).

This work has been performed in the spirit of the **PR**ebiotic **I**nterstellar **MO**lecular **S**urvey (PRIMOS) project. The PRIMOS key project began in January of 2008, and observations continue to expand its frequency coverage. This project provides high-resolution, high-sensitivity spectra of the Sgr B2(N-LMH) complex centered at (J2000) $\alpha = 17^{\rm h}47^{\rm m}19^{\rm s}.8$, δ = -28°22′17″ . The PRIMOS project is providing reduced data to the public with no proprietary period. Here, we endeavor to do the same.

A.3 Observations

The data presented here towards of the Sgr B2(N-LMH) complex are centered at (J2000) α = $17^{h}47^{m}19^{s}.8$, δ = -28°22′17″ . The observations were conducted on May 26, 2013 at the Caltech Submillimeter Observatory as part of science testing of the facility's remote observational capabilities using the 8 GHz broadband 230 GHz receiver. Pointing solutions were acquired every 2 hours on average, with pointing offsets consistent with previous nights to within a few arcseconds. The data were obtained in position switching mode with an offset of 2°.

The 230 GHz receiver at the CSO is a double-side band (DSB) receiver. Thus, multiple IF settings are necessary for a reliable deconvolution to single-side band (SSB) spectra. For these observations, three rest frequencies, separated by ∼8 GHz, were observed with at least 5 IF settings. This provides at least 5 different rest- and image-frequency combinations for each observed frequency.[1] Several additional, deeper integrations were obtained at slightly different rest frequencies and IFs and have been included in this data set.

The data were processed by two FFTS spectrometers. The first provides 1 GHz of DSB coverage with a frequency resolution of 122 kHz. The second FFTS spectrometer provides two, 4-GHz windows of DSB coverage with a frequency resolution of 269 kHz.

A.4 Data Analysis

The complete, raw dataset and reduction scripts are accessible at:

`http://tracker.cv.nrao.edu/PRIMOS/CSO_260_290_Survery_Data/.`

The preliminary reduction is presented here, and is available in ascii format through the **S**pectral **Li**ne **S**earch **E**ngine (SLiSE) accessible at: `http://www.cv.nrao.edu/~aremijan/SLiSE/`.

The procedures used to clean, baseline-subtract, and deconvolve the data for the preliminary reduction presented here are given in plain text in Appendix A, and will be described here in detail.

The reduction was performed using the CLASS package of the GILDAS suite of programs.[2] The raw observational spectra are adjusted to a rest frequency corresponding to a V_{lsr} = +64 km/s. First, the FFTS1 data were Hanning-smoothed to ∼244 kHz, then both FFTS1 and FFTS2 data were resampled to a resolution of 300 kHz (0.33 km/s at 275 GHz). Next, noise spurs from the

[1] Necessarily less redundancy is obtained near the edges of the observations.
[2] http://www.iram.fr/IRAMFR/GILDAS

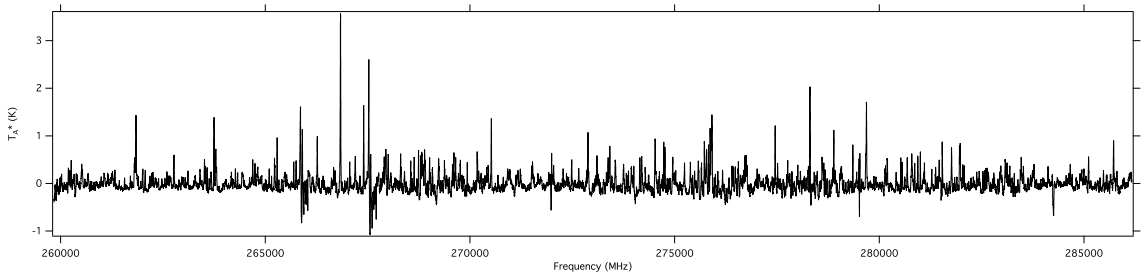

Figure A.1: Deconvolved and baseline-subtracted spectrum of Sgr B2(N) from 260 - 286 GHz.

spectrometers were removed and blanked. Finally, several scans were dropped from the record after a visual inspection revealed inconsistencies with the rest of the data set.

Continuum and baseline subtraction for spectral line observations of Sgr B2(N) is non-trivial. A cursory inspection of the DSB data reveals the spectra are likely confusion-limited, and virtually no baseline is visible. For the purposes of the preliminary reduction presented here, a third-order polynomial is fit to each spectrum and removed. This is discussed further below.

Finally, the spectra are deconvolved, allowing for intensity variations between sidebands. Because of the broad linewidths present in Sgr B2(N), the resulting spectrum is then smoothed twice more to a final resolution of 1.2 MHz (1.3 km/s at 275 GHz). This smoothed spectrum is presented in its entirety in Figure 1, and in 500 MHz-wide increments in Figures 2 - 53. The unsmoothed data have an RMS of $\sim$30 mK, while the smoothed data have an RMS of $\sim$15 mK.

A.5 Discussion

The preliminary reduction presented here is intended to serve as a "quick look" at the data. While it is likely a fairly faithful representation of the SSB spectrum, the result of the deconvolution is not unique, and interested users should exercise appropriate caution in its use. Here, we will discuss the limitations of this preliminary reduction, and provide strategies for mitigating them. These should also serve as a guide for those that wish to re-reduce the data themselves.

As discussed earlier, the robustness of the deconvolution relies heavily on having appropriate frequency sampling in the rest- and image-frequency domains for each observed frequency. While each frequency in the bulk of our observations have at least five settings, which should provide sufficient sampling, the edges of the observations do not. In particular, care should be taken when analyzing the first and last 1 GHz of data (i.e. 260 - 261 GHz and 285 - 286 GHz). While signals appearing in these regions are real, their assignment to the appropriate sideband is questionable.

To mitigate this, transitions from a molecule of interest should be identified in neighboring spectral windows or, in the case of the 260 - 261 GHz data, in the Nummelin et al. (1998) survey data.

The use of a third-order polynomial fit to the data to remove baselines is certainly not ideal. While simple and effective, this method suffers from sensitivity to large changes in the average intensity within a scan, for instance, due to an abnormally strong line. Further, the average intensity will be above the actual noise floor, with the result that the zero point of the intensity scale is somewhat higher than the noise floor. A visual inspection of the data reveals this offset is likely between 0.1 and 0.2 mK, and thus, the absolute intensities of the lines are expected to vary by at least this much (the relative intensities of the line peak to the surrounding baseline are likely much more robust).

Very bright lines can sometimes introduce ghosting artifacts into the SSB spectrum during deconvolution. Given that the brightest observed intensity in this spectrum is only $\sim$3 K (at 266.838 GHz [likely CH_3OH]), these ghosts are unlikely to be of any real concern; however, a meticulous reduction would remove the strongest signals from the spectrum prior to deconvolution, then manually stitch the signals back in afterwards. The trade-off is a slight increase in RMS noise in the image band corresponding to the removed line, as less data were available at that frequency during the deconvolution.

Finally, the resultant SSB spectrum was visually compared to the sum total of all DSB spectra. It was during this process that several scans were identified as inconsistent. In general, these were cases of 4 out of 5 settings at a particular frequency indicating the presence of a line in that sideband, while the fifth did not. The most common cause of this is bad lock in the receiver frequencies. While this visual inspection was thorough, due to the rough nature of this reduction, the interested user should take care to check the DSB spectra themselves against any particularly weak molecular signals. This is especially true for the identification of new molecular signals.

A more robust reduction and analysis is planned to follow in the coming months. Until then, interested users are encouraged to use (and re-reduce) the existing dataset as they see fit. We ask only that you cite our work as the data source, and please notify us by e-mail of any resulting publications or presentations. Those wishing for further observational or data-related details should contact the authors directly.

A.6 Spectra

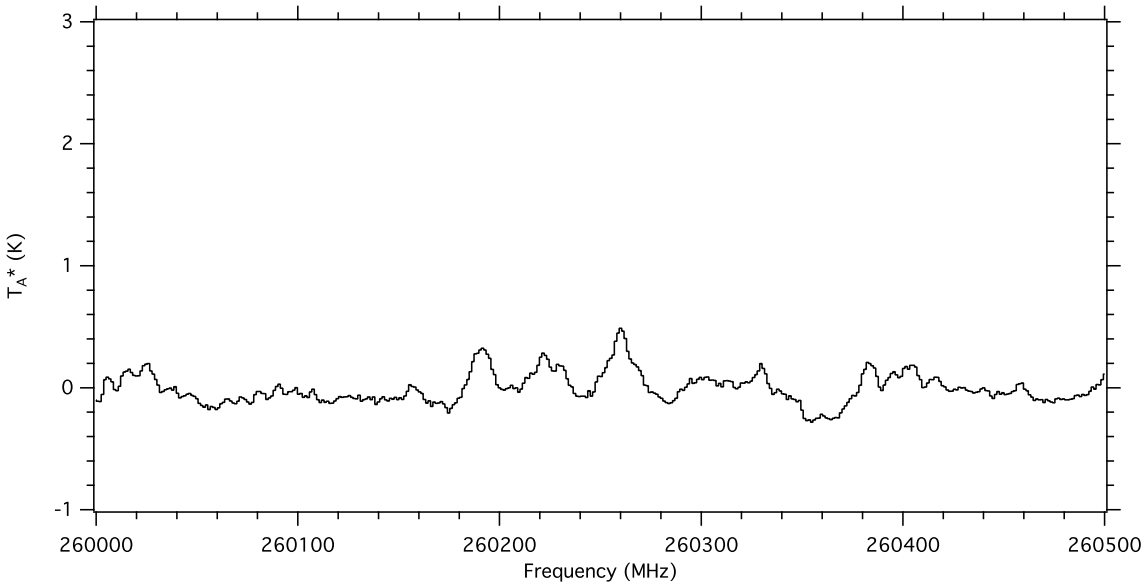

Figure A.2: Spectrum of Sgr B2(N) from 260.0 - 260.5 GHz

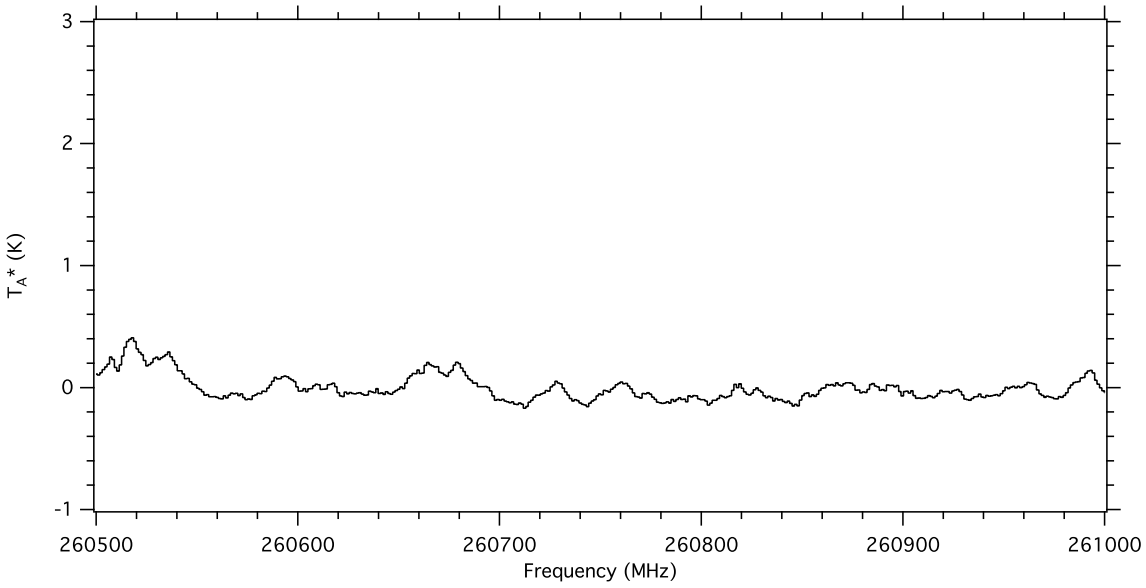

Figure A.3: Spectrum of Sgr B2(N) from 260.5 - 261.0 GHz

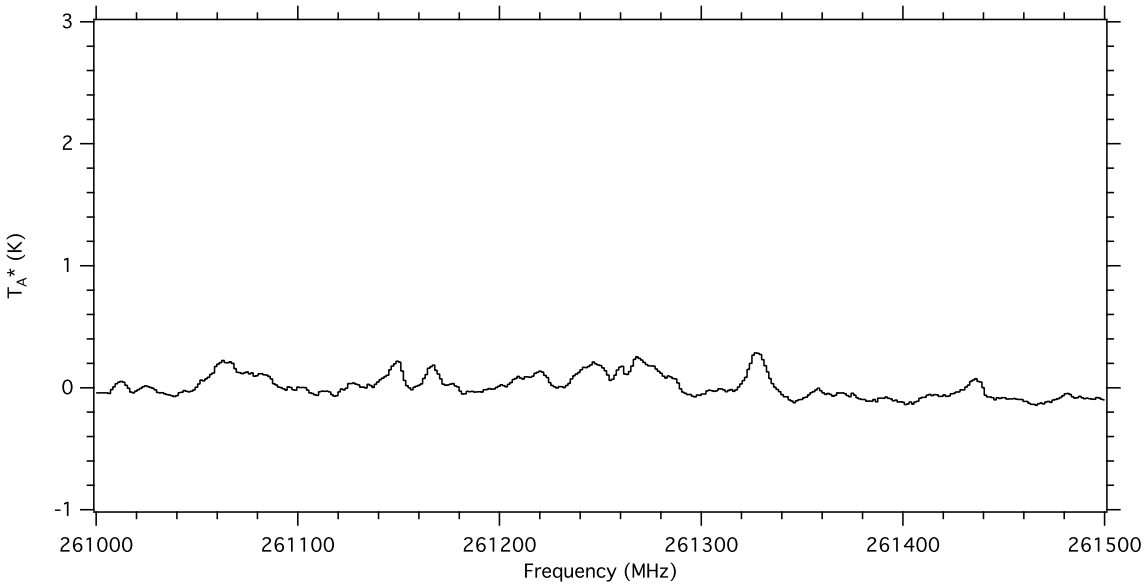

Figure A.4: Spectrum of Sgr B2(N) from 261.0 - 261.5 GHz

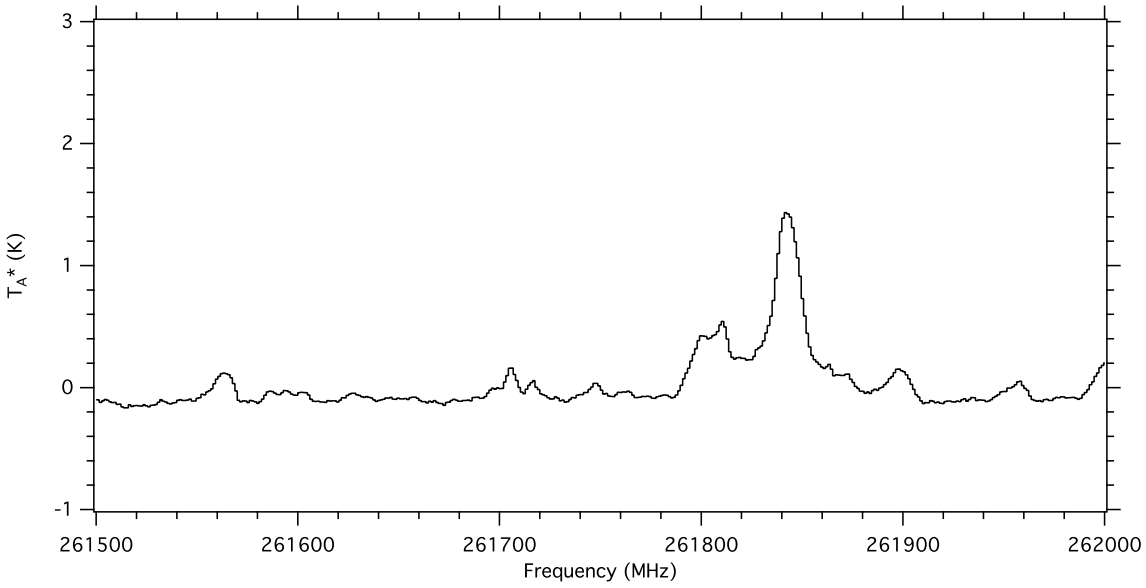

Figure A.5: Spectrum of Sgr B2(N) from 261.5 - 262.0 GHz

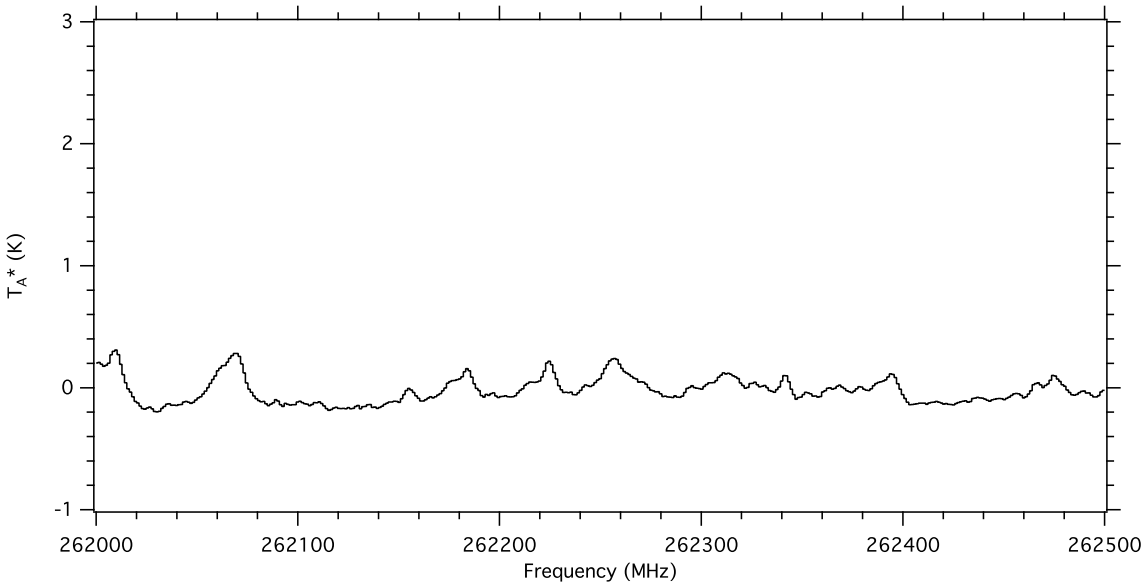

Figure A.6: Spectrum of Sgr B2(N) from 262.0 - 262.5 GHz

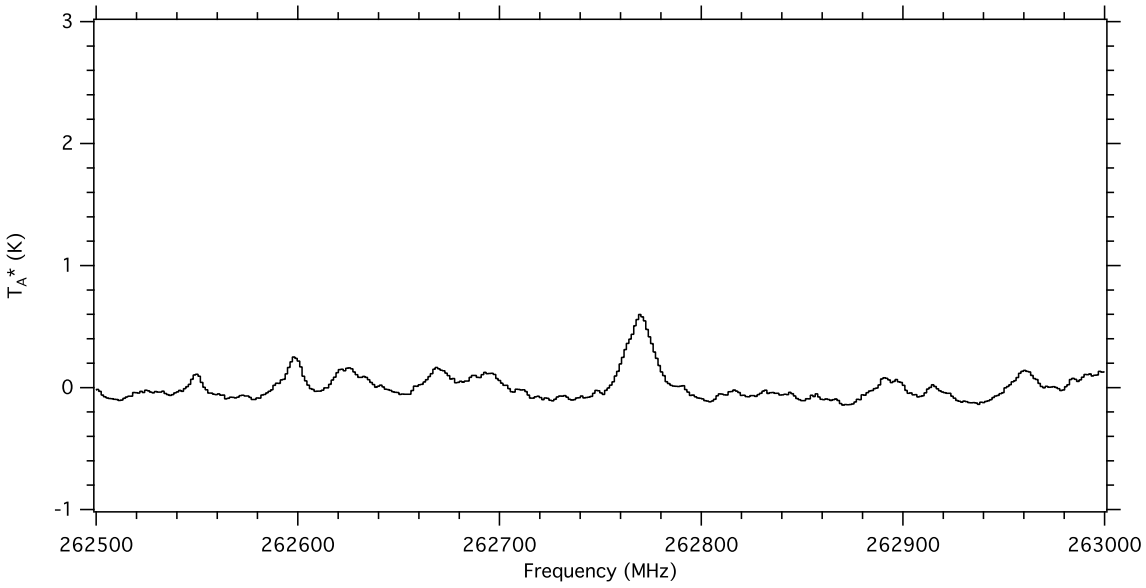

Figure A.7: Spectrum of Sgr B2(N) from 262.5 - 263.0 GHz

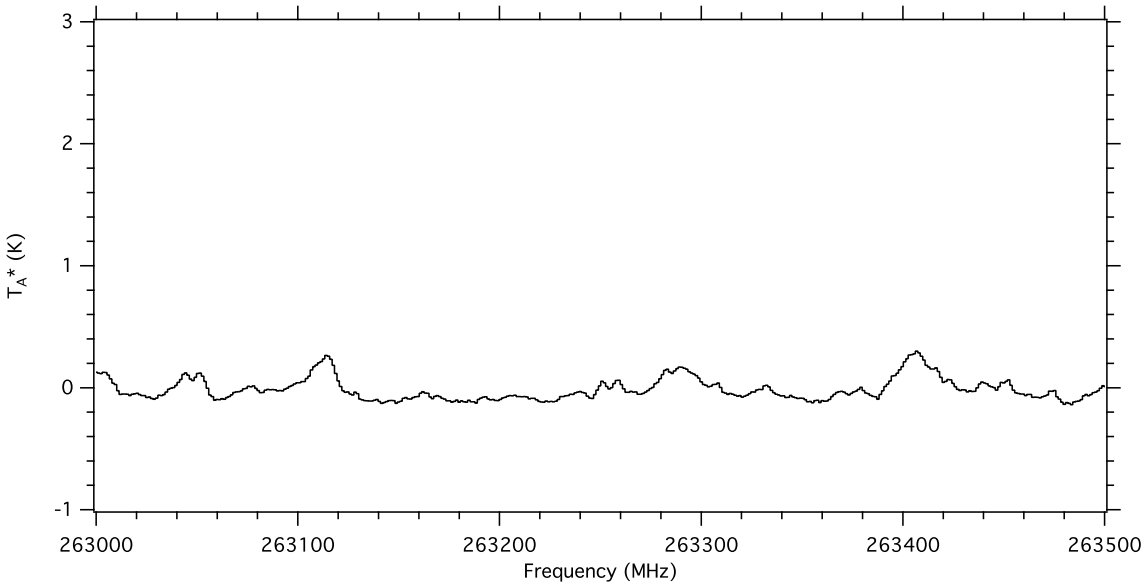

Figure A.8: Spectrum of Sgr B2(N) from 263.0 - 263.5 GHz

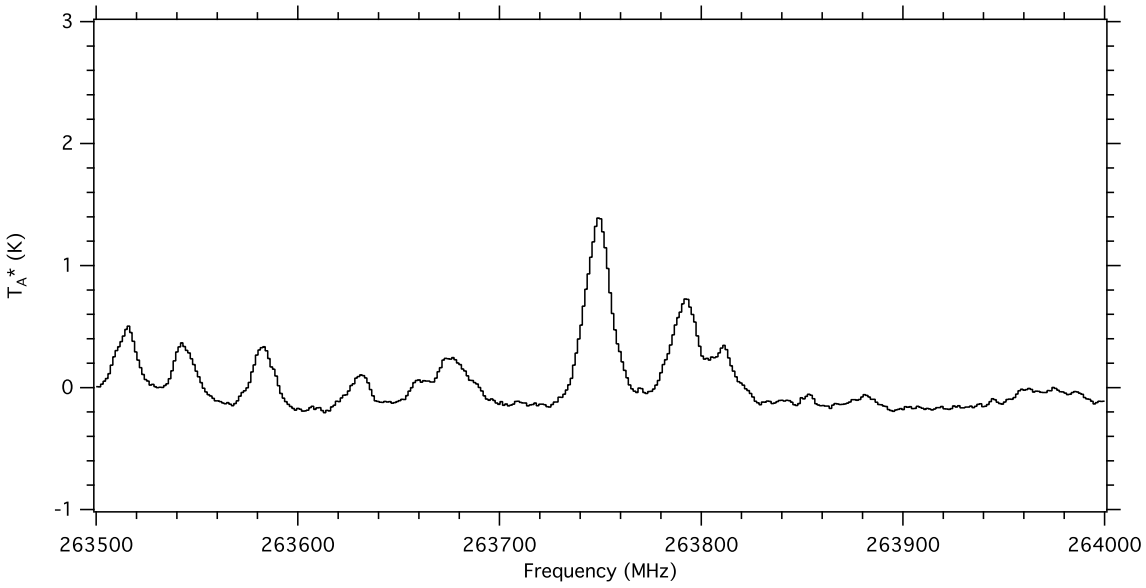

Figure A.9: Spectrum of Sgr B2(N) from 263.5 - 264.0 GHz

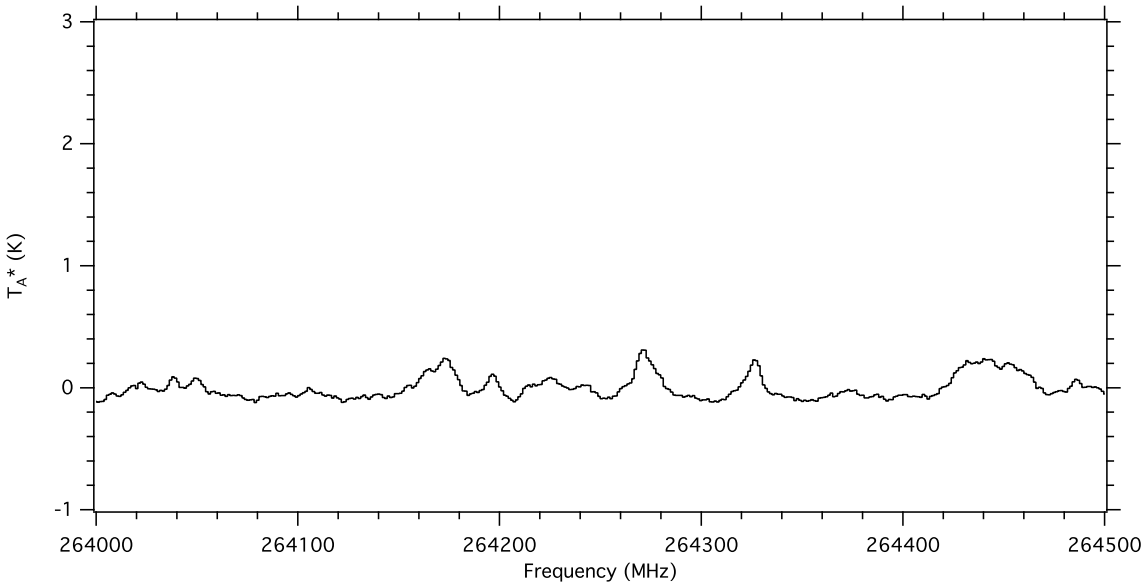

Figure A.10: Spectrum of Sgr B2(N) from 264.0 - 264.5 GHz

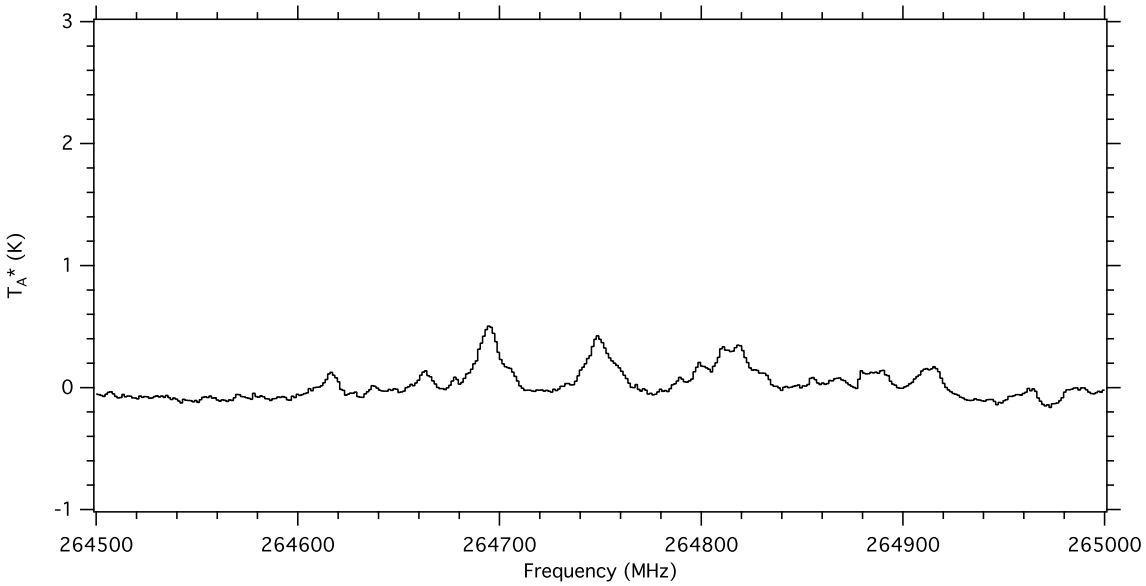

Figure A.11: Spectrum of Sgr B2(N) from 264.5 - 265.0 GHz

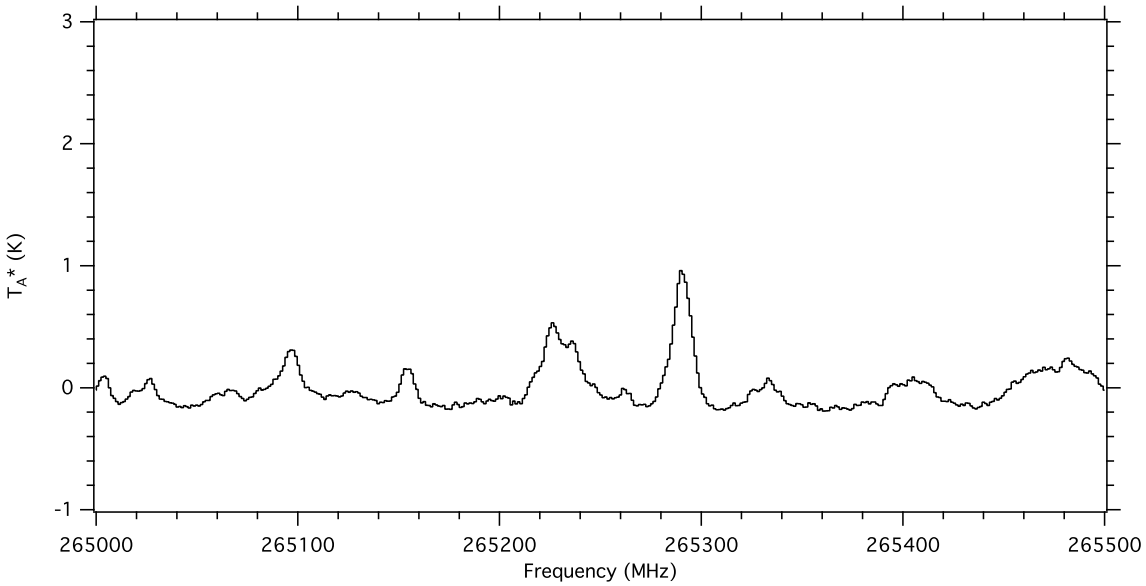

Figure A.12: Spectrum of Sgr B2(N) from 265.0 - 265.5 GHz

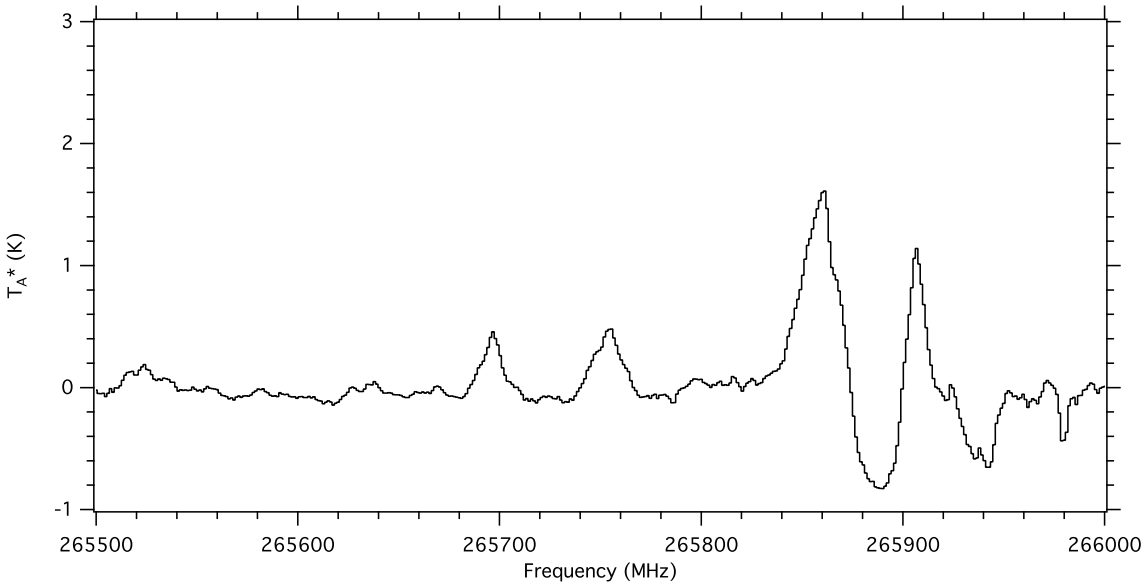

Figure A.13: Spectrum of Sgr B2(N) from 265.5 - 266.0 GHz

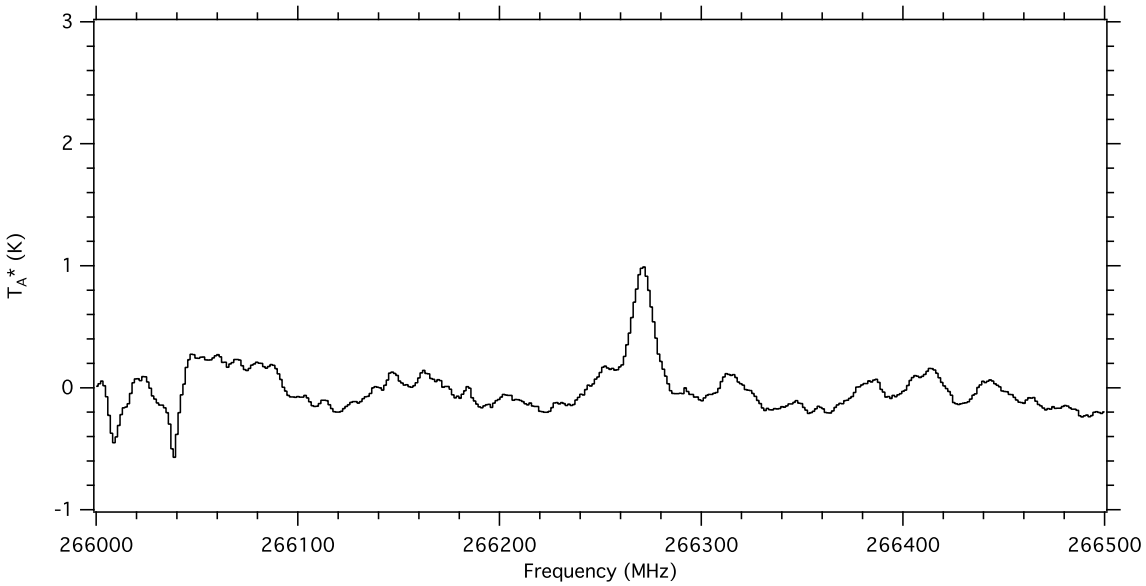

Figure A.14: Spectrum of Sgr B2(N) from 266.0 - 266.5 GHz

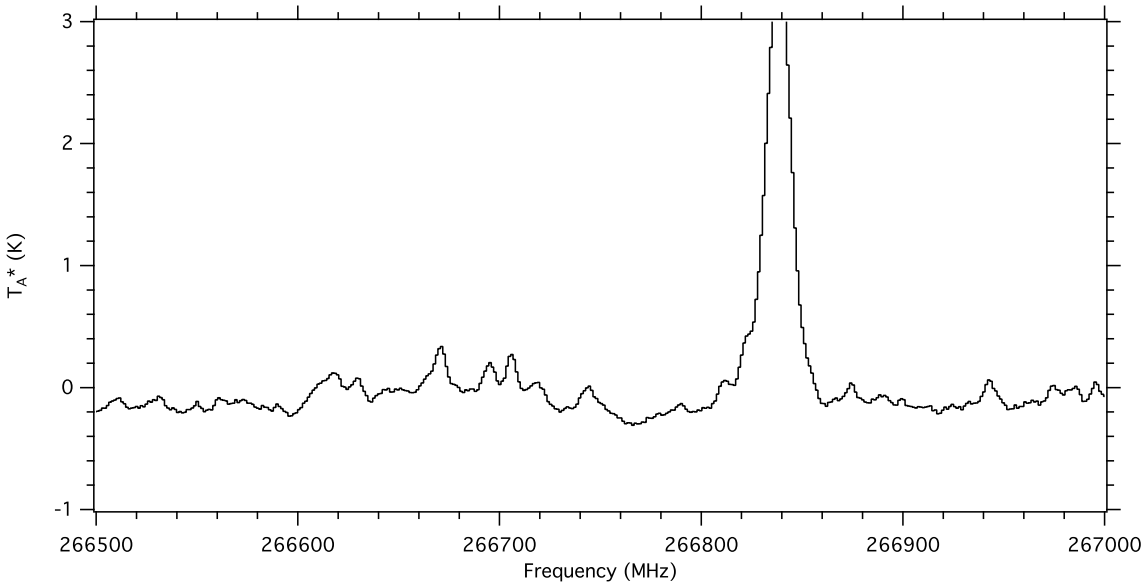

Figure A.15: Spectrum of Sgr B2(N) from 266.5 - 267.0 GHz

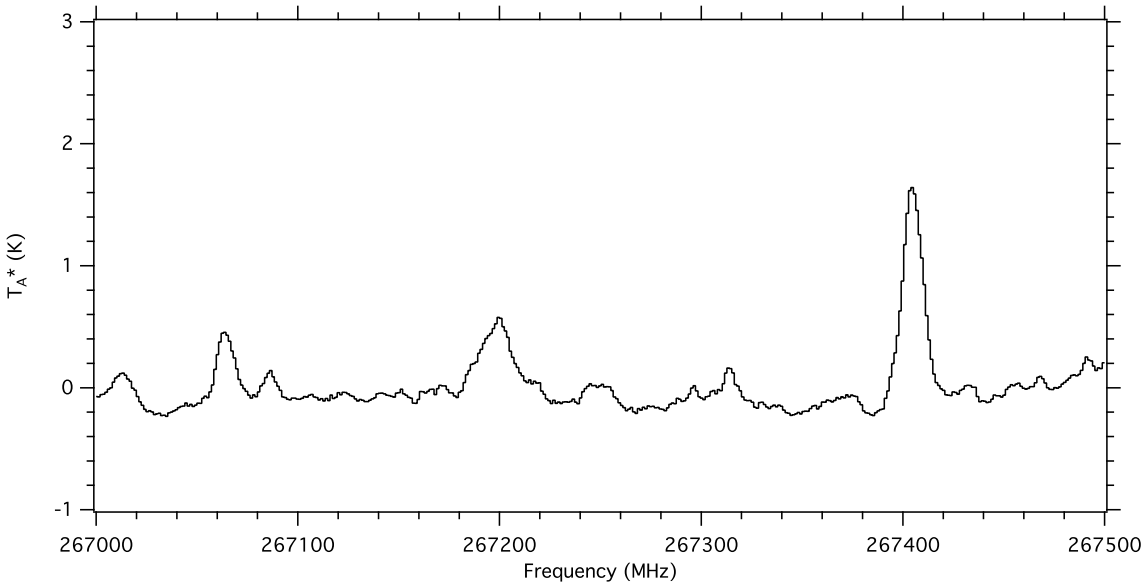

Figure A.16: Spectrum of Sgr B2(N) from 267.0 - 267.5 GHz

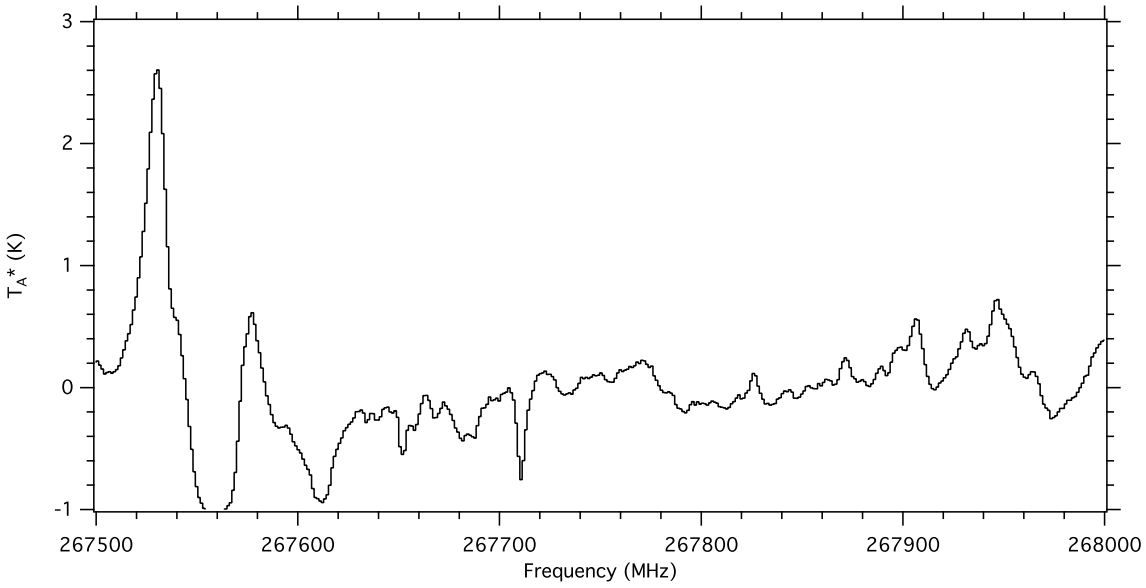

Figure A.17: Spectrum of Sgr B2(N) from 267.5 - 268.0 GHz

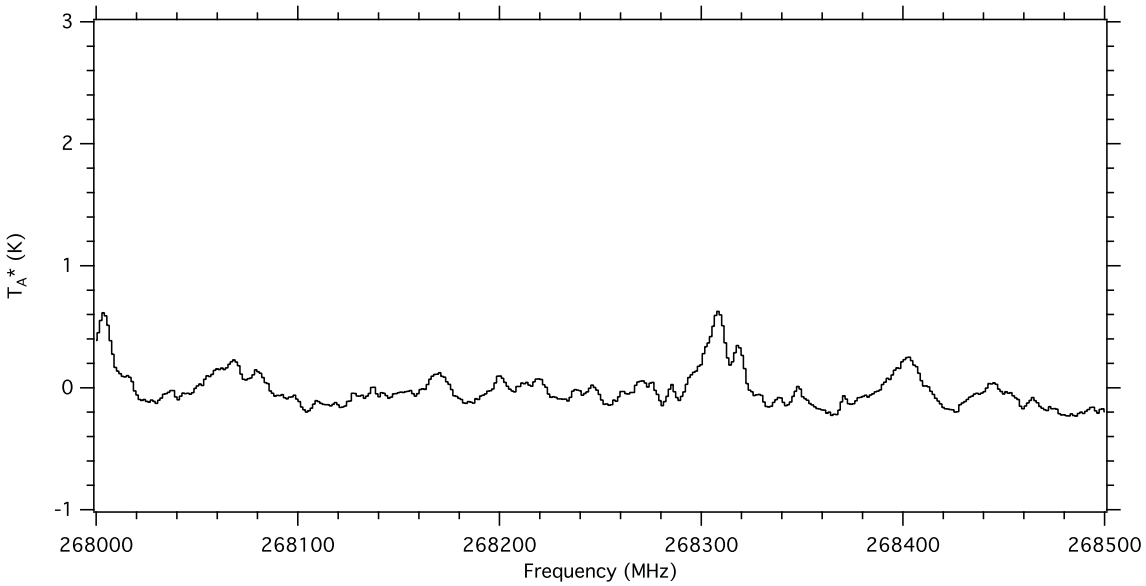

Figure A.18: Spectrum of Sgr B2(N) from 268.0 - 268.5 GHz

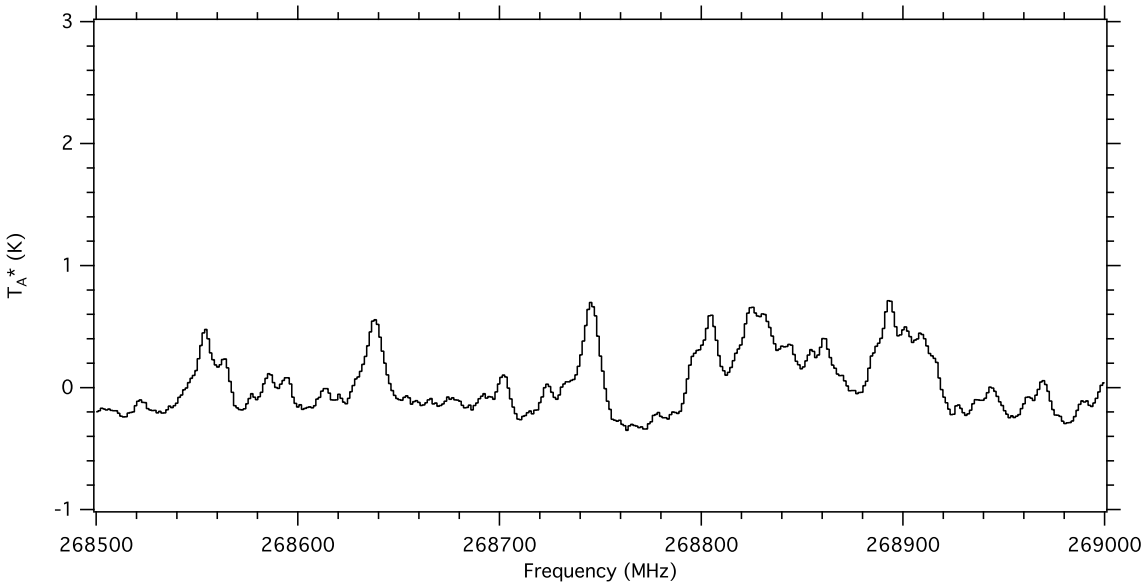

Figure A.19: Spectrum of Sgr B2(N) from 268.5 - 269.0 GHz

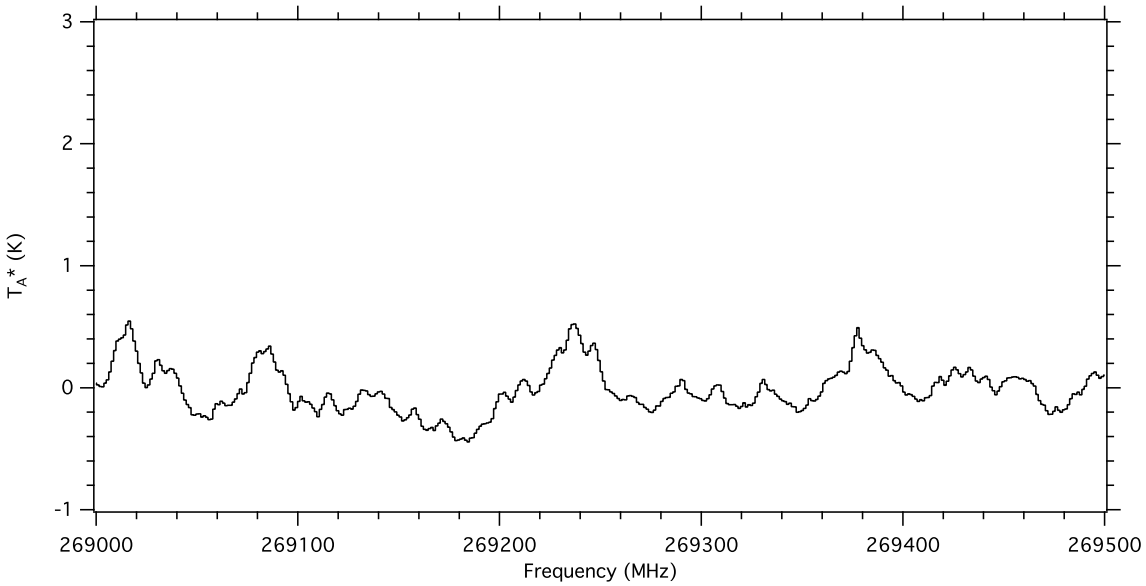

Figure A.20: Spectrum of Sgr B2(N) from 269.0 - 269.5 GHz

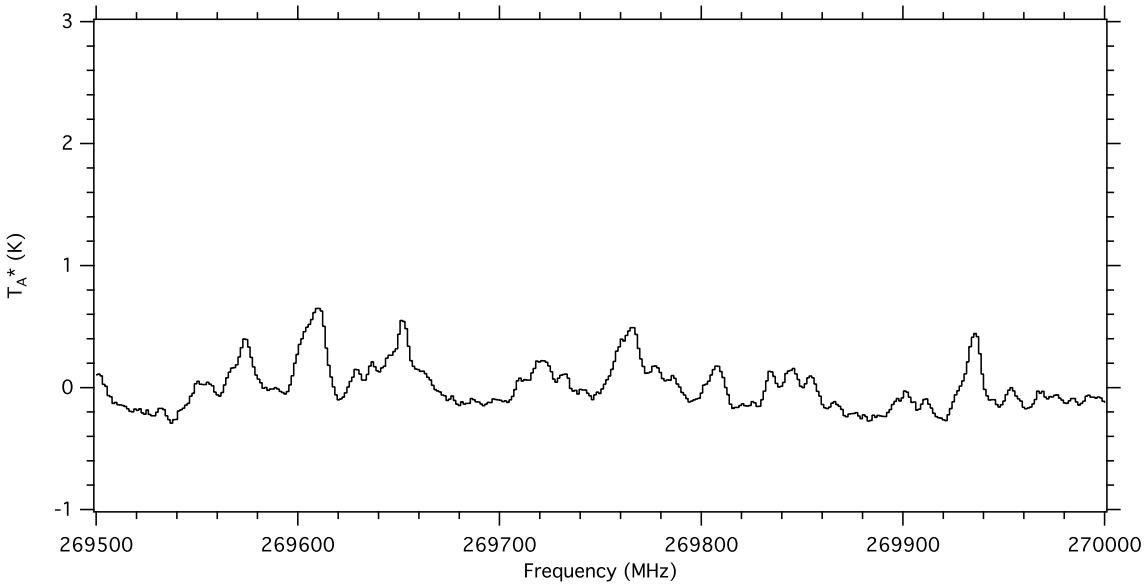

Figure A.21: Spectrum of Sgr B2(N) from 269.5 - 270.0 GHz

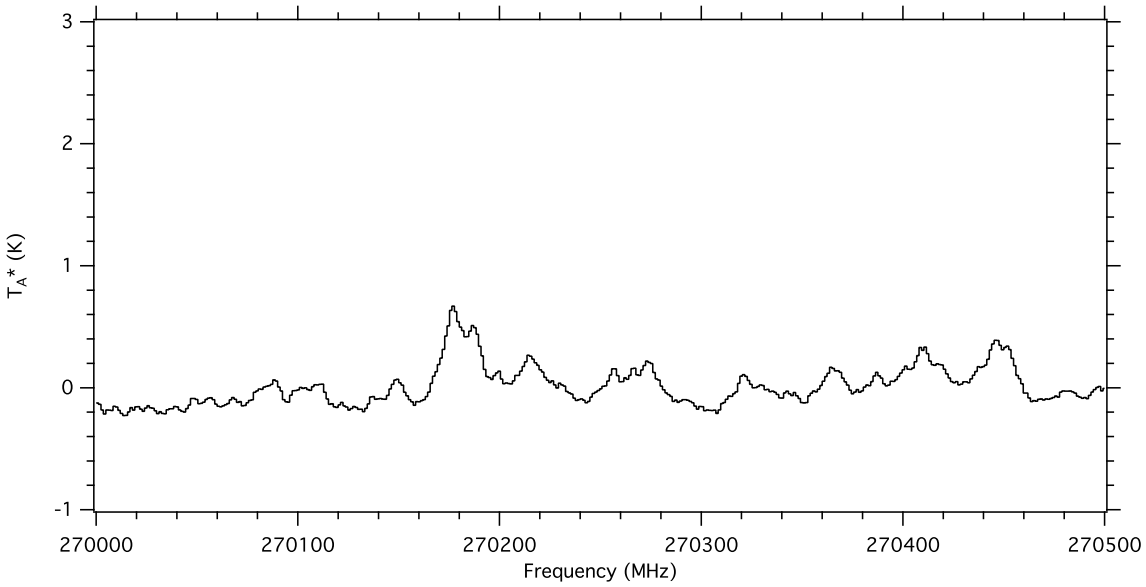

Figure A.22: Spectrum of Sgr B2(N) from 270.0 - 270.5 GHz

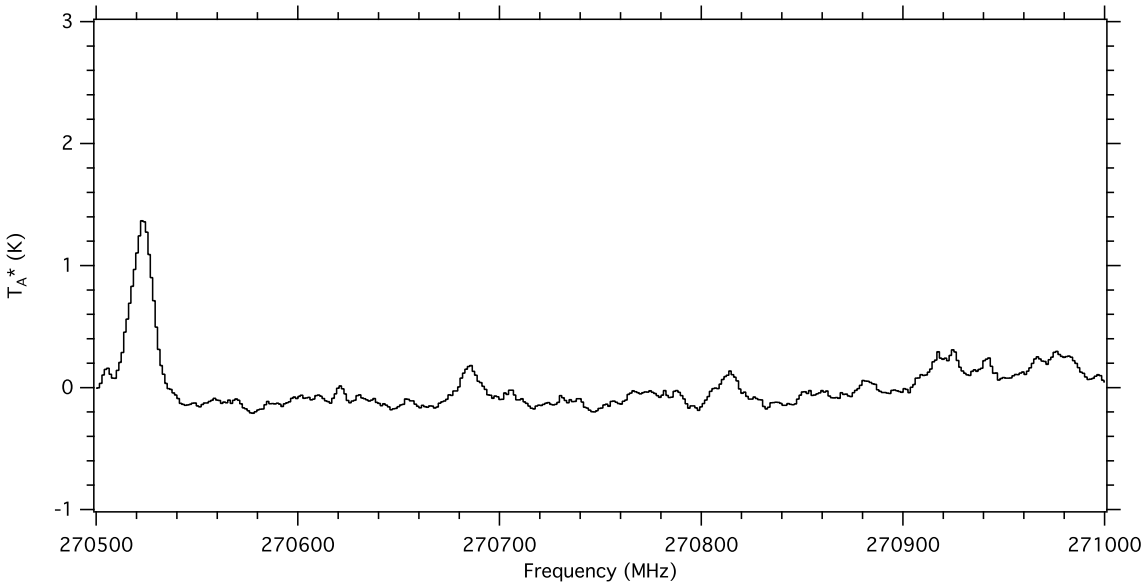

Figure A.23: Spectrum of Sgr B2(N) from 270.5 - 271.0 GHz

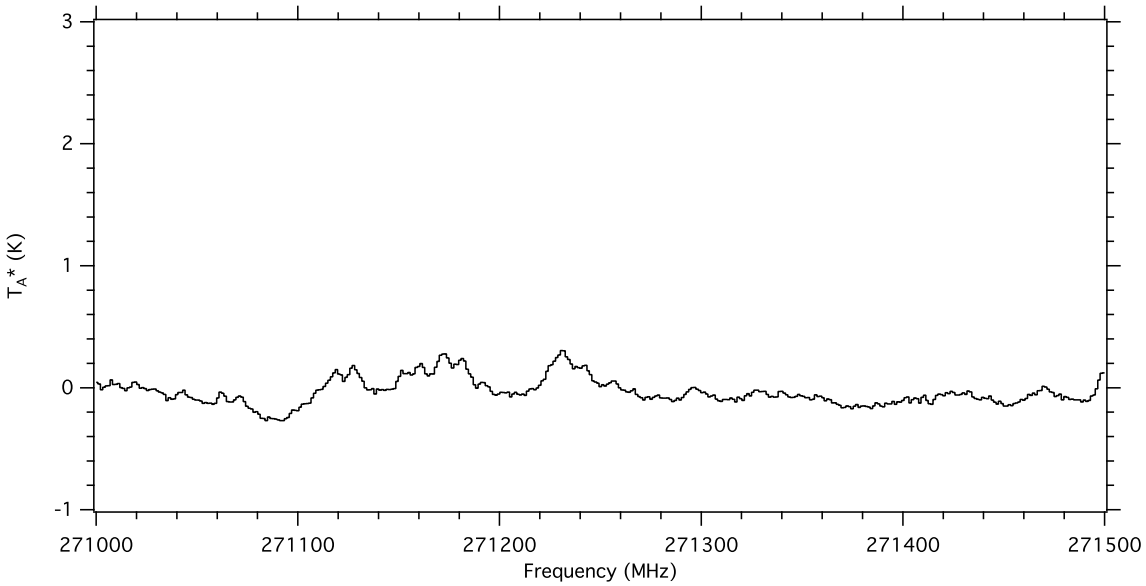

Figure A.24: Spectrum of Sgr B2(N) from 271.0 - 271.5 GHz

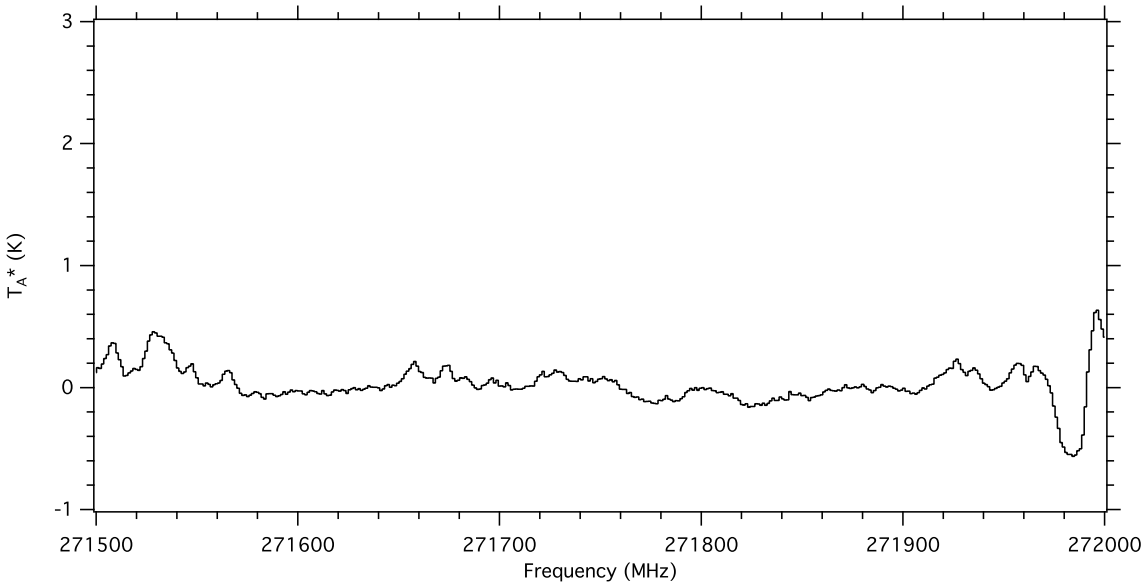

Figure A.25: Spectrum of Sgr B2(N) from 271.5 - 272.0 GHz

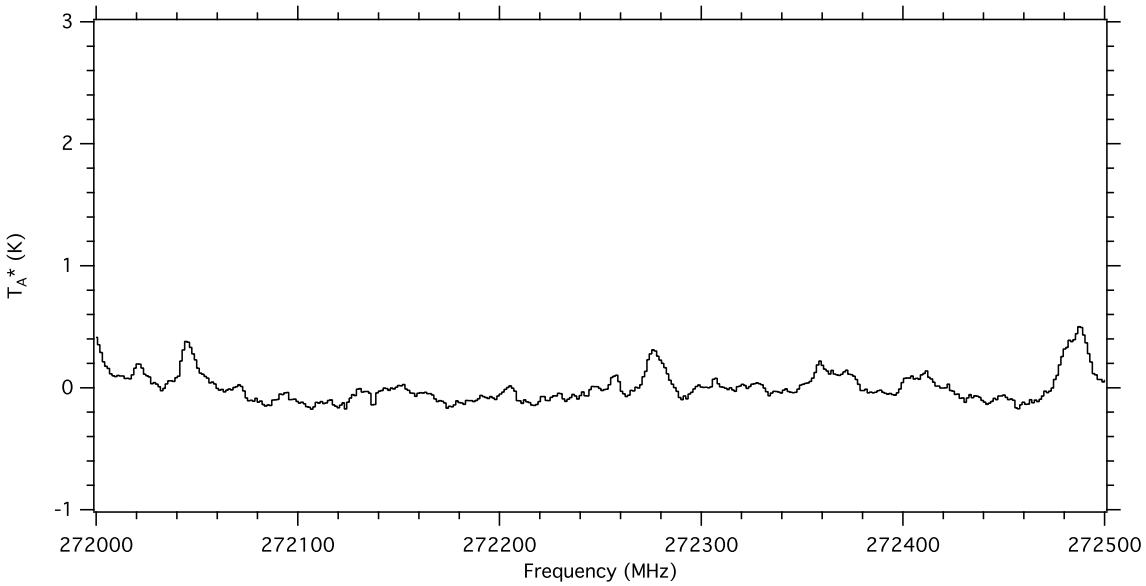

Figure A.26: Spectrum of Sgr B2(N) from 272.0 - 272.5 GHz

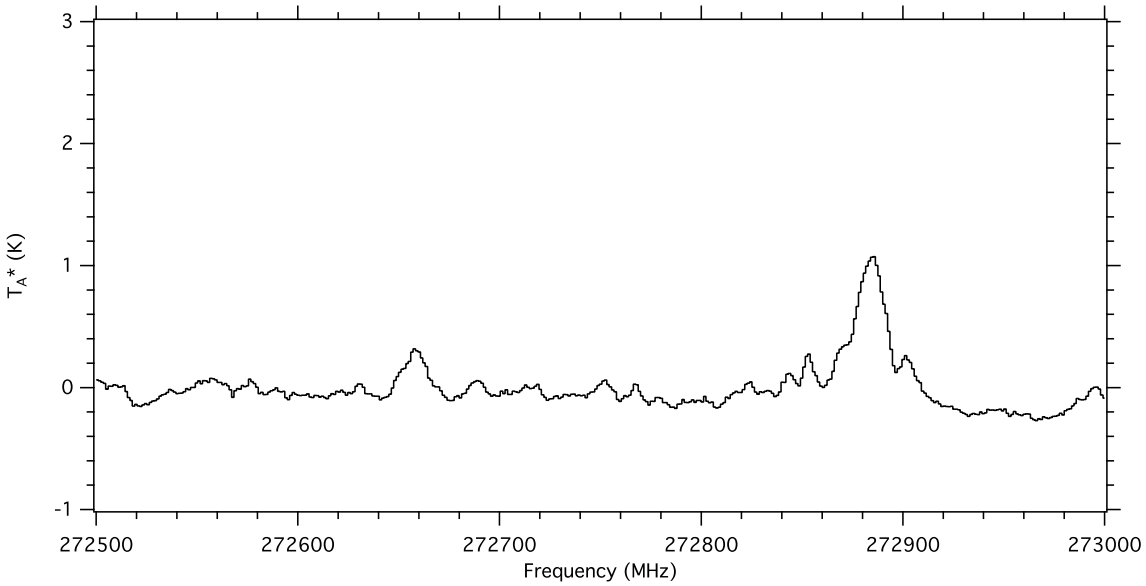

Figure A.27: Spectrum of Sgr B2(N) from 272.5 - 273.0 GHz

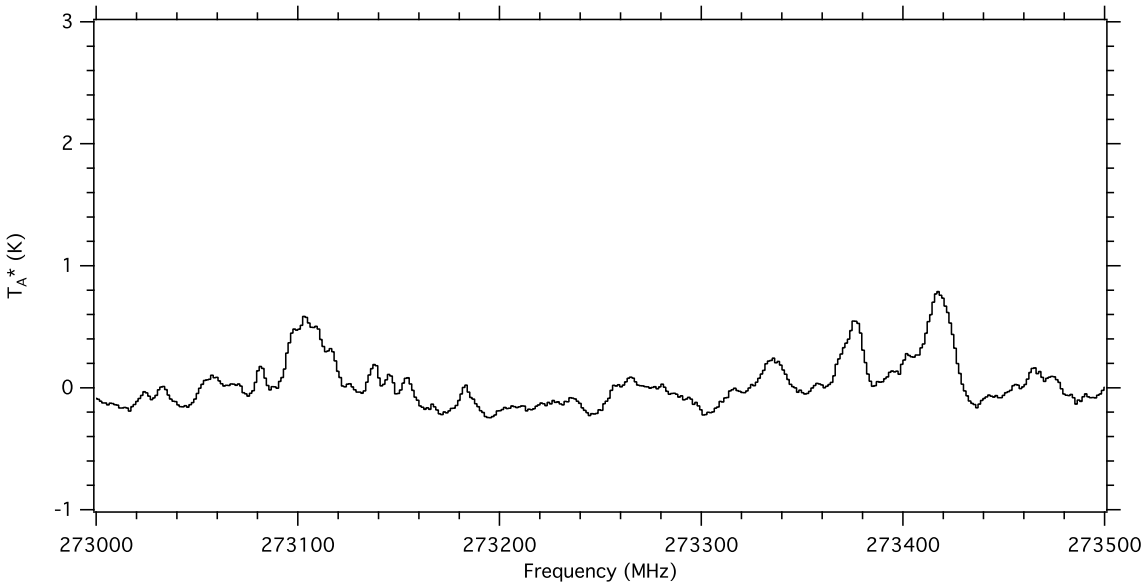

Figure A.28: Spectrum of Sgr B2(N) from 273.0 - 273.5 GHz

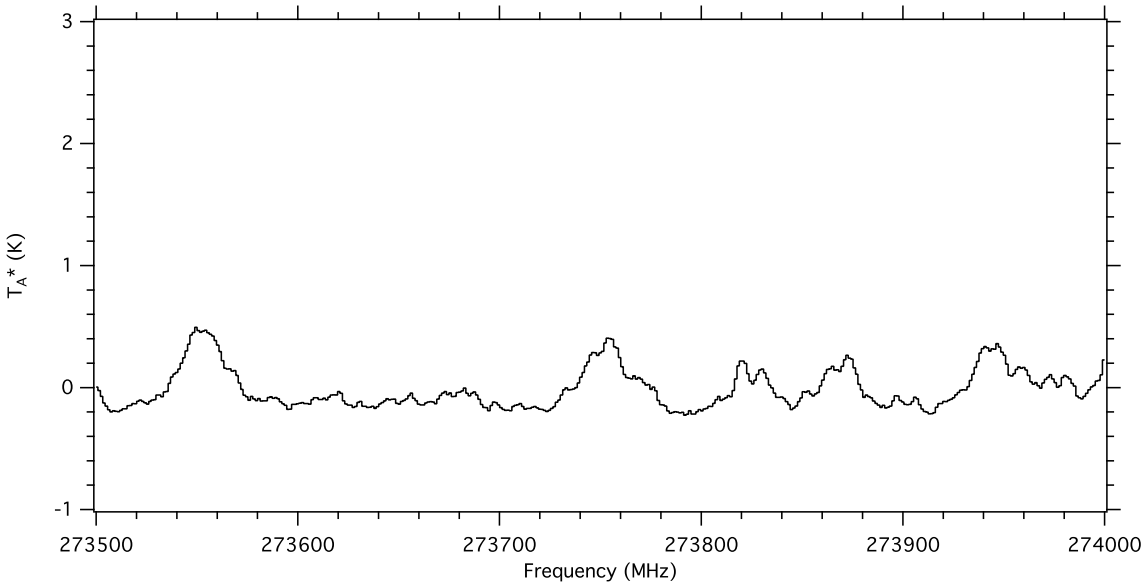

Figure A.29: Spectrum of Sgr B2(N) from 273.5 - 274.0 GHz

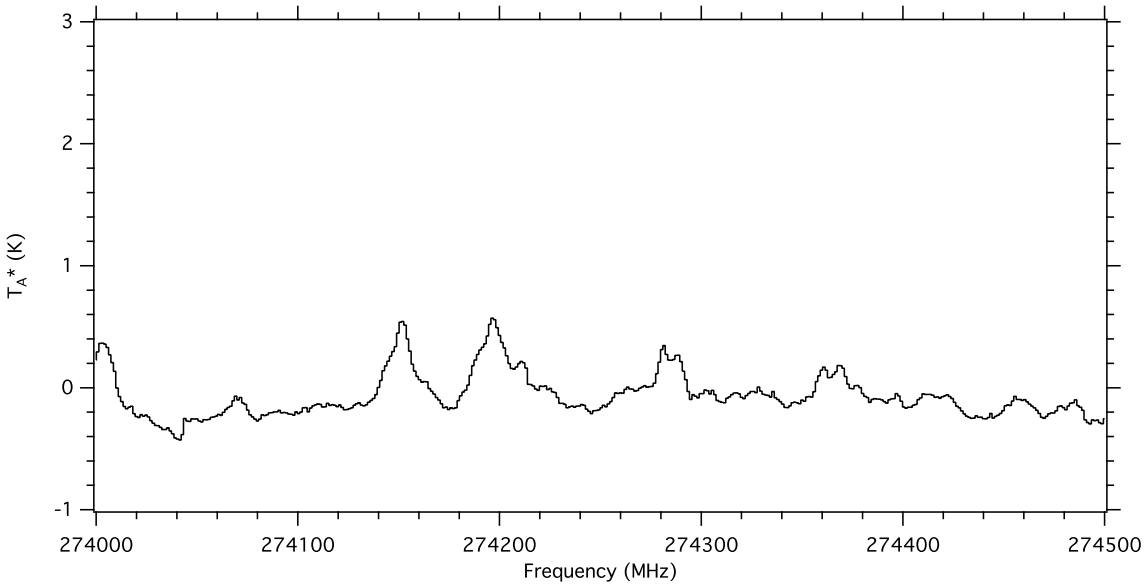

Figure A.30: Spectrum of Sgr B2(N) from 274.0 - 274.5 GHz

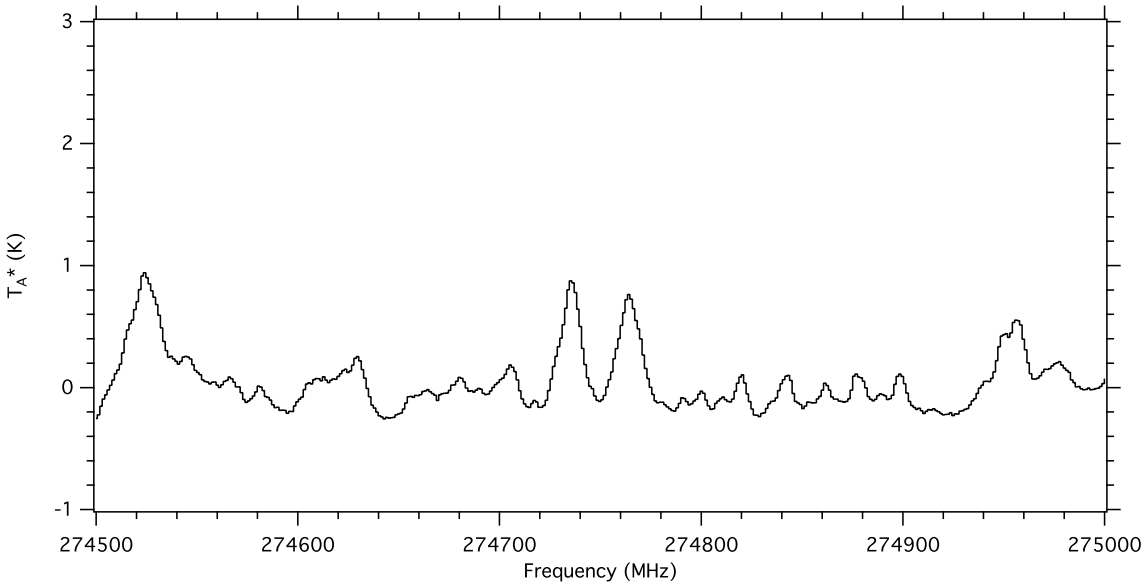

Figure A.31: Spectrum of Sgr B2(N) from 274.5 - 275.0 GHz

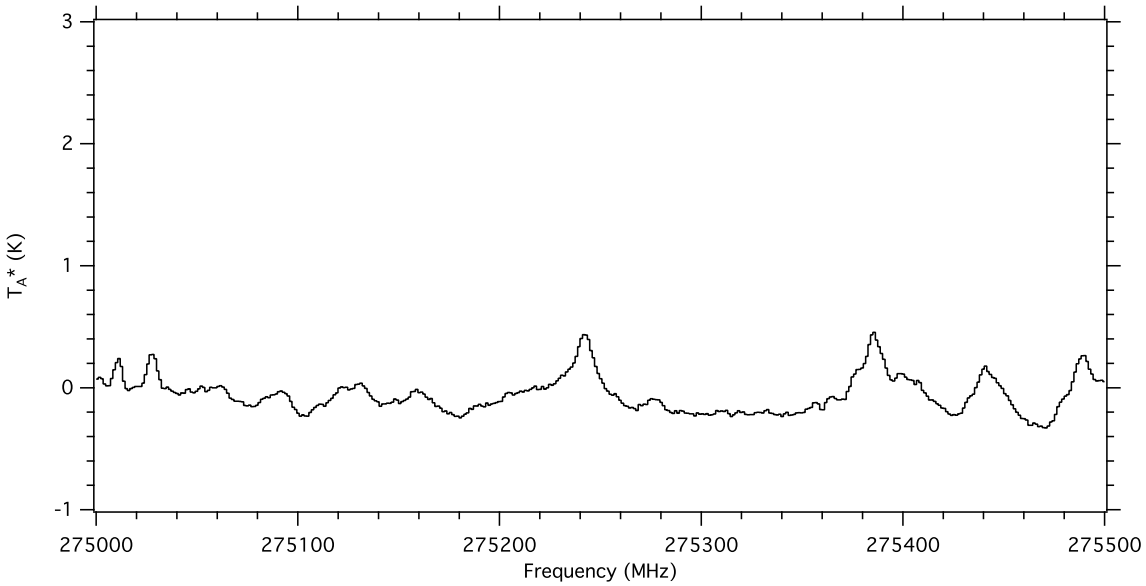

Figure A.32: Spectrum of Sgr B2(N) from 275.0 - 275.5 GHz

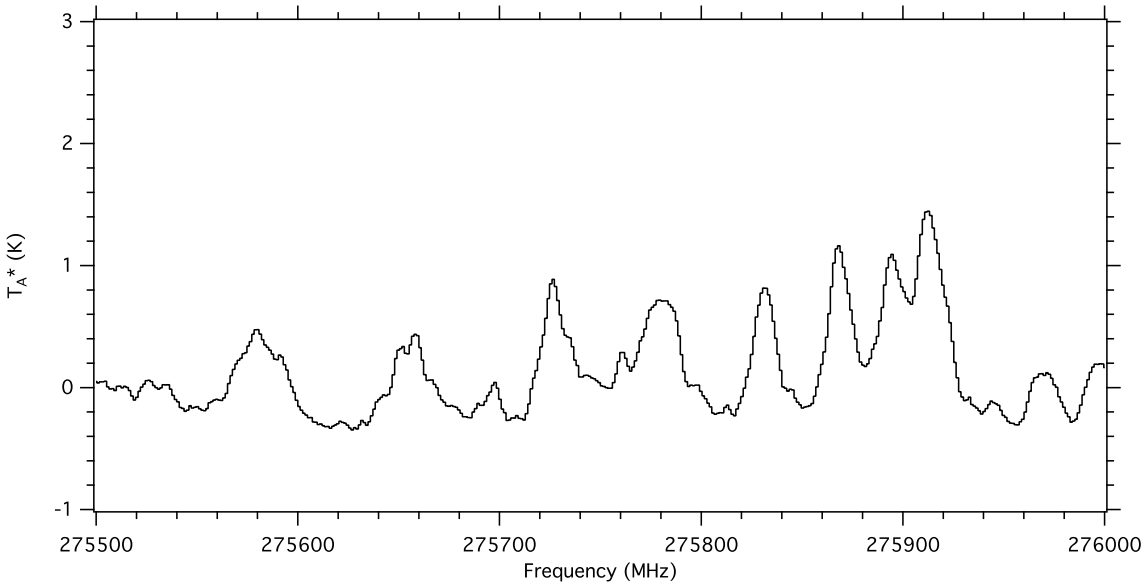

Figure A.33: Spectrum of Sgr B2(N) from 275.5 - 276.0 GHz

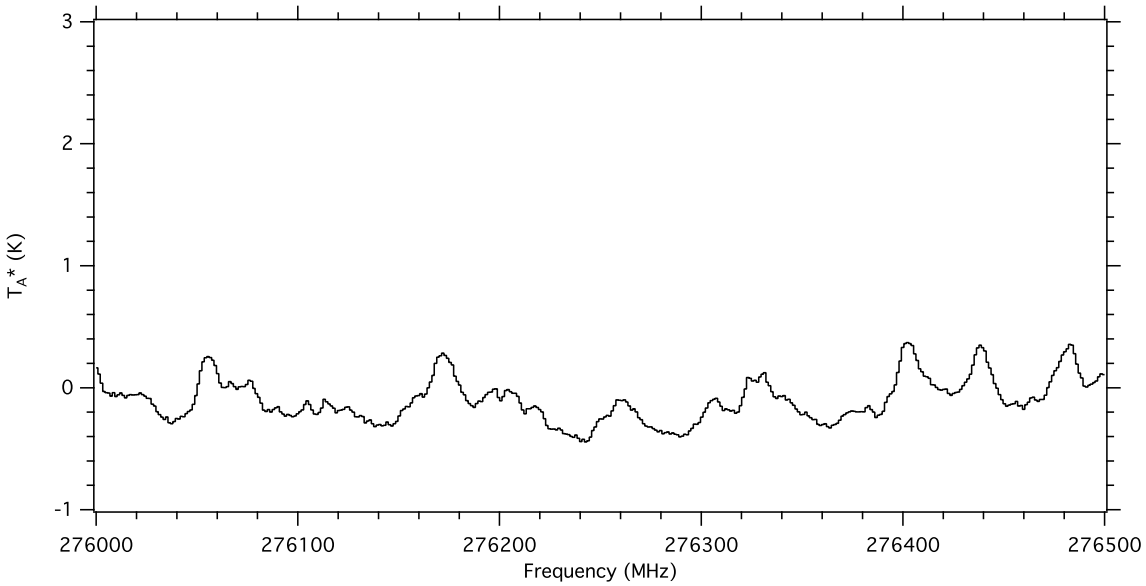

Figure A.34: Spectrum of Sgr B2(N) from 276.0 - 276.5 GHz

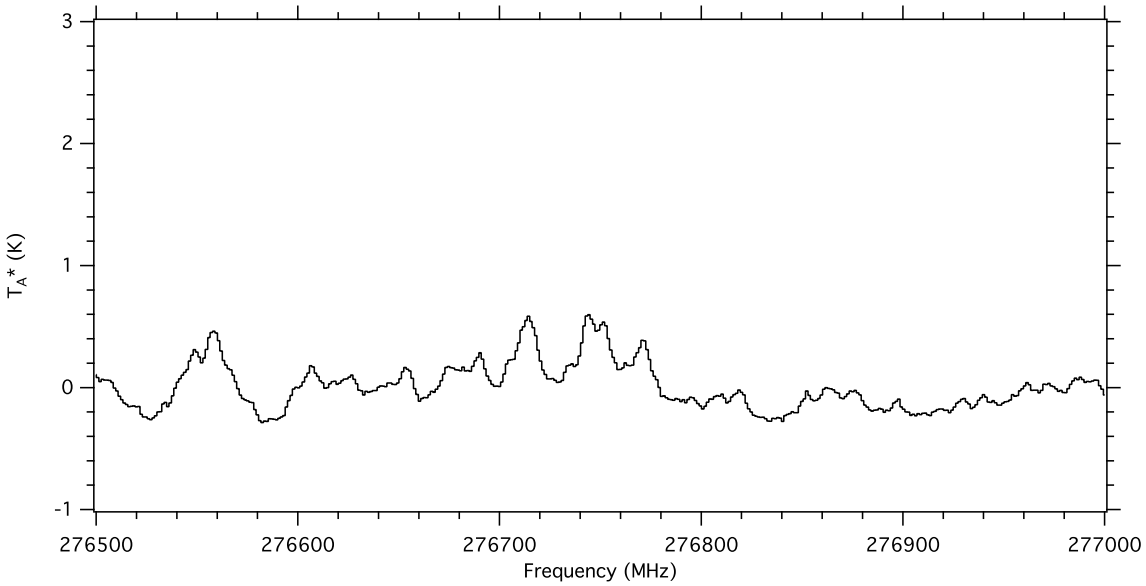

Figure A.35: Spectrum of Sgr B2(N) from 276.5 - 277.0 GHz

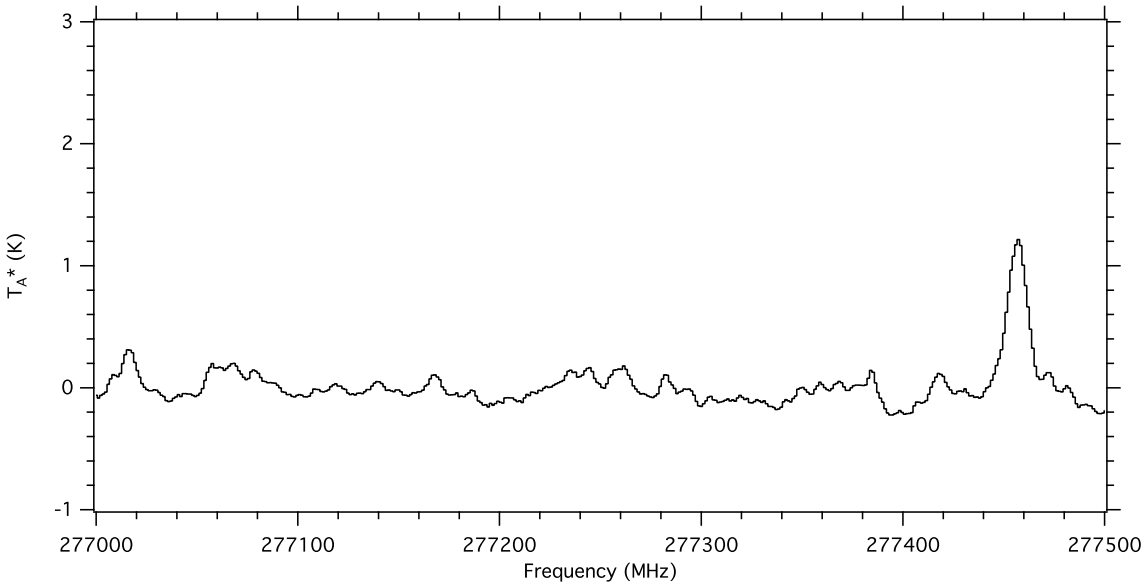

Figure A.36: Spectrum of Sgr B2(N) from 277.0 - 277.5 GHz

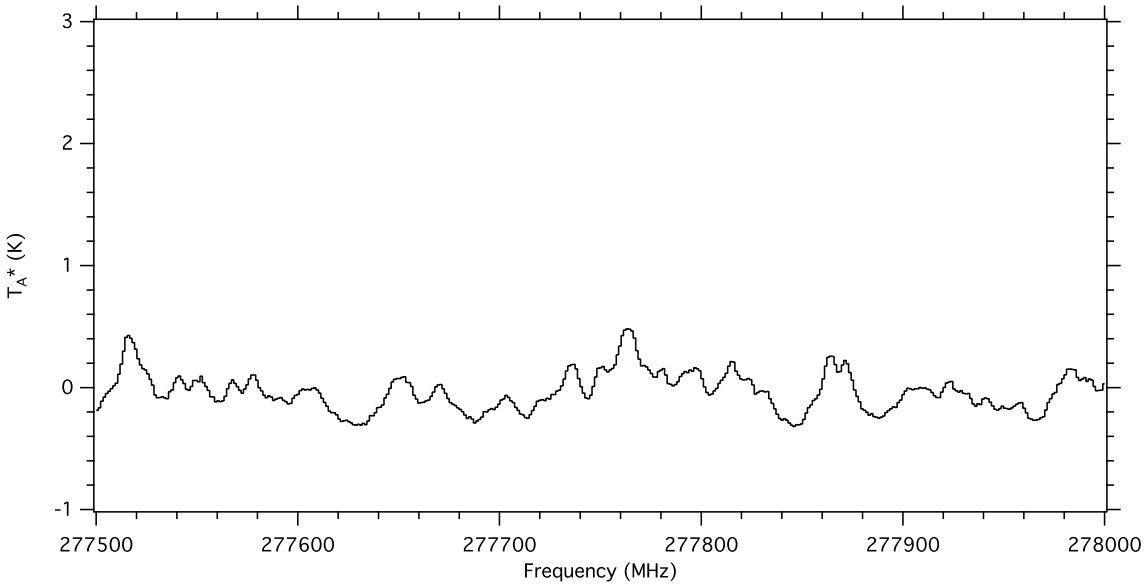

Figure A.37: Spectrum of Sgr B2(N) from 277.5 - 278.0 GHz

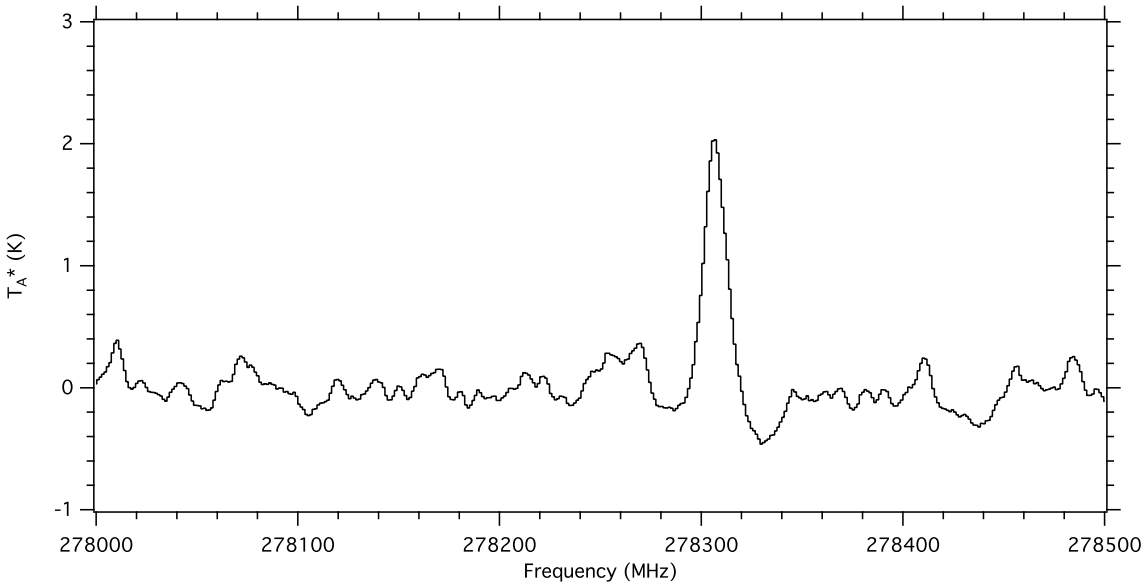

Figure A.38: Spectrum of Sgr B2(N) from 278.0 - 278.5 GHz

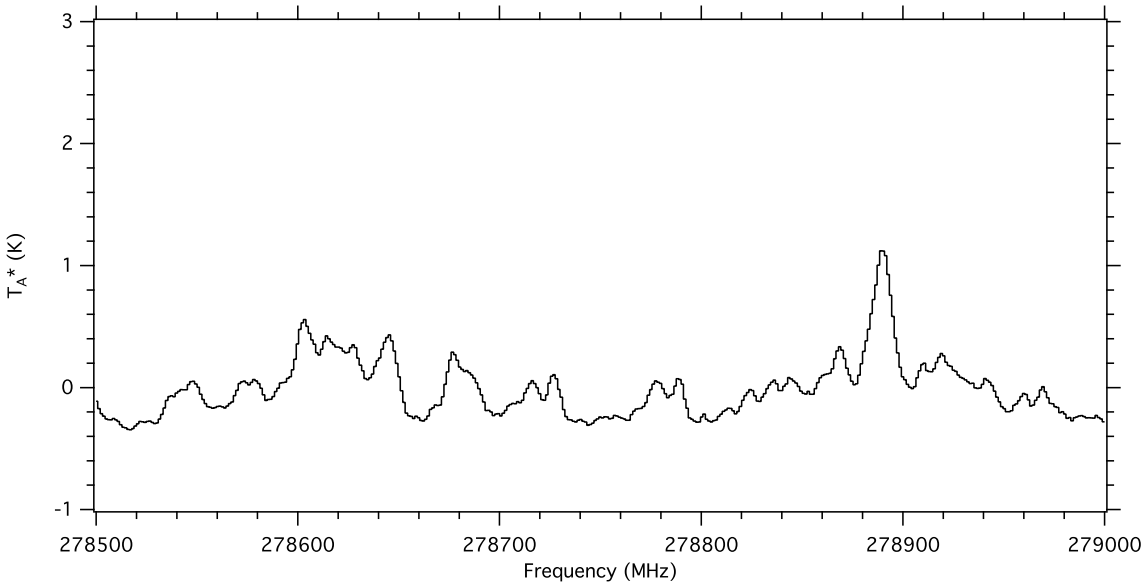

Figure A.39: Spectrum of Sgr B2(N) from 278.5 - 279.0 GHz

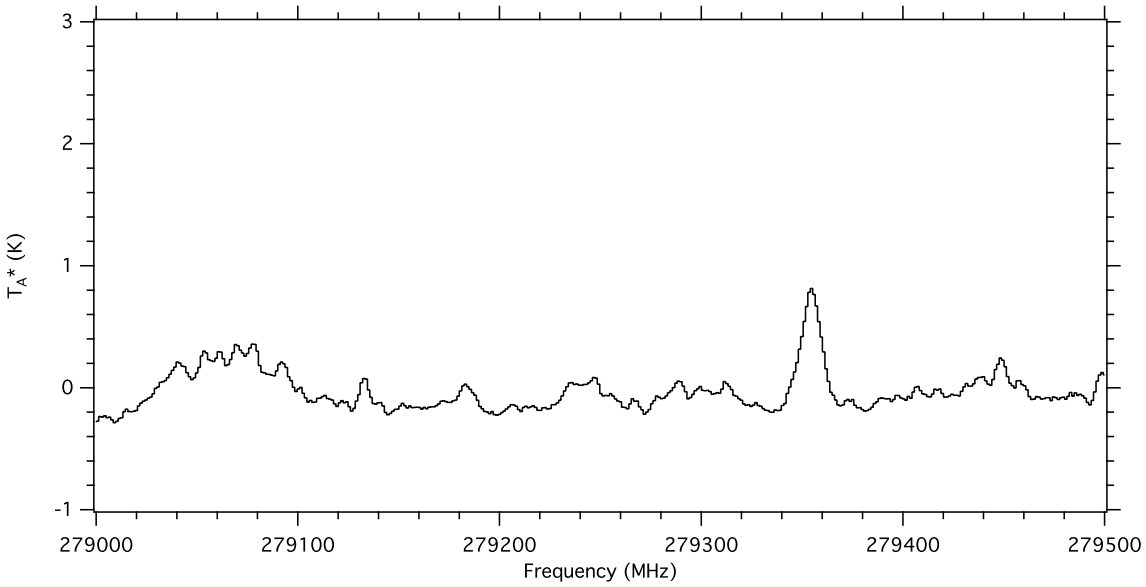

Figure A.40: Spectrum of Sgr B2(N) from 279.0 - 279.5 GHz

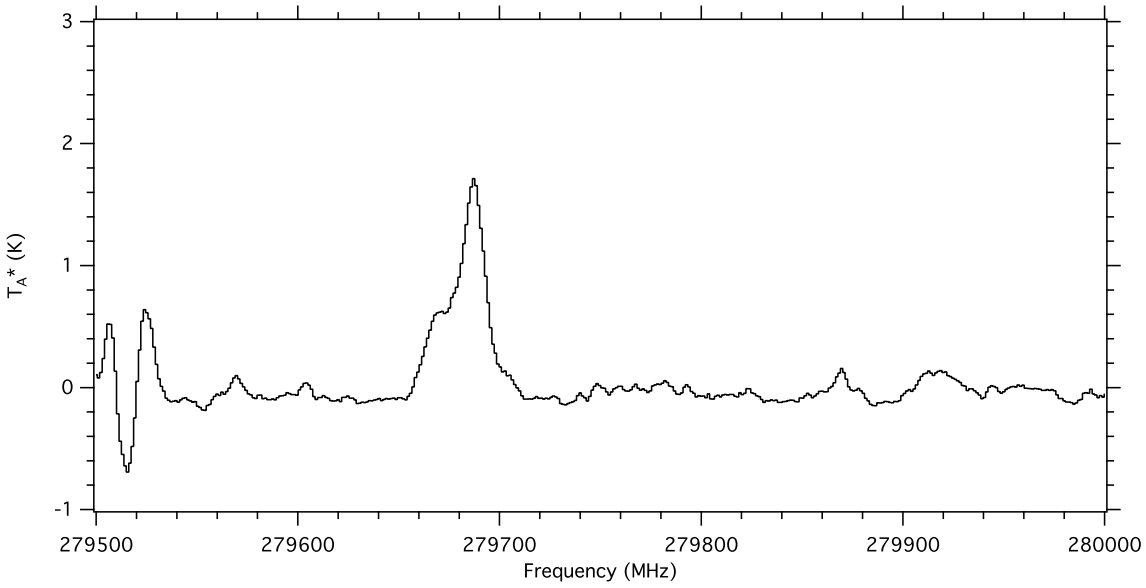

Figure A.41: Spectrum of Sgr B2(N) from 279.5 - 280.0 GHz

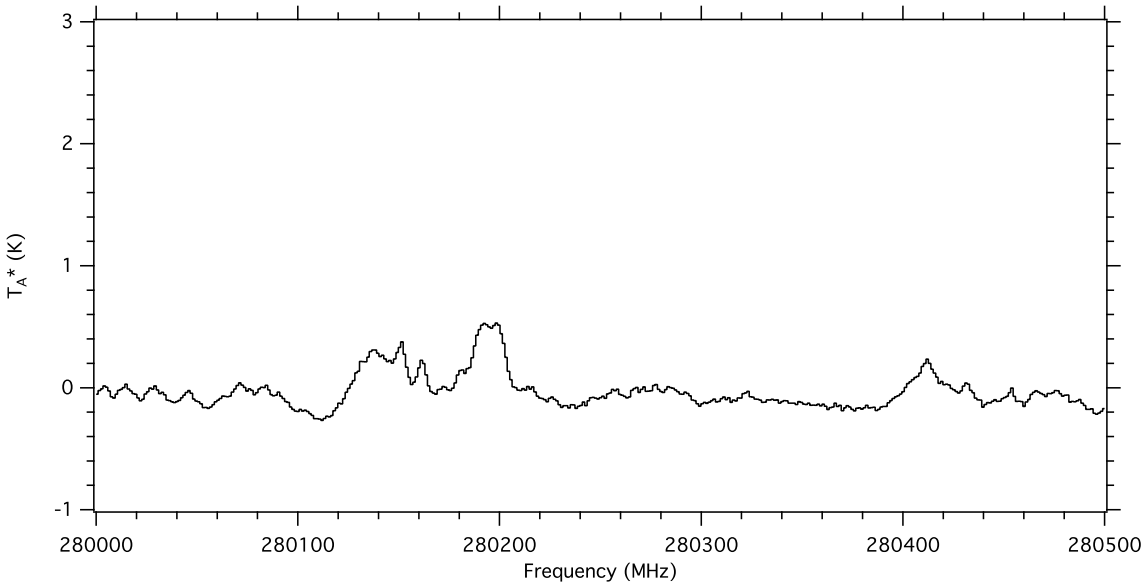

Figure A.42: Spectrum of Sgr B2(N) from 280.0 - 280.5 GHz

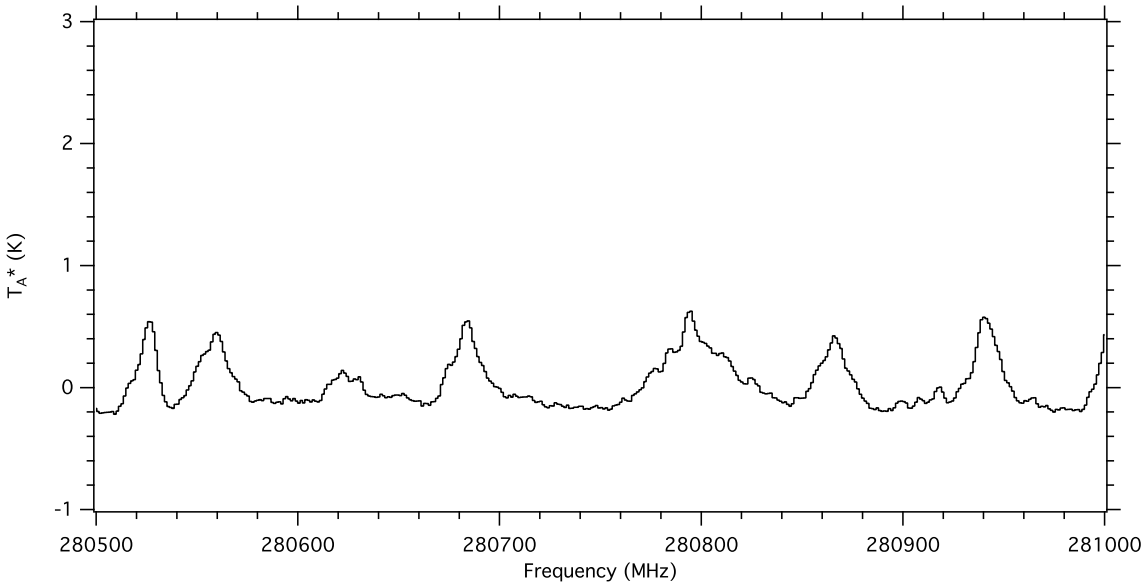

Figure A.43: Spectrum of Sgr B2(N) from 280.5 - 281.0 GHz

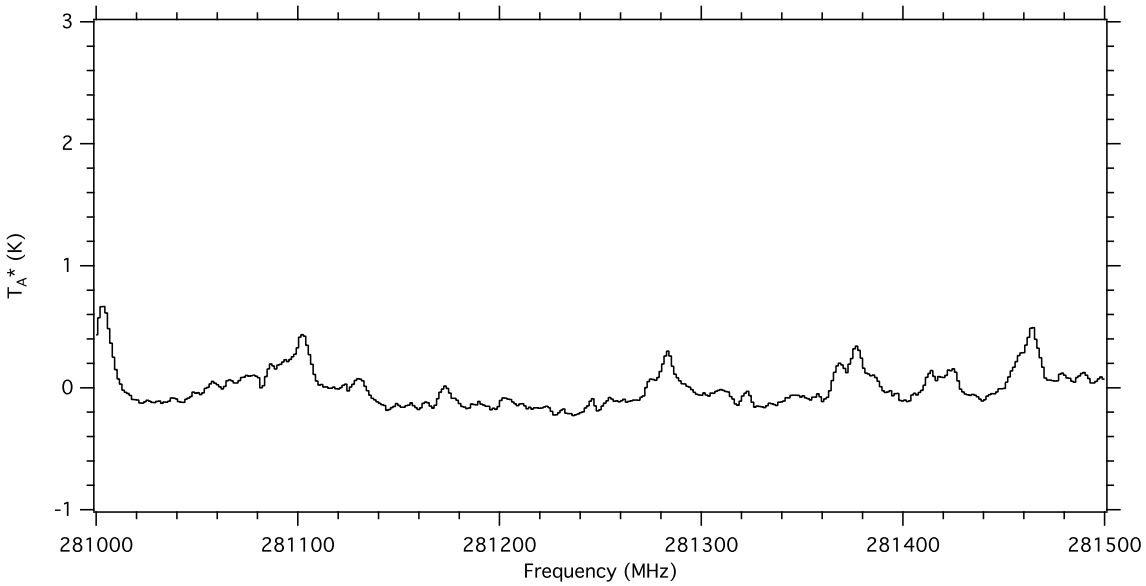

Figure A.44: Spectrum of Sgr B2(N) from 281.0 - 281.5 GHz

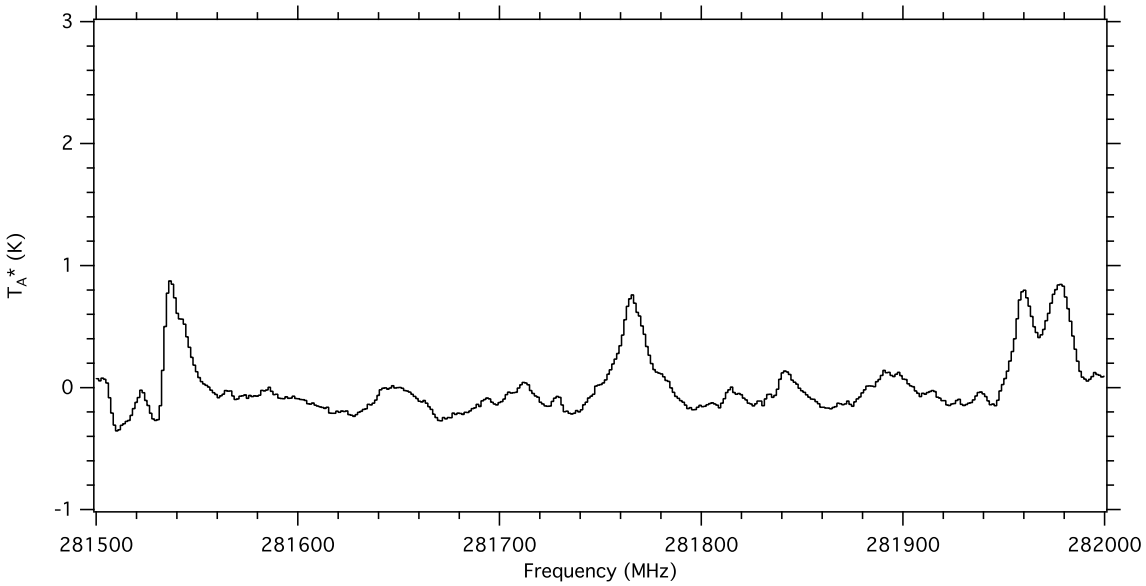

Figure A.45: Spectrum of Sgr B2(N) from 281.5 - 282.0 GHz

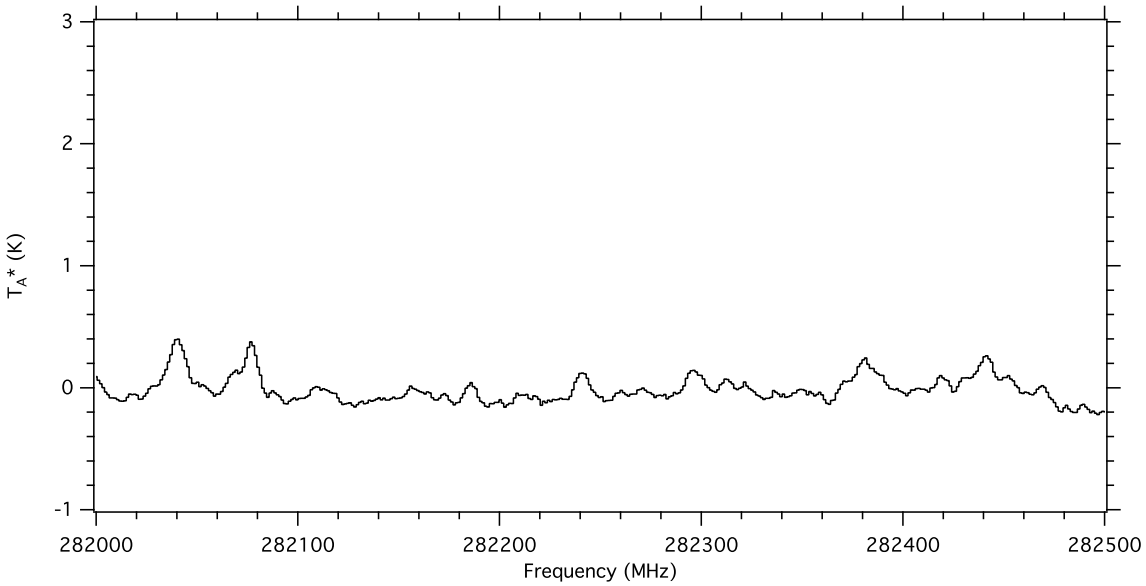

Figure A.46: Spectrum of Sgr B2(N) from 282.0 - 282.5 GHz

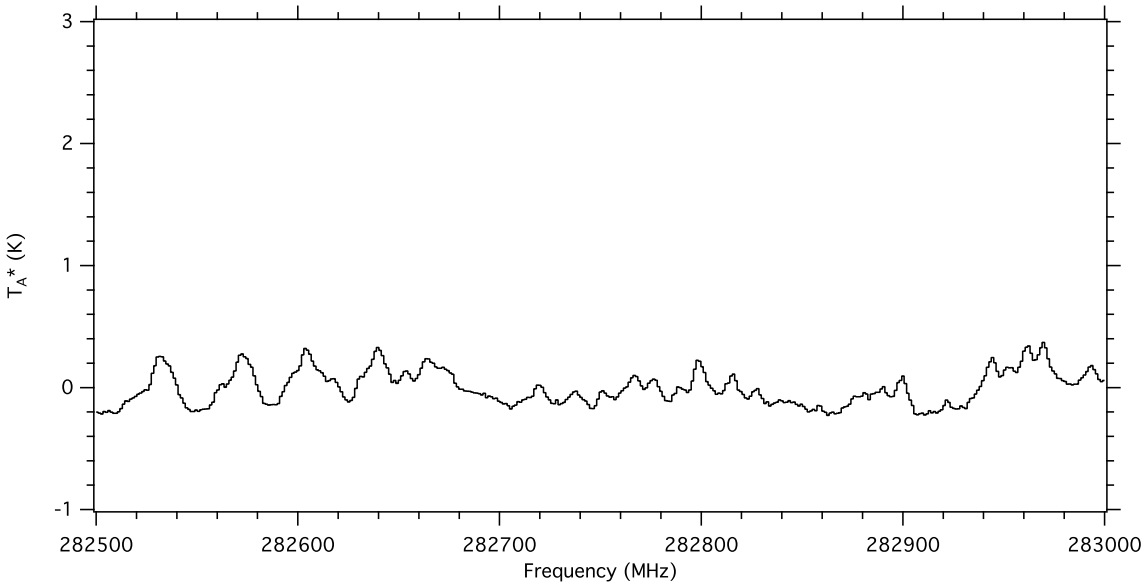

Figure A.47: Spectrum of Sgr B2(N) from 282.5 - 283.0 GHz

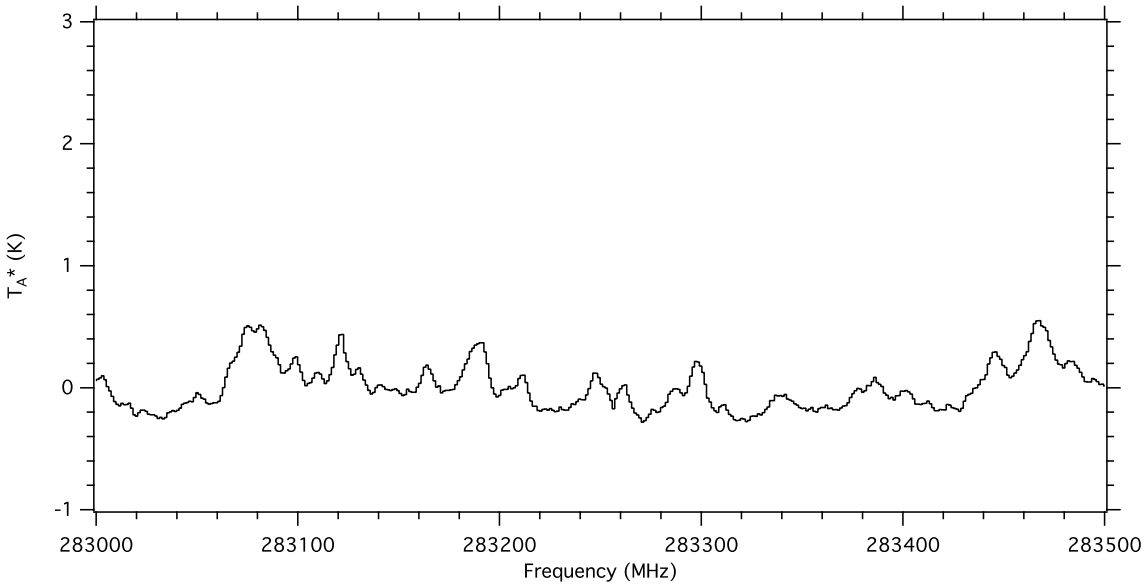

Figure A.48: Spectrum of Sgr B2(N) from 283.0 - 283.5 GHz

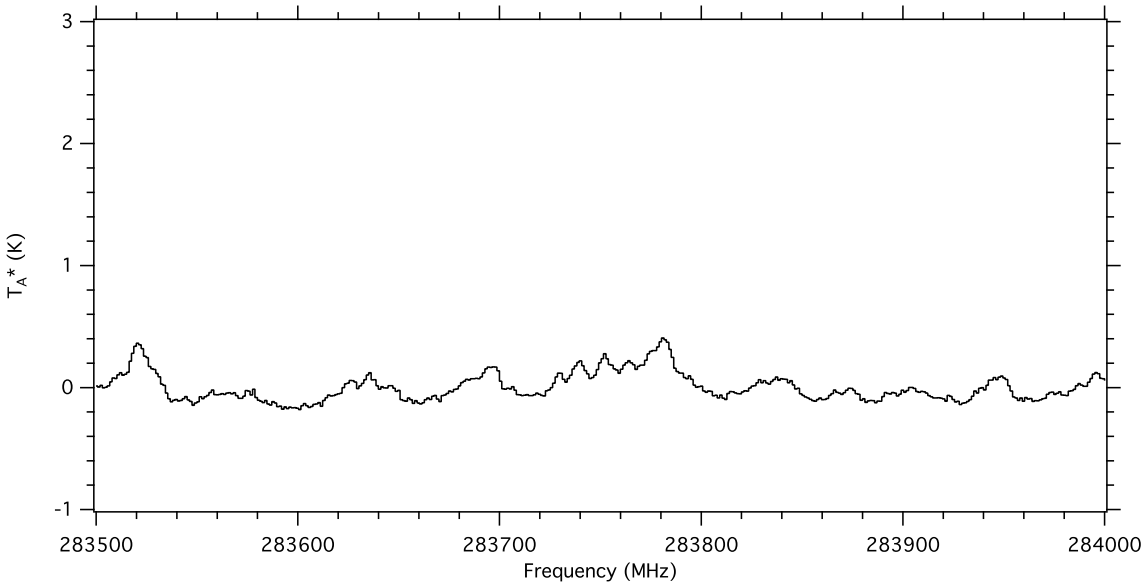

Figure A.49: Spectrum of Sgr B2(N) from 283.5 - 284.0 GHz

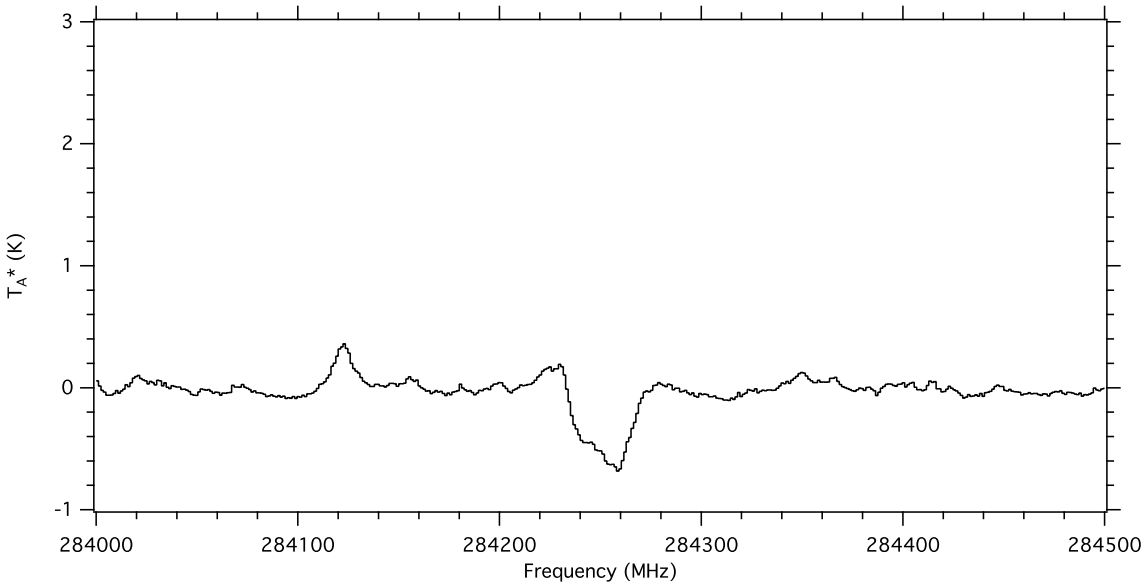

Figure A.50: Spectrum of Sgr B2(N) from 284.0 - 284.5 GHz

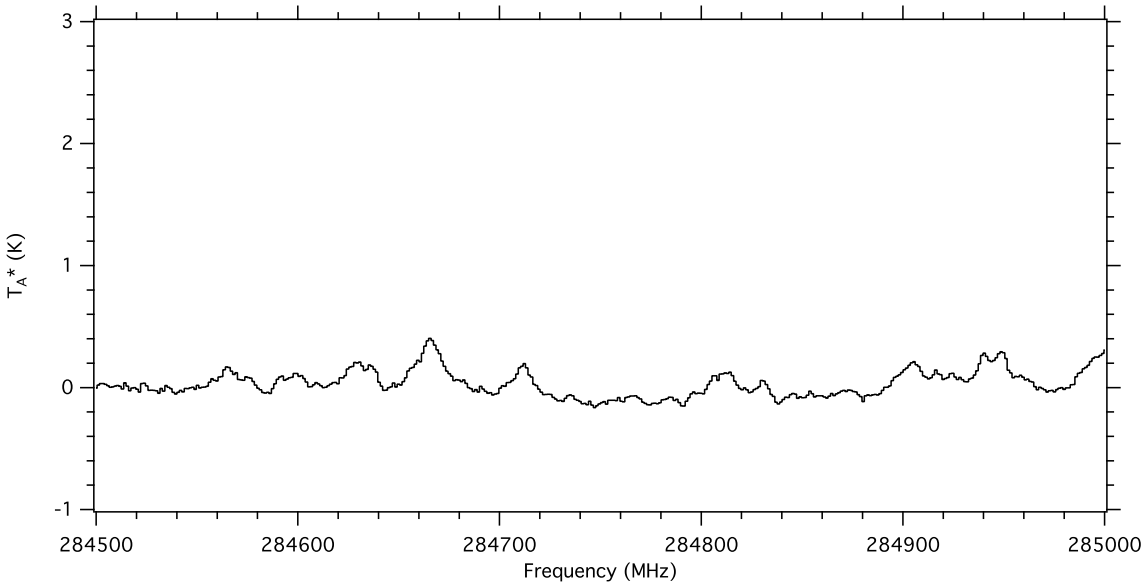

Figure A.51: Spectrum of Sgr B2(N) from 284.5 - 285.0 GHz

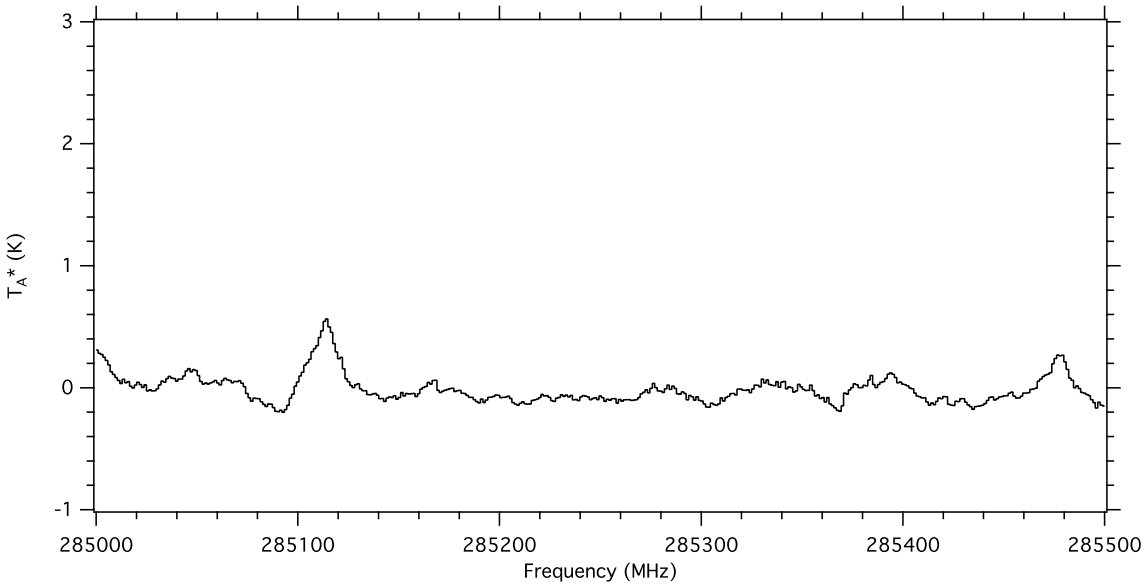

Figure A.52: Spectrum of Sgr B2(N) from 285.0 - 285.5 GHz

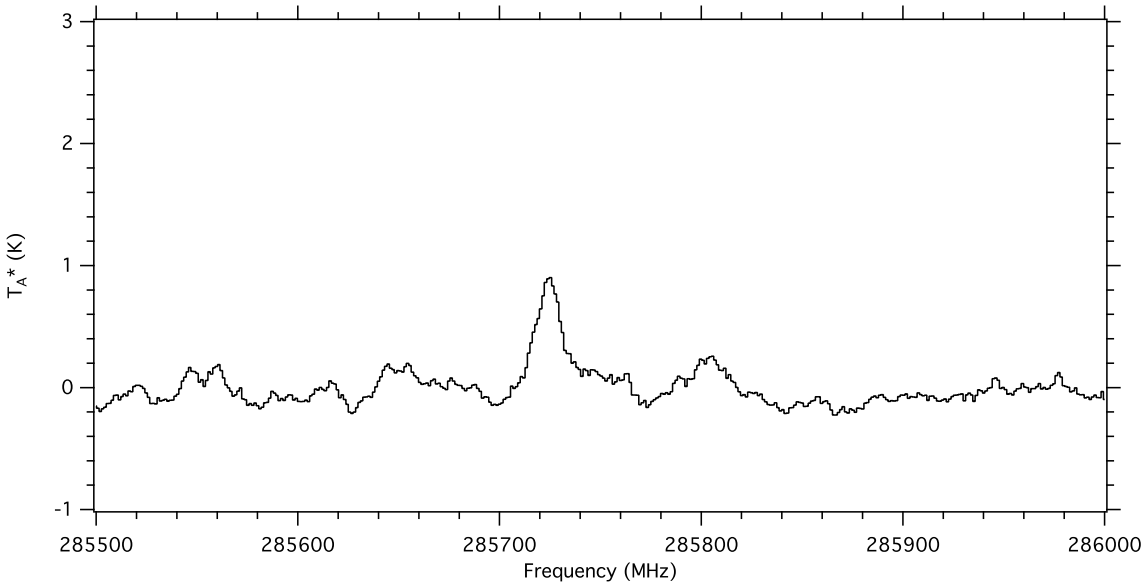

Figure A.53: Spectrum of Sgr B2(N) from 285.5 - 286.0 GHz

A.7 Deconvolution Routine

```
file in sgrb2n.dat
$rm sgrb2n.sm
file out sgrb2n.sm multiple
set tele "CSO FFTS 1W"
find

for i 1 to found
get n
smooth
write
next

set tele "CSO FFTS 2B1"
find

for i 1 to found
get n
write
next

set tele "CSO FFTS 2B2"
find

for i 1 to found
get n
write
next

set tele
set mode x t
set mode y t

file in sgrb2n.sm
$rm sgrb2n.rs
file out sgrb2n.rs multiple
set u c
set var spec write

find
for i 1 to found
get n
a\resam 'nchan/0.3*fres' 'rchan/0.3*fres' int(frequency) 0.3 f /nofft
write
next

set tele
set mode x t
set mode y t

file in sgrb2n.rs
```

```
$rm sgrb2n.cln
file out sgrb2n.cln multiple
set u c

set tele "CSO FFTS 1W"
find

for i 1 to found
get n
write
next

set tele "CSO FFTS 2B1"
find

for i 1 to found
get n
for j 3666 to 3670
draw k j
next
for j 5499 to 5503
draw k j
next
for j 1832 to 1837
draw k j
next
write
next

set tele "CSO FFTS 2B2"
find

for i 1 to found
get n
for j 3666 to 3670
draw k j
next
for j 5499 to 5503
draw k j
next
for j 1832 to 1837
draw k j
next
for j 5330 to 5337
draw k j
next
write
next

set tele
set mode x t
set mode y t

file in sgrb2n.cln
```

```
$rm sgrb2n.bas
file out sgrb2n.bas multiple
find

drop 4211
drop 4206
drop 4242
drop 4060
drop 4229
drop 4150

for i 1 to found
get n
set win 0 1
base 3
write
next

set tele
set mode x t
set mode y t

$rm sgrb2n.dec
$rm sgrb2n.igor
file in sgrb2n.bas
file out sgrb2n.dec multiple
set unit f f
set mode x t
set blanking -1000 0.1
find
initialize
set var spec read

deconv 1.e-6 400
write 1

smooth
smooth

write 2

file in sgrb2n.dec
find
get 1
plot
let ry 0 /where ry.eq.(-1000)

greg sgrb2n.txt /formatted

get 2
plot
let ry 0 /where ry.eq.(-1000)

greg sgrb2n.sm.txt /formatted
```

Appendix B

Spectral Line Catalog for C_3H^- Through 2 THz

```
Begin header information, taken from catdoc.pdf available at spec.jpl.nasa.gov
The catalog line files are composed of 80-character lines, with one line entry per
spectral line. The format of each line is:
FREQ, ERR, LGINT, DR, ELO, GUP, TAG, QNFMT, QN', QN''
(F13.4, F8.4, F8.4, I2, F10.4, I3, I7, I4, 6I2, 6I2)
FREQ: Frequency of the line in MHz.
ERR: Estimated or experimental error of FREQ in MHz.
LGINT: Base 10 logarithm of the integrated intensity in units of nm2MHz at 300 K.
(See Section 3 of catdoc.pdf for conversions to other units.)
DR: Degrees of freedom in the rotational partition function
(0 for atoms, 2 for linear molecules, and 3 for nonlinear molecules).
ELO: Lower state energy in cm?1 relative to the lowest energy
spinrotation level in ground vibronic state.
GUP: Upper state degeneracy.
TAG: Species tag or molecular identifier. A negative value flags that the line
frequency has been measured in the laboratory. The absolute value of TAG is then
the species tag and ERR is the reported experimental error. The three most significant
digits of the species tag are coded as the mass number of the species,
as explained in Section 1 of catdoc.pdf.
QNFMT: Identifies the format of the quantum numbers given in the field QN.
These quantum number formats are given in Section 5 and are different from
those in the first two editions of the catalog.
QN':  Quantum numbers for the upper state coded according to QNFMT.
QN'': Quantum numbers for the lower state.
End header information.  If necessary, delete this section before use.
     51.3968 84.9376-10.9985 3  118.4808 23  60006 30311 2 9      11 210
     71.9643118.9203-10.7612 3  127.4795 25  60006 30312 210      12 211
     98.1461162.1748-10.5456 3  137.2279 27  60006 30313 211      13 212
    130.8798216.2477-10.3486 3  147.7258 29  60006 30314 212      14 213
    171.1757282.8046-10.1679 3  158.9734 31  60006 30315 213      15 214
    220.1172363.6303-10.0017 3  170.9704 33  60006 30316 214      16 215
    220.8136185.3591 -9.1902 3   18.0141  3  60006 303 1 1 0       1 1 1
    278.8602460.6286 -9.8484 3  183.7169 35  60006 30317 215      17 216
    348.6338575.8220 -9.7067 3  197.2128 37  60006 30318 216      18 217
    430.7401711.3517 -9.5756 3  211.4579 39  60006 30319 217      19 218
```

```
   526.5542869.4771 -9.4541 3  226.4522 41  60006 30320 218      20 219
   662.4463556.0773 -8.4944 3   19.5070  5  60006 303 2 1 1       2 1 2
  1324.9087999.9999 -8.0519 3   21.7464  7  60006 303 3 1 2       3 1 3
  2208.2169999.9999 -7.7271 3   24.7321  9  60006 303 4 1 3       4 1 4
  3312.3922999.9999 -7.4717 3   28.4643 11  60006 303 5 1 4       5 1 5
  4637.4613999.9999 -7.2623 3   32.9428 13  60006 303 6 1 5       6 1 6
  6183.4559999.9999 -7.0862 3   38.1678 15  60006 303 7 1 6       7 1 7
  7950.4128999.9999 -6.9351 3   44.1390 17  60006 303 8 1 7       8 1 8
  9938.3737999.9999 -6.8039 3   50.8565 19  60006 303 9 1 8       9 1 9
 12147.3852999.9999 -6.6889 3   58.3203 21  60006 30310 1 9      10 110
 14577.4987999.9999 -6.5874 3   66.5303 23  60006 30311 110      11 111
 17228.7699999.9999 -6.4973 3   75.4865 25  60006 30312 111      12 112
 20101.2591999.9999 -6.4172 3   85.1887 27  60006 30313 112      13 113
 22489.8427  0.0055 -5.3136 3    0.0000  3  60006 303 1 0 1       0 0 0
 23195.0307999.9999 -6.3458 3   95.6370 29  60006 30314 113      14 114
 26510.1531999.9999 -6.2823 3  106.8313 31  60006 30315 114      15 115
 30046.6986999.9999 -6.2257 3  118.7716 33  60006 30316 115      16 116
 33804.7431999.9999 -6.1755 3  131.4577 35  60006 30317 116      17 117
 37784.3655999.9999 -6.1311 3  144.8895 37  60006 30318 117      18 118
 41985.6481999.9999 -6.0921 3  159.0671 39  60006 30319 118      19 119
 44755.9371185.2407 -4.5781 3   18.0141  5  60006 303 2 1 2       1 1 1
 44979.5035  0.0105 -4.4129 3    0.7502  5  60006 303 2 0 2       1 0 1
 45197.5697185.4775 -4.5696 3   18.0215  5  60006 303 2 1 1       1 1 0
 46408.6759999.9999 -6.0580 3  173.9903 41  60006 30320 119      20 120
 47176.5733999.9999 -4.1367 3  157.4935 39  60006 30319 119      20 020
 67133.5767277.6384 -3.9799 3   19.5070  7  60006 303 3 1 3       2 1 2
 67451.9244  0.4749 -4.2877 3   71.2343  7  60006 303 3 2 2       2 2 1
 67452.2118  0.9498 -4.2877 3   71.2343  7  60006 303 3 2 1       2 2 0
 67468.8003  0.0148 -3.8885 3    2.2505  7  60006 303 3 0 3       2 0 2
 67796.0391278.4389 -3.9715 3   19.5291  7  60006 303 3 1 2       2 1 1
 71698.4087999.9999 -3.7672 3  142.4979 37  60006 30318 118      19 019
 89510.8216369.7688 -3.5874 3   21.7464  9  60006 303 4 1 4       3 1 3
 89905.7714  1.4255 -4.2013 3  159.3937  9  60006 303 4 3 2       3 3 1
 89905.7715  1.4257 -4.2013 3  159.3937  9  60006 303 4 3 1       3 3 0
 89935.3236  1.0946 -3.7880 3   73.4843  9  60006 303 4 2 3       3 2 2
 89936.0421  2.2820 -3.7880 3   73.4843  9  60006 303 4 2 2       3 2 1
 89957.5512  0.0179 -3.5192 3    4.5011  9  60006 303 4 0 4       3 0 3
 90394.1298371.6674 -3.5790 3   21.7906  9  60006 303 4 1 3       3 1 2
 96120.5875999.9999 -3.5094 3  128.2514 35  60006 30317 117      18 018
111887.5404461.5429 -3.2934 3   24.7321 11  60006 303 5 1 5       4 1 4
112326.5868  2.6410 -4.2520 3  282.0839 11  60006 303 5 4 1       4 4 0
112326.5868  2.6410 -4.2520 3  282.0839 11  60006 303 5 4 2       4 4 1
112381.4510  2.7832 -3.7524 3  162.3927 11  60006 303 5 3 3       4 3 2
112381.4513  2.7840 -3.7524 3  162.3927 11  60006 303 5 3 2       4 3 1
112418.2295  2.1098 -3.4551 3   76.4842 11  60006 303 5 2 4       4 2 3
112419.6665  4.4849 -3.4551 3   76.4842 11  60006 303 5 2 3       4 2 2
112445.5741  0.0200 -3.2355 3    7.5017 11  60006 303 5 0 5       4 0 4
112991.7157465.2518 -3.2851 3   24.8058 11  60006 303 5 1 4       4 1 3
120442.0065999.9999 -3.3134 3  114.7541 33  60006 30316 116      17 017
134263.6014552.8714 -3.0589 3   28.4643 13  60006 303 6 1 6       5 1 5
134700.5944  4.4579 -4.4134 3  438.7579 13  60006 303 6 5 1       5 5 0
134700.5944  4.4579 -4.4134 3  438.7579 13  60006 303 6 5 2       5 5 1
134790.7455  4.5622 -3.8346 3  285.8307 13  60006 303 6 4 2       5 4 1
134790.7455  4.5622 -3.8346 3  285.8307 13  60006 303 6 4 3       5 4 2
```

```
134856.6218  4.8083 -3.4546 3  166.1413 13  60006 303 6 3 4       5 3 3
134856.6226  4.8104 -3.4546 3  166.1413 13  60006 303 6 3 3       5 3 2
134900.5187  3.6195 -3.2016 3   80.2341 13  60006 303 6 2 5       5 2 4
134903.0336  7.7763 -3.2016 3   80.2342 13  60006 303 6 2 4       5 2 3
134932.6871  0.0219 -3.0066 3   11.2525 13  60006 303 6 0 6       5 0 5
135588.6706559.2811 -3.0507 3   28.5748 13  60006 303 6 1 5       5 1 4
144661.6148999.9999 -3.1574 3  102.0060 31  60006 30315 115      16 016
156638.8733643.6651 -2.8649 3   32.9428 15  60006 303 7 1 7       6 1 6
157010.6364  6.9912 -4.6712 3  628.7638 15  60006 303 7 6 1       6 6 0
157010.6364  6.9912 -4.6712 3  628.7638 15  60006 303 7 6 2       6 6 1
157149.0799  7.0766 -4.0178 3  443.2510 15  60006 303 7 5 2       6 5 1
157149.0799  7.0766 -4.0178 3  443.2510 15  60006 303 7 5 3       6 5 2
157254.2724  7.2432 -3.5604 3  290.3269 15  60006 303 7 4 3       6 4 2
157254.2724  7.2432 -3.5604 3  290.3269 15  60006 303 7 4 4       6 4 3
157331.1819  7.6342 -3.2271 3  170.6396 15  60006 303 7 3 5       6 3 4
157331.1838  7.6389 -3.2271 3  170.6396 15  60006 303 7 3 4       6 3 3
157382.0679  5.7224 -2.9967 3   84.7339 15  60006 303 7 2 6       6 2 5
157386.0922 12.3738 -2.9967 3   84.7340 15  60006 303 7 2 5       6 2 4
157418.7080  0.0255 -2.8159 3   15.7534 15  60006 303 7 0 7       6 0 6
158184.8679653.8440 -2.8568 3   33.0975 15  60006 303 7 1 6       6 1 5
168778.4138999.9999 -3.0301 3   90.0072 29  60006 30314 114      15 015
179013.2247733.8345 -2.7005 3   38.1678 17  60006 303 8 1 8       7 1 7
179235.5351 10.3585 -5.0165 3  851.3828 17  60006 303 8 7 1       7 7 0
179235.5351 10.3585 -5.0165 3  851.3828 17  60006 303 8 7 2       7 7 1
179438.5982 10.4325 -4.2917 3  634.0011 17  60006 303 8 6 2       7 6 1
179438.5982 10.4325 -4.2917 3  634.0011 17  60006 303 8 6 3       7 6 2
179596.8208 10.5611 -3.7606 3  448.4930 17  60006 303 8 5 3       7 5 2
179596.8208 10.5611 -3.7606 3  448.4930 17  60006 303 8 5 4       7 5 3
179717.0621 10.8108 -3.3513 3  295.5723 17  60006 303 8 4 4       7 4 3
179717.0621 10.8108 -3.3513 3  295.5723 17  60006 303 8 4 5       7 4 4
179805.0295 11.3941 -3.0425 3  175.8876 17  60006 303 8 3 6       7 3 5
179805.0333 11.4033 -3.0425 3  175.8876 17  60006 303 8 3 5       7 3 4
179862.7538  8.5176 -2.8255 3   89.9836 17  60006 303 8 2 7       7 2 6
179868.7909 18.4953 -2.8255 3   89.9839 17  60006 303 8 2 6       7 2 5
179903.4547  0.0334 -2.6536 3   21.0043 17  60006 303 8 0 8       7 0 7
180780.1816749.0291 -2.6925 3   38.3740 17  60006 303 8 1 7       7 1 6
192791.4567999.9999 -2.9249 3   78.7579 27  60006 30313 113      14 014
201349.3188 14.6781 -5.4431 3 1105.8770 19  60006 303 9 8 1       8 8 0
201349.3188 14.6781 -5.4431 3 1105.8770 19  60006 303 9 8 2       8 8 1
201386.5241823.2903 -2.5588 3   44.1390 19  60006 303 9 1 9       8 1 8
201637.2742 14.7444 -4.6495 3  857.3615 19  60006 303 9 7 2       8 7 1
201637.2742 14.7444 -4.6495 3  857.3615 19  60006 303 9 7 3       8 7 2
201865.7084 14.8509 -4.0477 3  639.9865 19  60006 303 9 6 3       8 6 2
201865.7084 14.8509 -4.0477 3  639.9865 19  60006 303 9 6 4       8 6 3
202043.7106 15.0350 -3.5656 3  454.4837 19  60006 303 9 5 4       8 5 3
202043.7106 15.0350 -3.5656 3  454.4837 19  60006 303 9 5 5       8 5 4
202179.0095 15.3914 -3.1818 3  301.5670 19  60006 303 9 4 5       8 4 4
202179.0095 15.3914 -3.1818 3  301.5670 19  60006 303 9 4 6       8 4 5
202278.0628 16.2209 -2.8877 3  181.8853 19  60006 303 9 3 7       8 3 6
202278.0698 16.2378 -2.8877 3  181.8853 19  60006 303 9 3 6       8 3 5
202342.4530 12.1037 -2.6793 3   95.9831 19  60006 303 9 2 8       8 2 7
202351.0785 26.3586 -2.6793 3   95.9837 19  60006 303 9 2 7       8 2 6
202386.7450  0.0472 -2.5135 3   27.0052 19  60006 303 9 0 9       8 0 8
203374.4850844.9248 -2.5509 3   44.4042 19  60006 303 9 1 8       8 1 7
```

```
216699.8488999.9999 -2.8377 3   68.2581 25  60006 30312 112      13 013
223320.4480 20.0686 -5.9463 3 1391.5437 21  60006 30310 9 1        9 9 0
223320.4480 20.0686 -5.9463 3 1391.5437 21  60006 30310 9 2        9 9 1
223718.1349 20.1293 -5.0862 3 1112.5932 21  60006 30310 8 2        9 8 1
223718.1349 20.1293 -5.0862 3 1112.5932 21  60006 30310 8 3        9 8 2
223758.6402911.9427 -2.4353 3   50.8565 21  60006 30310 110       9 1 9
224038.0595 20.2213 -4.4161 3  864.0874 21  60006 30310 7 3        9 7 2
224038.0595 20.2213 -4.4161 3  864.0874 21  60006 30310 7 4        9 7 3
224291.8606 20.3684 -3.8638 3  646.7200 21  60006 30310 6 4        9 6 3
224291.8606 20.3684 -3.8638 3  646.7200 21  60006 30310 6 5        9 6 4
224489.6432 20.6220 -3.4078 3  461.2231 21  60006 30310 5 5        9 5 4
224489.6432 20.6220 -3.4078 3  461.2231 21  60006 30310 5 6        9 5 5
224640.0091 21.1119 -3.0395 3  308.3110 21  60006 30310 4 6        9 4 5
224640.0091 21.1119 -3.0395 3  308.3110 21  60006 30310 4 7        9 4 6
224750.1798 22.2477 -2.7551 3  188.6326 21  60006 30310 3 8        9 3 7
224750.1918 22.2767 -2.7551 3  188.6326 21  60006 30310 3 7        9 3 6
224821.0421 16.5797 -2.5526 3  102.7326 21  60006 30310 2 9        9 2 8
224832.9041 36.1817 -2.5526 3  102.7334 21  60006 30310 2 8        9 2 7
224868.3966  0.0675 -2.3911 3   33.7561 21  60006 30310 010       9 0 9
225967.6517941.6194 -2.4275 3   51.1880 21  60006 30310 1 9        9 1 8
240502.7470999.9999 -2.7661 3   58.5080 23  60006 30311 111      12 012
245111.0419 26.6484 -6.5228 3 1707.7808 23  60006 3031110 1      1010 0
245111.0419 26.6484 -6.5228 3 1707.7808 23  60006 3031110 2      1010 1
245648.4856 26.7052 -5.5979 3 1398.9929 23  60006 30311 9 2       10 9 1
245648.4856 26.7052 -5.5979 3 1398.9929 23  60006 30311 9 3       10 9 2
246085.8995 26.7869 -4.8616 3 1120.0557 23  60006 30311 8 3       10 8 2
246085.8995 26.7869 -4.8616 3 1120.0557 23  60006 30311 8 4       10 8 3
246129.4418999.7020 -2.3267 3   58.3203 23  60006 30311 111      10 110
246437.7852 26.9104 -4.2413 3  871.5605 23  60006 30311 7 4       10 7 3
246437.7852 26.9104 -4.2413 3  871.5605 23  60006 30311 7 5       10 7 4
246716.9486 27.1073 -3.7155 3  654.2016 23  60006 30311 6 5       10 6 4
246716.9486 27.1073 -3.7155 3  654.2016 23  60006 30311 6 6       10 6 5
246934.5122 27.4459 -3.2756 3  468.7113 23  60006 30311 5 6       10 5 5
246934.5122 27.4459 -3.2756 3  468.7113 23  60006 30311 5 7       10 5 6
247099.9560 28.0989 -2.9176 3  315.8042 23  60006 30311 4 7       10 4 6
247099.9560 28.0989 -2.9176 3  315.8042 23  60006 30311 4 8       10 4 7
247221.2786 29.6073 -2.6399 3  196.1294 23  60006 30311 3 9       10 3 8
247221.2982 29.6544 -2.6399 3  196.1294 23  60006 30311 3 8       10 3 7
247298.3980 22.0443 -2.4417 3  110.2318 23  60006 30311 210       10 2 9
247314.2165 48.1824 -2.4417 3  110.2330 23  60006 30311 2 9       10 2 8
247348.2272  0.0945 -2.2833 3   41.2569 23  60006 30311 011       10 010
248559.5552999.9999 -2.3191 3   58.7255 23  60006 30311 110       10 1 9
264199.3597999.9999 -2.7086 3   49.5076 21  60006 30310 110       11 011
266676.1047 34.5361 -7.1700 3 2054.1582 25  60006 3031211 1       1111 0
266676.1047 34.5361 -7.1700 3 2054.1582 25  60006 3031211 2       1111 1
267389.1364 34.5902 -6.1816 3 1715.9568 25  60006 3031210 2       1110 1
267389.1364 34.5902 -6.1816 3 1715.9568 25  60006 3031210 3       1110 2
267975.3785 34.6646 -5.3807 3 1407.1869 25  60006 30312 9 3       11 9 2
267975.3785 34.6646 -5.3807 3 1407.1869 25  60006 30312 9 4       11 9 3
268452.5074 34.7716 -4.6945 3 1128.2642 25  60006 30312 8 4       11 8 3
268452.5074 34.7716 -4.6945 3 1128.2642 25  60006 30312 8 5       11 8 4
268498.7977999.9999 -2.2306 3   66.5303 25  60006 30312 112       11 111
268836.3453 34.9329 -4.1011 3  879.7808 25  60006 30312 7 5       11 7 4
268836.3453 34.9329 -4.1011 3  879.7808 25  60006 30312 7 6       11 7 5
```

```
269140.8659 35.1896 -3.5917 3  662.4312 25  60006 30312 6 6      11 6 5
269140.8659 35.1896 -3.5917 3  662.4312 25  60006 30312 6 7      11 6 6
269378.2114 35.6303 -3.1625 3  476.9482 25  60006 30312 5 7      11 5 6
269378.2114 35.6303 -3.1625 3  476.9482 25  60006 30312 5 8      11 5 7
269558.7449 36.4791 -2.8118 3  324.0465 25  60006 30312 4 8      11 4 7
269558.7449 36.4790 -2.8118 3  324.0465 25  60006 30312 4 9      11 4 8
269691.2574 38.4322 -2.5390 3  204.3758 25  60006 30312 310      11 3 9
269691.2878 38.5056 -2.5390 3  204.3758 25  60006 30312 3 9      11 3 8
269774.3972 28.5963 -2.3440 3  118.4808 25  60006 30312 211      11 210
269794.9648 62.5788 -2.3439 3  118.4825 25  60006 30312 210      11 2 9
269826.0545  0.1287 -2.1879 3   49.5076 25  60006 30312 012      11 011
271150.0689999.9999 -2.2232 3   67.0166 25  60006 30312 111      11 110
287788.9467999.9999 -2.6642 3   41.2569 19  60006 303 9 1 9      10 010
287962.7528 43.8501 -7.8865 3 2430.4997 27  60006 3031312 1      1212 0
287962.7528 43.8501 -7.8865 3 2430.4997 27  60006 3031312 2      1212 1
288893.6287 43.9028 -6.8351 3 2063.0536 27  60006 3031311 2      1211 1
288893.6287 43.9028 -6.8351 3 2063.0536 27  60006 3031311 3      1211 2
289665.9980 43.9718 -5.9708 3 1724.8760 27  60006 3031310 3      1210 2
289665.9980 43.9718 -5.9708 3 1724.8760 27  60006 3031310 4      1210 3
290301.0227 44.0670 -5.2202 3 1416.1256 27  60006 30313 9 4      12 9 3
290301.0227 44.0670 -5.2202 3 1416.1256 27  60006 30313 9 5      12 9 4
290817.8538 44.2041 -4.5610 3 1137.2188 27  60006 30313 8 5      12 8 4
290817.8538 44.2041 -4.5610 3 1137.2188 27  60006 30313 8 6      12 8 5
290866.5768999.9999 -2.1454 3   75.4865 27  60006 30313 113      12 112
291233.6341 44.4102 -3.9843 3  888.7482 27  60006 30313 7 6      12 7 5
291233.6341 44.4102 -3.9843 3  888.7482 27  60006 30313 7 7      12 7 6
291563.5064 44.7376 -3.4860 3  671.4087 27  60006 30313 6 7      12 6 6
291563.5064 44.7376 -3.4860 3  671.4087 27  60006 30313 6 8      12 6 7
291820.6347 45.2989 -3.0644 3  485.9336 27  60006 30313 5 8      12 5 7
291820.6347 45.2989 -3.0644 3  485.9336 27  60006 30313 5 9      12 5 8
292016.2706 46.3790 -2.7190 3  333.0380 27  60006 30313 410      12 4 9
292016.2707 46.3791 -2.7190 3  333.0380 27  60006 30313 4 9      12 4 8
292160.0139 48.8550 -2.4499 3  213.3718 27  60006 30313 311      12 310
292160.0596 48.9650 -2.4499 3  213.3718 27  60006 30313 310      12 3 9
292248.9165 36.3344 -2.2574 3  127.4795 27  60006 30313 212      12 211
292275.0982 79.5887 -2.2573 3  127.4819 27  60006 30313 211      12 210
292301.6959  0.1705 -2.1032 3   58.5080 27  60006 30313 013      12 012
293739.0660999.9999 -2.1381 3   76.0611 27  60006 30313 112      12 111
308909.4404 54.7088 -8.6716 3 2836.9723 29  60006 3031413 1      1313 0
308909.4404 54.7088 -8.6716 3 2836.9723 29  60006 3031413 2      1313 1
310107.4618 54.7613 -7.5570 3 2440.1051 29  60006 3031412 2      1312 1
310107.4618 54.7613 -7.5570 3 2440.1051 29  60006 3031412 3      1312 2
311109.8368 54.8268 -6.6299 3 2072.6900 29  60006 3031411 3      1311 2
311109.8368 54.8268 -6.6299 3 2072.6900 29  60006 3031411 4      1311 3
311270.8193999.9999 -2.6330 3   33.7561 17  60006 303 8 1 8       9 0 9
311941.5240 54.9133 -5.8161 3 1734.5382 29  60006 3031410 4      1310 3
311941.5240 54.9133 -5.8161 3 1734.5382 29  60006 3031410 5      1310 4
312625.3144 55.0328 -5.0928 3 1425.8090 29  60006 30314 9 5      13 9 4
312625.3144 55.0328 -5.0928 3 1425.8090 29  60006 30314 9 6      13 9 5
313181.8335 55.2048 -4.4505 3 1146.9195 29  60006 30314 8 6      13 8 5
313181.8335 55.2048 -4.4505 3 1146.9195 29  60006 30314 8 7      13 8 6
313232.6481999.9999 -2.0695 3   85.1887 29  60006 30314 114      13 113
313629.5456 55.4633 -3.8850 3  898.4627 29  60006 30314 7 7      13 7 6
313629.5456 55.4633 -3.8850 3  898.4627 29  60006 30314 7 8      13 7 7
```

```
313984.7637 55.8733 -3.3946 3  681.1343 29  60006 30314 6 8      13 6 7
313984.7637 55.8733 -3.3946 3  681.1343 29  60006 30314 6 9      13 6 8
314261.6757 56.5755 -2.9786 3  495.6677 29  60006 30314 5 9      13 5 8
314261.6757 56.5755 -2.9786 3  495.6677 29  60006 30314 510      13 5 9
314472.4282 57.9257 -2.6373 3  342.7787 29  60006 30314 410      13 4 9
314472.4282 57.9255 -2.6373 3  342.7787 29  60006 30314 411      13 410
314627.4463 61.0078 -2.3711 3  223.1172 29  60006 30314 312      13 311
314627.5127 61.1679 -2.3711 3  223.1172 29  60006 30314 311      13 310
314721.8325 45.3574 -2.1805 3  137.2279 29  60006 30314 213      13 212
314754.5661 99.4300 -2.1804 3  137.2311 29  60006 30314 212      13 211
314774.9689  0.2204 -2.0278 3   68.2581 29  60006 30314 014      13 013
316326.4197999.9999 -2.0624 3   85.8592 29  60006 30314 113      13 112
329445.1870 67.2302 -9.5260 3 3274.1845 31  60006 3031514 1      1414 0
329445.1870 67.2302 -9.5260 3 3274.1845 31  60006 3031514 2      1414 1
330967.3189 67.2840 -8.3470 3 2847.2764 31  60006 3031513 2      1413 1
330967.3189 67.2840 -8.3470 3 2847.2764 31  60006 3031513 3      1413 2
332250.7775 67.3476 -7.3569 3 2450.4491 31  60006 3031512 3      1412 2
332250.7775 67.3476 -7.3569 3 2450.4491 31  60006 3031512 4      1412 3
333324.6279 67.4278 -6.4804 3 2083.0675 31  60006 3031511 4      1411 3
333324.6279 67.4278 -6.4804 3 2083.0675 31  60006 3031511 5      1411 4
334215.6120 67.5345 -5.6940 3 1744.9434 31  60006 3031510 5      1410 4
334215.6120 67.5345 -5.6940 3 1744.9434 31  60006 3031510 6      1410 5
334644.3396999.9999 -2.6153 3   27.0052 15  60006 303 7 1 7       8 0 8
334948.1497 67.6822 -4.9876 3 1436.2370 31  60006 30315 9 6      14 9 5
334948.1497 67.6822 -4.9876 3 1436.2370 31  60006 30315 9 7      14 9 6
335544.3417 67.8946 -4.3568 3 1157.3661 31  60006 30315 8 7      14 8 6
335544.3417 67.8946 -4.3568 3 1157.3661 31  60006 30315 8 8      14 8 7
335596.8806999.9999 -2.0018 3   95.6370 31  60006 30315 115      14 114
336023.9742 68.2136 -3.7994 3  908.9243 31  60006 30315 7 8      14 7 7
336023.9742 68.2136 -3.7994 3  908.9243 31  60006 30315 7 9      14 7 8
336404.5316 68.7190 -3.3149 3  691.6077 31  60006 30315 6 9      14 6 8
336404.5316 68.7190 -3.3149 3  691.6077 31  60006 30315 610      14 6 9
336701.2284 69.5837 -2.9033 3  506.1504 31  60006 30315 510      14 5 9
336701.2284 69.5837 -2.9033 3  506.1504 31  60006 30315 511      14 510
336927.1125 71.2452 -2.5651 3  353.2683 31  60006 30315 412      14 411
336927.1126 71.2455 -2.5651 3  353.2683 31  60006 30315 411      14 410
337093.4524 75.0227 -2.3012 3  233.6120 31  60006 30315 313      14 312
337093.5465 75.2496 -2.3012 3  233.6120 31  60006 30315 312      14 311
337193.0218 55.7640 -2.1121 3  147.7258 31  60006 30315 214      14 213
337233.3178122.3206 -2.1120 3  147.7302 31  60006 30315 213      14 212
337245.6911  0.2790 -1.9605 3   78.7579 31  60006 30315 015      14 014
338912.0031999.9999 -1.9950 3   96.4107 31  60006 30315 114      14 113
349488.8035 81.5323-10.4515 3 3743.2933 33  60006 3031615 1      1515 0
349488.8035 81.5323-10.4515 3 3743.2933 33  60006 3031615 2      1515 1
351400.2944 81.5890 -9.2058 3 3285.1736 33  60006 3031614 2      1514 1
351400.2944 81.5890 -9.2058 3 3285.1736 33  60006 3031614 3      1514 2
353023.7329 81.6524 -8.1515 3 2858.3162 33  60006 3031613 3      1513 2
353023.7329 81.6524 -8.1515 3 2858.3162 33  60006 3031613 4      1513 3
354392.6006 81.7287 -7.2120 3 2461.5318 33  60006 3031612 4      1512 3
354392.6006 81.7287 -7.2120 3 2461.5318 33  60006 3031612 5      1512 4
355537.9009 81.8258 -6.3630 3 2094.1860 33  60006 3031611 5      1511 4
355537.9009 81.8258 -6.3630 3 2094.1860 33  60006 3031611 6      1511 5
356488.1592 81.9555 -5.5937 3 1756.0917 33  60006 3031610 6      1510 5
356488.1592 81.9555 -5.5937 3 1756.0917 33  60006 3031610 7      1510 6
```

```
357269.4248 82.1354 -4.8990 3 1447.4097 33  60006 30316 9 7      15 9 6
357269.4248 82.1354 -4.8990 3 1447.4097 33  60006 30316 9 8      15 9 7
357905.2734 82.3941 -4.2764 3 1168.5586 33  60006 30316 8 8      15 8 7
357905.2734 82.3941 -4.2764 3 1168.5586 33  60006 30316 8 9      15 8 8
357908.9210999.9999 -2.6125 3   21.0043 13  60006 303 6 1 6       7 0 7
357959.1436999.9999 -1.9416 3  106.8313 33  60006 30316 116      15 115
358416.8141 82.7822 -3.7251 3  920.1328 33  60006 30316 7 9      15 7 8
358416.8141 82.7822 -3.7251 3  920.1328 33  60006 30316 710      15 7 9
358822.7039 83.3967 -3.2450 3  702.8289 33  60006 30316 610      15 6 9
358822.7039 83.3967 -3.2450 3  702.8289 33  60006 30316 611      15 610
359139.1867 84.4472 -2.8368 3  517.3815 33  60006 30316 511      15 510
359139.1867 84.4472 -2.8368 3  517.3815 33  60006 30316 512      15 511
359380.2185 86.4649 -2.5013 3  364.5070 33  60006 30316 413      15 412
359380.2187 86.4653 -2.5013 3  364.5070 33  60006 30316 412      15 411
359557.9300 91.0315 -2.2391 3  244.8562 33  60006 30316 314      15 313
359558.0604 91.3457 -2.2391 3  244.8562 33  60006 30316 313      15 312
359662.3614 67.6529 -2.0513 3  158.9734 33  60006 30316 215      15 214
359711.3028148.4782 -2.0512 3  158.9791 33  60006 30316 214      15 213
359713.6796  0.3470 -1.9007 3   90.0072 33  60006 30316 016      15 015
361495.6891999.9999 -1.9350 3  107.7156 33  60006 30316 115      15 114
371323.1202 97.7943-10.1354 3 3754.9510 35  60006 3031715 2      1615 1
371323.1202 97.7943-10.1354 3 3754.9510 35  60006 3031715 3      1615 2
373353.8726 97.8595 -9.0144 3 3296.8951 35  60006 3031714 3      1614 2
373353.8726 97.8595 -9.0144 3 3296.8951 35  60006 3031714 4      1614 3
375078.5849 97.9337 -8.0108 3 2870.0919 35  60006 3031713 4      1613 3
375078.5849 97.9337 -8.0108 3 2870.0919 35  60006 3031713 5      1613 4
376532.8318 98.0242 -7.0989 3 2473.3531 35  60006 3031712 5      1612 4
376532.8318 98.0242 -7.0989 3 2473.3531 35  60006 3031712 6      1612 5
377749.5549 98.1404 -6.2672 3 2106.0455 35  60006 3031711 6      1611 5
377749.5549 98.1404 -6.2672 3 2106.0455 35  60006 3031711 7      1611 6
378759.0633 98.2962 -5.5096 3 1767.9828 35  60006 3031710 7      1610 6
378759.0633 98.2962 -5.5096 3 1767.9828 35  60006 3031710 8      1610 7
379589.0357 98.5126 -4.8233 3 1459.3269 35  60006 30317 9 8      16 9 7
379589.0357 98.5126 -4.8233 3 1459.3269 35  60006 30317 9 9      16 9 8
380264.5237 98.8239 -4.2069 3 1180.4971 35  60006 30317 8 9      16 8 8
380264.5237 98.8239 -4.2069 3 1180.4971 35  60006 30317 810      16 8 9
380319.3062999.9999 -1.8881 3  118.7716 35  60006 30317 117      16 116
380807.9597 99.2905 -3.6602 3  932.0883 35  60006 30317 710      16 7 9
380807.9597 99.2905 -3.6602 3  932.0883 35  60006 30317 711      16 710
381064.0275999.9999 -2.6275 3   15.7534 11  60006 303 5 1 5       6 0 6
381239.1744100.0287 -3.1837 3  714.7979 35  60006 30317 611      16 610
381239.1744100.0287 -3.1837 3  714.7979 35  60006 30317 612      16 611
381575.4444101.2899 -2.7783 3  529.3611 35  60006 30317 512      16 511
381575.4444101.2899 -2.7783 3  529.3611 35  60006 30317 513      16 512
381831.6413103.7112 -2.4447 3  376.4946 35  60006 30317 414      16 413
381831.6416103.7119 -2.4447 3  376.4946 35  60006 30317 413      16 412
382020.7770109.1657 -2.1841 3  256.8498 35  60006 30317 315      16 314
382020.9540109.5922 -2.1841 3  256.8498 35  60006 30317 314      16 313
382129.7277 81.1228 -1.9973 3  170.9704 35  60006 30317 216      16 215
382178.7519  0.4249 -1.8475 3  102.0060 35  60006 30317 017      16 016
382188.4707178.1205 -1.9972 3  170.9778 35  60006 30317 215      16 214
384077.3506999.9999 -1.8818 3  119.7738 35  60006 30317 116      16 115
393155.8498116.0866 -9.9477 3 3767.3370 37  60006 3031815 3      1715 2
393155.8498116.0866 -9.9477 3 3767.3370 37  60006 3031815 4      1715 3
```

```
395305.8262116.1611 -8.8775 3 3309.3488 37  60006 3031814 4      1714 3
395305.8262116.1611 -8.8775 3 3309.3488 37  60006 3031814 5      1714 4
397131.7775116.2474 -7.9016 3 2882.6031 37  60006 3031813 5      1713 4
397131.7775116.2474 -7.9016 3 2882.6031 37  60006 3031813 6      1713 5
398671.3718116.3538 -7.0071 3 2485.9129 37  60006 3031812 6      1712 5
398671.3718116.3538 -7.0071 3 2485.9129 37  60006 3031812 7      1712 6
399959.4889116.4915 -6.1872 3 2118.6459 37  60006 3031811 7      1711 6
399959.4889116.4915 -6.1872 3 2118.6459 37  60006 3031811 8      1711 7
401028.2218116.6768 -5.4381 3 1780.6169 37  60006 3031810 8      1710 7
401028.2218116.6768 -5.4381 3 1780.6169 37  60006 3031810 9      1710 8
401906.8788116.9343 -4.7580 3 1471.9886 37  60006 30318 9 9      17 9 8
401906.8788116.9343 -4.7580 3 1471.9886 37  60006 30318 910      17 9 9
402621.9878117.3047 -4.1464 3 1193.1813 37  60006 30318 810      17 8 9
402621.9878117.3047 -4.1464 3 1193.1813 37  60006 30318 811      17 810
402677.2379999.9999 -1.8407 3  131.4577 37  60006 30318 118      17 117
403197.3051117.8596 -3.6035 3  944.7907 37  60006 30318 711      17 710
403197.3051117.8596 -3.6035 3  944.7907 37  60006 30318 712      17 711
403653.8371118.7371 -3.1299 3  727.5147 37  60006 30318 612      17 611
403653.8371118.7371 -3.1299 3  727.5147 37  60006 30318 613      17 612
404009.8957120.2355 -2.7267 3  542.0891 37  60006 30318 513      17 512
404009.8957120.2355 -2.7267 3  542.0891 37  60006 30318 514      17 513
404109.1743925.3167 -2.6652 3   11.2525  9  60006 303 4 1 4      5 0 5
404281.2760123.1109 -2.3949 3  389.2312 37  60006 30318 415      17 414
404281.2763123.1119 -2.3949 3  389.2312 37  60006 30318 414      17 413
404481.8910129.5565 -2.1355 3  269.5926 37  60006 30318 316      17 315
404482.1271130.1253 -2.1355 3  269.5927 37  60006 30318 315      17 314
404594.9975 96.2722 -1.9495 3  183.7169 37  60006 30318 217      17 216
404640.7252  0.5134 -1.8004 3  114.7541 37  60006 30318 018      17 017
404664.7711211.4649 -1.9494 3  183.7262 37  60006 30318 216      17 215
406656.8603999.9999 -1.8346 3  132.5853 37  60006 30318 117      17 116
414986.8992136.5285 -9.8144 3 3780.4512 39  60006 3031915 4      1815 3
414986.8992136.5285 -9.8144 3 3780.4512 39  60006 3031915 5      1815 4
417256.0598136.6133 -8.7720 3 3322.5348 39  60006 3031914 5      1814 4
417256.0598136.6133 -8.7720 3 3322.5348 39  60006 3031914 6      1814 5
419183.2134136.7130 -7.8136 3 2895.8500 39  60006 3031913 6      1813 5
419183.2134136.7130 -7.8136 3 2895.8500 39  60006 3031913 7      1813 6
420808.1214136.8372 -6.9310 3 2499.2111 39  60006 3031912 7      1812 6
420808.1214136.8372 -6.9310 3 2499.2111 39  60006 3031912 8      1812 7
422167.6020136.9989 -6.1196 3 2131.9871 39  60006 3031911 8      1811 7
422167.6020136.9989 -6.1196 3 2131.9871 39  60006 3031911 9      1811 8
423295.5322137.2170 -5.3769 3 1793.9937 39  60006 3031910 9      1810 8
423295.5322137.2170 -5.3769 3 1793.9937 39  60006 303191010      1810 9
424222.8504137.5206 -4.7017 3 1485.3948 39  60006 30319 910      18 9 9
424222.8504137.5206 -4.7017 3 1485.3948 39  60006 30319 911      18 910
424977.5608137.9572 -4.0940 3 1206.6114 39  60006 30319 811      18 810
424977.5608137.9572 -4.0940 3 1206.6114 39  60006 30319 812      18 811
425032.8082999.9999 -1.7989 3  144.8895 39  60006 30319 119      18 118
425584.7450138.6109 -3.5540 3  958.2399 39  60006 30319 712      18 711
425584.7450138.6109 -3.5540 3  958.2399 39  60006 30319 713      18 712
426066.5859139.6440 -3.0828 3  740.9792 39  60006 30319 613      18 612
426066.5859139.6440 -3.0828 3  740.9792 39  60006 30319 614      18 613
426442.4345141.4076 -2.6814 3  555.5654 39  60006 30319 514      18 513
426442.4345141.4076 -2.6814 3  555.5654 39  60006 30319 515      18 514
426729.0177144.7907 -2.3510 3  402.7165 39  60006 30319 416      18 415
```

```
426729.0182144.7922 -2.3510 3  402.7165 39  60006 30319 415      18 414
426941.1698152.3350 -2.0927 3  283.0847 39  60006 30319 317      18 316
426941.4798153.0818 -2.0927 3  283.0847 39  60006 30319 316      18 315
427043.9268555.5478 -2.7354 3    7.5017  7  60006 303 3 1 3       4 0 4
427058.0476113.1997 -1.9074 3  197.2128 39  60006 30319 218      18 217
427099.4167  0.6131 -1.7589 3  128.2514 39  60006 30319 019      18 018
427140.1538248.7285 -1.9073 3  197.2244 39  60006 30319 217      18 216
429234.0908999.9999 -1.7931 3  146.1499 39  60006 30319 118      18 117
436816.1755159.2395 -9.7122 3 3794.2937 41  60006 3032015 5      1915 4
436816.1755159.2395 -9.7122 3 3794.2937 41  60006 3032015 6      1915 5
439204.4782159.3356 -8.6874 3 3336.4530 41  60006 3032014 6      1914 5
439204.4782159.3356 -8.6874 3 3336.4530 41  60006 3032014 7      1914 6
441232.7953159.4501 -7.7409 3 2909.8325 41  60006 3032013 7      1913 6
441232.7953159.4501 -7.7409 3 2909.8325 41  60006 3032013 8      1913 7
442942.9814159.5939 -6.8669 3 2513.2478 41  60006 3032012 8      1912 7
442942.9814159.5939 -6.8669 3 2513.2478 41  60006 3032012 9      1912 8
444373.7933159.7823 -6.0620 3 2146.0691 41  60006 3032011 9      1911 8
444373.7933159.7823 -6.0620 3 2146.0691 41  60006 303201110      1911 9
445560.8922160.0370 -5.3243 3 1808.1134 41  60006 303201010      1910 9
445560.8922160.0370 -5.3243 3 1808.1134 41  60006 303201011      191010
446536.8467160.3918 -4.6531 3 1499.5454 41  60006 30320 911      19 910
446536.8467160.3918 -4.6531 3 1499.5454 41  60006 30320 912      19 911
447331.1381160.9019 -4.0484 3 1220.7871 41  60006 30320 812      19 811
447331.1381160.9019 -4.0484 3 1220.7871 41  60006 30320 813      19 812
447385.8866999.9999 -1.7623 3  159.0671 41  60006 30320 120      19 119
447970.1736161.6655 -3.5109 3  972.4359 41  60006 30320 713      19 712
447970.1736161.6655 -3.5109 3  972.4359 41  60006 30320 714      19 713
448477.3148162.8718 -3.0417 3  755.1912 41  60006 30320 614      19 613
448477.3148162.8718 -3.0417 3  755.1912 41  60006 30320 615      19 614
448872.9549164.9300 -2.6419 3  569.7900 41  60006 30320 515      19 514
448872.9549164.9300 -2.6419 3  569.7900 41  60006 30320 516      19 515
449174.7616168.8774 -2.3126 3  416.9507 41  60006 30320 417      19 416
449174.7623168.8795 -2.3126 3  416.9507 41  60006 30320 416      19 415
449398.5108177.6318 -2.0552 3  297.3259 41  60006 30320 318      19 317
449398.9122178.5986 -2.0552 3  297.3260 41  60006 30320 317      19 316
449518.7545132.0040 -1.8706 3  211.4579 41  60006 30320 219      19 218
449554.6436  0.7244 -1.7226 3  142.4979 41  60006 30320 020      19 019
449614.5687290.1283 -1.8705 3  211.4722 41  60006 30320 218      19 217
449867.9013277.9096 -2.8610 3    4.5011  5  60006 303 2 1 2       3 0 3
451808.9144999.9999 -1.7568 3  160.4676 41  60006 30320 119      19 118
472580.7645 92.6692 -3.1156 3    2.2505  3  60006 303 1 1 1       2 0 2
517781.0816 92.6895 -2.5578 3    0.7502  3  60006 303 1 1 0       1 0 1
517999.1479278.1674 -2.3388 3    2.2505  5  60006 303 2 1 1       2 0 2
518326.3866556.6066 -2.1970 3    4.5011  7  60006 303 3 1 2       3 0 3
518762.9653928.2742 -2.0935 3    7.5017  9  60006 303 4 1 3       4 0 4
519309.1069999.9999 -2.0135 3   11.2525 11  60006 303 5 1 4       5 0 5
519965.0903999.9999 -1.9496 3   15.7534 13  60006 303 6 1 5       6 0 6
520731.2502999.9999 -1.8974 3   21.0043 15  60006 303 7 1 6       7 0 7
521607.9771999.9999 -1.8545 3   27.0052 17  60006 303 8 1 7       8 0 8
522595.7170999.9999 -1.8191 3   33.7561 19  60006 303 9 1 8       9 0 9
523694.9721999.9999 -1.7899 3   41.2569 21  60006 30310 1 9      10 010
524906.3002999.9999 -1.7661 3   49.5076 23  60006 30311 110      11 011
526230.3146999.9999 -1.7471 3   58.5080 25  60006 30312 111      12 012
527667.6847999.9999 -1.7323 3   68.2581 27  60006 30313 112      13 013
```

```
 529219.1355999.9999 -1.7213 3   78.7579 29  60006 30314 113      14 014
 530885.4475999.9999 -1.7138 3   90.0072 31  60006 30315 114      15 015
 532667.4570999.9999 -1.7095 3  102.0060 33  60006 30316 115      16 016
 534566.0557999.9999 -1.7083 3  114.7541 35  60006 30317 116      17 017
 536582.1909999.9999 -1.7099 3  128.2514 37  60006 30318 117      18 018
 538716.8650999.9999 -1.7143 3  142.4979 39  60006 30319 118      19 019
 540050.1107 92.6697 -2.6965 3    0.0000  3  60006 303 1 1 1       0 0 0
 540971.1358999.9999 -1.7212 3  157.4935 41  60006 30320 119      20 020
 562316.2050277.9102 -2.4877 3    0.7502  5  60006 303 2 1 2       1 0 1
 584470.2783555.5483 -2.3330 3    2.2505  7  60006 303 3 1 3       2 0 2
 606512.2996925.3168 -2.2093 3    4.5011  9  60006 303 4 1 4       3 0 3
 628442.2888999.9999 -2.1061 3    7.5017 11  60006 303 5 1 5       4 0 4
 650260.3161999.9999 -2.0179 3   11.2525 13  60006 303 6 1 6       5 0 5
 671966.5023999.9999 -1.9413 3   15.7534 15  60006 303 7 1 7       6 0 6
 693561.0190999.9999 -1.8740 3   21.0043 17  60006 303 8 1 8       7 0 7
 715044.0883999.9999 -1.8147 3   27.0052 19  60006 303 9 1 9       8 0 8
 736415.9835999.9999 -1.7621 3   33.7561 21  60006 30310 110       9 0 9
 757677.0287999.9999 -1.7155 3   41.2569 23  60006 30311 111      10 010
 778827.5992999.9999 -1.6743 3   49.5076 25  60006 30312 112      11 011
 799868.1215999.9999 -1.6379 3   58.5080 27  60006 30313 113      12 012
 820799.0738999.9999 -1.6060 3   68.2581 29  60006 30314 114      13 013
 841620.9855999.9999 -1.5782 3   78.7579 31  60006 30315 115      14 014
 862334.4380999.9999 -1.5542 3   90.0072 33  60006 30316 116      15 015
 882940.0646999.9999 -1.5339 3  102.0060 35  60006 30317 117      16 016
 903438.5506999.9999 -1.5170 3  114.7541 37  60006 30318 118      17 017
 923830.6335999.9999 -1.5034 3  128.2514 39  60006 30319 119      18 018
 944117.1035999.9999 -1.4928 3  142.4979 41  60006 30320 120      19 019
1076841.3755999.9999 -1.8441 3  175.5383 39  60006 30319 218      20 119
1101592.2423999.9999 -1.8204 3  160.4676 37  60006 30318 217      19 118
1123680.7914999.9999 -1.8252 3  173.9903 39  60006 30319 217      20 120
1126231.3356999.9999 -1.8003 3  146.1499 35  60006 30317 216      18 117
1143926.5242999.9999 -1.8040 3  159.0671 37  60006 30318 216      19 119
1150758.4683999.9999 -1.7842 3  132.5853 33  60006 30316 215      17 116
1164294.5613999.9999 -1.7861 3  144.8895 35  60006 30317 215      18 118
1175173.4575999.9999 -1.7722 3  119.7738 31  60006 30315 214      16 115
1184783.3285999.9999 -1.7720 3  131.4577 33  60006 30316 214      17 117
1199476.1248999.9999 -1.7646 3  107.7156 29  60006 30314 213      15 114
1205391.3319999.9999 -1.7618 3  118.7716 31  60006 30315 213      16 116
1223666.2954999.9999 -1.7620 3   96.4107 27  60006 30313 212      14 113
1226117.1577999.9999 -1.7558 3  106.8313 29  60006 30314 212      15 115
1246959.4722999.9999 -1.7545 3   95.6370 27  60006 30313 211      14 114
1247743.7987999.9999 -1.7646 3   85.8592 25  60006 30312 211      13 112
1267917.0221999.9999 -1.7584 3   85.1887 25  60006 30312 210      13 113
1271708.4674999.9999 -1.7732 3   76.0611 23  60006 30311 210      12 111
1288988.6341999.9999 -1.7682 3   75.4865 23  60006 30311 2 9      12 112
1295560.1384999.9999 -1.7887 3   67.0166 21  60006 30310 2 9      11 110
1310173.2154999.9999 -1.7846 3   66.5303 21  60006 30310 2 8      11 111
1319298.6514999.9999 -1.8123 3   58.7255 19  60006 303 9 2 8      10 1 9
1331469.7531999.9999 -1.8090 3   58.3203 19  60006 303 9 2 7      10 110
1342923.8502999.9999 -1.8457 3   51.1880 17  60006 303 8 2 7       9 1 8
1352877.3147999.9999 -1.8431 3   50.8565 17  60006 303 8 2 6       9 1 9
1366435.5814999.9999 -1.8913 3   44.4042 15  60006 303 7 2 6       8 1 7
1374395.0479999.9999 -1.8893 3   44.1390 15  60006 303 7 2 5       8 1 8
1389833.6950999.9999 -1.9531 3   38.3740 13  60006 303 6 2 5       7 1 6
```

```
1396022.1804999.9999 -1.9517 3   38.1678 13  60006 303 6 2 4       7 1 7
1413118.0442999.9999 -2.0378 3   33.0975 11  60006 303 5 2 4       6 1 5
1417758.0201999.9999 -2.0368 3   32.9428 11  60006 303 5 2 3       6 1 6
1436288.4852999.9999 -2.1579 3   28.5748  9  60006 303 4 2 3       5 1 4
1439601.9551999.9999 -2.1572 3   28.4643  9  60006 303 4 2 2       5 1 5
1459344.8773927.6403 -2.3413 3   24.8058  7  60006 303 3 2 2       4 1 3
1461553.4534926.5443 -2.3408 3   24.7321  7  60006 303 3 2 1       4 1 4
1482287.0827556.4476 -2.6746 3   21.7906  5  60006 303 2 2 1       3 1 2
1483612.0632555.8258 -2.6743 3   21.7464  5  60006 303 2 2 0       3 1 3
1526886.6843999.9999 -1.1697 3  175.5383 41  60006 30320 218      20 119
1529081.0299999.9999 -1.1604 3  160.4676 39  60006 30319 217      19 118
1531174.9669999.9999 -1.1538 3  146.1499 37  60006 30318 216      18 117
1533167.0561999.9999 -1.1502 3  132.5853 35  60006 30317 215      17 116
1535055.9361999.9999 -1.1495 3  119.7738 33  60006 30316 214      16 115
1536840.3224999.9999 -1.1522 3  107.7156 31  60006 30315 213      15 114
1538519.0077999.9999 -1.1582 3   96.4107 29  60006 30314 212      14 113
1540090.8612999.9999 -1.1680 3   85.8592 27  60006 30313 211      13 112
1541554.8290999.9999 -1.1820 3   76.0611 25  60006 30312 210      12 111
1542909.9331999.9999 -1.2005 3   67.0166 23  60006 30311 2 9      11 110
1544155.2719999.9999 -1.2242 3   58.7255 21  60006 30310 2 8      10 1 9
1545290.0196999.9999 -1.2538 3   51.1880 19  60006 303 9 2 7       9 1 8
1546313.4260999.9999 -1.2905 3   44.4042 17  60006 303 8 2 6       8 1 7
1547224.8167999.9999 -1.3360 3   38.3740 15  60006 303 7 2 5       7 1 6
1548023.5924999.9999 -1.3926 3   33.0975 13  60006 303 6 2 4       6 1 5
1548709.2293999.9999 -1.4645 3   28.5748 11  60006 303 5 2 3       5 1 4
1549281.2786924.7646 -1.5597 3   24.8058  9  60006 303 4 2 2       4 1 3
1549739.3663555.3792 -1.6960 3   21.7906  7  60006 303 3 2 1       3 1 2
1550083.1936277.8899 -1.9344 3   19.5291  5  60006 303 2 2 0       2 1 1
1550745.5681278.0686 -1.9342 3   19.5070  5  60006 303 2 2 1       2 1 2
1551063.9158556.1817 -1.6958 3   21.7464  7  60006 303 3 2 2       3 1 3
1551488.4178927.0449 -1.5593 3   24.7321  9  60006 303 4 2 3       4 1 4
1552019.1070999.9999 -1.4640 3   28.4643 11  60006 303 5 2 4       5 1 5
1552656.0243999.9999 -1.3918 3   32.9428 13  60006 303 6 2 5       6 1 6
1553399.2189999.9999 -1.3349 3   38.1678 15  60006 303 7 2 6       7 1 7
1554248.7480999.9999 -1.2891 3   44.1390 17  60006 303 8 2 7       8 1 8
1555204.6769999.9999 -1.2521 3   50.8565 19  60006 303 9 2 8       9 1 9
1556267.0788999.9999 -1.2220 3   58.3203 21  60006 30310 2 9      10 110
1557436.0350999.9999 -1.1979 3   66.5303 23  60006 30311 210      11 111
1558711.6346999.9999 -1.1789 3   75.4865 25  60006 30312 211      12 112
1560093.9742999.9999 -1.1645 3   85.1887 27  60006 30313 212      13 113
1561583.1585999.9999 -1.1541 3   95.6370 29  60006 30314 213      14 114
1563179.2998999.9999 -1.1475 3  106.8313 31  60006 30315 214      15 115
1564882.5175999.9999 -1.1442 3  118.7716 33  60006 30316 215      16 116
1566692.9390999.9999 -1.1442 3  131.4577 35  60006 30317 216      17 117
1568610.6986999.9999 -1.1472 3  144.8895 37  60006 30318 217      18 118
1570635.9380999.9999 -1.1530 3  159.0671 39  60006 30319 218      19 119
1572768.8059999.9999 -1.1615 3  173.9903 41  60006 30320 219      20 120
1595280.6915 92.5311 -1.6528 3   18.0215  5  60006 303 2 2 1       1 1 0
1595501.5770 92.9467 -1.6527 3   18.0141  5  60006 303 2 2 0       1 1 1
1617535.0462277.5340 -1.5989 3   19.5291  7  60006 303 3 2 2       2 1 1
1618197.8517279.1371 -1.5988 3   19.5070  7  60006 303 3 2 1       2 1 2
1618243.2513999.9999 -6.3680 3  157.4935 39  60006 30319 217      20 020
1639674.3308554.8785 -1.5413 3   21.7906  9  60006 303 4 2 3       3 1 2
1640657.7411999.9999 -6.3951 3  142.4979 37  60006 30318 216      19 019
```

```
1641000.3171559.0574 -1.5411 3   21.7464  9  60006 303 4 2 2       3 1 3
1661698.4305924.4362 -1.4875 3   24.8058 11  60006 303 5 2 4       4 1 3
1663092.3866848.0797 -6.4279 3  128.2514 35  60006 30317 215       18 018
1663909.1619933.3111 -1.4872 3   24.7321 11  60006 303 5 2 3       4 1 4
1683607.2335999.9999 -1.4388 3   28.5748 13  60006 303 6 2 5       5 1 4
1685544.6412669.8926 -6.4669 3  114.7541 33  60006 30316 214       17 017
1686924.6552999.9999 -1.4384 3   28.4643 13  60006 303 6 2 4       5 1 5
1705400.6309999.9999 -1.3955 3   33.0975 15  60006 303 7 2 6       6 1 5
1708012.0903521.3648 -6.5125 3  102.0060 31  60006 30315 213       16 016
1710047.1459999.9999 -1.3950 3   32.9428 15  60006 303 7 2 5       6 1 6
1727078.5167999.9999 -1.3572 3   38.3740 17  60006 303 8 2 7       7 1 6
1730492.4521399.0089 -6.5655 3   90.0072 29  60006 30314 212       15 015
1733277.0635999.9999 -1.3565 3   38.1678 17  60006 303 8 2 6       7 1 7
1748640.7881999.9999 -1.3236 3   44.4042 19  60006 303 9 2 8       8 1 7
1752983.5770299.5550 -6.6267 3   78.7579 27  60006 30313 211       14 014
1756614.9173999.9999 -1.3227 3   44.1390 19  60006 303 9 2 7       8 1 8
1770087.3453999.9999 -1.2943 3   51.1880 21  60006 30310 2 9       9 1 8
1775483.4477219.9512 -6.6971 3   68.2581 25  60006 30312 210       13 013
1780061.2974999.9999 -1.2932 3   50.8565 21  60006 30310 2 8       9 1 9
1791418.0916999.9999 -1.2689 3   58.7255 23  60006 30311 210       10 1 9
1797990.1788157.3638 -6.7781 3   58.5080 23  60006 30311 2 9       12 012
1803616.8736999.9999 -1.2677 3   58.3203 23  60006 30311 2 9       10 110
1812632.9336999.9999 -1.2473 3   67.0166 25  60006 30312 211       11 110
1820502.0168109.1772 -6.8713 3   49.5076 21  60006 30310 2 8       11 011
1827282.3966999.9999 -1.2459 3   66.5303 25  60006 30312 210       11 111
1833731.7811999.9999 -1.2292 3   76.0611 27  60006 30313 212       12 111
1843017.3400 72.9943 -6.9790 3   41.2569 19  60006 303 9 2 7       10 010
1851058.6971999.9999 -1.2276 3   75.4865 27  60006 30313 211       12 112
1854714.5476999.9999 -1.2143 3   85.8592 29  60006 30314 213       13 112
1865534.6581 46.6360 -7.1042 3   33.7561 17  60006 303 8 2 6       9 0 9
1874946.6864999.9999 -1.2127 3   85.1887 29  60006 30314 212       13 113
1875581.1497999.9999 -1.2026 3   96.4107 31  60006 30315 214       14 113
1888052.6122 28.1418 -7.2512 3   27.0052 15  60006 303 7 2 5       8 0 8
1896331.5080999.9999 -1.1938 3  107.7156 33  60006 30316 215       15 114
1898947.3561999.9999 -1.2008 3   95.6370 31  60006 30315 213       14 114
1910569.9747 15.7693 -7.4265 3   21.0043 13  60006 303 6 2 4       7 0 7
1916965.5466999.9999 -1.1879 3  119.7738 35  60006 30317 216       16 115
1923061.7783999.9999 -1.1920 3  106.8313 33  60006 30316 214       15 115
1933085.6491  7.9940 -7.6403 3   15.7534 11  60006 303 5 2 3       6 0 6
1937483.1934999.9999 -1.1848 3  132.5853 37  60006 30318 217       17 116
1947291.1054999.9999 -1.1860 3  118.7716 35  60006 30317 215       16 116
1955598.6697  3.5096 -7.9105 3   11.2525  9  60006 303 4 2 2       5 0 5
1957884.3807999.9999 -1.1842 3  146.1499 39  60006 30319 218       18 117
1971636.5702999.9999 -1.1827 3  131.4577 37  60006 30318 216       17 117
1978108.2018  1.2280 -8.2737 3    7.5017  7  60006 303 3 2 1       4 0 4
1978169.0444999.9999 -1.1862 3  160.4676 41  60006 30320 219       19 118
1996099.4862999.9999 -1.1821 3  144.8895 39  60006 30319 217       18 118
```

Appendix C

FTIR Spectra of Ices Studied in the THz-TDS

Where available, spectra of unsaturated samples of species studied in the FTIR are presented here. These spectra are background-subtracted using a scan of the blank substrate, but have had no correction made to the baseline in post-processing. They are intended as a guide to future work for a qualitative identification of an ice species probed by the FTIR, and not for quantitative assignment of vibrational modes or intensities.

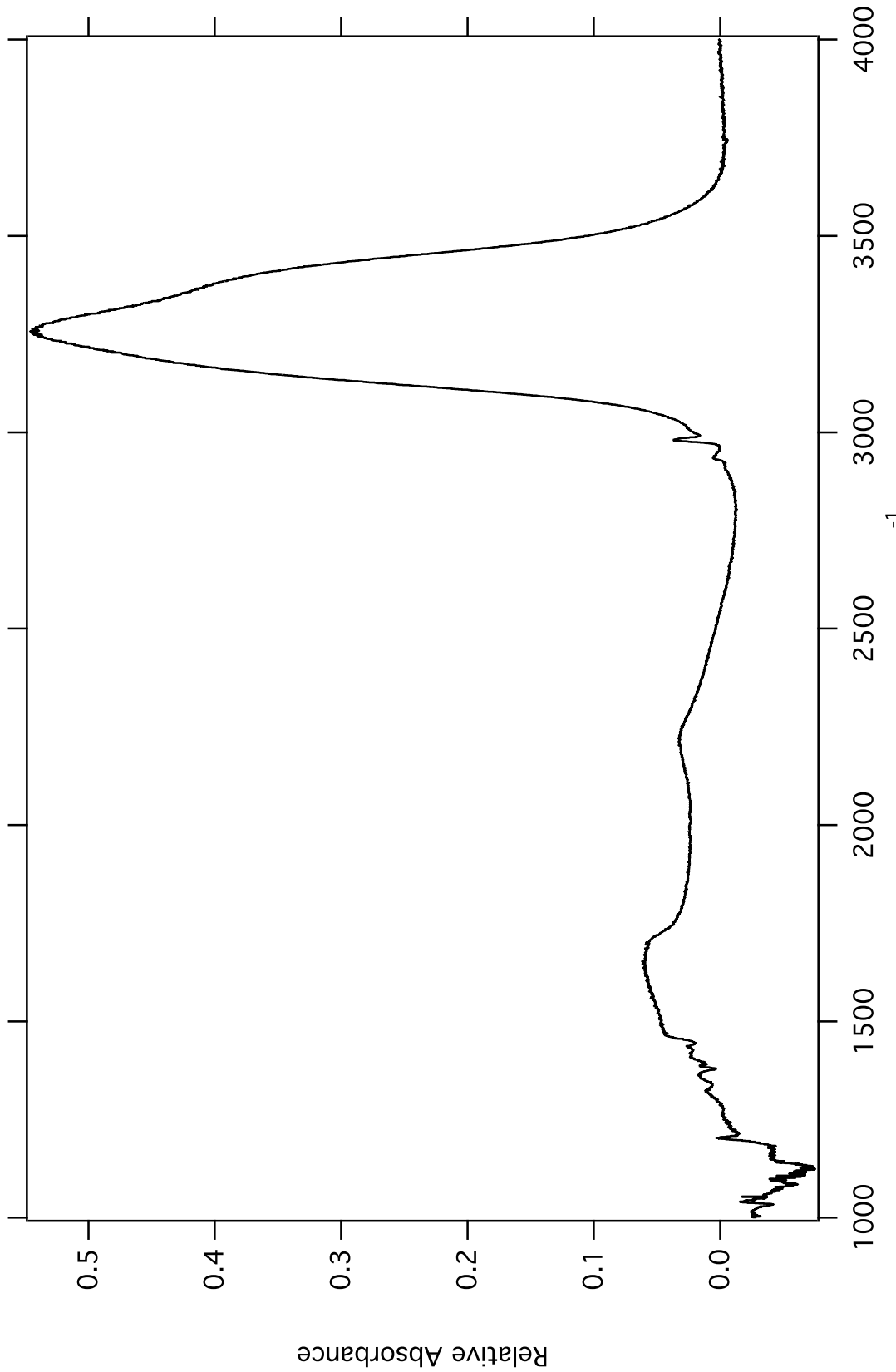

Figure C.1: FTIR spectrum of amorphous water at 10 K.

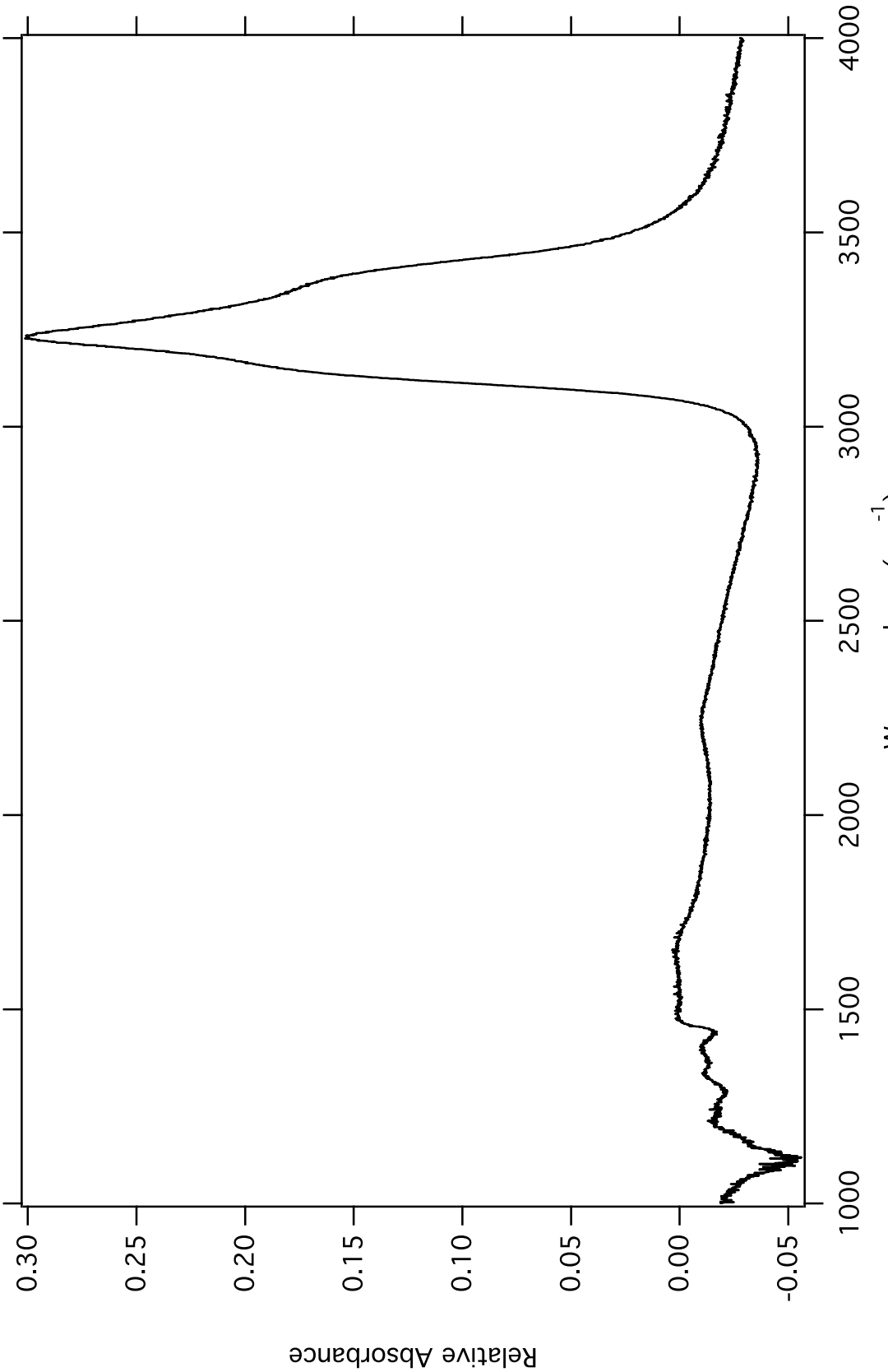

Figure C.2: FTIR spectrum of crystalline water at 140 K.

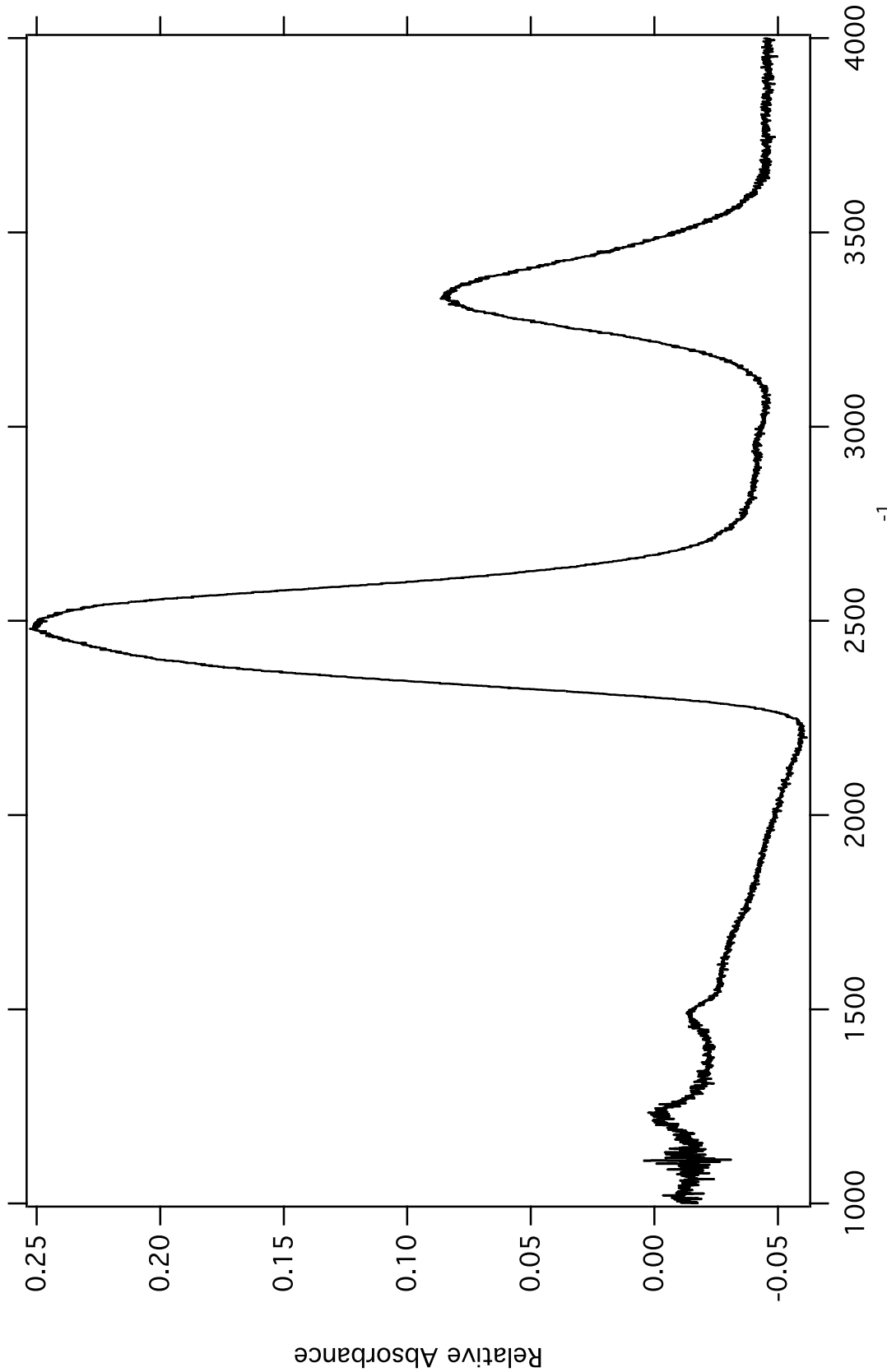

Figure C.3: FTIR spectrum of amorphous D_2O at 10 K.

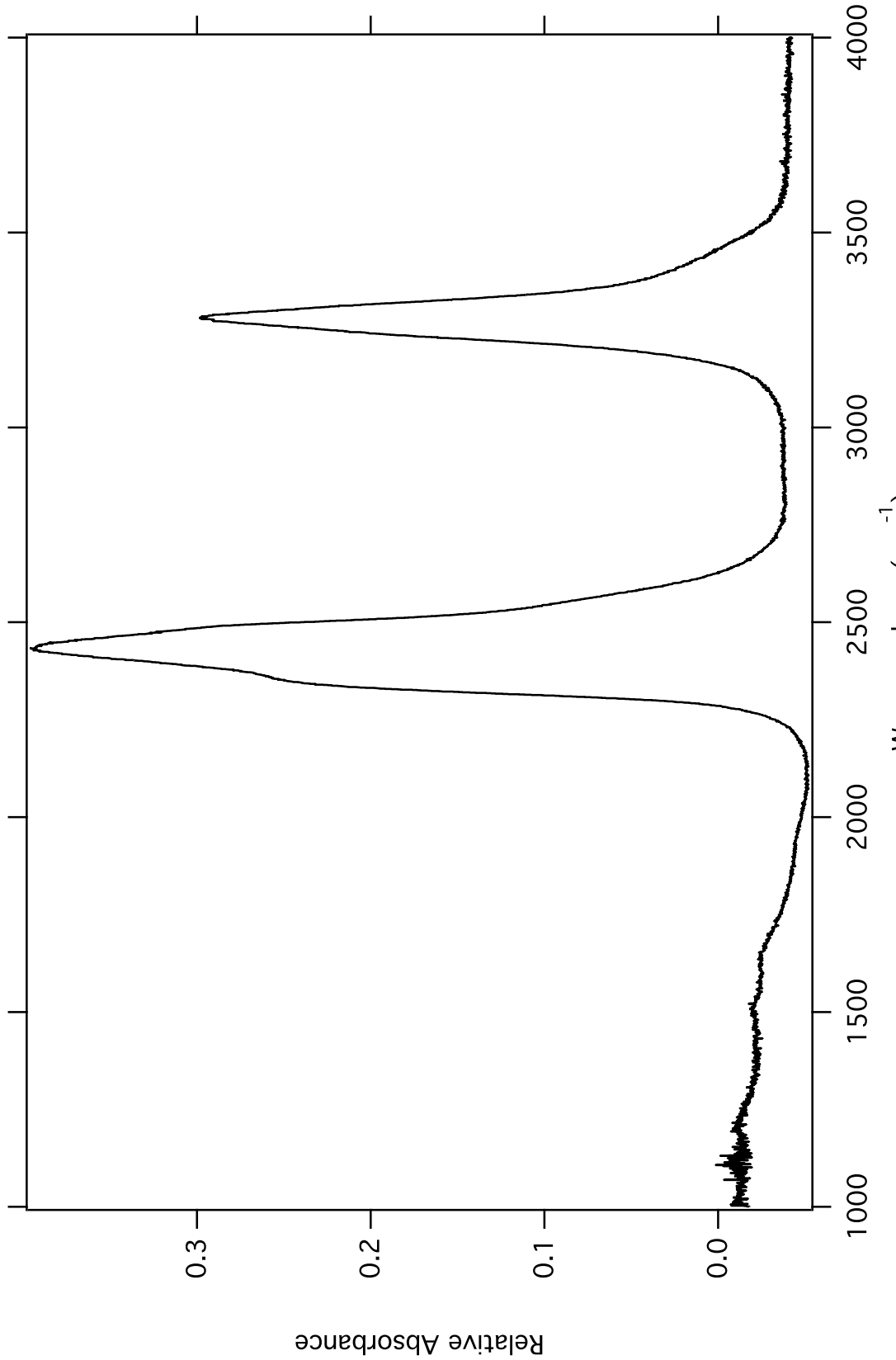

Figure C.4: FTIR spectrum of crystalline D_2O at 150 K.

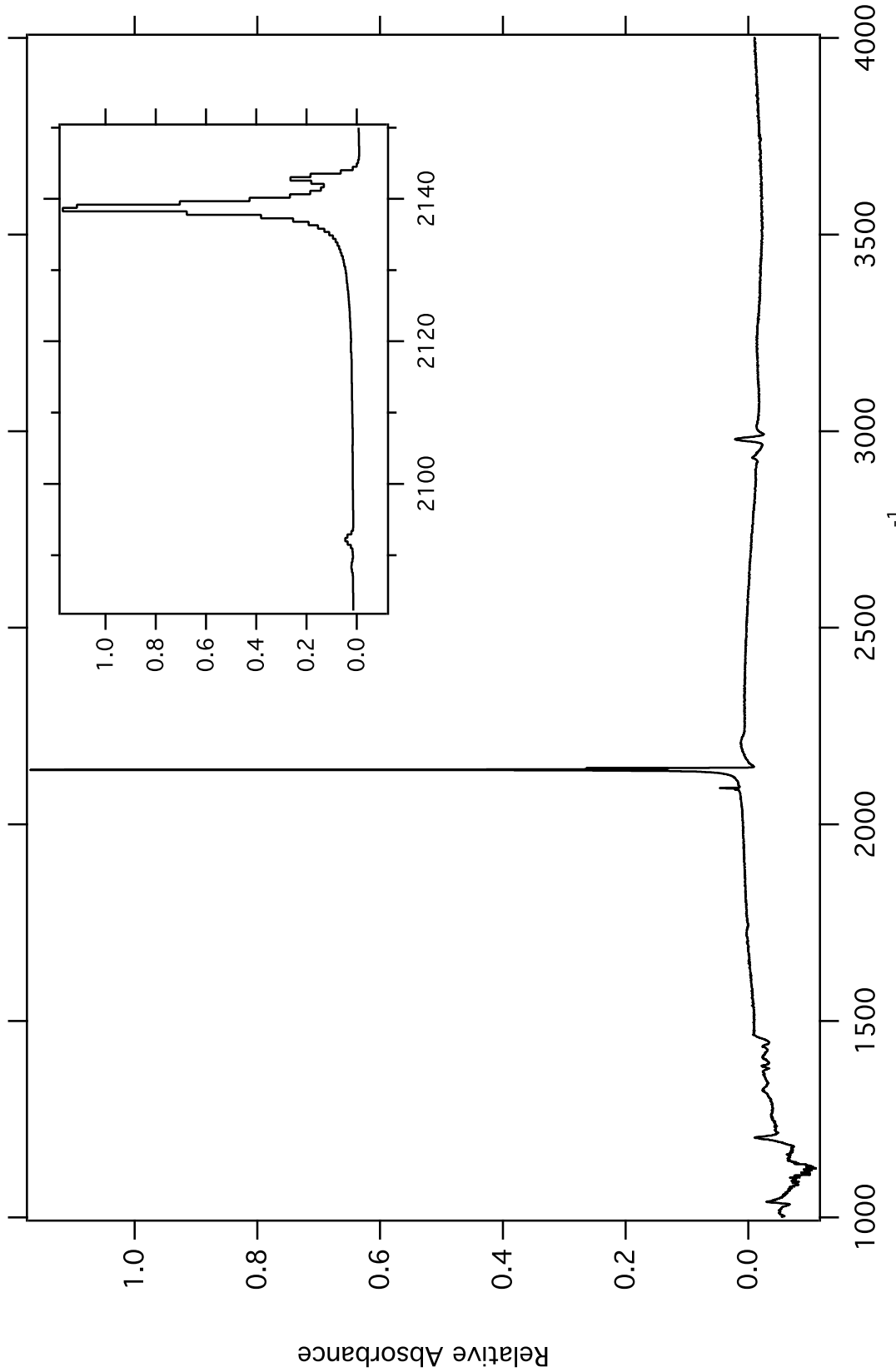

Figure C.5: FTIR spectrum of crystalline CO at 30 K. Inset shows detail.

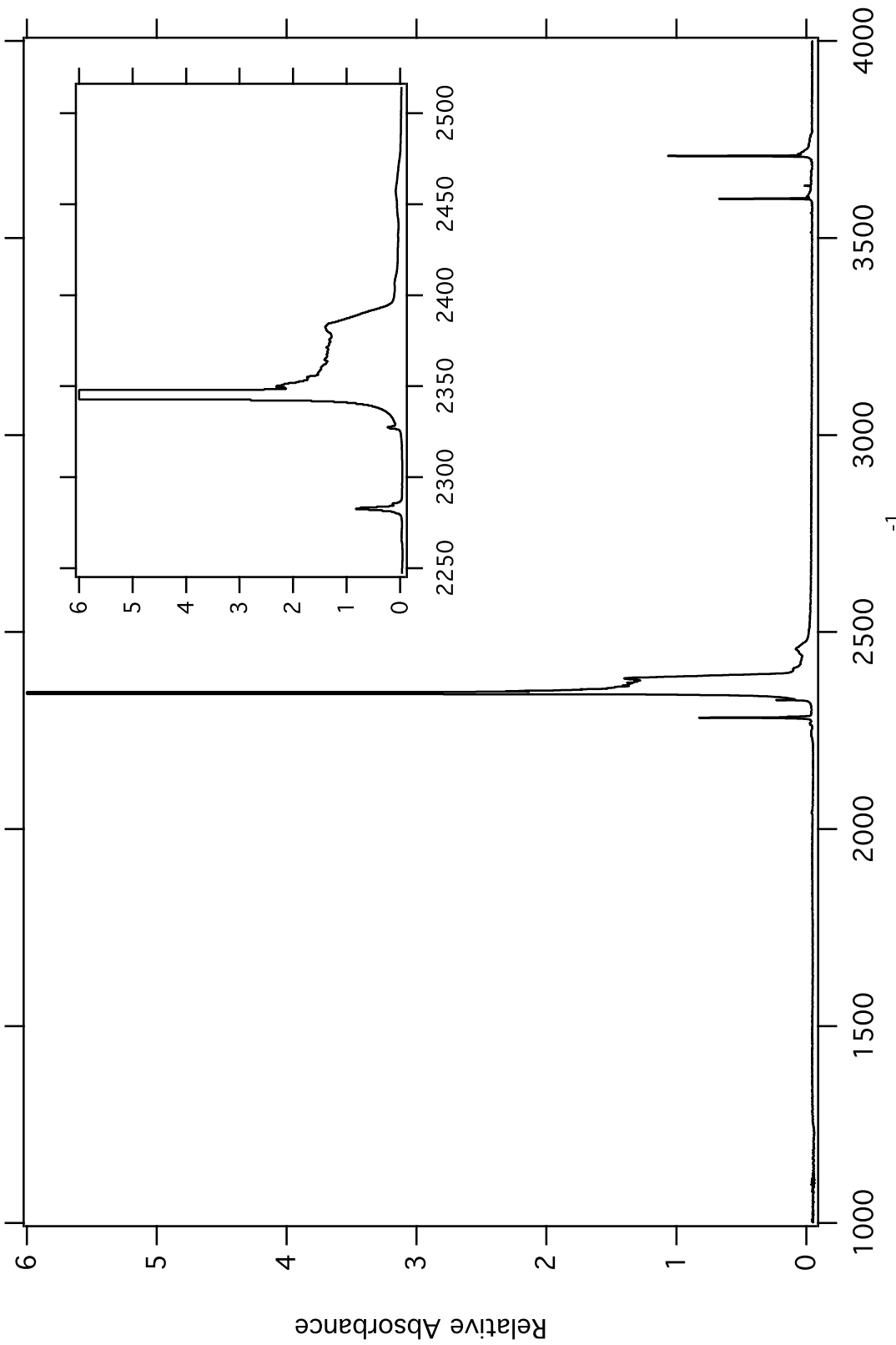

Figure C.6: FTIR spectrum of crystalline CO_2 at 75 K. Inset shows detail.

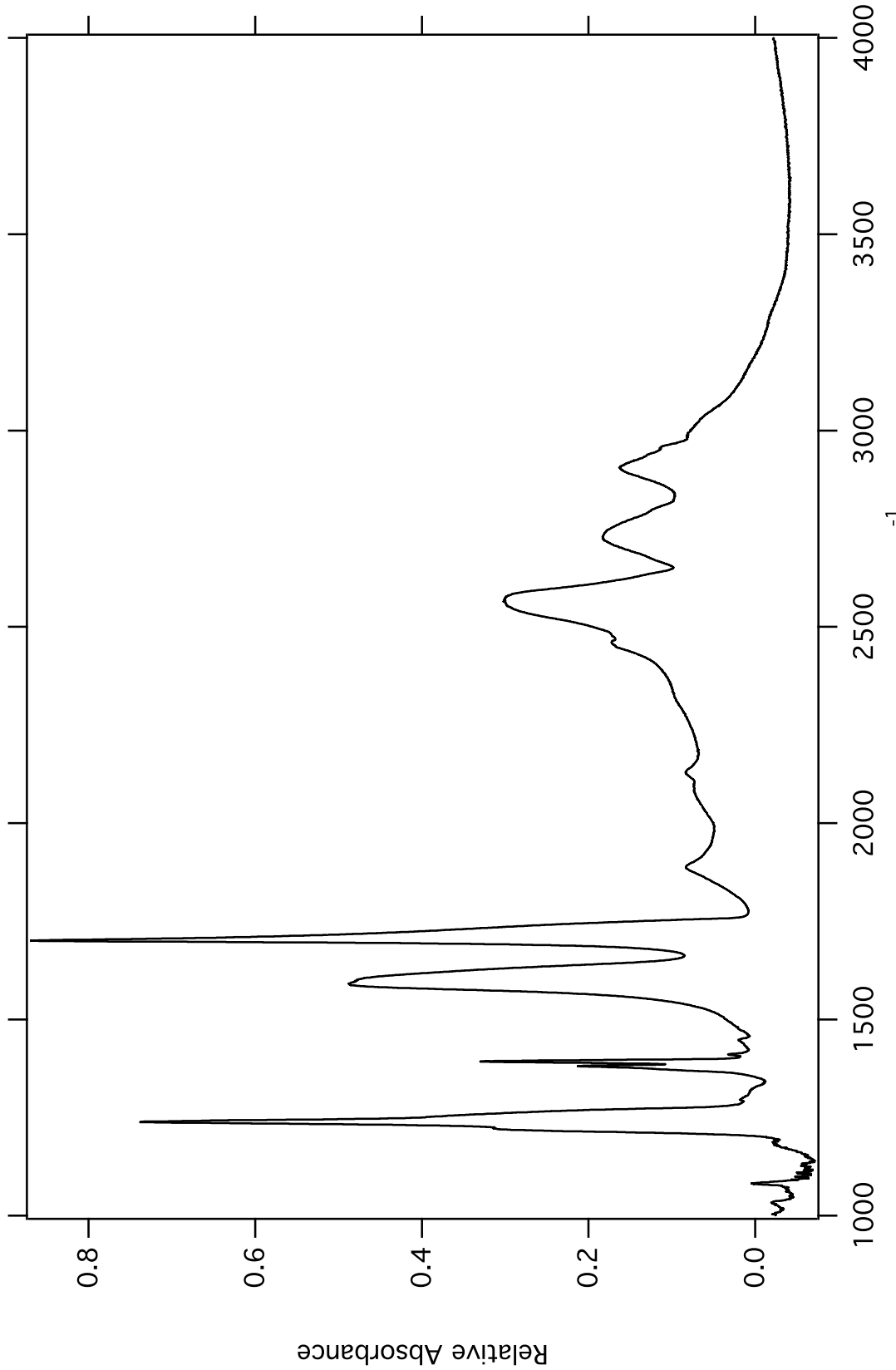

Figure C.7: FTIR spectrum of crystalline formic acid at 150 K.

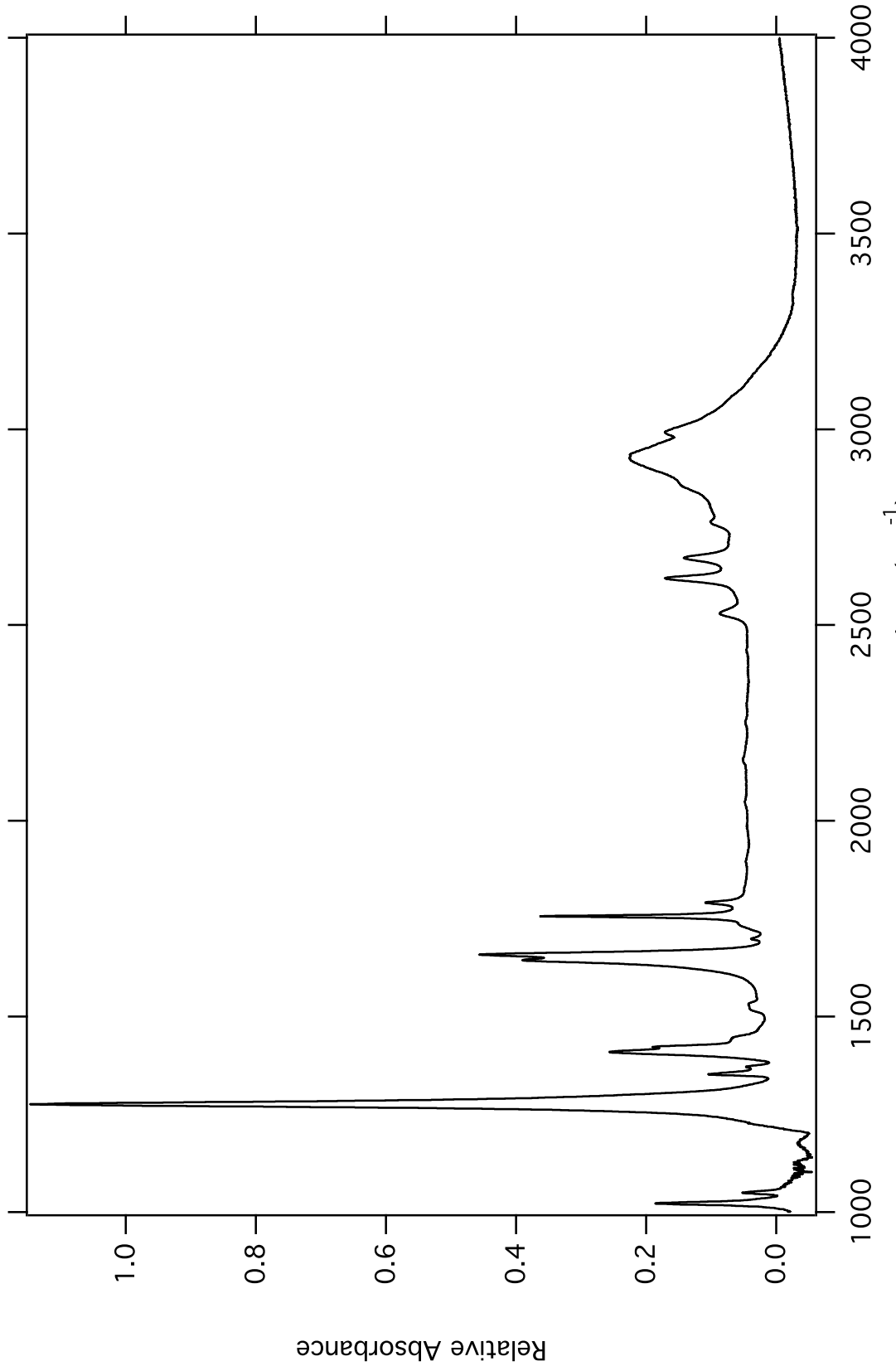

Figure C.8: FTIR spectrum of crystalline acetic acid at 180 K.

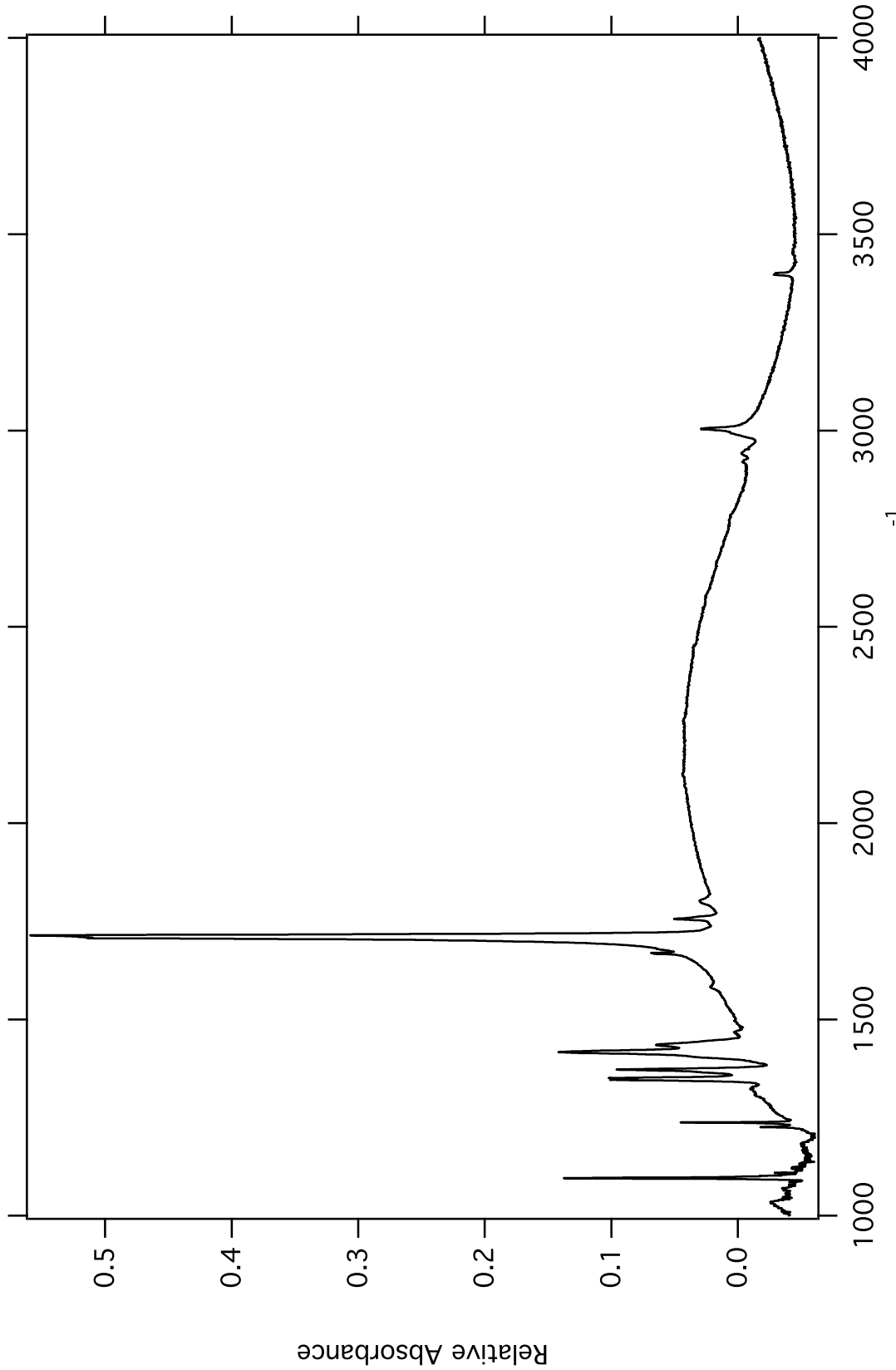

Figure C.9: FTIR spectrum of crystalline acetone at 140 K.

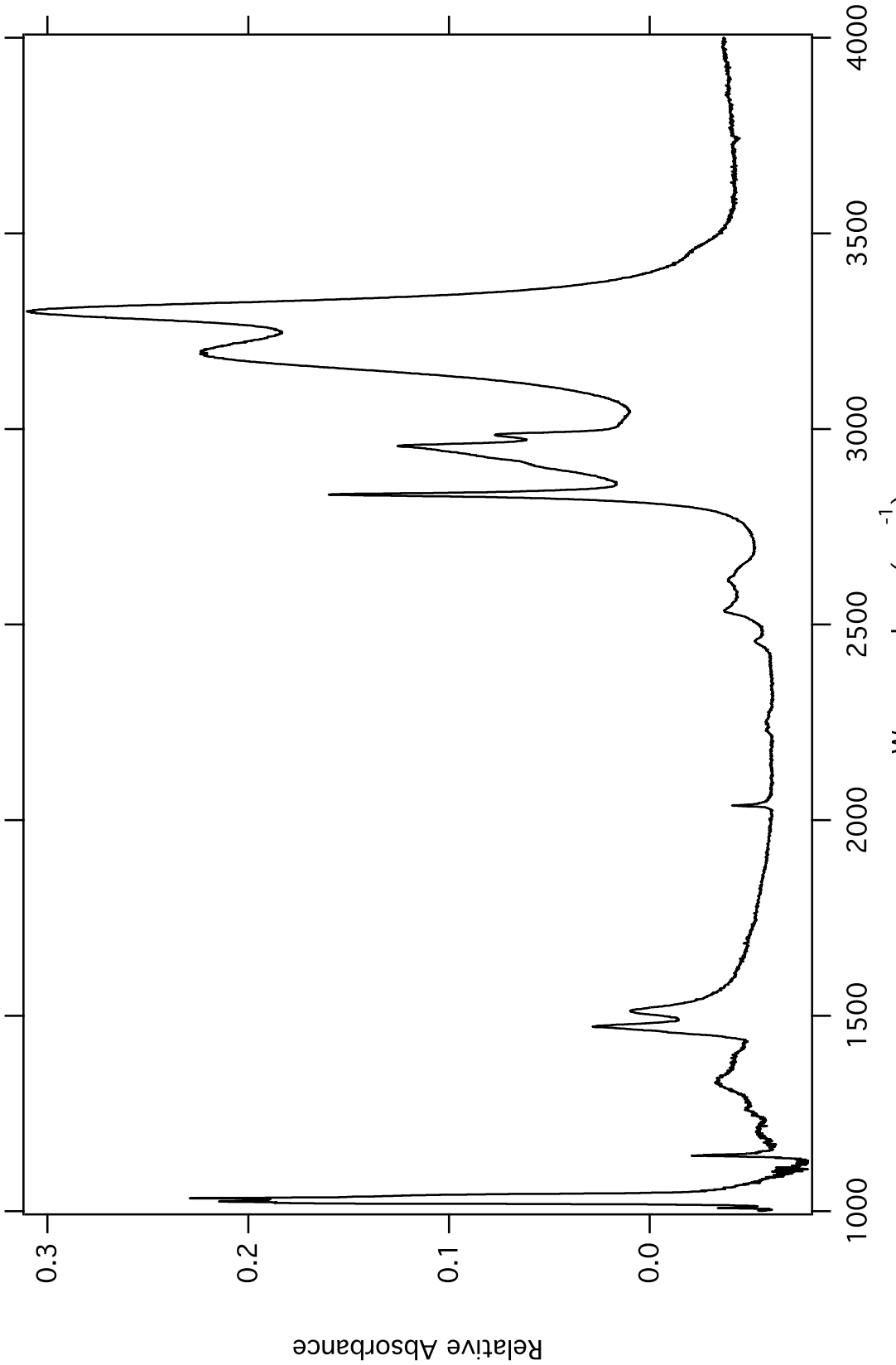

Figure C.10: FTIR spectrum of crystalline methanol at 140 K.

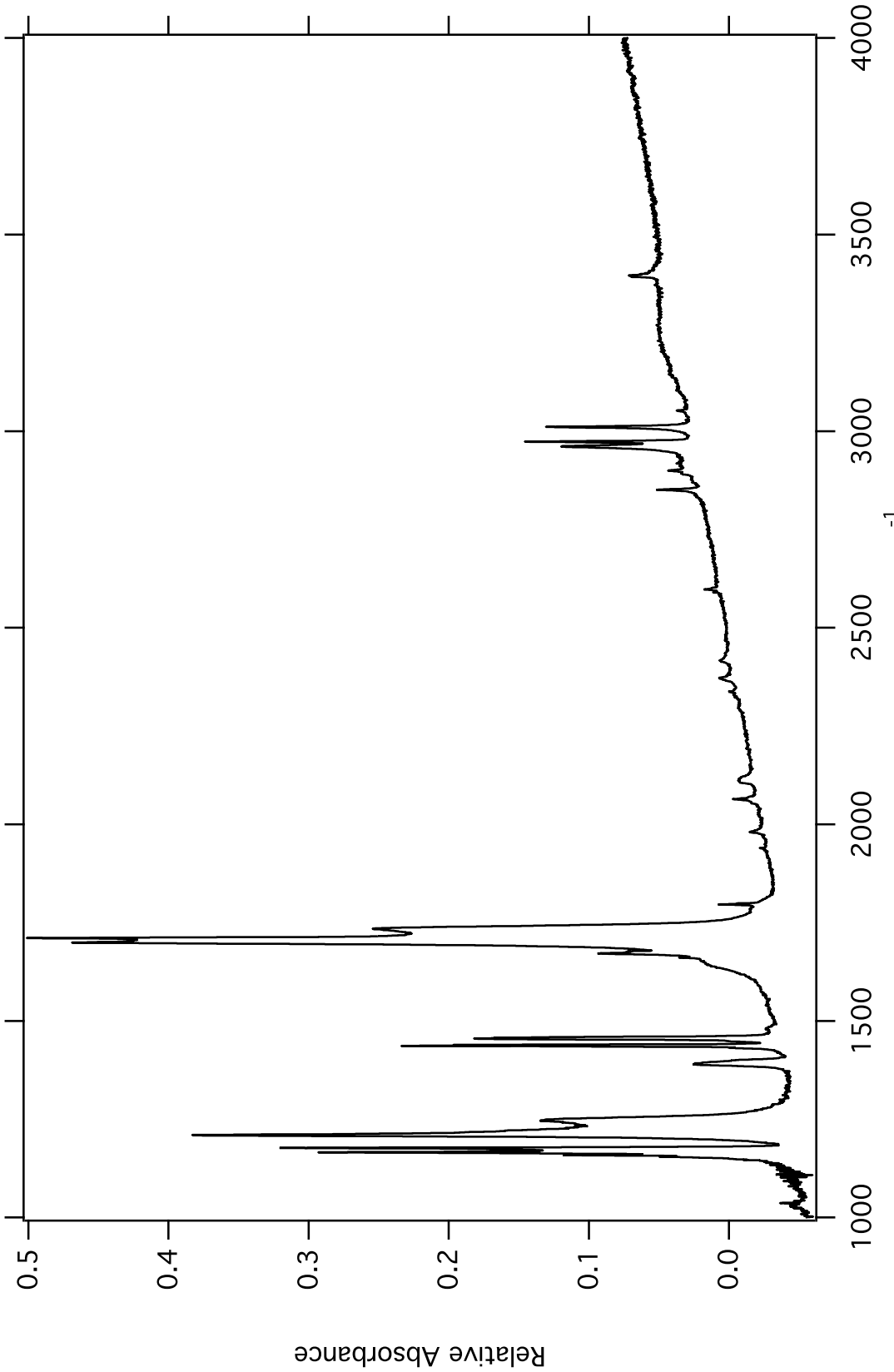

Figure C.11: FTIR spectrum of crystalline methyl formate at 135 K.